OXIDATION OF ALUMINIUM-MAGNESIUM ALLOYS AT ELEVATED TEMPERATURE IN THE SOLID, SEMI-LIQUID AND LIQUID STATES

A THESIS SUBMITTED FOR

THE DEGREE OF DOCTOR OF PHILOSOPHY

BY

M.P. SILVA

DEPARTMENT OF MATERIALS TECHNOLOGY,
BRUNEL, THE UNIVERSITY OF WEST LONDON,
UXBRIDGE,
MIDDLESEX,
ENGLAND.

MAY 1987

Dedicated

To

The Memory Of

My Father

C O N T E N T S

A C K N O W L E D G E M E N T S

The author wishes to thank Mr. D. Talbot for advice, encouragement and invaluable discussion during the course of the investigation and Professor M. Bevis for the provision of laboratory facilities.

The author wishes to express his appreciation to the ALCOA Technical Center, Pittsburgh, U.S.A. for the provision of some of the materials for the investigation and to ALCAN International, Banbury, U.K. for chemical analyses of the materials investigated. Acknowledgement is also made to Mr. R. Davis for assistance in the foundry.

The author also acknowledges financial support provided by the Science and Engineering Research Council (SERC), Swindon, U.K.

Finally, thanks are due to Dr. M.J. Edirisinghe and Dr. B.S. Abeysuriya for helpful comments on the presentation, and to Mrs. S. Speed for typing the thesis.

-----oOo-----

A B S T R A C T

Sensitive thermogravimetric equipment was used to monitor the oxidation rates of Al-1 to 9% Mg alloys in 0.21 oxygen/0.79 helium mixtures with and without 0.03 atm water vapour pressure, in the temperature range 500-725^{o}C which include their respective solid, semi-liquid and liquid states. These measurements were supported by structural and topographical studies of oxide films using SEM, X-ray diffraction, and TEM with electron diffraction and EDX techniques. The objective was to provide information in the context of dross formation during melting operations.

The only oxidation product observed was MgO. The oxidation rates do not follow simple rate laws. The rate normally increases as the temperature is raised except for a curious inverse relationship for liquid alloys just above the liquidus temperatures due to the formation of undulating surfaces. An amorphous MgO film formed on liquid alloys restricted the initial oxidation but, following an incubation period, crystallisation of the film induced breakaway oxidation. The crystallisation was promoted by high magnesium contents, high temperatures and moist atmospheres. The oxidation rates for alloys in the semi-liquid state were as follows:

(i) for < 50% liquid, the rates were faster than those for wholly solid alloys due to preferential oxidation of magnesium-enriched liquid fractions along grain boundaries.

(ii) for > 50% liquid, the rates were initially faster than those for wholly liquid alloys due to the presence of solid phase particles which acted both as disruptive stress-raisers and as sources of nuclei for crystallisation of the amorphous oxide film over the liquid phase.

For the moist atmosphere,

(i) wholly solid alloys and semi-liquid alloys with < 50% liquid

oxidised initially faster but eventually slower than in the dry atmosphere. These effects are explained by enhanced initial oxidation but suppressed subsequent nucleation of tertiary MgO particles and by the injection of OH^- ions into the oxide.

(ii) wholy liquid alloys and semi-liquid alloys with > 50% liquid oxidised faster than in the dry atmosphere because of the injection of OH^- ions into the oxide with consequent disruptive effects caused by hydrogen absorption by the alloy.

The addition of 0.003% Be to Al-8% Mg alloy decreased the oxidation rate markedly by toughening the MgO films preventing cracking and hence the nucleation of tertiary MgO. Small additions of Mn or Zr offset the effect of Be and probably enhanced the Mg^{2+} ion conductivity in the oxide by the injection of Mn^{2+}, Mn^{4+} or Zr^{4+} ions. For alloys with Be, although breakaway eventually occurred it was not initiated by crystallisation of the amorphous film and moisture in the atmosphere increased the oxidation throughout the temperature range, 500-725^{o}C.

1. INTRODUCTION

Magnesium is one of the most important alloying elements in the aluminium industry. It is a component not only of the high-strength age-hardening Al-Cu-Mg-Si and Al-Zn-Mg-Cu alloys, but also of a range of alloys characterised by medium strength, good impact resistance, high resistance to corrosion and good machinability in which it is the predominant alloying element. These characteristics underlie the use of these alloys in many applications[1] of which one of the more important is the mass production of beverage containers.

Quiescent melts of pure aluminium and magnesium-free commercial aluminium alloys oxidise relatively slowly at normal melt processing temperatures because the oxide formed offers a high degree of protection from further oxidation, but it is well-known that aluminium-magnesium alloys melted under the same conditions oxidise much more rapidly. This rapid oxidation necessitates special care in melting practice.

In comparison with other alloying elements, the use of magnesium represents a significant raw material cost for aluminium alloys because the price of magnesium is about twice that of aluminium. It is found that magnesium is lost by preferential oxidation during melting and alloying and the quantity of dross produced is proportional to the amount of magnesium in the alloy. It has been estimated[2] that on average this loss is 9% of the magnesium used in the aluminium industry; thus an operation using 75,000 tonnes of magnesium annually with a 6% oxidation loss incurs an annual direct loss of £11,119,500, assuming the October 1986 price of magnesium, i.e. £2471 per tonne[3]. This loss represents magnesium metal which was charged into the furnace but which never emerged in the final product.

In addition to the direct loss of magnesium, the oxidation also produces substantial indirect losses[4]. The large quantity of dross generated by

these alloys creates a thermally insulating blanket on the melt surface, impeding heat transfer to the metal from the radiating furnace side-walls and roof, thus increasing the energy required for melting and therefore incurring extra cost. The thermally insulating effect also leads to a longer heating time compared with that for other alloys with a consequent reduction in the productive efficiency of a furnace. The frequent furnace skimming required increases the total metal loss in melting because the skimming operation by which the oxide layer is removed unavoidably removes some of the underlying metal.

A further problem of much concern is the incorporation of oxide into the melt during casting, creating difficulties in subsequent metal working processes and giving rise to defective products with poor quality. Another major penalty is unsoundness in casting giving degraded mechanical properties[5] caused by metal-mould reaction during casting.

Beryllium is sometimes added to aluminium-magnesium alloys to alleviate these difficulties. Small additions,0.0001% beryllium, dramatically reduce the magnesium loss and >0.0005% beryllium gives an added benefit in preventing segregation of magnesium in the molten alloy. However, beryllium compounds are toxic and the use of beryllium is restricted because of its carcinogenic effects[6].

The need to alleviate all of these difficulties and economic penalties is becoming increasingly urgent and significant with the modern need to recycle secondary metal which possesses a large surface area to volume ratio and with the escalation in energy cost continuously. For this purpose it is desirable to prescribe melting practices with suitable holding times and temperatures to minimise dross formation and oxidation losses. This is facilitated if systematic knowledge of the oxidation behaviour of aluminium-magnesium alloys is available for different stages during the

melting process. Considerable progress has been made on the basis of experience in melting and casting, but this empirical work has not hitherto been systematically guided by knowledge of the fundamental process by which solid, liquid and particularly semi-liquid aluminium-magnesium alloys oxidise.

In contrast, recent years have seen increased emphasis on fundamental aspects of metal-oxygen interaction and an improved appreciation of oxidation behaviour. This progress has to a large extent been due to the availability of improved equipment with high resolution and to the use of more refined experimental techniques. Oxidation kinetics have been studied with greater precision through the use of sensitive microbalances operating in controlled atmospheres at high temperatures. Improved electron microscopy, electron and x-ray analytical techniques and high temperature metallographic techniques have provided insight into the nature of oxides. Moreover, improved diffusivity, electrical conductivity and ionic conductivity measuring techniques, together with the mechanical testing techniques have given further insight into the defect structure and mechanical properties of oxides. It has also been possible, with ultra-high vacuum techniques, to study the initial adsorption of oxygen, oxide nucleation and nuclei growth on metal surfaces, using low-energy diffraction and other similar techniques.

Consequently, several kinetic, structural, and mechanistic studies on the oxidation of aluminium-magnesium alloys have been reported. Individual studies have in general been confined either to liquid or solid alloys, to low or high magnesium contents, to binary or commercial alloys, or to dry or moist atmospheres. This information does not yield comprehensive comparisons of the degree of oxidation between solid and liquid alloys, between different magnesium contents, or between different atmospheres. The absence of any information for the semi-liquid state is a particularly serious

disadvantage in approaching problems of dross formation.

The strategy in the present approach was to conduct isothermal oxidation studies on alloys with a range of magnesium contents at various temperatures including their respective solid, semi-liquid, and liquid states, under the same experimental conditions in selected atmospheres. Truly isothermal oxidation kinetics have not hitherto been reported, i.e. nominally isothermal kinetics have always included heating samples to the test temperatures in the oxidising atmosphere. The preliminary oxidation during heating creates uncertainty in theoretical interpretation.

Oxidation rate measurements were made using a sensitive thermogravimetric microbalance operating in controlled atmospheres for correlation with appropriate structural information on the oxidation products obtained using electron optical techniques and X-ray diffraction.

A fruitful approach to the present work requires consideration of the following topics:

(i) Oxygen adsorption and nucleation.

(ii) Theoretical and empirical growth laws.

(iii) Defect structures and transport mechanisms in oxides.

(iv) Stresses in oxides.

(v) Oxidation of alloys and of aluminium-magnesium alloys in particular.

(vi) Hydrogen absorption by aluminium-magnesium alloys.

These topics are reviewed in the first few sections of the thesis.

2. PRINCIPLES OF OXIDATION OF METALS

In this Chapter several generalised concepts which may be applied to interpret the phenomena observed in the present work are considered. Growth and transport mechanisms accompanied by oxide theories for continuous oxide films are first described. These ideas are modified for application to real oxides because the idealised theoretical models, developed using numerous simplifying assumptions for ease of mathematical manipulation, are seldom directly applicable to phenomena observed experimentally. Impurities in the metal and also stress generation due to incompatibility between the metal and the scale, are examples of factors which can contribute to deviations from idealised models leading to multiphase oxide structures, and cracking and spalling of the films with complex oxidation kinetics.

2.1. Reaction Tendency

A metal oxide forms by transfer of electrons from the metal to oxygen in its environment, so that the overall reaction:

$$2M + \frac{x}{2} O_2 \longrightarrow M_2O_x$$

is the summation of the partial ionic reactions:

$$2M \longrightarrow 2M^{x+} + 2xe^-$$

and

$$\frac{x}{2} O_2 + 2xe^- \longrightarrow xO^{2-}$$

The reaction is spontaneous if the Gibbs free energy change is negative and since the entropy change is negative due to the disappearance of oxygen gas, metal oxides become progressively less stable with increasing temperature by virtue of the relationship[7]:

$$\frac{d}{dT} \Delta G^{\ominus} = - \Delta S^{\ominus} \qquad \text{..... (2.1)}$$

This is reflected in the upward slope of the lines in the well-known oxygen potential diagram reproduced in Figure 1[8]. The lines for more noble

metals which are less easily oxidised occur near the top of the diagram but some normally reactive metals at the bottom of the diagram also resist oxidation by initially forming coherent impervious oxide films.

2.2. Oxygen Adsorption, Oxide Nucleation and Growth

The initial process in the metal oxygen interaction is the adsorption of oxygen molecules at the surface of a film-free solid[9,10]. Since this process results in a decrease in both the surface free energy and the entropy implying a decrease in enthalpy, the adsorption is an exothermic process, as evident in the relation:

$$\Delta G = \Delta H - T\Delta S \quad \ldots\ldots\ldots\ldots\ldots\ldots (2.2)$$

Adsorption is further classified as physisorption and chemisorption[11,12].

In physisorption, gases are bound to the surface by weak Van der Walls' forces. This is a low temperature reversible process which proceeds without significant activation energy so that the rate controlling step is the impingement of the oxygen molecules on the surface[11].

In contrast, chemisorption involves the rearrangement of valence electrons of the metal and of the adsorbed gas atoms to form bonds which are many orders of magnitude stronger than those for physisorption. Although chemisorption has often been considered as a slow process requiring activation energy, it has now been shown that on clean metals rapid chemisorption can occur without any apparent activation energy[13,14].

The application of modern electron optical techniques, e.g. LEED, HEED, FEM, FIM, AES and XPS[14-16], provides greater insight into the kinetics of adsorption, and the chemical nature and structure of the adsorbed layer. The most widely used low energy electron diffraction (LEED) technique has established that the structure of the adsorbed gas layer depends on the nature of the adsorbate and on the nature, crystal structure, purity, defect

structure and temperature of the adsorbent.

Oxygen adsorption on nickel has been thoroughly investigated[17-20] and serves as a prototype for other metal oxygen interactions. Despite this, the chemical interactions during chemisorption are still not perfectly understood[21], but the process can, in general, be visualised as the development and reconstruction of an adsorbed layer forming a sub-oxide of two-dimensional structure in a place exchange mechanism[22-25]. An example of the mechanisms suggested in the model advanced by Fehlner and Mott[25] in which oxygen molecules are dissociatively chemisorbed by interchange of oxygen atoms adjacent to the adsorbed molecules with the underlying metal atoms, as illustrated in Figure 2[25].

The nucleation process, following chemisorption producing the two-dimensional sub-oxide, plays an important role in the formation of a three-dimensional true oxide film. The formation of discreate oxide crystallites as nuclei is a fairly general phenomena which was first detected by Bardolle and Benard[26] while studying the oxidation of iron at elevated temperature.

In a comprehensive study, Gronlund[27] distinguished three successive stages in the development of oxide nuclei in copper, as illustrated in Figure 3.

(1) An incubation period which terminates when a given number of nuclei suddenly appear on the surface.
(2) A period of lateral growth of nuclei, ending when they impinge to form a complete oxide layer.
(3) A period of uniform outward growth producing an oxide layer of appreciable thickness.

The nature and size of the nuclei are both pressure and temperature dependent.

Extensive supporting evidence for this growth process has been observed for other metals of which the most recent is by Hart and Maurin[28] for aluminium and Hayden et al[29] for magnesium-aluminium alloys. A detailed treatment of the influence of crystal surfaces, temperature and pressure on the process is available elsewhere[30].

The transition by which three-dimensional nuclei form within the adsorbed layer is still unresolved. On one hand, it is argued that the nucleation sites may be at surface heterogenieties, e.g. defects or impurities of high chemical potential[31]. Alternatively, it is possible that nuclei may form homogeneously by a transition of the two-dimensional chemisorbed layer. An oxygen depleted zone around the nuclei prevents the formation of new centres of growth, as shown in Figure 4[32].

2.3. Defect Structures and Transport Mechanisms in Oxides

In the growth process following nucleation, the rate determining step is usually the transport of reacting species through the oxide which is controlled by the defect structure providing the transport mechanism.

2.3.1. Defect Structures

No real crystal structure is perfect but contains structural imperfections classified as[33]:

(1) Point or lattice defects.

(2) Line defects.

(3) Plane defects.

Point defects include lattice vacancies, interstitial atoms, and misplaced substitutional atoms. Line defects are dislocations. Plane defects comprise stacking faults, internal surfaces such as grain boundaries, and external surfaces.

In a crystal, all types of defects are thermodynamically favoured at temp-

eratures above absolute zero. The imperfections which most directly influence transport mechanism through oxide films are point defects. These are of several different kinds and although all are always present to some degree, one type usually predominates in a particular solid, so that it is customary for most purposes to explain the properties of a single crystal in terms of a single defect type. The notation describing the various types of point defects used throughout this work is given in Table 1.

Defect structures are reviewed in detail by Kofstad[34], Kroger[35], and Jarzebski[36] and the following brief description of oxides is given to show how they may be classified according to the predominating defect structures.

2.3.2. Statistical Analysis of Defect Stability

At absolute zero, atoms or ions on the normal lattice on a crystal remain immobile. At higher temperatures, to satisfy the conditions required, in general, for thermodynamic equilibrium when a compact scale is formed on a metal, the crystals of oxide must contain point defects. If the equivalent numbers of complementary defects are found, stoichiometry[36] is preserved, but if they are unbalanced the crystals exhibit non-stoichiometry[37]. This is because energy is expended in incorporating the point defects, but the entropy of the system increases extremely at first and then more slowly as the number of defects increases. Thus the equilibrium condition, when the free energy of the system is minimum, is satisfied only by a finite degree of defects, i.e. α_e, as illustrated schematically in Figure 5. Moreover, defect equilibria with a large positive enthalpy of formation which are not favoured at low temperatures become significant at high temperatures because of the influence of the temperature on the entropy term in equation (2.2). Thus the transport mechanisms are stimulated by increasing number of defects required for the

condition of lowest free energy[35].

2.3.3. Stoichiometric Oxides

Although, in principle, all oxides are non-stoichiometric, some pure oxides exhibit no appreciable deviation from stoichiometry. The essential feature of stoichiometric oxides is that the equivalence between metal and oxygen atoms is conserved through the formation of complementary point defects. Although there are other possibilities[38], the widely used Schottky[39,40] and Frenkel[41] disorders are schematically illustrated in Figures 6 and 7 respectively and are exhibited by oxides adopting close-packed structures with a large percentage of ionic bonding. Schottky disorder represents equivalent concentrations of cation and anion vacancies. In Frenkel disorder, the defects are limited either to the cation or the anion lattice. Since the migration of these lattice defects are fast in comparison with electronic defects, these oxides exhibit ionic-conducting properties and are classified according to the nature of defect type:

(a) Anionic Oxides

The conduction, here, is led by anions, either as a result of vacancy diffusion on the anion lattice or by movement of interstitial anions.

(1) Anion Vacancies

These are oxides with either Schottky or anionic Frenkel disorder where anions and not cations are the mobile species. The oxidation reaction at the oxide/metal interface can be written as:

$$2M \rightleftharpoons M_2O_y + y(O^{2-}\square)/x + 2y(e\bullet)/x \quad \ldots\ldots\ldots\ldots\ldots\ldots (2.3)$$

The anion vacancies diffuse to the oxide/oxygen interface and react with gaseous oxygen:

$$(O^{2-}\square)/x + 2(e\bullet)/x \longrightarrow (O^{2-}\square)/o + 2(e\bullet)/o \quad \ldots\ldots\ldots\ldots\ldots (2.4)$$

$$(O^{2-}\square)/o + 1/2\ O_2 + 2(e\bullet)/o \rightleftharpoons O^{2-}/o \quad \ldots\ldots\ldots\ldots\ldots (2.5)$$

The activities of intrinsic anion defects at equilibrium for equation (2.3) is given by:

$$a\left[(O^{2-}\square)/x\right]\ a^2\ \left[(e\bullet)/x\right] = K \qquad \ldots\ldots\ldots\ldots\ldots\ldots\ (2.6)$$

where K is the equilibrium constant.

Assuming that the concentrations of $(O^{2-}\square)$ and of $(e\bullet)$ are so dilute that Henry's law applies, then

$$a(O^{2-}\square) \propto n(O^{2-}\square) \quad \text{and} \quad a(e\bullet) \propto n(e\bullet)$$

and since also for electroneutrality

$$n(O^{2-}\square) = n(e\bullet) = n$$

Hence the concentration of defects at equilibrium for equation (2.3) is described by:

$$n^3 = n\left[(O^{2-}\square)/x\right]\ n^2\ \left[(e\bullet)/x\right] = K_1 \qquad \ldots\ldots\ldots\ldots\ldots\ldots\ (2.7)$$

$$\therefore\ n = K_1^{1/3} \qquad \ldots\ldots\ldots\ldots\ldots\ldots\ (2.8)$$

Therefore, both scale-forming and defect-injecting reactions take place at the oxide/metal interface and the reaction is independent of the oxygen pressure.

(2) Anion Interstitials

These are oxides with anionic Frenkel disorder. The defects introduced at the oxygen/oxide interface diffuse through the oxide for scale-forming reaction at the oxide/metal interface:

$$1/2\ O_2 \rightleftharpoons (O^{2-}\bullet)/o + 2(e\square)/o \qquad \ldots\ldots\ldots\ldots\ldots\ (2.9)$$

$$2M + y(O^{2-}\bullet)/x + 2y(e\square)/x \rightleftharpoons M_2O_y \qquad \ldots\ldots\ldots\ldots\ldots\ (2.10)$$

By analogy with equation (2.6), the concentration of intrinsic defects at equilibrium for equation (2.9) shows that the reaction is pressure-dependent:

$$n^3 = n[(O^{2-}\bullet)/x]\ n^2\ [(e\square)/x] = K_1(P_{O_2})^{1/2} \quad \ldots\ldots\ldots\ldots\ (2.11)$$

$$\therefore\ n = K_1^{1/3}(P_{O_2})^{1/6} \quad \ldots\ldots\ldots\ldots\ (2.12)$$

(b) Cationic Oxides

Cation conduction occurs as a consequence of the movement of cations either by interstitial diffusion or by lattice vacancy diffusion.

(1) Cation Vacancies

These are oxides with either Schottky or cationic Frenkel disorder where cations and not anions are the mobile species. Although not an oxide a well-known example of this type conductor is silver chloride, as illustrated in Figure 8[41].

$$1/2\ Cl_2 \rightleftharpoons AgCl + (Ag^+\square)/o + (e\square)/o \quad \ldots\ldots\ldots\ldots\ (2.13)$$

$$Ag + (Ag^+\square)/x + (e\square)/x \rightleftharpoons Ag^+/x \quad \ldots\ldots\ldots\ldots\ (2.14)$$

Both scale-forming and defect-injecting reactions occur at the scale/gas interface and the defects are consumed at scale/metal interface.

Considering the equivalent assumptions used for equation (2.6) the concentration of defects at equilibrium for equation (2.13) reveals that the reaction is pressure-dependent:

$$n^2 = n[(Ag^+\square)/o]n\ [(e\square)/o] = K_1(P_{Cl_2})^{1/2} \quad \ldots\ldots\ldots\ldots\ (2.15)$$

$$\therefore\ n = K_1^{1/2}(P_{Cl_2})^{1/4} \quad \ldots\ldots\ldots\ldots\ (2.16)$$

(2) Cation Interstitials

These are oxides with cationic Frenkel disorder. The reactions can be written as:

$$M \rightleftharpoons (M^{y+}\bullet)/x + y(e\bullet)/x \quad \ldots\ldots\ldots\ldots\ (2.17)$$

$$2(M^{y+}\bullet)/o + 2y(e\bullet)/o + y/2\ O_2 \rightleftharpoons M_2O_y \quad \ldots\ldots\ldots\ldots\ (2.18)$$

The scale-forming reaction takes place at the oxide/oxygen interface consuming the interstitial defects transported from the oxide/metal interface.

By analogy with equation (2.6), the concentration of defects at equilibrium for equation (2.17) shows that the reaction is pressure-independent because the defect-injecting reaction occurs at the oxide/metal interface:

$$n^{y+1} = n\left[(M^{y+}\bullet)/x\right]\ n^{y}\left[(e\bullet)/x\right] = K_1 \qquad \text{.....(2.19)}$$

$$\therefore\ n = K_1^{\frac{1}{y+1}} \qquad \text{.....(2.20)}$$

2.3.4. Non-Stoichiometric Oxides

Non-stoichiometric oxides do not contain equivalent concentrations of point defects[42,43]. Hence the net imbalance of electrical charge induced by non-stoichiometry is compensated by the creation of electronic defects, utilizing the energy levels available in the crystal. The existence of such electronic defects is often schematically represented by assigning either valence changes to certain ions or electrons to interstitial positions in the structure.

If the movement of lattice defects are slow in comparison with electronic defects, oxides exhibit semi-conducting properties. The nature of electronic defects provides a convenient classification for oxides as p-type and n-type:

(a) p-type Oxides

Metal deficient oxides conduct electricity by the movement of positive holes and thus oxides with this type of conductivity through positive carriers are said to be p-type oxides.

(1) Cation Vacancies

An example of this type is nickel oxide, NiO, as shown in Figure 9[44]. Both scale-forming and defect-injecting reactions take place at the oxide/oxygen interface:

$$1/2\ O_2 \rightleftharpoons NiO + (Ni^{2+}\square)/o + 2(e\square)/o \quad \ldots\ldots\ldots\ldots\ldots(2.21)$$

But the defects diffuse across the scale and are eliminated at the oxide/metal interface.

$$(Ni^{2+}\square)/o + 2(e\square)/o \longrightarrow (Ni^{2+}\square)/x + 2(e\square)/x \quad \ldots\ldots\ldots\ldots(2.22)$$

$$(Ni^{2+}\square)/x + Ni + 2(e\square)/x \rightleftharpoons Ni^{2+}/x \quad \ldots\ldots\ldots\ldots\ldots(2.23)$$

By analogy with equation (2.6), the concentration of defects at equilibrium for equation (2.21) is pressure-dependent:

$$n = n\left[(Ni^{2+}\square)/o\right]\ n^2\left[(e\square)/o\right] = K_1(P_{O_2})^{1/2} \quad \ldots\ldots\ldots\ldots\ldots(2.24)$$

$$n = K_1^{1/3}.(P_{O_2})^{1/6} \quad \ldots\ldots\ldots\ldots\ldots(2.25)$$

(2) Anion Interstitials

In principle, a p-type oxide can be formed with excess anions but the accommodation of interstitial oxygen anions is precluded by geometric considerations for all but the largest cations and it is doubtful if any real oxide of this type actually exists.

If they exist, such defects would be injected at the oxide/oxygen interface:

$$1/2\ O_2 \rightleftharpoons (O^{2-}\bullet)/o + 2(e\square)/o \quad \ldots\ldots\ldots\ldots\ldots(2.26)$$

These defects diffuse to the oxide/metal interface to participate in the scale-forming reaction at that interface:

$$2M + y(O^{2-}\bullet)/x + 2y(e\square)/x \rightleftharpoons M_2O_y \quad \ldots\ldots\ldots\ldots\ldots(2.27)$$

By analogy with equation (2.6), the concentration of defects at equil-

ibrium for equation (2.26) reveals that the reaction is pressure-dependent:

$$n^3 = n\left[(O^{2-}\bullet)/o\right]\ n^2\ \left[(e\square)/o\right] = K_1(P_{O_2}{}^{1/2}) \quad \ldots\ldots\ldots\ldots\ldots(2.28)$$

$$\therefore\ n = \cdot\ K_1{}^{1/3}\ (P_{O_2}{}^{1/6}) \quad \ldots\ldots\ldots\ldots\ldots(2.29)$$

According to equations (2.25) and (2.29) the defect concentration and hence the electrical conductivity in all p-type oxides increases with increasing oxygen pressure.

(b) n-type Oxides

The electronic conductivity of metal excess oxides occur by the migration of free electrons and thus they are defined as n-type, i.e. negative carrier, oxides. The characteristic feature, here, is that the electronic defects are excess electrons in the conduction band compensating for the positive lattice charge imbalance due either to cation interstitials or anion vacancies, as described below.

(1) Cation Interstitials

This is exemplified by zinc oxide, ZnO, as schematically shown in Figure 10[45]. The defect-injecting reaction takes place at the oxide/metal interface by zinc atoms entering the scale interstitially:

$$ZnO \rightleftharpoons {}^1/_2\ O_2 + (Zn^{y+}\bullet)/x + y(e\bullet)/x \quad \ldots\ldots\ldots\ldots\ldots(2.30)$$

Defects diffuse across the scale and the oxidation reaction proceeds at the oxide/oxygen interface.

$$(Zn^{y+}\bullet)/o + {}^1/_2\ O_2 + y(e\bullet)/o \rightleftharpoons ZnO \quad \ldots\ldots\ldots\ldots\ldots(2.31)$$

Considering the equivalent assumptions used for equation (2.6) the concentration of defects at equilibrium for equation (2.30) reveals that the reaction is pressure-dependent:

$$n = n\left[(Zn^{y+}\bullet)/x\right]\ n^{y}\ \left[(e\bullet)/x\right] = K_1(P_{O_2})^{-1/2} \quad \text{.....(2.32)}$$

$$\therefore\ n = K_1^{\frac{1}{y+1}} . (P_{O_2})^{\frac{-1}{2(y+1)}} \quad \text{.....(2.33)}$$

(2) Anion Vacancies

A classical example of this type is titania, TiO_2. Both oxide-forming and defect-injecting reactions take place at the oxide/metal interface without changing the cation positions.

$$1/2\ TiO_2 \rightleftharpoons 1/2\ O_2 + (O^{2-}\square)/x + 2(e\bullet)/x \quad \text{.....(2.34)}$$

The defects produced migrate to the oxide/oxygen interface and are eliminated.

$$(O^{2-}\square)/o + 1/2\ O_2 + 2(e\bullet)/o \rightleftharpoons O^{2-}/o \quad \text{.....(2.35)}$$

By analogy with equation (2.6), the concentration of defects at equilibrium for equation (2.34) is:

$$n = n\left[(O^{2-}\square)/x\right]\ n^{2}\ \left[(e\bullet)/x\right] = K_1\ (P_{O_2})^{-1/2} \quad \text{.....(2.36)}$$

$$\therefore\ n = K_1^{1/3} \cdot (P_{O_2})^{-1/6} \quad \text{.....(2.37)}$$

According to equations (2.33) and (2.37), for all n-type oxides the defect concentration and hence the electrical conductivity decreases with increasing oxygen pressure.

2.3.5. Defect Structure of Magnesium Oxide

Apart from the influence of regions of disorder, e.g. grain boundaries, the defects in an oxide which control oxidation are point defects which provide transport mechanism for the reacting species. The defect character of bulk oxides can be assessed by three general approaches:

(i) measurement of self-diffusion coefficients for the oxide components and for impurity species.

(ii) electrical conductivity measurements.

(iii) measurement of the ionic transference number.

(a) Pure Magnesium Oxide

Magnesium forms only one oxide, MgO which has the simple cubic structure with a lattice parameter of 0.42nm. It is the oxide of a strong electropositive alkaline earth metal and, as expected, it exhibits features characteristic of ionic oxides, e.g. its density exceeds that of the metal.

Most of the evidence for its defect structure is provided by the results of electrical conductivity measurements. In interpreting this evidence, two features are of fundamental importance:

(i) whether the oxide exhibits predominantly ionic conductivity characteristics of a stoichiometric oxide.

(ii) whether the conductivity observed is intrinsic or extrinsic.

Mitoff considered that pure magnesium oxide can exhibit electronic conductivity at temperatures > 1000°C based on his observation of low values for the EMF_s of differential oxygen cells using magnesium oxide as the electrolytic element[46] and the matter has not been finally resolved. Davies[47] and Schmalzried[48] for example, were inclined to ascribe Mitoff's observation to experimental uncertainties. Moreover, Reiling and Hensley[49] calculated the band gap for magnesium oxide from spectral analysis of luminescence and found the value to be very high, i.e. 8.7eV, which implies that electronic conductivity in the pure oxide is possible only at very high temperatures, i.e. > 1000°C. There is strong evidence for electronic conductivity in impure magnesium oxide[50] but, there again, it becomes significant at temperatures > 1200°C.

It is, however, generally agreed that magnesium oxide is always predominantly ionic at temperatures between 400 and 1000°C. The evidence is a comparison of the activation energy for electrical conductivity with the activation

energies for ionic conductivity calculated from the self-diffusion data of the charge-carrying species, i.e. either Mg^{2+} or O^{2-} ions assembled from results given by Mitoff[46], Davies[47], Lindner and Parfitt[51], Oishi and Kingery[52], Weigelt and Haase[53], Lempicki[54], and Lewis and Wright[55]. In making this comparison the concept of intrinsic and extrinsic conductivity must first be introduced.

When the logarithm of electrical conductivity of an ionic solid is plotted against the reciprocal of the thermodynamic temperature, the slope yields the activation energy for conduction and it is commonly observed that above a critical temperature the activation energy is significantly higher than below it, as indicated by two straight lines with an inflection at the point of intersection. This is taken to indicate that the conductivity is intrinsic and extrinsic in the higher and lower temperature ranges respectively. The difference is ascribed to the fact that the activation energy for intrinsic conduction contains a term for the activation energy for creating the charge-carrying defects at the surface. Extrinsic conductivity is conductivity which arises as a result of an imbalance of cation and anion charge-carriers and may be due either to an excess of one of the oxide components or to the presence of an unsuspected foreign ion.

Pure magnesia exhibits intrinsic and extrinsic behaviour, as illustrated in Figure 11. This Figure reproduces Davies' [47] results for conductivity measurements carried out on pure crystalline magnesium oxide in atmospheres of argon with 0.001% oxygen and of argon with 1% oxygen. The differences in the results for two atmospheres are due to an oxygen-dependent change in the charge-carriers from Mg^{2+} to O^{2-}. Thus according to conditions four types of charge carriers are identified, i.e. intrinsic Mg^{2+}, extrinsic Mg^{2+}, intrinsic O^{2-} and extrinsic O^{2-}, all characterised by particular activation energies, as given in Table 2.

Figure 11 shows that intrinsic conductivity for either Mg^{2+} or O^{2-} does not

persist below 1000°C. Comparison of the activation energies given in Table 2 shows that Mg^{2+} is the more mobile of the two species. Conductivity results do not unequivocally identify the diffusing charge carriers in the oxide and for further classification, recourse is made to direct diffusion measurements. Conductivities can be calculated from diffusion coefficients for the charge carriers, so that a comparison with experimentally-determined conductivities can be made, using the Nernst-Einstein equation:

$$\mu = \frac{ze}{kT} D \qquad \text{.....(2.38)}$$

If the mobility, μ is expressed in terms of conductivity, σ:

$$\sigma = \frac{c z^2 e^2}{kT} D \qquad \text{.....(2.39)}$$

where c and z are concentration of the charge carriers and their valence respectively, and e is the electronic charge.

With equation (2.39), Davies[47] has used Lindner and Parfitt's[51] values for the self-diffusion of Mg^{2+} and Oishi and Kingery's[52] values for the self-diffusion of O^{2-} to calculate the ionic conductivities expected for Mg^{2+} and O^{2-} as the charge carriers respectively. The results of these calculations given in Figures 12 and 13 show that the activation energies obtained from the diffusivity results correspond exactly with those found for electrical conductivity by other workers[46,47,53-55]. Direct evidence for ionic conductivity comes from the experimental results of Schmalzried[48] who compared the ionic nature using magnesium oxide as the electrolyte in a differential oxygen cell which showed 100% ionic conductivity at temperatures < 1100°C.

The fact that both species, Mg^{2+} and O^{2-} are mobile is consistent with Schottky disorder in the oxide. Moreover, energy of formation of Schottky pair can be calculated from the differences in activation energies for

intrinsic and extrinsic conductivity. Davies' [47] calculation yields values of 5.2 and 5.1eV for creation of Mg^{2+} and O^{2-} vacancies respectively.

All of the above considerations taken together provide strong evidence that in interpreting the present work which was carried out for the temperature range 500-725°C, pure magnesium oxide can be considered as a wholly ionic oxide with Schottky disorder exhibiting extrinsic conductivity. According to the oxygen potential, either species can diffuse but Mg^{2+} ions are more mobile than O^{2-} ions[52].

(b) The Influence of Impurities on the Defect Structure of Magnesium Oxide

The defect structure of magnesium oxide is very sensitive to impurities, and the most significant evidence is provided by electrical conductivity measurements and spectral analysis of induced luminescence. There are two cases to consider, i.e.

(i) impurities already present in the oxide, either as residues or as deliberate additions, i.e. dopants, and

(ii) impurities induced from the environment.

Solute ions have various effects on the oxide. Size differences between the impurities and the native ions strain the lattice, and polarisation effects due to impurities is different from that of the native ions. If there are differences in valency between the impurities and native ions, the conditions for electrical neutrality is changed imparting extrinsic character.

The addition of 1% mole of monovalent, divalent and tetravalent cation oxides to pure magnesium oxide was thoroughly investigated by Weigelt and Haase[53], and showed that ionic conductivity increased with increasing ionic radius and the valency of the added cation, as shown in Figure 14.

Glass[56] and Glass and Searle[57] later found from spectral analysis of luminescence of magnesium oxide at temperatures in the range 400-900°C that the incorporation of trivalent and tetravalent cations, e.g. Cr^{3+} and Mn^{4+} ions, leads to the formation of impurity-vacancy complexes by the interaction between cation impurities and compensated vacancies. It requires less energy for formation than that for Schottky defect pair and also influences the self-diffusion for cations. This explains why the added cation impurities increase the Mg^{2+} ion diffusion and hence the conductivity as noticed by Weigelt and Haase[53].

An example of particular importance of impurities induced into magnesium oxide from the environment is the protonation of the oxide surface, i.e. surface hydrolysis, when exposed to atmospheric water vapour.

This effect was noted by Johnson et al[58] in an investigation on dielectric loss in magnesium oxide. They found that at atmospheres in the range 550-800°C the ionic conductivity increased with increasing water vapour pressure. They ascribed this effect to the interaction of water vapour with O^{2-} ions on the magnesium oxide surface, forming monovalent OH^- ions:

$$H_2O + O^{2-} \longrightarrow 2OH^- \qquad \text{.....(2.40)}$$

Cation vacancies are required for charge compensation so that the overall reaction is:

$$Mg^{2+} + O^{2-} + H_2O \rightleftharpoons Mg^{2+} + 2OH^-/o + Mg^{2+}\square/o \qquad \text{.....(2.41)}$$

By analogy with equation (2.6), the concentration of defects at equilibrium for equation (2.41) is:

$$n(Mg^{2+}\square/o)\ n^2\ (OH^-/o) = K_1(P_{H_2O}) \qquad \text{.....(2.42)}$$

$$n(Mg^{2+}\square/o) = K_1^{1/3}(P_{H_2O})^{1/3} \qquad \text{.....(2.43)}$$

Since the conductivity is proportional to the number of charge carriers, equation (2.43) results in a water vapour dependence of conductivity, σ:

$$\sigma = K_2 K_1^{1/3} (P_{H_2O})^{1/3} \quad \text{.....(2.44)}$$

where K_2 is the proportionality constant.

From the constancy of the dielectric loss after an initial decrease due to the presence of water vapour, Johnson et al[58] concluded that the hydrolysis is a surface effect and the OH^- groups diffuse only very slowly into the bulk of the oxide.

The incorporation of OH^- groups with cation vacancies was further confirmed by the finding of Glass and Searle[57] who detected OH^- impurity-cation vacancy complexes from the spectral analysis of luminescence in the temperature range 400-900°C.

2.3.6. Defect Structure of Other Oxides Relevant to Aluminium-Magnesium Alloys

(a) Beryllium Oxide

Some of the alloys examined in the present work contained small quantities of added beryllium which, as is well-known, has a pronounced effect in reducing the oxidation rate of aluminium alloys[59,60]. For this reason it is appropriate briefly to review the defect structure of beryllium oxide.

Beryllium oxide is the only oxide of a strongly electropositive alkaline earth metal with a hexagonal close-packed Wurtzite structure and a higher density than the metal. It is therefore expected to be an ionic oxide.

According to Cline and Newkirk[61], and Bruin et al[62], it has so far proved impossible to obtain beryllium oxide of sufficient purity to examine the intrinsic region at temperatures < 2100°C. For temperatures in the range 1000-2100°C, experimental evidence is available to show that beryllium oxide is an impurity-induced extrinsic ionic oxide. The principal

evidence is the similarity of activation energy for self-diffusion coefficients[63,64] measured directly and calculated from electrical conductivity measurements[61,62]. Differential oxygen cells using beryllium oxide as the electrolytic element show that the proportion of ionic conductivity is close to 100%[65]. A further factor indicating the ionic character of the oxide is the oxygen pressure independence of ionic and electrical conductivity[61,65].

The agreement of the directly measured cation self-diffusion data with the similar data calculated from electrical conductivity measurements[62], together with the higher self-diffusion coefficients for Be^{2+} ions in comparison to O^{2-} ions[66] implies that cations are the principal charge carriers for ionic conduction.

For temperatures < 1000°C the electrical transport mechanism is more complex and the defect character of the oxide is unresolved. The principal difficulty is the irreproducibility of results both for electrical conductivity and for diffusion coefficients as between different investigators. It is notable that not only the absolute values but also the activation energies obtained differ very considerably[61]. These differences are variously ascribed to the effect of the nature and concentration of impurities, of grain boundaries, of the history of sample and to the errors arising from, e.g. electrical conductivity in the gas phase and along the free surface of the samples used[61,62].

(b) Aluminium Oxide

Since the base metal of the alloys used in the present work is aluminium, it is appropriate to review defect structure of the oxides of aluminium. Some twenty species of aluminium oxides and hydroxides are known[67]. On pure aluminium the only oxide species identified as a result of thermal oxidation at temperatures > 500°C are eta-alumina[68] and alpha-alumina[69].

(i) Eta-Alumina

Eta-alumina has been identified as an oxidation product on aluminium only when the metal is oxidised in humid atmospheres. It is a water stabilised spinel containing < 5% H_2O and is unstable with respect to α-alumina at low oxygen potentials at the oxide/metal interface. Little is known in detail of its defect structure, but in common with other spinels, most of the tetrahedral and octahedral sites are vacant[70].

(ii) Alpha-Alumina

α-alumina has a close-packed hexagonal (rhombic) structure[68] and its density, 3.98gcm^{-3} is higher than that of the metal, 2.70gcm^{-3}.

Cohen[71] reviewed work on the defect structure of α-alumina carried out prior to 1959 and classified the oxide as a semiconductor at high temperatures. Since then Pappis and Kingery[72] investigated electrical conductivity of α-alumina at high temperatures and at oxygen partial pressures of 10^{0} to 10^{-10} atms. They found that α-alumina is a p-type conductor at high oxygen pressures, i.e. 10^{0} to 10^{-5} atms and an n-type conductor at low oxygen pressures, i.e. < 10^{-5} atm. Harrop and Creamer[73], and Champion[74] studied single crystals and compared the results of electrical conductivity measurements with the ionic conductivity calculated from diffusion data of other workers using Nernst-Einstein relation (equation 2.39). They found that the ionic conductivity was too small to account for the observed results and concluded that the conductivity of these single crystals was predominantly electronic in character. On the other hand, Davies[75], in a critical re-evaluation of available information together with his results based on activation energies, concluded that α-alumina is an ionic conductor, with both Al^{3+} and O^{2-} ions as the charge carriers and exhibits both intrinsic and extrinsic nature at temperatures above and below 1000^{o}C.

Using galvanic-cell measurements Schmalzried[76] investigated the ionic transference number of commercially obtained pure α-alumina and found that the polycrystalline α-alumina is almost completely an electronic conductor above 1300°C and a mixed conductor at temperatures below that temperature.

Peters[77] determined the thermoelectric power of α-alumina single crystals in the temperature range 400-1000°C. His results indicated that the thermoelectric power is positive and decreases linearly with increasing temperature. The positive values reveal that the charge carriers are positive, i.e. Al^{3+} in the observed temperature range.

Later, Matsumura[78] re-examined the material using EMF, conductivity and thermoelectric measurements. From the results of ionic transference number given in Figure 15 and electrical conductivity, he concluded that above 1325°C α-alumina is a predominantly electronic conductor, while below this temperature it is a mixed conductor, becoming mainly ionic at 825°C. He separated the total electrical conductivity into its ionic and electronic parts. Consequently, the observed activation energies for the ionic part are 0.8eV for single crystals and 2.4eV for polycrystals while for the electronic part they are 3.0eV for single crystals and 3.7eV for polycrystals. From the low values for ionic part he suggested that the ionic part of conductivity of both single-crystal and polycrystalline α-alumina is due to an extrinsic character.

The sign of the thermoelectric EMF given in Figure 16 indicates that the charge carriers are negative above about 1200°C and positive below that temperature. This is interpreted to mean that the electronic part of the electrical conductivity is due to electron holes and the ionic part is due to Al^{3+} ion vacancies.

The above brief review reveals that α-alumina is an oxide of the same general character as magnesium oxide. For the temperature range of

interest in the present work, i.e. 500-725°C, it is essentially an ionic oxide exhibiting extrinsic conductivity with the cations Al^{3+} as the only important charge carriers.

(c) Magnesium Aluminate

Magnesium aluminate, $MgAl_2O_4$, has the structure typical of spinels with the general formula XY_2O_4 where X and Y are divalent and trivalent cations respectively. The structure is based on an FCC lattice of O^{2-} ions with the Mg^{2+} and Al^{3+} ions occuping the tetrahedral and octahedral interstices respectively, forming a lattice with a large unit cell containing 8 Mg^{2+}, 16 Al^{3+} and 32 O^2 ions[79]. Only half of the octahedral interstices and one eighth of the tetrahedral interstices in the O^{2-} lattice are occupied by cations so that whereas the positions of the O^{2-} ions are fixed, the arrangement of the cations is variable.

As explained earlier, the defect structure can be characterised by (a) comparing activation energies for electrical conductivity and ionic conductivity calculated from self-diffusion data, (b) comparing values of self-diffusion coefficients for the component species of the oxide, (c) measurement of ionic transference numbers. Although the material has been available in both single and polycrystalline form, little work to identify defect character had been done until very recently.

Using EMF measurement with the spinel as the electrolyte, Sonder[80] showed that $MgAl_2O_4$ is an ionic conductor in the temperature range 725-1425°C. The absence of electronic conduction was also evident from the oxygen pressure independence of conductivity. Application of the Nernst-Einstein relation (equation 2.39) to the values for ionic conductivity yields a value of the activation energy for diffusion of charge-carrying ions much lower than the activation energy for self-diffusion of oxygen directly determined by Reddy and Cooper[81], and Ando and Oishi[82]. Moreover, these O^{2-} self-diffusion coefficients[81,82] are about six orders of magnitude smaller

than the self-diffusion data for Mg^{2+}[83]. This implies that the diffusing species is not oxygen. Since iron impurities were found to be without effect at these high temperatures, the further implication is that the conductivity is intrinsic and the charge carriers must be either Mg^{2+} ions or Al^{3+} ions, or both. Inspection of the unit cell suggests that Mg^{2+} are the charge carriers because only a small fraction of the tetrahedral interstices are occupied by Mg^{2+} ions[79].

In a lower temperature range, i.e. 125-990°C Bates and Garnier[84] found evidence of impurity-induced extrinsic conductivity with the intrinsic/extrinsic inflection at a temperature between 325-375°C. Only below this temperature is the electrical conductivity found to depend significantly on the oxygen pressure.

Cochran et al[85] found that during thermal oxidation of aluminium-magnesium alloys, the rate of formation of magnesium oxide is increased if $MgAl_2O_4$ spinel is nucleated. This appears to be direct evidence for Mg^{2+} diffusion in $MgAl_2O_4$ spinel.

Taking all of the above information together, i.e. structural information, electrical properties and diffusion data, it seems reasonably certain that in the temperature range of interest in the present work, i.e. 500-725°C magnesium aluminate is a purely ionic oxide with Mg^{2+} as the charge-carrying diffusing species.

2.3.7. Diffusion in Oxides

In general, diffusion describes the atomic process responsible for the random motion of every atom in a solid as a consequence of thermal agitation. Diffusion in an oxide, when a compact adherent film is formed on a metal surface separating the reactants, is described as the transport of reactants via imperfections under the influences of both temperature and concent-

ration gradient. Thus the defects discussed in the previous sections sustain the growth of a continuous oxide layer by permitting the diffusion of reactants through the oxide.

Diffusion theory is a highly specialised topic concerned with atomistics[86-88] and mathematical modelling[89,90]. The following brief summary covers only those aspects necessary to interpret the kinetics of a growing oxide scale.

(a) Mathematics of Diffusion

A solute comprising non-interacting atoms in an isotropic single phase obeys Fick's laws of diffusion[91].

$$F = -D \cdot \frac{dc}{dx} \qquad \text{.....(2.38)}$$

(Fick's first law)

where F = The diffusive flux in the x-direction.

c = The concentration of diffusing species normal to the diffusive flux.

x = The space co-ordinate measured.

D = Diffusivity.

In most diffusion processes encountered in practical problems, the concentration of diffusing species changes with time. Mathematical treatment of these non-steady state conditions leads to the equation:

$$\frac{\partial c}{\partial t} = D \cdot \frac{\partial^2 c}{\partial x^2} \qquad \text{.....} \quad (2.45)$$

(Fick's second law)

These equations can be solved explicitly for particular geometries applying appropriate boundary and initial conditions to represent any particular problem.

The temperature-dependence of diffusivity for a singly-activated process is adequately described by Arrhenius' relation:

$$D = D_0 \exp\left(-\frac{E}{RT}\right) \qquad \text{.....(2.46)}$$

where E, R, T and D_0 are activation energy for diffusion, gas constant, temperature and frequency factor respectively.

(b) Mechanisms of Diffusion

Thermal agitation induces atoms of the diffusing species to jump between sites in a solid. In a crystal lattice this atomic motion takes place due to the migration of point defects through different mechanisms described below[88].

Vacancy Mechanism

If one of the atoms on an adjacent normal site jumps into an unoccupied site, the atom is said to have diffused by a vacancy mechanism, as schematically illustrated in Figure 17(a).

Interstitial Mechanism

This mechanism involves the movement of an atom from one interstitial site to one of its nearest-neighbour interstitial sites without permanently displacing any of the matrix atoms, as illustrated schematically in Figure 17(b). During this movement, a lattice distortion is probable and thus this is encouraged only when the interstitial atoms are small in comparison with the atoms on the normal lattice.

Interstitialcy Mechanism

If the interstitial mechanism is not feasible due to extensive lattice distortion, an alternative mechanism, i.e. the interstitialcy mechanism is feasible whereby an interstitial atom displaces one of its nearest-neighbours on a normal lattice into another interstitial position, itself occupying the original site of the displaced atom,

as illustrated schematically in Figure 17(c)

(c) High Diffusivity Paths

Besides point defects, oxides also contain dislocations and grain boundaries each of which plays a major part in the diffusion process by providing disordered high diffusivity paths to mobile species. Short-circuit diffusion through grain boundaries and dislocations can predominate over bulk diffusion at temperatures $< 0.5T_m$ (melting temperature) for most oxides[86,92,93] and is thus relevant to diffusive transport.

Direct quantitative measurements of short-circuit diffusion in growing oxides were not possible until recently because they are experimentally difficult. In default it was assumed that short-circuit diffusion is faster at low temperatures because of the low activation energy.

Recently, Atkinson and his co-workers[92-95] extensively studied the diffusion of nickel in growing nickel oxide through grain boundaries and dislocations at moderate temperatures, i.e. $< 1000^{o}C$ and proved that the diffusion coefficients for both are higher than those for bulk diffusion. There is further evidence which extends these findings to the other oxides[96-98]. Some investigators have attributed these to their extrinsic character due to the presence of principal impurities.

(d) Appraisal of Diffusion Rates Using Marker Techniques

Identification of the diffusing species and their relative mobilities in oxide films are prime requisites for elucidating the oxidation mechanisms. If the defect structure and the diffusion coefficients of the defects over the whole stability range of the oxide are known, the growth mechanisms may be deduced theoretically. Unfortunately, in most cases such detailed and accurate information is not available for oxides and as an alternative, markers are commonly used to identify the diffusion processes in

a growing scale[99] as originally used by Pfeil[100].

Inert markers, prepared either by depositing a noble metal as a porous film or by placing it in the form of a thin wire on the unoxidised metallic substance, have been used in marker techniques. The location of the marker is determined subsequent to oxidation. When the oxide is compact and pore-free, so that growth takes place by diffusion, the marker position is dependent on the relative diffusion rates of reacting species.

If the marker remains at the oxide/metal interface after oxidation, as shown in Figure 18(a), growth is by the outward migration of metal cations to the oxide surface, whereas if the marker is found at the oxide/oxygen interface, as shown in Figure 18(b), growth is by the diffusion of oxygen to the oxide/metal interface. If on the other hand oxygen and metal both diffuse, the marker is located within the scale, as shown in Figure 18(c), at a position determined by the relative diffusion rates of metal and oxygen, i.e.

$$\frac{\text{Diffusion rate of cations}}{\text{Diffusion rate of anions}} = \frac{\text{Distance from the oxygen interface}}{\text{Distance from the metal interface}}$$

(e) Diffusion in Magnesium Oxide

Diffusion characteristics in magnesium oxide have been studied by many workers due mainly to its technological importance.

(i) Bulk Self-diffusion

The self diffusion of both magnesium[51,101] and oxygen[52,102] in magnesium oxide has been studied at various temperatures > 750°C and pressures of oxygen. Oishi and Kingery[52] compared their oxygen data at temperatures > 1300°C with magnesium diffusion data of Lindner and Parfitt[51] at temperatures > 1400°C and concluded that diffusion of oxygen is about two orders of magnitude slower than that for magnesium. Oishi and Kingery proposed, by analogy with similar measurements on aluminium oxide,

that their oxygen diffusion coefficients reflected extrinsic diffusion. However, it is questioned by Rovner[102] who believed that his oxygen diffusion coefficients in the temperature range 950-1150°C represented intrinsic diffusion while at low temperatures, i.e. < 950°C, those represented extrinsic diffusion. However, Harding et al[101] found intrinsic and extrinsic Mg^{2+} ion self diffusion over the temperature range 1300 to 1750°C. The results of these workers are presented graphically in Figure 19.

(ii) Grain Boundary Diffusion

Davies[47] found that the experimental values he obtained for the electrical conductivity of polycrystalline MgO were higher than the corresponding values determined for single crystals by Mitoff and values calculated from diffusion data obtained by Lindner and Parfitt[51] for single crystals. He attributed this effect to the influence of grain boundaries. Moreover, Davies concluded with the same activation found by these workers that same mechanism of diffusion was operative through grain boundaries.

Makenzie et al[103] reported that the doping of magnesium oxide bicrystals with 0.7% iron enhanced oxygen grain boundary diffusion by a factor of five over that in samples containing 0.1% total of aluminium and calcium at 1700°C.

From the measurements of the electrical breakdown strength of magnesium oxide, Murata et al[104] inferred that the ionic conductivity of the oxide and hence the probable diffusivity of magnesium is enhanced by the presence of dislocations and grain boundaries in the temperature range 1000-1400°C.

A more recent mathematical model of "pipe diffusion" for oxygen in magnesium oxide showed that "pipe diffusion" can dominate over bulk diffusion and requires only about 75% of the activation energy for bulk diffusion[105].

This was ascribed to the decrease in energy for vacancy formation rather than to the reduction in migration energy in that highly disturbed region.

(iii) Impurity Diffusion

A number of workers have performed bulk and grain boundary diffusion of impurities in magnesium oxide.

Mortlock[106] analysed the available results for diffusion of divalent impurities in single-crystal magnesium oxide at temperatures > 1000°C and noted that the energy for migration of these impurities become progressively higher with increasing cation radii.

Wuensch and Vasilos[107] too analysed the available data for the diffusion of cation impurities and showed that except in very pure magnesium oxide intrinsic diffusion is not feasible and a concentration of impurity of the order of 0.02% is sufficient to cause impurity diffusion in single-crystal magnesium oxide at temperatures up to its melting point. In addition, they observed the preferential grain boundary diffusion of Co^{2+} and Ni^{2+} ions in bicrystals of magnesium oxide at temperatures <1300°C[108]. This enhancement was ascribed to an extrinsic, rather than intrinsic, property of the boundary resulting from impurity segregation, e.g. Ca^{2+}, Si^{4+}, Fe^{2+}, at the boundary below 1300°C.

2.4. Coherent Films and Growth Theories

Growth theories for coherent oxide films have been reviewed in detail by Kubaschewski and Hopkins[109], Hauffe[110], Smeltzer and Young[111], Fehlner and Mott[25], and Atkinson[95]. There now follows a brief resumé of the essential principles.

The theoretical approach is first developed as the simplifying assumption that the oxide films are coherent, adherent to the substrate, homogeneous and of uniform thickness. The treatment is usually further simplified

by considering two limiting cases:

(a) films which are so thin that the growth kinetics are dominated by electric fields established by electrons emitted from the metal.

(b) films which are so thick that local equilibrium is established at the oxide/metal and oxide/atmosphere interfaces so that the growth kinetics are rate-controlled by thermally activated diffusive transport through the film.

These two cases are not only theoretically convenient but practically significant because the former corresponds to the oxidation of metals at ambient temperatures and the latter is often experienced by metals in service at elevated temperatures.

2.4.1. Thin Films and the Cabrera-Mott Theory

At ambient and slightly elevated temperatures clean surfaces of most metals exposed to oxygen, oxidise rapidly at first but after a short time, i.e. 1-20h the reaction virtually ceases. The oxide films formed in this manner are very thin of the order of 2-20nm. The rate laws for such oxidation observed experimentally, as illustrated in Figure 20, are logarithmic; i.e. of the form:

$$x = K \log (at + t_o) + A \qquad \text{.....(2.47)}$$

or inverse logarithmic; i.e. of the form:

$$1/x = B - K \log t \qquad \text{.....(2.48)}$$

where x, t, and K are the oxide thickness, time and rate constant respectively, and A, a, B are constants.

Logarithmic rate laws are more often observed than inverse laws at low temperatures and have been observed for calcium[112], magnesium[113] and copper[114]. Inverse logarithmic laws have been observed for alumin-

ium[115]. In some cases it is difficult to distinguish between logarithmic and inverse logarithmic laws; for example, both logarithmic[116] and inverse logarithmic[117] laws have been reported for iron in the temperature range 0-120°C. In other cases a transition from logarithmic to inverse logarithmic laws has been observed on slight increase of temperature, e.g. by Vermilyea[118] for tantalum in the temperature range 100-300°C.

The essential theoretical basis to interpret logarithmic and inverse logarithmic oxidation was developed by Cabrera and Mott[119-121]. The theory applies to thin films, < 20nm, at low temperatures, < 200°C, where there is insufficient thermal activation to provide ionic diffusion and it describes the kinetics in terms of electric fields established across the oxide by direct ionisation of oxygen atoms adsorbed at the oxide/atmosphere interface.

Oxygen atoms produced by dissociation of molecules in the gas phase are adsorbed on the surface of the growing oxide films. These atoms provide traps for electrons transferred from the metal both by quantum-mechanical tunnelling and by thermionic emission. Mott[119] assumed that before the transfer of electrons from the metal, the empty electron energy levels of the adsorbed oxygen atoms are below the top of the Fermi distribution in the metal. The transfer of electrons to the oxygen atoms converts them to oxygen ions, raising the electron energy level until it equals the top of the Fermi distribution in the metal, as illustrated in Figure 21[119]. The effect is to produce at equilibrium a potential drop, v across the oxide of thickness, x, so that an electric field, $F = v/x$ is established. The potential is of the order of one or two volts, but since the oxide thickness < 10nm, the electric field is very strong, of the order of 10^6 V cm^{-1}. This strong field is sufficient to drive cations through the oxide so that the ion transport can occur at low temperature.

There is a limit to the thickness of oxide that can be produced by electron tunnelling alone, and two cases can be distinguished:

(a) Very thin films, < 5nm where the oxidation rate is controlled by electron tunnelling. This leads to the derivation of a temperature-independent logarithmic rate law.

(b) Thin films, > 5nm for which electron tunnelling is no longer effective and oxide growth ceases unless the temperature is high enough to permit electrons ejected from the metal by thermionic emission to pass through the conduction band of the oxide and thence to continue the ionisation of adsorbed oxygen, thus maintaining the electric field, as illustrated in Figure 21. This assumption leads to the derivation of an inverse logarithmic rate law.

An important difference between the effects of electron tunnelling and thermionic emission on film formation is that due to electron tunnelling the transport of electrons is rate-controlling and the process is temperature independent whereas due to thermionic emission, rate control is exercised by ion transport which is temperature dependent.

The basic Cabrera-Mott theories are developed on the assumption that ions and electrons are independent diffusing species in the film and the local space charge due to this independent electron migration can be disregarded.

Detailed application of the theory is complex[25,122] and it has been modified on numerous occasions to take account of ion transport mechanisms, e.g. anion and cation migration by vacancy or interstitial mechanism and the effect of pressure etc.[25,120].

2.4.2. Thick Films and the Wagner Theory

It is often found that the oxide films formed on metals at elevated

temperatures during service or during production processes is so thick that the second limiting case applies and frequently, but not always, the time-dependence of the oxide thickness is parabolic, i.e.:

$$x^2 = Kt \qquad \text{.....(2.49)}$$

where x, K and t are oxide thickness, rate constant and time respectively.

The standard derivation of this Wagner's law[123] is due to Hoar and Price[124] and is developed by considering the oxidising system as an electrolytic cell, and is given in Appendix 1. The generally accepted theoretical approach applied is due to Wagner[123] and is based on the following fundamental assumptions:

1. The oxide film is so thick that the short range electric fields (< 20nm), on which the Cabrera-Mott theories are based, can be disregarded, so that the oxide can be regarded as electrically neutral.
2. The film is adherent, coherent, homogeneous and of uniform thickness.
3. Local thermodynamic equilibrium prevails at the oxide/atmosphere and oxide/metal interfaces, i.e. the reactions at the interfaces are considered to be instantaneous and rate control of the oxide film growth is determined by thermally-activated diffusive transport of the reacting species through the film.
4. The diffusing species are cations, anions and electrons and the diffusion of any one of these species can be rate-controlling according to circumstances.

The driving force for the oxidation process is the free energy change of the overall reaction which is manifest as a difference in the population of defects at the oxide/metal and the oxide/atmosphere interfaces. This provides the concentration gradient sustaining the diffusive transport of the reacting species. The detailed kinetics depend on the nature of its

oxide and is illustrated by the following examples:

(a) Semi-conducting (Electronic) Oxides

(i) p-type Oxides with Cation Vacancies

As discussed in section 2.3.4, the equilibrium cation vacancy population in the oxide of a metal with valency, y is:

$$n = K^{\frac{1}{y+1}} \cdot P_{O_2}^{\frac{1}{2(y+1)}} \qquad \text{.....(2.25)}$$

so that if the external and internal dissociation pressures for an oxidising system, metal/oxide/metal, are p(g) and p(d) respectively, the corresponding cation vacancy population, n(g) and n(d) are:

$$n(g) = K^{\frac{1}{y+1}} \cdot p(g)^{\frac{1}{2(y+1)}} \qquad \text{.....(2.50)}$$

$$n(d) = K^{\frac{1}{y+1}} \cdot p(d)^{\frac{1}{2(y+1)}} \qquad \text{.....(2.51)}$$

Since p(g) > p(d), metal ion vacancies are continuously produced at the oxide/oxygen interface and consumed at the oxide/metal interface which is equivalent to the continuous outward migration of cations sustaining oxidation at the oxide/oxygen interface. This is illustrated in Figure 22.

(ii) p-type Oxides with Anion Interstitials (hypothetical)

Irrespective of the metal valency, the equilibrium interstitial anion defect population is:

$$n = K^{1/3} \cdot P_{O_2}^{1/6} \qquad \text{.....(2.29)}$$

Since p(g) > p(d), interstitial oxygen ions are produced at the oxide/oxygen interface and consumed at the oxide/metal interface by oxidation, i.e. the kinetics are the direct inward diffusion of anions.

(iii) n-type Oxides with Anion Vacancies

The equilibrium anion vacancy population is:

$$n = K^{1/3} \cdot P_{O_2}^{-1/6} \qquad \text{.....(2.37)}$$

Since p(g) > p(d), oxygen ion vacancies are produced at the oxide/metal interface and consumed at the oxide/oxygen interface with the simultaneous inward migration of an equivalent number of oxygen ions to the oxide/metal growth interface for oxidation. This is illustrated in Figure 23.

(iv) n-type Oxides with Cation Interstitials

The equilibrium interstitial cation defect population in the oxide of a metal with valency, y is:

$$n = K^{\frac{1}{y+1}} \cdot P_{O_2}^{-\frac{1}{2(y+1)}} \qquad \text{.....(2.33)}$$

Interstitial metal ions are produced at the oxide/metal interface and consumed at the oxide/oxygen interface, i.e. the kinetics are the direct outward diffusion of cations.

(b) Ionic-conducting Oxides

(i) Anionic Oxides with Anion Vacancies

These are oxides exhibiting either Schottky or anionic Frenkel disorder where anions and not cations are the mobile species. As explained in section 2.3.3, the equilibrium anion vacancy population is:

$$n = K^{1/3} \qquad \text{.....(2.8)}$$

Since the intrinsic anion vacancy population in an anionic oxide is oxygen pressure independent vacancies are produced at the oxide/metal interface independently of the external oxygen pressure and

consumed at the oxide/oxygen interface. This is equivalent to the inward migration of oxygen ions to the oxide/metal interface which is the growth interface for the oxide film.

(ii) Anionic Oxides with Anion Interstitials

These are oxides with anionic Frenkel disorder. The equilibrium interstitial anion defect population in the oxide of a metal is:

$$n = K^{1/3} \cdot P_{O_2}^{1/3} \qquad \text{.....(2.12)}$$

Since p(g) > p(d), interstitial oxygen ions are produced at the oxide/oxygen interface and consumed at the oxide/metal interface by oxidation, i.e. the kinetics are the direct inward diffusion of oxygen ions.

(iii) Cationic Oxides with Cation Vacancies

These are oxides exhibiting either Schottky or cationic Frenkel disorder where cations and not anions are the mobile species. The equilibrium cation vacancy population in the oxide of a metal with valency, y is:

$$n = K^{\frac{1}{y+1}} \cdot P_{O_2}^{\frac{1}{2(y+1)}} \qquad \text{.....(2.16)}$$

Since p(g) > p(d), metal ion vacancies are produced at the oxide/oxygen interface and consumed at the oxide/metal interface. This is equivalent to the outward migration of cations maintaining oxidation at the oxide/oxygen interface.

(iv) Cationic Oxides with Cation Interstitials

These are oxides with cationic Frenkel disorder. The equilibrium interstitial anion defect population in the oxide of a metal with valency, y is:

$$n = K^{\frac{1}{y+1}} \qquad \text{.....(2.20)}$$

Interstitial metal ions are produced at the oxide/metal interface independently of the external oxygen pressure and are consumed at the oxide/oxygen interface, i.e. the kinetics are the direct outward diffusion of cations.

2.5. Discontinuous Scales and Empirical Growth Laws

In the foregoing discussion, oxide films or scales on metals have been considered to remain compact and adherent so that oxidation proceeds in conformity with one or more of the simple temperature-dependent rate laws. In practice, many oxide films contain pores and/or cracks due either to aggregation of vacancies at the oxide/metal interface or to generation of stresses during the oxidation reaction. These have a significant influence on the oxidation kinetics which in consequence exhibit deviations from the simple rate-law kinetics due to the formation of discontinuous films. Quantitative explanations have been advanced together with models to account for the deviations and some of them are briefly reviewed here.

2.5.1. Constant Rate Laws and Linear Oxidation

Some metals oxidise at a constant rate when exposed to oxygen.

If an oxide is sufficiently porous, whatever the mechanism of creation of the non-protective oxide, it is frequently observed that the rate of oxidation is constant with time, i.e. linear, as shown in Figure 20, i.e.:

$$x = K t \qquad \text{.....(2.52)}$$

where x, t and K are oxide thickness, time and rate constant respectively.

The rate-determining step of linear kinetics are attributed to interface processes, i.e. adsorption, or to interface reaction as modelled in Figure 24.

Linear oxidation kinetics have been observed[100,125,126] in several metals,

e.g. calcium, cerium, magnesium, niobium, thorium, tungsten and uranium, and according to Aylmore et al[127] correlate well with observed densities which are lower than the true densities,presumably due to porosity.

2.5.2. Rate Transition Laws

In some oxidation processes, the initial rate law persists for only a limited period and is then superceded by another or alternatively passes through a transition period before another rate law is established. Sometimes this transition is not associated with a change in mechanism. The overall rate of a process comprising several consecutive steps is determined by the rate of the slowest step and if the hitherto slowest step eventually becomes more rapid than some other step in the process, this latter step then controls the overall rate.

Rate transition kinetics can be ascribed to either the formation of a new oxide or to change in the nature of oxide.

(a) Paralinear Oxidation

Some metals have been found to oxidise initially at a protective parabolic rate which gradually transforms to a non-protective linear rate. This situation arises when an inner-barrier scale growing at a parabolic rate by a diffusion process, is being simultaneously depleted and transformed at a constant rate to a non-protective outer-porous scale by a secondary process. The thickness of the inner layer tends to a limiting value when the rate of its formation is equal to the rate of transformation to the outer layer, as illustrated and modelled respectively in Figures 25 and 26. This well-recognised phenomena is termed the paralinear rate law (curve C) and is obtained by the summation of the curves describing the formation of the inner-compact layer (curve A) and the outer-porous layer (curve B), as illustrated in Figure 25. The growth of these layers are described by the equations:

$$\frac{dy}{dt} = \frac{a}{y} - b \qquad \text{.....(2.53)}$$

$$\frac{dz}{dt} = fb \qquad \text{.....(2.54)}$$

$$\frac{dw}{dt} = \frac{dy}{dt} + \frac{dz}{dt} \qquad \text{.....(2.55)}$$

The thickness of the inner layer tends to a limiting value, i.e. $y_{max} = a/b$ with increasing time and hence the overall rate of oxidation, dw/dt attains a constant value, fb.

Integration gives the total weight gain:

$$w = y + z = \frac{a}{b} \ln\left(\frac{a}{a-by}\right) + b(f-1)t \qquad \text{.....(2.56)}$$

where y, z and w represent the mass gains of the inner-compact layer, outer-porous layer and the entire scale respectively, and a, b and f are constants, f being the molar mass of oxide in the outer layer to that in the inner layer.

The integrated forms of equations (2.53), (2.54) and (2.55) are shown by curves A, B and C respectively in Figure 25.

The outer-porous layer is formed either by the cracking of the outer region of the growing oxide scale, so that both layers are chemically the same,or by the transformation of the outer region of the compact layer to a higher oxide which offers no significant barrier to the reactive gas.

Loriers[128] was the first to interpret paralinear oxidation by the model given in Figure 26 on the basis of results he obtained for cerium. He concluded that a compact layer of Ce_2O_3 is concurrently transformed to an outer-porous higher oxide CeO_2 at a constant rate while the consumption of cerium is controlled by diffusion in the compact Ce_2O_3 layer. Subsequently, Webb et al[129] applied the same model to explain the paralinear oxidation of tungsten with reference to the formation of lower and higher

oxides.

Haycock[130] showed that Loriers' paralinear model is, in principle, also widely applicable to explain paralinear rate laws for metals which form compact inner and porous outer layers of the same oxide, but he obtained a somewhat different equation. He applied it successfully to the sulphidation of iron and the oxidation of aluminium, magnesium, calcium and hafnium. The cracking which transform the inner layer to the outer-porous layer has been ascribed to the stress induced recrystallisation and grain growth[130-132].

(b) Breakaway Oxidation

In some cases an initial protective oxide grows at a decreasing rate until it attains a critical thickness beyond which it grows at an increasing rate associated with the development of cracks until it attains a maximum linear rate. This oxidation pattern is referred to as breakaway kinetics and is illustrated in Figure 27. It is explained by greater difficulty in nucleating cracks than in propagating them. This accounts both for the long induction period during which stresses are developed sufficient to activate crack nucleation and for the sudden transition to a rapid linear rate during which cracks propagate easily.

The oxidation of niobium[133] at 500°C, and magnesium[125] at 525°C are example metals for which breakaway kinetics have been observed experimentally.

Khanna and Gnanamoorthy[134] studied the oxidation of ferritic steels and observed breakaway kinetics at temperatures > 900°C. Results are explained on the basis of the rupture of the protective oxide resulting from the formation of iron chromate spinel.

Cocharn et al[85] have reported that liquid aluminium-magnesium alloys

exhibit breakaway kinetics during oxidation. In their view an amorphous film is responsible for the induction period which transforms to either crystalline magnesia or magnesium aluminate spinel during the transition to linear kinetics.

The induction period is influenced by factors such as temperature, rate of heating to the oxidising temperature, humidity, ambient oxygen pressure and the degree of homogenisation of the metal prior to oxidation.

2.5.3. Development of Stresses in Oxides

The presence of growth stresses are predominant contributors to the development of discontinuous scales.

As an oxide grows on a metal stresses can develop which may eventually rupture it, so that it ceases to protect the metal. Stresses are commonly manifest by blistering, shear-cracking, and flaking indicating compressive stresses as illustrated in Figure 28 or by simple fracture indicating tensile stresses[135], i.e. the manner in which the scale fails indicates the stress system acting in the plane of the interface.

The presence of stresses in oxides can be demonstrated experimentally. In Evans' classic experiment[136], an oxide film of progressively increasing thickness was detached from nickel specimen, as illustrated in Figure 29. The thicker part of the oxide wrinkled indicating the development of compressive stresses during its growth while the thinner part of the film was broken and curled up with the convex side corresponding to the surface adjacent to the metal, implying not only a stress but also a stress gradient in the scale. Another interesting example was given by Pawel and Campbell[137]. The technique was to oxidise a thin strip of niobium on one side only so that stress in the oxide was indicated by the elastic deformation of the metal. A series of specimens were oxidised for successively longer periods and it was found that as oxidation proceeded the strips

curled up into smaller and smaller radii until the strip eventually rolled up.

Several factors collectively contribute in various degrees to the stresses in an oxide film and the origin of stresses is a complex phenomena which has received much attention[138]. There now follows a brief review of the potential sources of stresses but it is important to bear in mind that the dominant causes of stresses vary from system to system.

(a) Stresses due to Volume Differences Between the Oxide and the Underlying Metal

The earliest attempt to account for stresses due to volume differences was due to Pilling and Bedworth[139]. Their theory was based on the erroneous concept that the oxygen ions are the only species mobile in the scale and that they react with metal ions at the oxide/metal interface. During this process the metal ions in the oxide would attempt to expand or contract to preserve the epitaxial relation with the underlying metal lattice but would be constrained by the neighbouring oxygen ions thereby generating either a compressive or tensile stress in the oxide. The determining factor was considered to be the ratio of the volume of oxide formed per metal ion to the volume of oxide per metal atom. If the ratio were greater than one, the stress would be compressive and the film would be continuous. If the ratio were less than one, the stress would be tensile and the film would be discontinuous because oxides are weakly in tension. Now that the kinetics of oxidation are better understood and the basis of the theory is discredited. Moreover, it fails to provide information on the magnitude of stresses and it does not take into account the plasticity of oxide or other possible stress relieving mechanisms. Nevertheless, the concept of volume ratio is still useful because it indicates the state of stress in the system.

(b) Epitaxial Stresses

The oxide films frequently grow epitaxially to minimise the activation energy for nucleation and the consequent epitaxial constraints progressively diminish and usually become negligible in thick scales. However, some epitaxy can persist even in thick scales, e.g. tantalum[140].

(c) Stresses due to Compositional Changes

Stresses can develop from a change of composition during oxidation either in the oxide or in the metal near the interface, according to the view of Richmond et al[141]. Although the effect is expected for alloys due to selective oxidation, it can also occur for pure metals, e.g. oxygen dissolution in tantalum or niobium during oxidation.

(d) Recrystallisation Stresses

Recrystallisation of scales can generate stresses, as reported by Jaenicke and Leistikow[142], and Haycock[129]. However, Stringer[138] has considered that growth stresses may induce recrystallisation so that in other circumstances recrystallisation may act as a stress relieving mechanism.

(e) Point Defect Stresses

Stresses can be generated in thick films of oxide which exhibit large deviations from stoichiometry, e.g. FeO, because the gradient of defects across the scale influences the lattice parameter. Furthermore, metals which oxidise by outward migration of cations can in principle develop a vacancy gradient within the metal substrate due to vacancy injection from the scale. Relaxation around these vacancies could influence the lattice parameter and generate a stress in the substrate which could be transferred to the metal[143,144]. The degree of vacancy supersaturation is however, quite small since vacancies can be precipitated as voids at suitable sinks such as oxide/metal interface and grain boundaries within the

substrate. Moreover, Hancock and Hurst[145] have pointed out that the vacancies may indeed provide stress relief by enhancing creep within the substrate.

(f) Stresses due to Oxide Growth Within the Scale

Jaenicke et al[143] have pointed out that for a stressed oxide in which only the cation is mobile the development of defects, i.e. pores and cracks admit oxygen stimulating oxidation within the scale. This concept has been extended by Rhines and Wolf[146] to include not only the inward migration of oxygen through microcracks but also oxygen diffusion via grain boundaries, thus leading to the generation of compressive stresses within the scale if it results in oxide formation at sites within the scale, as illustrated in Figure 30.

(g) Stresses due to Specimen Geometry

An important source of growth stresses is due to the finite size of specimens and to the resultant curvatures. The nature of the stresses developed depends on the degree of curvature and on the mechanism of scale growth. Hancock and Hurst[145] have reported that the cationic and anionic oxidation of convex surfaces tends to yield compressive and tensile stresses respectively. During cationic oxidation of convex surfaces, the initial oxide forms in compression, but since the geometry of the system tends to diminish this effect as the oxide thickens, the stress in the scale at the oxide/metal interface eventually becomes tensile. Anionic oxidation of convex surfaces forms a scale in which the stress is initially tensile but which diminishes as the oxide recedes from the metal as new oxide is formed underneath at the oxide/metal interface.

2.5.4. Stress Relief in Oxides

Initially, the stresses generated in a growing oxide are accommodated elastically but they are ultimately relieved when they reach values suff-

icient to cause deformation or fracture of the oxide, the substrate or the oxide/metal interface. The manner in which the stress is relieved depends on the mechanical properties of the oxide and substrate. Four mechanisms of stress relief are available:

(a) Oxide cracking.

(b) Oxide spalling.

(c) Plastic deformation of the oxide.

(d) Plastic deformation of the substrate.

Stress relief by either of the first two mechanisms produces a discontinuous unprotective scale but the stress relief by either of the last two mechanisms maintains the continuity of the scale that it remains protective.

(a) Oxide Cracking

Oxides are in general weak in tension and stress relief by cracking is a direct consequence of tensile stresses. It occurs, therefore, when the volume ratio of oxide to metal is less than one and the oxide has little plasticity. Examples include oxides formed on calcium, magnesium and sodium.

(b) Spalling and Scale-Metal Adherence

Spalling can be induced by compressive stresses within an oxide which cause exfoliation if they cannot be accommodated by plastic deformation of either the scale or substrate. An early example is Tylecote's[147] observation that cupric oxide films spall from copper if oxidised below 700°C.

Resistance to spalling is improved if the scale/metal adherence is improved and it is known that this can be accomplished by the addition of trace elements, either as alloy components[148] or as dispersion of stable oxides[149]. Examples include the use of yttrium, scandium, lanthanum, or hafnium to improve oxide adherence for nickel cobalt and iron based

oxidation resistance alloys. The mechanism by which scale adherence is improved is not clear but among suggestions put forward[148,150] are (i) enhancement of oxide plasticity, (ii) inhibition of vacancy coalesence at the oxide/metal interface, (iii) modification of scale growth process, (iv) provision of oxide intrusions which anchor the scale to the substrate, (v) formation of a graded oxide layer between scale and the metal with an intermediate coefficient of thermal expansion, (vi) improvement of adhesive bonds between metal and oxide atoms, (vii) sulfide scavenging to prevent sulfur segregation at the oxide/metal interface.

(c) Plastic Deformation of the Oxide

Plastic deformation is a common mechanism for stress relief in high temperature oxidation. It has further advantages in surpressing vacancy supersaturation at the oxide/metal interface during cationic oxidation and in hindering scale exfoliation which leads to spalling.

The effect of temperature on plasticity is often overlooked, yet many examples are known, including the earliest observation by Pilling and Bedworth[139] that copper oxidises parabolically at 800°C due to the plastic deformation of the oxide, but discontinuously at 500°C because the oxide is brittle and fractures at the lower temperature. Stephenson and Nicholls[151] found that the plasticity of the chromium oxide scales formed on nimonic alloys in the temperature range 700-1000°C, is inversely proportional to the film thickness. Douglass[152] has shown that anion-deficient zirconia is more plastic than stoichiometric zirconia at elevated temperature. Spriggs and Vasilos[153] observed that the plasticity of alumina is enhanced by any porosity it contains. However, this advantage can be offset by a reduction in the ability of the oxide to withstand spalling, as has been shown by Dunnington et al[154] with extensive studies on iron. At low temperature plasticity occurs by slip and is favoured by large grain size, but at high temperature it occurs by creep and is favoured

by small grain size[155,156].

Thus plasticity in oxides is a complex characteristic and is determined by a wide range of factors including not only the intrinsic nature of the material but also its defect structure, microstructure, thickness, whether or not it is porous etc.

(d) Deformation of the Substrate Metal

In appropriate circumstances stress relief can occur by deformation in the metal underlying an oxide film. Factors favouring deformation in the substrate are that it is a thin section or liquid. The substrate deformation may be either tensile or compressive. For example, Stringer[157] observed permanent dilation of up to 7% of the diameter on very thin walled tubes of tantalum, Noden et al[158] found extensions of up to 2% of the length of oxidised stainless steel tubes, and Roy and Burgess[159] found extensions up to 1.8% on zircaloy-2. On the other hand, Jones and Willoughby[160] found that magnesium tubes actually contracted during oxidation even with superimposed extensional creep loading. Against this evidence Grosskreutz and McNeil[161] have pointed out that slip steps formed during the deformation of the substrate could penetrate the oxide film causing it to crack or detach from the substrate.

3. PRINCIPLES OF OXIDATION OF ALLOYS

The same general principles apply to the oxidation of alloys as for pure metals, but because alloys contain two or more oxidisable constituents, additional parameters must be taken into account to describe the oxidation behaviour which is consequently more complex.

3.1. Classification of Alloy Oxidation.

If information is available the constituent of an alloy which oxidises preferentially can be predicted thermodynamically. Such predictions have been used to systematise the experimental results obtained for many binary alloys.

A useful common classification, due to Moreau and Bernard[162] applies to a binary alloy AB where B is the minor constituent. It is based on the influence of oxygen pressure and of the activity of the alloying element on the oxidation mode.

Two principal categories are identified depending on whether, in the prevailing conditions, one or both elements of the alloy oxidise.

Category 1 (One element only oxidises)

This category has two sub-divisions:

(a) The minor constituent B alone oxidises

This applies if the external oxygen pressure P_{O_2} is above the dissociation pressure of oxide BO but below that of oxide AO, i.e:

$$P_{O_2}\ (\text{oxide BO}) < P_{O_2} < P_{O_2}\ (\text{oxide AO})$$

There are two possibilities:

(i) Element B undergoes internal oxidation, as illustrated in Figure 31.

(ii) Element B undergoes exclusively external oxidation, as

illustrated in Figure 32.

It is evident that the occurrence of either of these depend upon the relative diffusion rates of oxygen and of the element B in the system. A high diffusion rate for oxygen favours internal oxidation, as illustrated in Figure 31, e.g. for silver rich Ag-Si system, while a slow diffusion rate promotes external oxidation, as illustrated in Figure 32, e.g. for iron rich Fe-Cr system. The reaction rate is governed, in the case of internal oxidation, by diffusion of oxygen in the metal and in the case of external oxidation by diffusion of the element B in either alloy or oxide, whichever step is slower.

(b) The host element A alone oxidises

This occurs when the oxygen pressure is above the dissociation pressure of the alloy AO but below that of oxide BO, i.e:

$$P_{O_2} \text{ (oxide AO)} < P_{O_2} < P_{O_2} \text{ (oxide BO)}$$

Two possibilities can again arise:

(i) The non-oxidisable element B is dispersed in the oxide AO, as illustrated in Figure 33, e.g. for copper rich Cu-Au system.

(ii) The non-oxidisable element B is enriched by selective oxidation of the host element, as illustrated in Figure 34.

If the external layer of the oxide AO is non-protective rapid oxidation of A produces a surface zone enriched in B, leading to the incorporation of B into the oxide by reaction scheme 1(b)i. If on the other hand, the oxide AO is formed as a coherent protective scale the rate control exercised on the oxidation of A allows time for the excess of B to diffuse away into the bulk of the alloy by reaction scheme 1(b)ii.

Category 2 (Element A and B oxidise simultaneously)

If the oxygen pressure is higher than the dissociation pressures of both oxides, A and B oxidise simultaneously, i.e:

$$P_{O_2} \text{ (oxide AO)} < P_{O_2} > P_{O_2} \text{ (oxide BO)}$$

Two possibilities can arise:

(a) The two phases AO and BO are mutually insoluble. If the oxide layer is two-phase, two cases are viable.

(i) The alloying element B oxidises more readily than the host metal. Element B tends to oxidise first forming particles of BO oxide surrounded initially by the metal A and later by the oxide AO forming subsequently.

(ii) The alloying element B oxidises less readily than the host metal A. Metal A oxidises, first engulfing metal B. These particles subsequently oxidise to BO. In contrast with the previous case there is no internal oxidation.

(b) Both cations combine with oxygen ions to form a new oxide. Again two cases are possible.

(i) The two oxides AO and BO form a solid solution (A,B)O, as illustrated in Figure 35. A classical example is provided by Ni-Co alloys in which the metal is covered by a single-phase layer of (Ni,Co)O.

(ii) Formation of a double oxide: The composition of the double oxide varies within only the limits allowed by normal non-stoichiometry. It is most often observed in a two-phase oxide system in which spinel is dispersed in a matrix of the oxide of the dominant component. For a low content of the alloying element there may be internal oxidation, as illustrated in Figure 36 for nickel rich Ni-Cr alloys where the $NiCr_2O_4$ phase

is dispersed in a matrix of nickel oxide[163].

3.2. Oxidation Rates for Alloys

The oxidation rate of a metal may be modified by alloying so that the oxide is either more or less protective.

3.2.1. Single-Phase Coherent Scales

By Wagner's theory[123] when a metal forms a thick and coherent film, the oxidation rate is determined by diffusion of either ions or electrons across the scale.

If a metal contains a small quantity of another element, i.e. < 3%, soluble in its oxide, the resultant doped oxide may exhibit modified defect concentration whose effect on both the electrical conductivity of the oxide and the oxidation rate of the metal are predictable by the well-known Wagner-Hauffe[164] valence theory summarised in Table 3.

To illustrate the theory, consider the addition of a small quantity of lithium to nickel which forms a p-type oxide. Every Li^+ ion replacing a Ni^{2+} ion is a negative charge in nickel oxide lattice. To preserve electrical neutrality, one positive hole ($e\square$) must be created for each Li^+ ion introduced. The product $n[Ni^{2+}\square]n^2[e\square]$ is fixed by the reaction governing the non-stoichiometry of nickel oxide and so $n[Ni^{2+}\square]$ falls and the oxidation rate is reduced[165]. By similar argument, an alloying element yielding higher valent cations, e.g. Cr^{3+}, increases the oxidation rate[166]. These are illustrated in Figure 37.

When the oxidation product is an n-type oxide, e.g. zinc oxide, the conditions are reversed according to Hauffe and Vierk[167]. A monovalent ion like Li^+ enters the oxide layer in place of Zn^{2+} ion by destroying one free electron ($e\bullet$). Hence $n[Zn^{2+}\bullet]$ the concentration of interstitial Zn^{2+} ions increases by virture of the product $n[Zn^{2+}\bullet]n^2[e\bullet]$ describing the

non-stoichiometry leading to an increase in the oxidation rate. Similarly, higher valent cations like Cr^{3+} cause an opposite effect to decrease the oxidation rate, as illustrated in Figure 38[166].

Although not an ionic oxide, a well-known example of an ionic conductor with cation vacancies is silver bromide, AgBr. Slightly diluted silver with cadmium ejects Cd^{2+} ions into the AgBr layer during the bromination of silver increasing the concentration of Ag^+ vacancies, i.e. $n[Ag^+\square]$. Since the product $n[Ag^+\square]n\,[e\square]$ is fixed by the equilibrium for non-stoichiometry, the increasing $n[Ag^+\square]$ reduces the positive hole concentration with the consequent decrease in the rate of bromination, as illustrated in Figure 39[168].

Although the Wagner-Hauffe model provides a quantitative explanation for the effect of dilute alloys, it produces good numerical agreement only in a small number of cases. The assumptions made are so restrictive and it is evident that it fails completely to predict the observed behaviour in a large number of reactions.

3.2.2. Multiphase Scales

If the alloying element is present in low concentrations but above that for which it is soluble in the oxide of the parent metal, a second oxide, e.g. the oxide of the second element or a spinel with both cations, is formed and the oxide becomes multiphase altering the oxidation rate.

One example is the spinel $NiCr_2O_4$ which is formed in the oxidation of nickel-chromium alloys when the chromium content is high enough and the oxidation rate is decreased[163]. A further example is the effect of magnesium on the oxidation of aluminium-magnesium alloy. Although the presence of magnesium in impurity level could reduce the rate of alumina formation, the high magnesium contents could lead to the formation of either magnesium oxide and/or spinel $MgAl_2O_4$ and the oxidation is accelerated[169].

4. OXIDATION OF ALUMINIUM-MAGNESIUM SYSTEM

4.1 Oxidation of Pure Aluminium

Progress towards the development of a consistent theoretical approach to the oxidation of solid and liquid aluminium has been slow and controversial because of inconsistencies in experimental results. With hindsight, the difficulties that have been experienced can be attributed to the use of techniques with inadequate sensitivity to measure the very small mass gains, to uncertainties in the role of phase equilibria and to insufficient appreciation of the effect of extrinsic factors especially impurities introduced into the oxide from the metal or from the oxidising atmosphere, as explained in Sections 2.3.6.(b) and 3.2.1.

Nominally, pure aluminium oxidises very slowly and complex growth laws can be observed when the metal is oxidised in nominally pure oxygen. Gulbransen[170], and Gulbransen and Wysong[171] recognised the need for equipment with very high resolution to monitor the small mass changes expected. Their work illustrates the vital importance of maintaining consistency in the purity of metal samples and in sample preparation techniques. Unfortunately, their work was performed using oxygen of unspecified purity and dryness. Their results for 2h tests fitted parabolic and linear rate laws for the temperature ranges 350-475^{o}C and 475-550^{o}C respectively.

Smeltzer[172] extended Gulbransen and Wysong's[171] work to much longer periods of oxidation, i.e. up to 24 hours, in the temperature range 400-600^{o}C in dry oxygen using a similar technique. He broadly confirmed their general results that the kinetics are parabolic at temperatures <475^{o}C. Smeltzer[172] found that at all temperatures the oxidation rate was initially rapid but decreased abruptly to a slower rate at a critical mass gain which was dependent on the temperature, e.g. at 35 μg cm^{-2} at 600^{o}C. He represented his results empirically by fitting them to two parabolas in sequence for

every temperature. Thus the oxidation was described by two parabolic rate constants applicable to the thin and thick scales formed at early and later stages.

Aylmore et al's[173] experimental results for high purity aluminium sheet samples oxidised for up to 400h in dry oxygen in the temperature range 400-650°C, broadly confirm Smeltzer's[172] work, i.e. the marked departure from simple parabolic kinetics at high temperatures but they were unable to identify a sequence of parabolas. They ascribed this to the formation of initial amorphous layer which was assumed to offer no impediment, until it transformed to crystalline state.

Blackburn and Gulbransen[174], Cochran and Sleppy[175], and Hunter and Fowle [68] all compared the oxidation of aluminium in nominally dry and moist atmospheres. Blackburn and Gulbransen[174] observed more rapid oxidation of metallographically polished samples in moist oxygen than in dry oxygen in the temperature range 500-625°C. Cochran and Sleppy[175] observed slightly faster oxidation in moist oxygen than in dry oxygen and found that oxidation followed a near linear rate law to a mass gain of 3μg cm^{-2} and then decreased rapidly with further weight gain. In contrast, Hunter and Fowle[68] observed that in the low temperature range 125-275°C, the oxidation of chemically polished samples of high purity aluminium was slower in moist air than in dry air. Both Cochran and Sleppy[175], and Hunter and Fowle[68] observed by electron diffraction that the films formed on their samples were composed mainly of eta-alumina whether the oxidising atmosphere was nominally dry or moist. Since the eta-alumina structure is unstable unless it contains water, as explained in Section 2.3.6.(b). This observation implies that the nominally dry oxygen or air employed contains sufficient residual water vapour to invalidate the comparison.

Beck et al[176] studied the relation between the growth kinetics and struct-

ure of oxide films formed on high purity aluminium, in nominally dry oxygen over the temperature range 450-575^{o}C, for greatly extended periods of time. The overall growth was treated as a summation of two independent and distinct processes, the growth of the overlying amorphous film, and the growth of eta-alumina crystals. They found that the growth of the amorphous film followed the parabolic rate law.

The only significant results available for the oxidation of liquid pure aluminium are Dholiwar's[69] extensive studies at 730^{o}C, in which oxidation rates determined thermogravimetrically were related to the structures of oxide films growing on liquid aluminium exposed to dry and moist oxygen. The essential features of the work were:

(a) Oxidation was isothermal, i.e. the oxidising atmosphere was excluded while the samples were raised to and stabilised at the test temperatures in a closed evacuated system.

(b) For dry atmospheres a liquid nitrogen cold trap was applied during the whole of the test period and for moist atmospheres a reservoir of liquid water was maintained within the system.

A clear difference was observed between the effects of dry and moist oxygen. In dry oxygen the oxide formed was α-alumina (corundum) and oxidation was characterised by a parabolic growth law following an initial period of about 10 minutes, during which a linear growth law was observed. In moist oxygen, oxidation was characterised by an initial rapid oxidation rate during which the oxide was eta-alumina under which a sub-film of α-alumina was nucleated at the oxide/metal interface. The sub-film spread until after about 15 minutes it completely covered the interface and exercised rate-control. From this point onwards the oxidation rate was similar to that for dry oxygen. This is interpreted in terms of the water vapour potentials at the oxide/metal and oxide/atmosphere interfaces. This pre-

dicts that in moist oxygen or air, eta-alumina is stable at the oxide/atmosphere interface whereas α-alumina is stable at the oxide/metal interface. Structures determined by electron diffraction in oxide films lifted from the liquid metal were consistent with this concept.

4.2 Oxidation of Pure Magnesium

As explained in Section 2.3.7(e) both cations and anions diffuse very slowly in magnesium oxide which is an ionic oxide and hence it would be anticipated that magnesium would oxidise very slowly if the oxidation of the metal took place by migration of ions under diffusive control through a barrier layer of magnesium oxide. Unfortunately, magnesium cannot exploit the nature of the oxide to form a protective film and it has been known for a long time[139] that the scale formed on magnesium metal is of limited value in protecting it against continued oxidation. The reasons for this are (i) the volume ratio of oxide to metal is adverse, i.e. 0.81[139], and as a result, the scale fissures continuously, (ii) magnesium has a high vapour pressure[177], e.g. 13.3Pa at 515°C and 133Pa at 725°C, so that the metal vapour can easily escape through fissures and oxidise directly to give a loose-powdery product on the metal surface. This explains why earlier investigators[139,170,178] had difficulty in obtaining consistent results for the oxidation of magnesium.

Gulbransen[179] measured the oxidation kinetics of magnesium while the evaporation of magnesium occurred at temperatures in the range 400-500°C for periods of up to 6h, using a vacuum microbalance technique. His conclusions were that at temperatures > 475°C oxidation was linear and hence was non-protective while at temperatures ≤450°C the linear rate continued only for an initial period and was followed by a diminishing rate as the film thickened and hence was protective.

Leontis and Rhines[180] extended Gulbransen's work to higher temperatures,

i.e. 400-575°C, and obtained somewhat different results. At low temperatures and in the early stages of oxidation at high temperatures the oxide film was protective, but after the initial period at high temperatures, oxidation proceeded rapidly with linear kinetics. They ascribed these effects to the initial formation of protective thin films and the subsequent formation of thick films which cracked spontaneously giving rise to the rapid linear oxidation. Leontis and Rhines[180] results are much more relevant to the normal mode of oxidation of magnesium than Gulbransen's[179] results because Gulbransen initiated oxidation by admitting oxygen to magnesium specimens which were being used for evaporation rate measurements and hence the surface roughness may have significantly influenced the results[125] by triggering a premature rapid oxidation for all of the temperatures he examined.

In addition to the above difficulties, other investigators have found that the oxidation of magnesium is sensitive to impurities. This is expected in view of the sensitivity of magnesium oxide to extrinsic factors, as explained in Section 2.3.5(b).

It has been shown that impurities injected by the atmosphere can alter the oxidation kinetics. Gregg and Jepson[125] observed that oxidation is sensitive to OH^- ion impurities injected into the oxide by water vapour present in the atmosphere. They measured the oxidation rate of 0.15mm thick coupons of magnesium at temperatures 350-600°C in moist and dry atmospheres. In dry air there was an induction period before oxidation commenced following a primary linear rate law; above 525°C oxidation also exhibited rapid breakaway following the primary linear branch. The presence of moisture in oxygen was found to reduce the temperature at which oxide films ceased to have protective properties, i.e. it shortened the induction period, increased the rate of primary linear oxidation but it inhibited breakaway oxidation. The effect was ascribed to an increase in the cation

vacancy population in magnesium oxide due to the incorporation of OH^- ions. Their work also exemplified the importance of maintaining a constant sample preparation scheme during an oxidation programme without which oxidation tends to vary considerably. Moreover, Castle et al[181] have shown how other gaseous impurities can influence the oxidation kinetics. Using 1.6mm magnesium coupons they found that oxidation at temperatures $\geq 500^oC$ was rapid with breakaway kinetics in flowing oxygen but was slow and protective for 300h at static oxygen at 13330 Pa. They speculatively attributed the cause to cracking of the film due to impurities which had a proportionately greater effect in flowing oxygen because the impurities were continuously re-supplied. They traced the impurities to hydrocarbon contamination of the oxygen gas from lubricants used during manufacture.

Hayden et al[29], Leontis and Rhines[180], and Nelson[182] examined the effects of impurities in the metal. In investigating the protective nature of magnox alloys at room temperature Hayden et al[29] found that oxidation on evaporated magnesium films was slower than on films of magnox alloys because ionic magnesium oxide nucleated easily on magnox alloys. They ascribed this effect to the injection of Al^{3+} ions from magnox alloys into magnesium oxide providing cation vacancies which might expedite the diffusion process essential for the two-dimensional oxide precursor to nucleate ionic magnesium oxide. The results of Leontis and Rhines[180] favour this argument for oxidation at high temperatures because they observed that the addition of aluminium to pure magnesium up to the solubility limit increased the oxidation rate. This implies that the defect injection in magnesium oxide increased with increasing amount of substitutional aluminium which only participated in the defect injection process. Nelson[182], on the other hand produced evidence that small quantities of beryllium added to magnesium, i.e. 0.0005%, suppressed the oxidation of both liquid and solid magnesium.

4.3 Oxidation of Aluminium-Magnesium Alloys

4.3.1 Solid Alloys

Elucidation of the fundamental principles which determine the oxidation of solid aluminium-magnesium alloys presents a difficult problem which has attracted the attention of numerous investigators for a long time. Early work[59,183,184,185] can be disregarded because the techniques then available were inadequate to monitor the small mass gains or to determine the morphology and structures of the oxide films formed. In addition, clear interpretation of the results obtained was precluded by failure to appreciate the influence of sample condition and of extrinsic factors, especially the impurities introduced into the oxide from the metal or from the oxidising atmosphere, as explained in Section 2.3.5(b).

Real progress has been possible only since the advent of techniques and the development of adequate concepts of oxide structure, as described in Sections 2.3.3 and 2.3.5. Even so, many of the important factors remain unresolved and are still the subject of controversy. Several important aspects of the oxidation process have emerged. These are:

(i) The nature of the rate laws governing the process.

(ii) Differences in oxidation rate for dry and moist atmospheres.

(iii) The influence of a pre-existing oxide film formed at ambient temperature or during heating to any prescribed test temperature.

(iv) The nature and morphology of the phases present in the oxide film, especially magnesium oxide and spinel $MgAl_2O_4$.

(v) The particular influence of certain elements in inhibiting oxidation, especially beryllium.

(i) Oxidation Rate Laws

Using sensitive thermogravimetric equipment, weight gain data and rate laws

have been reported by various workers for long and short exposure times.

Cochran and Sleppy[175] found that the oxidation kinetics of commercial aluminium -2.5% magnesium alloys both under dry and moist atmospheres, do not conform to any recognised oxidation law, but are more nearly parabolic than linear for exposures up to 16h in the temperature range 350-550^{o}C. Field et al[186,187] using aluminium -4.2% magnesium alloys, observed that the oxidation law under a dry atmosphere is paralinear at 480^{o}C and 520^{o}C but pseudo-parabolic at 575^{o}C,while under a moist atmosphere it is pseudo-parabolic at all three temperatures. Wefers[188] identified three regimes of oxidation kinetics on commercial aluminium -0.8% magnesium alloys in dry atmospheres which fitted to parabolic, linear and non-linear rate laws. Although the transitions between these laws are well defined, none of the isotherms showed all three regimes within a period of 16h oxidation. Moreover, Lea and Ball[189] managed to fit their kinetic data for commercial aluminium -2.5% magnesium alloys to a paralinear rate law for both dry and moist atmospheres.

The various oxidation laws that have been observed imply that there is no generally accepted rate law for the oxidation of aluminium-magnesium alloys. Hence the oxidation of aluminium-magnesium alloys is not controlled by a single simple mechanism, e.g. by the diffusion of species through a protective coherent oxide film, which would yield a parabolic rate law but is complex with a combination of theoretical or empirical rate laws prevailing at various stages of oxidation in dry or moist atmospheres.

Since the weight gains observed by the above workers also vary widely from one to another, it is clear that at high temperatures the oxidation behaviour is sensitive to the experimental conditions, e.g. to surface roughness, to the thermal history of the samples, and to impurities, making it difficult to reproduce any given set of results.

(ii) Comparison of oxidation in dry and moist atmospheres

Differences in the oxidation kinetics in different atmospheres have long been experienced by many workers. Cochran and Sleppy's[175] results on commercial aluminium -2.5% magnesium alloys in the temperature range 350-550°C indicated that the oxidation rate in moist atmospheres is initially faster than that in dry atmospheres but after an elapse of 20 minutes the oxidation rate in dry atmospheres becomes faster so that eventually after > 12h, the mass gain of oxide formed in dry atmospheres is in fact greater than that formed in moist atmospheres with equivalent experimental conditions. On the contrary, Field et al[187] observed that in the temperature range 480-575°C with exposures of up to 5h, the oxidation of aluminium -4.2% magnesium alloys in dry atmospheres is initially faster than that in moist atmospheres, but is subsequently slower. Thus for oxidation periods in excess of 60 min, the total mass of oxide formed was greater in moist atmospheres. Lea and Ball[189] using commercial aluminium -2.5% magnesium alloys at 500°C found an oxidation pattern similar in general to that reported by Field et al[187] but with the difference that the time after which the total mass of oxide formed in moist air exceeded that for dry air was delayed until about 100h. Wefers[188] found that the mass gain of aluminium -1% magnesium commercial alloys at 550°C was always 15-20% higher when the moisture was present in the oxidising atmosphere irrespective of the period of oxidation.

Thus the results of the various investigators which have sought to compare oxidation in dry and in moist atmospheres are conflicting so that no firm conclusion is possible without further investigation.

(iii) The influence of a pre-existing oxide film

It is well established[186,188,190,191] that for temperatures < 350°C an amorphous oxide film develops on aluminium-magnesium alloys but at higher temperatures it continuously transforms, yielding crystalline γ-alumina

and also magnesium oxide. The presence of γ-alumina in the film at higher temperatures, i.e. > 500°C, depends on the magnesium content of the alloy, the mode of heating the sample to the test temperature and the atmosphere. High magnesium contents in the alloy stimulate rapid diffusion of magnesium to the oxide/metal interface, promoting fast reduction of the γ-alumina film while slow heating in an oxidising atmosphere can lead to the further development of γ-alumina layer. Some investigators have reported[186,187,189] that if the film is predominantly γ-alumina it is protective because they found that the initial oxidation followed a parabolic rate law, i.e. the process was under diffusion control. However, another possibility[190] is that if an abundance of γ-alumina is formed during the initial period of oxidation, especially if the samples are heated to the test temperature in an oxidising atmosphere an alternative reaction which is detrimental to the formation of a protective film can occur, i.e. the γ-alumina may be reduced not to magnesium oxide but to the spinel, $MgAl_2O_4$, which is very defective and hence the oxidation rate is accelerated.

(iv) The nature and morphology of the phases present in the oxide film

Investigations concerned with the nature and growth morphology of the oxide films have been carried out using electron optical techniques. The results have revealed that duplex crystalline films of magnesium oxide develop due both to the reduction of initially formed γ-alumina layer by magnesium[190, 191,192] and to the direct reaction of magnesium with atmospheric oxygen[190]. The spinel, $MgAl_2O_4$ has also been observed in a few cases.

Brock and Hine[191] showed that amorphous γ-alumina formed anodically on aluminium -3% magnesium alloys was degraded and transformed fully or partially to a much less protective film consisting either of magnesium oxide alone or of a mixture of magnesium oxide and amorphous γ-alumina.

Field et al[186] analysed the oxide morphology for aluminium -4.2% magnesium

alloys using TEM and SEM techniques. Their approach was to observe the oxide morphology on samples already bearing a natural air-formed film because they regarded freshly produced surface is an artificial condition. The preformed films were produced by storing coupon-samples 0.2mm thick in air for 14 days after preparation. The development of magnesium oxide was observed by both possible mechanisms, as described above. They were of the opinion that the magnesium oxide phase was nucleated at the oxide/metal interface and grew outwards through the initial γ-alumina film.

In a later investigation Wefers[188] drew conclusions on the growth morphology which differed fundamentally from that of Field et al[186]. He exposed samples of commercial aluminium alloys, with magnesium contents in the range 0.8-1.5% to oxidation for 16h and found that the proportion of crystalline γ-alumina increased at the expense of amorphous alumina as the temperature increased within the range 400-500°C. For temperatures > 500°C magnesium oxide islands were observed on top of the γ-alumina layer which he assumed grew by diffusion of magnesium through the layer.

Ritchie et al[190] carried out an investigation broadly similar to that of Brock and Hine[191], but using evaporated aluminium -1.2% magnesium films, i.e. 0.1 and 5μm thick. They reached the same conclusion except that the spinel, $MgAl_2O_4$ appeared only after a few hours of oxidation and suggested that the early formation of $MgAl_2O_4$ was prevented by the high activation energy needed to form that by the reduction of a γ-alumina film.

With in situ observation using TEM, Scamans and Butter[192] studied the growth morphology of oxide films formed on aluminium -5% magnesium alloy foils of 0.5μm thick. In the temperature range 400-525°C with a low oxygen pressure, i.e. 1.33×10^{-2}Pa, they observed rapid nucleation and growth of both magnesium oxide and spinel $MgAl_2O_4$ with a secondary form of magnesium oxide developing by the reduction of an amorphous γ-alumina surface

layer. In contrast to the work by Ritchie et al[190] it seems that this rapid nucleation of $MgAl_2O_4$ was due to the combined effect of the use of very low oxygen pressure and of ultrafine alloy foils.

Using the ESCA technique, Leighly and Alam[169] recently studied the oxide layer developed when magnesium was present in aluminium at very low levels, i.e. 0.05-0.1%. They also found that the oxide developed at 475°C was a duplex layer with spinel $MgAl_2O_4$ superimposed on an underlying magnesium oxide film. The formation of $MgAl_2O_4$ in this occasion can be explained by the very low magnesium activity which stabilises the $MgAl_2O_4$ phase thermodynamically, as discussed later in Section 8.4.1(a).

Lea and Ball[189], using samples of 0.5mm thick coupons made from commercial aluminium -0.8 and 2.5% magnesium alloys, attempted to understand the growth morphology of the oxide layer in an investigation of oxidation kinetics during heat treatment. They proposed that magnesium diffusion through crystalline γ-alumina above 350°C, formed an magnesium oxide layer on top of the γ-alumina and an $MgAl_2O_4$ layer sandwiched between γ-alumina and magnesium oxide. His proposal for the morphology of the γ-alumina and the magnesium oxide overlayer is acceptable because he identified these structures by Augur electron spectroscopy (AES). However, the assumption for the formation of $MgAl_2O_4$ is not so acceptable because he could not identify it. Although the reaction is feasible, it is unlikely that it actually occurs on the basis of the argument advanced by Ritchie et al[190] that the reaction for the formation of spinel $MgAl_2O_4$ requires high activation energy.

(v) The influence of elements in inhibiting oxidation, especially beryllium

Whitaker and Heath[193], Hine and Guminski[59], and Field et al[186,187,194] appreciated the pronounced effect of beryllium impurities in the alloys which inhibit oxidation. On two different occasions, Field et al have identified protective beryllium oxide[186,187] and the spinel $BeMgAl_4O_8$[194]

during the oxidation of aluminium -4 to 5% magnesium alloys containing 0.01% and 0.1% beryllium. From structural evidence, they proposed that beryllium both delayed the reduction of the air-formed γ-alumina film, and replaced the magnesium oxide overlayer by a thin protective layer of either the spinel $BeMgAl_4O_8$[194] or beryllium oxide. Hine and Guminski[59] observed that additions of 0.001% and 0.01% beryllium protected commercial aluminium -3.5% magnesium alloys against oxidation. They attributed this to the formation of a layer of beryllium oxide which is protective by virtue of a favourably high volume ratio. The free energy change for formation of beryllium oxide and the rapid diffusion rate of beryllium in the alloy can be assumed to permit selective oxidation. However, Whitaker and Heath[193] could not accept all of these proposals because they found that additions of 0.004% and 0.15% beryllium gave protection against the oxidation of aluminium -10% magnesium alloys and yet the addition of 0.035% beryllium had no effect. Consequently, he could not ascribe this to the protective character of beryllium oxide but instead attributed it to the mechanical strength of the oxide because the oxide films developed on alloys having 0.004 and 0.15% beryllium were markedly tougher than that formed on alloys having 0.035% beryllium.

4.3.2 Liquid Alloys

Very little work has been carried out on the oxidation of liquid aluminium-magnesium alloys. Some early investigators were included in a general review by Drouzy and Mascre[195], who drew attention to the scarcity of published information at that time. They quoted work by Balicki[196] and by Thiele[197] which showed that liquid aluminium-magnesium alloys yielded swollen black oxide films, an effect which increased as the magnesium content was increased. Both authors identified spinel, $MgAl_2O_4$ as the essential component of the films and Balicki considered that the $MgAl_2O_4$ is formed from magnesium oxide produced in the early stages of the oxidation

when the oxide growth followed a linear law. Balicki's[196] investigation was confined to 1h periods and magnesium contents of up to 10%, but Thiele's[197] work employed very long periods, i.e. up to 160h, and a wider range of magnesium contents, i.e. up to 20%.

Later investigations by Cochran et al[85], Belitskus[198], and Haginoya and Fukusako[199] established the following features which apply to the oxidation of liquid aluminium-magnesium alloys:

(i) There is an initial induction period during which oxidation is slow. During the induction period the molten metal surface is covered with an X-ray indifferent, i.e. amorphous, oxide layer assumed, but not proven, to be either magnesium oxide[198] or $MgAl_2O_4$[199]. Cochran et al[85] found on aluminium -1.83% magnesium alloys that the induction period varied from 1 to 30h with increasing temperature from 660°C to 850°C while Belitskus[198] found it to be ∿ 5h at 750°C on aluminium -4 to 4.5% magnesium alloys. Haginoya and Fukusako[199] observed an induction period of about 10 min on aluminium -10% magnesium alloys at 750°C.

(ii) The induction period is followed by rapid breakaway oxidation associated with the appearance of crystalline phases. Cochran et al[85] and Haginoya and Fukusako[199] identified both magnesium and $MgAl_2O_4$ by X-ray diffraction but Belitskus[198] could not identify $MgAl_2O_4$ and found only crystalline magnesium oxide. It is worth noting that Cochran et al[85], Belitskus[198], and Haginoya and Fukusako[199] oxidised the samples until the magnesium contents were exhausted and hence the formation of $MgAl_2O_4$ during extended oxidation after induction period can be attributed to the consumption of all the magnesium in the samples. However, the initial formation of $MgAl_2O_4$, i.e. during or just after a short induction period, can be ascribed to the growth of an γ-Al_2O_3 layer during the heating of samples to the test

temperature, as discussed in Section 8.4.2(a). This is supported by the view of Haginoya and Fukusako[199] that the initial amorphous layer is $MgAl_2O_4$.

(iii) The induction period and the subsequent rapid oxidation associated with the appearance of crystalline phases applies to all of the aluminium-magnesium alloys irrespective of the oxidation temperature and the nature of the oxidising atmosphere. For example, Cochran et al[85] made their observations on cylindrical samples 32mm diameter x 6mm high of a 1.83% magnesium alloy oxidised in high pressure air, 66MPa†, at various temperatures in the range 660-850°C and on similar samples of alloys with 1-14% magnesium oxidised in the same temperature range in a variety of oxidising atmospheres; Belitskus[198] used 25mm diameter x 6mm high cylindrical samples of aluminium -4 to 4.5% magnesium alloys oxidised in dry air at 750°C; Haginoya and Fukusako[199] used 8.5g samples of alloys with 2-12% magnesium oxidised in dry air at temperatures in the range 650°C-900°C.

(iv) The induction period is decreased by increasing temperature or increasing magnesium content but increased by prior homogenisation, fast melting to test temperature, and the addition of beryllium to the alloy as observed by Cochran et al[85].

(v) Seeding the melt with crystalline magnesium oxide or $MgAl_2O_4$ prior to oxidation causes earlier breakaway oxidation[85] and this evidence confirms the view that the breakaway oxidation is promoted by the crystallisation of the initially formed amorphous films.

(vi) The presence of small beryllium additions markedly reduces the oxidation of liquid alloys[85,196,197]. Balicki[196] observed that the oxidation

---

† This seems to be a very high pressure

rate of aluminium -10% magnesium alloy decreased progressively as the beryllium content was increased in the range 0.0005 to 0.1% and Thiele[197] concluded that 0.001, 0.0015, 0.004 and 0.02 beryllium concentrations were sufficient to protect alloys containing 3,5,10 and 20% magnesium respectively. Cochran et al[85] demonstrated that as little as 0.001% beryllium inhibited the oxidation by increasing the induction period for an aluminium -3.5% magnesium alloy at 800°C, as it had been earlier reported by Thiele[197].

In all of this work on liquid aluminium-magnesium alloys there are two important omissions.

(a) No attempt has been made to assess the influence of water vapour on the oxidation kinetics or on the oxide film morphology.

(b) None of the work was carried out under "truly" isothermal conditions. This is an obstacle to clear interpretation of the results in view of the established fact that breakaway is induced by the appearance of crystalline phases and is therefore likely to be very sensitive to the thermal history of the sample both in preparation and during heating to the test temperature. This undoubtedly explains the influence on the induction period of the rate of heating observed by Cochran et al[85] and the very short induction period observed by Haginoya and Fukusako[199] in comparison with the induction period found by Belitskus[198].

5. HYDROGEN ABSORPTION BY ALUMINIUM-MAGNESIUM ALLOYS

It is well-known that aluminium-magnesium alloys can absorb hydrogen by reaction with water vapour when heated in humid atmospheres[200]. The hydrogen is formed by the reaction of water vapour with the metal:

$$2Al + 3H_2O \rightleftharpoons Al_2O_3 + 3H \quad \ldots\ldots\ldots\ldots\ldots\ldots \quad (5.1)$$

or

$$Mg + H_2O \rightleftharpoons MgO + 2H \quad \ldots\ldots\ldots\ldots\ldots\ldots \quad (5.2)$$

so that the kinetics of hydrogen absorption and the kinetics of oxidation are mutually dependent. In particular, if the oxide formed is magnesium oxide the hydrogen produced can, in principle, inject OH^- ions as the extrinsic defects into the oxide:

$$O^{2-} + H_2O = 2\,OH^- \quad \ldots\ldots\ldots\ldots\ldots\ldots \quad (5.3)$$

The ability of aluminium-magnesium alloys to absorb hydrogen and the subsequent effects of the absorbed gas on the alloy depend upon the nature of hydrogen occlusion within the metal. From a comprehensive review by Talbot[200], it is clear that hydrogen can be occluded in aluminium-magnesium in several different forms, namely physical solution and trap sites of various kinds. These will now be examined.

5.1. Hydrogen Solution

Hydrogen is the only gas which dissolves with a measurable solubility in aluminium and aluminium-magnesium alloys. Size factors determine that the hydrogen must dissociate on dissolution, so that:

$$H_2\ (gas) \rightleftharpoons 2H\ (solution) \quad \ldots\ldots\ldots\ldots\ldots\ldots \quad (5.4)$$

The pressure and temperature dependence of the dissolved hydrogen are

given by:

$$\text{Isotherm:} \quad \frac{C}{C^{\ominus}} = \left[\frac{p}{p^{\ominus}}\right]^{0.5} \qquad \ldots\ldots\ldots\ldots\ldots\ldots \quad (5.5)$$

where C is the dissolved hydrogen concentration in equilibrium with an arbitrary gas pressure, p and $C^{\ominus}$ is the dissolved hydrogen at the standard pressure, $p^{\ominus}$ and temperature, $0^{o}C$. Both C and $C^{\ominus}$ are expressed in units of cm^3 of hydrogen per 100g.

$$\text{Isobar:} \quad \log\left[\frac{C}{C_u}\right] = \frac{-\Delta H^{\ominus}}{2RT} + \text{Constant} \ldots\ldots\ldots\ldots\ldots \quad (5.6)$$

where C is the dissolved hydrogen concentration and C_u is the standard unit defined as 1 cm^3 of hydrogen measured at $0^{o}C$ and 1 atm pressure per 100g of metal.

The accommodation of hydrogen in substitutional solution is precluded by the size factors together with valence considerations so that the simplest assumption is that the solute hydrogen is accommodated as non-interacting atoms, all occupying equivalent interstitial sites.

The solubility of hydrogen in liquid aluminium-magnesium alloys is somewhat higher than that in pure aluminium[201] and increases with magnesium content. This is illustrated in Table 4 which gives results obtained by Stephenson[201].

More recently, investigations by Grior 'Eva and Danilkin[202] yielded analogous results for aluminium-magnesium alloys containing magnesium up to 6% confirming that the solubility increases with increasing temperature or magnesium content. They interpreted the data on the basis that the addition of magnesium to aluminium caused an increase in the "Fermi" energy level which in turn decreased the interstitial electron density in the metal. Since the hydrogen solubility was assumed to be inversely proport-

ional to the interstitial electron density, the addition of magnesium was to enhance the solubility of hydrogen.

The only recorded result for the solubility of hydrogen in solid aluminium-magnesium alloys is given by Eborall and Ransley[203] who found values of 0.058 and 0.043cm^3/100g for aluminium -7% magnesium alloys at 500°C after saturation periods of 6 and 24h respectively. These values are appreciably greater than the corresponding values for pure aluminium[204], i.e. 0.015cm^3/100g.

5.2 Forms of Hydrogen Traps

The equation (5.6) probably represents the solution of hydrogen in a liquid metal reasonably well[201] but if the whole of the hydrogen contained in a solid metal were in interstitial solution, it would assume a degree of perfection in the structure which is quite unrepresentative of normal aluminium-magnesium alloys and is even difficult to achieve under laboratory conditions. Consequently, hydrogen is distributed not only in interstitial solution, but also in other occluded forms, usually referred to as hydrogen trap sites. The total hydrogen content in such materials is the sum of quantities in true interstitial solution and in other occluded forms:

$$1/2\ H_2\ (gas) \rightleftharpoons H(solution) \rightleftharpoons H(trap\ sites) \quad ..... \quad (5.7)$$

Several kinds of trap sites have been identified and it is convenient to classify them into three main types, atomic traps, molecular traps and chemical traps.

5.2.1. Atomic Traps

In principle, an association between solute atoms and lattice defects is expected because of the relief of lattice strain[205]. Although there is no information on aluminium-magnesium alloys, such an effect has been

demonstrated by Foster et al[206] who used tritium to study the distribution of hydrogen in aluminium. Using autoradiography he concluded that the dissolved gas segregated to lattice defects.

5.2.2. Molecular Traps

There are two distinct forms of molecular traps. If large defects are present in the metal, they constitute one form because molecular hydrogen accumulates within them until it reaches a pressure that is in equilibrium with the dissolved interstitial atomic hydrogen. The other form of trap is due to the spontaneous precipitation of hydrogen within the solid metal producing widely distributed very small spherical pores identified by Talbot and Granger[207] as"secondary porosity". They suggested that the precipitation of the gas required the simultaneous condensation of vacancies to provide the voids to receive the gas phase.

5.2.3. Chemical Traps

Although aluminium-magnesium alloys do not form stable hydrides under conditions of metallurgical interest[200], other elements present as impurities may react with hydrogen to form hydrides as precipitates. The additional hydrogen that the metal can absorb in this way may be regarded as being chemically trapped. A typical example is that the near stoichiometric conversion of sodium to sodium hydride when it is present as an impurity in aluminium-magnesium alloys[208]:

$$1/2\ H_2\ (gas) + M(in\ alloy) \rightleftharpoons MH\ (precipitate) \quad ..... \quad (5.8)$$

5.3 Porosity Formation during Casting

Because the solubility of hydrogen is very much lower in solid than that in liquid metal, some of the gas is expelled during casting from the solution and is entrapped in the solid structure. The expelled gas could be nucleated both in the liquid during solidification and in the solid

immediately afterwards, generating two different kinds of porosity, distinguished by terms "interdentritic (or primary) porosity", and "secondary porosity"[207]. It is worth noting that the porosity formation could take place only if the hydrogen dissolved can exceed certain critical values appropriate to the casting conditions and composition of the material.

5.4. Effect of Hydrogen Absorption on Oxidation

When liquid and semi-liquid aluminium-magnesium alloys are exposed to moisture at elevated temperature, the oxidation causes the alloys to blister, blacken and become embrittled characteristically with a significant increase in the hydrogen content in the alloy[193,203,204,209]. The absorbed hydrogen can in turn disrupt the oxide film affecting the subsequent oxidation.

5.4.1. Blistering

The formation of both surface blisters and blisters within the metal has frequently been observed in aluminium-magnesium alloys during the reaction with moist atmospheres at elevated temperatures. These blisters eventually contribute to the disruption of the superficial oxide film leading to further oxidation. Surface blisters appear in a few seconds after oxidation at discontinuities, i.e. oxide/metal interface, due to the accumulation of hydrogen evolved during oxidation[210]. Moreover, pre-existing discontinuities such as primary and secondary porosities can develop into internal blisters. This is because the growth of these internal defects which eventually coalesce to form blisters proceeds with continuous absorption of hydrogen because the pressure of hydrogen in them exceeds the restraining forces of the surrounding metal[211].

5.4.2. Hydrogen Embrittlement

This complex phenomena is not well understood and there are a number of

controversial mechanisms[210,212,213] which have been proposed to account for the hydrogen embrittlement of aluminium-magnesium alloys.

Previous studies have shown that magnesium segregates *along the grain* boundaries of aluminium-magnesium alloys under all heat-treatment conditions prior to use[214] and it has been cited as the major cause of embrittlement. Tuck[212] suggested that Mg-H complexes form at grain boundaries in the temperature range 380-450^{o}C during heat-treatment when the pressure in the hydrogen porosity reached 100-200 atm. When the alloys were heated in the temperature range 400-500^{o}C, these precipitated Mg-H complexes at grain boundaries dissociated evolving hydrogen accommodated in bubbles at high pressure, i.e. 100-200 atm. These bubbles were believed to promote decohesion along grain boundaries exposing more surface area for oxidation. On the other hand, Scamans and Rehal[210], and Montgrain et al[213] on the basis of experimental evidence suggested that the formation of hydrogen permeable films of crystalline magnesium oxide provided easy access to protons. These protons were released at grain boundary/metal interface as bubbles of molecular hydrogen with consequent intergranular failure promoting further oxidation.

6. EXPERIMENTAL

Two approaches were adopted in the experimental work:

(a) The determination of oxidation kinetics.

(b) The identification and characterisation of the oxide films formed.

6.1 Experimental Materials

The materials were obtained from two sources:

(a) Binary aluminium-magnesium alloys were prepared from high purity aluminium and magnesium in 5.0 kg melts of five different compositions and chill-cast into square ingots 8 cm x 8 cm x 30 cm. A 4 mm layer was machined from all cast surfaces of the ingots to remove magnesium segregates. Two longitudinal bars each 24 cm x 2 cm diameter were machined near to the machined surfaces of every ingot to provide stocks from which samples were taken, avoiding the central zone where some unsoundness or segregates might occur.

(b) Binary alloys containing small additions of beryllium, beryllium + manganese, and beryllium + zirconium were supplied by the Aluminium Company of America in the form of cross-sections taken from 15 cm diameter continuously cast ingots. Again a 4 mm layer was machined from the cast surface to remove magnesium segregates. Four bars each 15 cm x 2 cm diameter were machined from each ingot with their axes parallel to the axis of the ingot, avoiding both the ingot surface and the central zone as before.

All the materials were heat-treated at the highest safe temperatures, i.e. 50-150^{o}C below the equilibrium solidus temperatures, for 48 hours in a forced air circulation furnace to homogenise them. Samples from the homogenised bars produced from melts cast at Brunel University were analysed by ALCAN International Ltd. The materials supplied by the Aluminium

Company of America were analysed by that Company. The Analyses and corresponding heat-treatment temperatures are given in Tables 5 and 6.

6.2. Determination of Liquidus and Solidus Temperatures

The solidus and liquidus temperatures of the materials available were determined so that in designing the oxidation experiments, suitable test temperatures could be selected. Direct experimental determination of these values on the actual materials used provided a check on published values available in the literature[215].

The technique used was the Smith thermal analysis technique (STA)[216] in which a sample is heated or cooled in a furnace at a controlled rate designed to maintain a constant temperature difference across a thermal barrier placed between the sample and the furnace environment. The measured temperatures were applied to the input of a BBC mini-computer with a programme designed to analyse the results in convenient graphic and digital forms from which the arrest points could be accurately extracted. The technique is described in greater detail in Appendix 2.

The values for the arrests on heating and cooling the same sample differed by $\leq 3^{o}C$ and the values accepted were the average values.

6.3. The Determination of Oxidation Kinetics

The oxidation kinetics for solid, semi-liquid, and liquid aluminium-magnesium alloys were all determined by a thermogravimetric method.

The thermogravimetric system comprises an assembly of three integrated systems:

(i) A high-sensitivity microbalance, supplied by Sartorius Ltd., model 4410.

(ii) An ancillary recording system supplied with the microbalance.

(iii) The specimen chamber and its associated vacuum system, gas

trains and furnace designed and constructed at Brunel University.

These arrangements are illustrated schematically in Figure 40 and a general view of the equipment is shown in the photograph given in Figure 41.

6.3.1. The Sartorius Microbalance

The microbalance selected for the present work must comply with the following essential requirements.

(i) It must have a sensitivity and stability of better than 10 μg. This requirement is imposed by the expectation that the mass increase during oxidation on a sample of convenient size may be as small as 1 mg.

(ii) The balance must have a total loading capacity > 10g, to accommodate the combined mass of sample and a crucible to contain it.

(iii) The suspension arrangement must permit close control of the sample temperature and the oxidising atmosphere.

The Sartorius microbalance, model 4410, satisfies these requirements. It employs a lightweight metallised quartz tube as the balance beam, ensuring excellent mechanical and thermal stability; the beam is supported on a torsion band, thereby eliminating frictional resistance. The arrangement provides a loading capacity of 25 g with a sensitivity of 1 μg. When mounted on a convenient concrete pillar in the laboratory, free from excessive vibration and with suitable precautions to eliminate interference from electric fields, the balance is stable to ±2 μg indefinitely. A special feature is that the whole weighing system is contained within a sealed unit which can be evacuated to high vacuum or filled with any desired atmosphere.

The balance functions on the principle of automatic electromagnetic force compensation. The torque produced by the mass to be weighed creates an electrical counter-torque. The beam is maintained in equilibrium with only

a minimal deflection, i.e. a maximum of 0.2 mm at the end of the beam. The compensating current required for this purpose is generated automatically and is a measure of the weight to be determined. A pan is provided on one side of the balance to permit coarse taring with counterweights.

6.3.2. Ancillary Recording System

The ancillary recording system comprises a digital voltmeter (DVM), a digital/analog converter (DAC) and a chart recorder. The output from the balance is displayed on the DVM. The DAC converts measured values into proportional voltages which are fed into a chart recorder, Figure 42.

6.3.3. Specimen Chamber and its Associated Vacuum System, Gas Train, and Furnace.

The general arrangement is illustrated schematically in Figure 40.

The specimen Chamber, A, is constructed of fused silica and secured to the microbalance tube, B, with a sprung clamp on a vacuum-tight 'O' ring ball joint, C. This facilitates easy dismantling for sample loading. The specimen chamber is earthed as shown in Figure 43, by a metal wire wound around it to prevent accumulation of static electricity. The sample is placed in a preconditioned recrystallised alumina crucible suspended by a platinum cradle, D, which in turn is suspended by a silica filament, E, from the microbalance. A thermocouple is inserted into the specimen chamber, with the hot junction located 0.5 cm above the sample surface, through a seal in a slica cap, F, which is fitted to the microbalance by an 'O' ring ball joint also secured with a sprung clamp. The temperature in the chamber can be maintained to $\pm 1^{o}C$ and is recorded on a calibrated digital thermometer.

Radiation shields, G, are mounted on the tube to protect the balance and 'O' ring joint from the furnace radiation. In the balance design the

mechanism is protected from convection currents by two baffles located in the microbalance tube.

The furnace, H, is constructed around a 40 mm internal diameter, 2 mm wall thickness alumina porcelain tube. It is mounted on bearings and can be raised around the specimen chamber and secured in position as required. The furnace temperature is controlled to $\pm 2^{o}C$.

The vacuum system, i.e. between taps T_1 and T_2, can be evacuated via taps T_3 and T_4 by a mercury-in-glass diffusion pump, J, backed by a mechanical rotary pump. Liquid nitrogen cold traps K, L and M are provided to freeze out water vapour and pressure measurements can be made on a Pirani gauge, N, and a manometer, P.

Two gas trains are provided to supply the required oxidising atmosphere. One gas train supplies high purity helium, i.e. 99.999%†, through a purification and drying system comprising a 40 cm column of copper turnings, Q, heated to $300^{o}C$, a 40 cm column of silica gel, R, and the liquid nitrogen cold trap, K. The other gas train supplies dry and moist high purity oxygen, i.e. 99.998%†, to synthesise dry or moist atmospheres respectively. For dry atmospheres the oxygen was dried by passing the high purity oxygen initially through a 30 cm 'U' tube, S, of silica gel and then through the liquid nitrogen trap, L. For experiments using moist atmospheres, the system was modified as follows. The cold trap, L, was replaced by a bubbling tube half-filled with distilled water, and a water finger also half-filled with distilled water was attached at W in the microbalance system. The moist oxygen was then prepared and admitted by bubbling the high purity oxygen very slowly, i.e. 100 $cm^3 sec^{-1}$, through water maintained at $25^{o}C$ at which temperature the equilibrium water vapour pressure is

---

† Supplied with guaranteed analysis certified by the manufacturers.

3040 Pa (0.03 atm). In preliminary measurements it was confirmed that the water vapour pressure reached the equilibrium value.

The purpose of these two gas trains is to supply an inert atmosphere initially in which the sample can be heated to and stabilised at any required temperature before oxidation is commenced, and then to introduce oxygen. Helium is selected for the inert atmosphere to avoid interference with the function of the balance by the effects of convection currents which are experienced with heavier gases such as argon or nitrogen.

The pair of high vacuum greaseless taps T_1 and T_2 are provided to isolate the whole system including the microbalance tube and both gas trains during preliminary evacuation to remove all the traces of air. The pair of similar taps T_5 and T_6 are provided to isolate the microbalance tube from either gas train while it is initially filled with oxygen or helium before a test is commenced.

6.3.4. Experimental Procedure

(a) Selection of Test Temperatures

The experiments were conducted at 25°C intervals in the temperature range 500-725°C which included the solidus and liquidus temperatures for all of the alloys. In addition, some intermediate temperatures were selected to include at least three test temperatures within the melting ranges of alloys with small melting ranges. The test temperatures selected in the melting ranges are superimposed on the aluminium-magnesium binary phase equilibrium diagram given in Figure 44.

(b) Sample Preparation

The samples were prepared to a standard surface condition to minimise the effect of surface texture on the results.

Samples in the form of discs, 16 mm diameter x 6 mm thick, were machined on a lathe to a fine surface finish. These dimensions were chosen so that samples to be oxidised at temperatures above the liquidus temperature would fit closely into the thermobalance crucible when placed flat, thereby minimising disturbance of the metal during melting. Immediately before use, every sample was ground on all faces with 600 grade silicon carbide paper, etched for one minute in 2.5 M sodium hydroxide solution to remove any surface contamination, rinsed first in distilled water and then in ethyl alcohol and thoroughly dried.

(c) Calibration of Microbalance

Before any measurements were made the microbalance was calibrated according to the manufacturer's instructions given in detail in Appendix 3. The operation of the balance was thoroughly checked and was found to comply in every respect with the manufacturer's specification.

(d) Thermogravimetric Determination

The prepared samples were placed in the crucible. Samples to be oxidised below the temperatures at which the solid fraction was <50% were placed on edge in the crucible so that the oxidised surface could be identified with the original complete geometric surface of the sample. Samples to be oxidised above the temperatures at which the solid fraction was >50% would not preserve their geometric shape and so were placed flat in the crucible and the exposed surface comprised the upper flat surface and the cylindrical surface which retracted away from the crucible sides under the influence of surface tension.

The reaction tube was placed in position, clamped to the balance enclosure and the whole system was evacuated, i.e. between taps T_1 and T_2 (Figure 40), to a pressure <0.1 Pa (10^{-6} atm). The oxidising atmosphere was intended to represent dry or moist air with the nitrogen replaced by helium to avoid

the experimental difficulties due to convection currents, as described earlier. Preliminary tests showed that if the samples were heated in vacuum, there was an appreciable loss of magnesium by evaporation from the alloy.

To suppress the magnesium evaporation, procedures were devised so that the sample was heated to and stabilised at the test temperature in dry helium at 0.79 atm pressure and the oxygen was introduced at the start of the test to give a total pressure of 1 atm after the sample had reached the test temperature.

For experiments using dry oxidising atmospheres the procedure was as follows. The pure helium was admitted via tap T_1 with the sample cold, upto tap T_6 with liquid nitrogen still applied to the two cold traps K and L in Figure 40. The sample was heated by the preheated furnace and the temperature in the specimen chamber rose to the test temperature within 7-10 min. After the sample temperature was stabilised by holding it at the test temperature for another 10 min, tap T_5 was closed, the liquid nitrogen on cold trap, L, was removed and then the pure oxygen was introduced via tap, T_2, using tap, T_6, to control the admission of dry oxygen to the specimen chamber.

For experiments using moist oxidising atmospheres the procedure was as follows. With liquid nitrogen still applied to the water finger, W, and cold trap, K, the helium was admitted into the gas train and microbalance system upto tap T_6. The sample was heated and stabilised at the test temperature as for the dry atmosphere. Finally, tap, T_5, was closed, the liquid nitrogen was removed from the water finger, and the pure oxygen was introduced via tap, T_2, using tap, T_6, to control the admission of moist oxygen to the specimen chamber. During the oxidation, saturated water vapour pressure in the specimen chamber was maintained by the water

exposed to the oxidising atmosphere in the water finger.

Oxygen consumed in the course of oxidation was continuously replenished as required from the oxygen supply via the gas train.

Oxidation started with the admission of oxygen and the balance was immediately tared. The mass gain was recorded as a function of time on the chart recorder operating at 1 cm per minute. The experiments were conducted for two or three hour periods as appropriate to the degree of oxidation observed.

The oxide structures formed on samples were preserved for characterisation by cooling them to room temperature in vacuum.

6.4. Identification and Characterisation of the Oxide Films

The following techniques were used to study the chemical nature, structure, and the topography of the oxide films.

(1) X-ray Diffractometry.
(2) Scanning Electron Microscopy (SEM).
(3) Transmission Electron Microscopy (TEM).

6.4.1. X-ray Diffractometry

The X-ray diffractometer was used to identify the structures of oxides using bulk samples from which insufficient oxide powder could be collected for the Debye-Scherrer powder photographic technique. A brief description of its principle of operation is given in Appendix 4.

The X-ray diffraction spectra obtained were compared with spectra derived from interplanar spacings given in the ASTM powder diffraction data files for anticipated oxides and for the metal substrate.

6.4.2. Scanning Electron Microscopy

A Cambridge S250 stereoscan with a resolution of ~10 nm at 10 kV was used

in the present study to examine the topographical details of oxide films. The general principle of operation is described in Appendix 5.

The oxidised samples were attached with double-sided adhesive tape to the standard specimen stubs for location in the specimen chamber. Care was taken to ensure that the sample was in electrical contact with the stub by applying colloidal silver, i.e. silver dag, between the edge of the sample and the stub.

6.4.3. Transmission Electron Microscopy.

The TEM offers by far the best method for examining and identifying oxide films.

A JEOL 100 CX Temscan with a resolution of ~0.5 nm at 100 kV accelerating potential was used in the present work. The operation of the instrument is briefly described in Appendix 6 (a).

(a) Sample Preparation

To obtain thin samples of oxide film for the penetration of electrons, the oxide film formed on the alloy sample was scraped-off gently with a sharp blade over the surface to obtain powder from the oxide. The powder was then collected by suspending it in acetone. The suspended oxide particles were further collected by pipetting the suspension on to carbon-films, 50 nm thick, supported on standard copper grids, for viewing in the TEM.

(b) Characterisation of Oxide Films

The nature of oxide, i.e. whether amorphous or crystalline, was determined from its electron diffraction pattern. A diffuse diffraction pattern is characteristic of an amorphous oxide while a clear ring diffraction pattern is characteristic of a crystalline oxide.

(c) Identification of the Crystal Structure of Oxide Films

For oxides found to be crystalline, three approaches were used on any particular diffraction pattern to establish the identity of the oxides present:

(i) Comparison of the unknown diffraction pattern with diffraction patterns of pure aluminium, magnesium oxide, and α-alumina obtained under the same experimental conditions. This was accomplished by visually matching the negative films of unknown diffraction patterns with the known patterns using a light box.

(ii) Comparison of the interplanar spacings calculated as described in Appendix 6 (b) with standard interplanar spacings of anticipated oxides extracted from the ASTM powder diffraction data files given in Appendix 6 (c).

(iii) Elemental analysis of the selected areas used for electron diffraction by the STEM-EDX facility provided. If the selected area of the oxide comprised only magnesium oxide, only the energy peak for magnesium would appear; if it comprised aluminium or α-alumina, only the energy peak for aluminium would appear; if it comprised only spinel, $MgAl_2O_4$, the ratio of the energy peak heights Al:Mg would be 2:1.

Oxides found to be amorphous would be identified only by elemental analysis using STEM-EDX facility as described in (iii) above.

7. RESULTS

7.1 Thermal Analysis Results

The results for solidus and liquidus temperatures obtained using STA are given in Table 7. Literature values[215] are also given in the table for comparison. Values extracted from Table 7 are plotted in the form of a partial phase equilibrium diagram for the aluminium-magnesium system in Figure 45. Table 7 and Figure 45 show good agreement between the experimental and literature values.

7.2. Thermogravimetric Results for Oxidation

In presenting the thermogravimetric results two difficulties arise:

(a) Assessment of the effective surface area for alloys oxidised with a solid fraction > 50%.

(b) Selection of convenient scales on which to compare widely different oxidation rates.

(a) Assessment of the effective surface area

As described in section 6.3.4.(d), samples heated above temperatures at which the solid fraction is > 50%, did not maintain their rigid geometric shape during oxidation and so they were oxidised flat on the crucible bottom exposing only the top circular surface and the retracted cylindrical surface. Visual examination of any sample oxidised in this mode revealed that the nominally unexposed bottom circular surface was discoloured suggesting that this surface did in fact contribute significantly to the oxidation. The effect of the bottom surface on the total mass gain was assumed as follows. Samples representing all of the alloys were heated to temperatures at which the solid fraction was 50%. One sample of every alloy was oxidised on edge and another flat in the crucible in both dry and moist atmospheres. The results are given in Figures 46-49. In every case the total mass of oxide

formed was less for the sample mounted flat than for those on edge but the difference was not so great as it would have been if no oxidation at all occurred on the nominal unexposed face. A correction was applied in which an "equivalent effective fraction of the surface area" for the bottom unexposed face was calculated by fitting the oxidation curves for the flat samples to the curves for the corresponding samples mounted on edge. The essence of this technique is illustrated by the corrected curve for the 5.1% magnesium alloys oxidised at 610°C in dry atmospheres given in Figure 50.

The equivalent effective fraction of the surface areas of the bottom sample faces for all of the alloys determined in this way are given in Table 8. The correction actually applied to the thermogravimetric results obtained for samples oxidised flat are the average values given in the last column of the table. It is noteworthy that the correction is very similar, i.e. 0.25 ± 0.04 for all of the alloys irrespective of the atmosphere.

(b) Selection of Convenient Scales

Since the total mass gains observed increased by over two orders of magnitudes as the magnesium content was increased within the range 1-9%, the mass gain/time curves could not all be displayed with sufficient sensitivity on the same mass-gain scale. These scales were chosen on which to present the results:

Alloy with nominal wt% Mg	Scale length for 1 mg/cm^2
Al- 1% Mg	60 cm
Al- 3% Mg	60 cm
Al- 5% Mg	20 cm
Al- 7% Mg	2.5 cm
Al- 9% Mg	2.5 cm
Al- 8% Mg-0.003% Be	40 cm
Al- 8% Mg-0.003% Be-0.24% Mn	40 cm
Al- 8% Mg-0.003% Be-0.12% Zr	40 cm

7.2.1. Results for Aluminium Magnesium Binary Alloys

The thermogravimetric results for the oxidation of the aluminium-magnesium binary alloys corrected for effective area are given in Figures 51-60, as the recorded traces reproduced in a convenient format. These traces recorded mass gain as a function of time for all of the alloys in the temperature range 500-725^{o}C in moist and dry mixtures of 0.21 oxygen/0.79 helium, i.e. with and without 3040 Pa (0.03 atm) water vapour pressure. The results are arranged as follows:

Figure 51 : Al-1.3% Mg alloy in dry atmospheres.
Figure 52 : Al-1.3% Mg alloy in moist atmospheres.

Figure 53 : Al-3.1% Mg alloy in dry atmospheres.
Figure 54 : Al-3.1% Mg alloy in moist atmospheres.

Figure 55 : Al-5.1% Mg alloy in dry atmospheres.
Figure 56 : Al-5.1% Mg alloy in moist atmospheres.

Figure 57 : Al-7.4% Mg alloy in dry atmospheres.
Figure 58 : Al-7.4% Mg alloy in moist atmospheres.

Figure 59 : Al-9.3% Mg alloy in dry atmospheres.
Figure 60 : Al-9.3% Mg alloy in moist atmospheres.

Selected curves from Figures 53 and 54 for solid aluminium-3.1% magnesium alloys and from Figures 57 and 58 for solid aluminium-7.4% magnesium alloys, are reassembled in Figures 61 and 62 respectively to compare the oxidation kinetics in dry and moist atmospheres.

Figures 63-72 give the results from Figures 51-60 in the same sequence but replotted on a parabolic scale, i.e. Δm^2 v time.

7.2.2. Results for Aluminium-Magnesium-Beryllium Alloys

The thermogravimetric results corrected for effective area for the oxidation

of the aluminium-magnesium-beryllium alloys, i.e. aluminium-magnesium binary alloys containing small amounts of beryllium, beryllium + manganese, and beryllium + zirconium, are given in Figures 73-78 as the recorded traces reproduced in a convenient format. These traces record mass gain as a function of time for all of the alloys in the temperature range 500-725^{o}C in moist and dry mixtures of 0.21 oxygen/0.79 helium, i.e. with and without 3040 Pa (0.03 atm) water vapour pressure. The results are arranged as follows:

Figure 73 : Al-8.2% Mg-0.003% Be alloy in dry atmospheres.

Figure 74 : Al-8.2% Mg-0.003% Be alloy in moist atmospheres.

Figure 75 : Al-8.16% Mg-0.003% Be-0.24% Mn in dry atmospheres.

Figure 76 : Al-8.16% Mg-0.003% Be-0.24% Mn in moist atmospheres.

Figure 77 : Al-8.13% Mg-0.003% Be-0.12% Zr in dry atmospheres.

Figure 78 : Al-8.13% Mg-0.003% Be-0.12% Zr in moist atmospheres.

Figures 79-84 give the results from Figures 73-78 in the same sequence but replotted on a parabolic scale, i.e. Δm^2 v time.

Tables 9(a) and (b) give the results for the calculated magnesium contents of the Al-Mg and Al-Mg-Be alloys exhibiting the highest mass gains after 2h and 3h oxidation respectively in the solid, semi-liquid, and liquid states. These results show that the magnesium loss during 2h or 3h oxidation was insignificant in comparison with the initial magnesium content, i.e. the bulk magnesium content remained fairly constant.

7.3. TEM Observations

Figures 85-97 show the transmission electron micrographs and corresponding electron diffraction patterns of oxide samples removed by scraping off the thermogravimetrically oxidised alloy samples in moist and dry mixtures of 0.21 oxygen/0.79 helium, i.e. with and without 3040 Pa (0.03 atm) water vapour pressure. Both by comparison of the diffraction patterns with known

diffraction patterns obtained under the same conditions and by reference to the ASTM powder diffraction data files, all the diffraction patterns could be matched only to magnesium oxide. Figures 98-100 show the correlation of Figures 87-89 respectively with the corresponding points on the mass gain curves.

Figures 85-92 give the TEM micrographs of oxide samples removed from aluminium-magnesium binary alloys:

Figures 85 a,b,c : Oxide developed respectively after 30 min, 1h and 2h oxidation at 525^{o}C on solid Al-3.1% Mg alloy in the moist atmosphere. (x 120,000).

Figures 85 d,e,f : Electron diffraction patterns from areas shown in Figures 85 a,b and c respectively.

Figures 86 a,b,c : Oxide developed respectively after 30 min, 1h and 2h oxidation at 525^{o}C on solid Al-7.4% Mg alloy in the dry atmosphere. (x 120,000).

Figures 86 d,e,f : Electron diffraction patterns from areas shown in Figures 86 a,b, and c respectively.

Figures 87 a,b : Oxide developed respectively after 30 min and 2h oxidation at 700^{o}C on liquid Al-3.1% Mg alloy in the dry atmosphere (x 120,000).

Figures 87 c,d : Electron diffraction patterns from areas shown in Figures 87 a and b respectively.

Figures 88 a,b,c : Oxide developed respectively after 30 min, 1h and 2h oxidation at 650^{o}C on liquid Al-5.1% Mg alloy in the moist atmosphere. (x 120,000).

Figures 88 d,e,f : Electron diffraction patterns from areas shown in Figures 88 a,b and c respectively.

Figures 89 a,b,c : Oxide developed respectively after 5 min, 10 min and 2h oxidation at 675°C on liquid Al-9.3% Mg alloy in the dry atmosphere. (x 120,000).

Figures 89 d,e,f : Electron diffraction patterns from areas shown in Figures 89 a,b and c respectively.

Figures 90 a,b,c : Oxide developed respectively after 5 min, 15 min and 2h oxidation at 625°C in the moist atmosphere on Al-3.1% Mg alloy with < 50% liquid in the semi-liquid state. (x 120,000).

Figures 90 d,e,f : Electron diffraction patterns from areas shown in Figures 90 a,b, and c respectively.

Figures 91 a,b : Oxide developed respectively after 30 min and 2h oxidation at 640°C in the dry atmosphere on Al-3.1% Mg alloy with > 50% liquid in the semi-liquid state. (x 120,000).

Figures 91 c,d : Electron diffraction patterns from areas shown in Figures 91 a and b respectively.

Figures 92 a,b : Oxide developed respectively after 15 min and 2h oxidation at 610°C in the dry atmosphere on Al-7.4% Mg alloy with > 50% liquid in the semi-liquid state. (x 120,000)

Figures 92 c,d : Electron diffraction patterns from areas shown in Figures 92 a and b respectively.

Figures 93-97 give TEM the micrographs of oxide samples removed from Al-Mg-Be alloys.

Figures 93 a,b,c : Oxide developed respectively after 45 min, 1.5h and 3h oxidation at 525°C on solid Al-8.2% Mg-0.003% Be alloy in the moist atmosphere. (x 160,000).

Figures 93 d,e,f : Electron diffraction patterns from areas shown in Figures 93 a,b, and c respectively.

Figures 94 a,b,c : Oxide developed respectively after 30 min, 1h and 2h oxidation at 700°C on liquid Al-8.16% Mg-0.003% Be-0.24% Mn alloy in the dry atmosphere. (x 160,000)

Figures 94 d,e,f : Electron diffraction patterns from areas shown in Figures 94 a,b, and c respectively.

Figures 95 a,b,c : Oxide developed respectively after 30 min, 45 min and 3h oxidation at 700°C on liquid Al-8.13% Mg-0.003% Be-0.12% Zr alloy in the moist atmosphere.(x 160,000)

Figures 95 d,e,f : Electron diffraction patterns from areas shown in Figures 95 a,b and c respectively.

Figures 96 a,b,c : Oxide developed respectively after 45 min, 1.5h and 3h oxidation at 575°C in the dry atmosphere on Al-8.2% Mg-0.003% Be alloy with < 50% liquid in the semi-liquid state. (x 160,000)

Figures 96 d.e.f : Electron diffraction patterns from areas shown in Figures 96 a,b and c respectively.

Figures 97 a,b : Oxide developed respectively after 15 min and 3h oxidation at 610°C in the moist atmosphere on Al-8.13% Mg-0.003% Be-0.12% Zr alloy with > 50% liquid in the semi-liquid state. (x 160,000)

Figures 97 c,d : Electron diffraction patterns from areas shown in Figures 97 a and b respectively.

Figures 98, 99 and 100 show the correlation of Figures 87,88 and 89 respectively with the corresponding points on the mass gain/time curves extracted from Figures 53, 56 and 59.

7.4. X-ray Diffraction Results

Figures 101-112 give the X-ray diffraction spectra obtained by diffracting Cu Kα radiation for 20 min over the thermogravimetrically oxidised samples in moist and dry mixtures of 0.21 oxygen/0.79 helium, i.e. with and without 3040 Pa (0.03 atm) water vapour pressure. Comparison of the spectra with that derived from interplanar spacings given in the ASTM powder diffraction data files for anticipated oxides showed that the only oxide present was magnesium oxide.

Figures 101-108 give X-ray diffraction spectra for Al-Mg binary alloys.

Figure 101 : X-ray diffraction spectra obtained after 2h oxidation of solid Al-1.3% Mg alloy at 525^{o}C in the moist atmosphere.

Figure 102 : X-ray diffraction spectra obtained after 2h oxidation of solid Al-7.4% Mg alloy at 525^{o}C in the dry atmosphere.

Figure 103 : X-ray diffraction spectra obtained after 2h oxidation of liquid Al-3.1% Mg alloy at 700^{o}C in the moist atmosphere.

Figure 104 : X-ray diffraction spectra obtained after 2h oxidation of liquid Al-9.3% Mg alloy at 700^{o}C in the dry atmosphere.

Figure 105 : X-ray diffraction spectra obtained after 2h oxidation of semi-liquid Al-5.1% Mg alloy with < 50% liquid at 600^{o}C in the moist atmosphere.

Figure 106 : X-ray diffraction spectra obtained after 2h oxidation of semi-liquid Al-9.3% Mg alloy with < 50% liquid at 550^{o}C in the dry atmosphere.

Figure 107 : X-ray diffraction spectra obtained after 2h oxidation of semi-liquid Al-3.1% Mg alloy with > 50% liquid at 640^{o}C in the dry atmosphere.

Figure 108 : X-ray diffraction spectra obtained after 2h oxidation of semi-liquid Al-7.4% Mg alloy with > 50% liquid at 610°C in the moist atmosphere.

Figures 109-112 give X-ray diffraction spectra for Al-Mg-Be alloys.

Figure 109 : X-ray diffraction spectra obtained after 3h oxidation of solid Al-8.2% Mg-0.003% Be alloy at 525°C in the dry atmosphere.

Figure 110 : X-ray diffraction spectra obtained after 3h oxidation of liquid Al-8.13% Mg-0.003% Be-0.12% Zr alloy at 700°C in the moist atmosphere.

Figure 111 : X-ray diffraction spectra obtained after 3h oxidation of semi-liquid Al-8.13% Mg-0.003% Be-0.12% Zr alloy with < 50% liquid at 575°C in the dry atmosphere.

Figure 112 : X-ray diffraction spectra obtained after 2h oxidation of semi-liquid Al-8.16% Mg-0.003% Be-0.24% Mn alloy with > 50% liquid at 610°C in the moist atmosphere.

7.5. SEM Observations

Figures 113-147 give the scanning electron micrographs which show the topographical details of the thermogravimetrically oxidised samples in moist and dry mixtures of 0.21 oxygen/0.79 helium, i.e. with and without 3040 Pa water vapour pressure.

Figures 113-134 give the SEM micrographs of the surfaces of oxide films formed on Al-Mg binary alloys.

Figures 113 a,b : Surfaces of the oxide films after 30 min and 2h oxidation at 525°C on solid Al-1.3% Mg alloy in the dry atmosphere. (x 300)

Figures 113 c,d : Surfaces of the oxide films after 30 min and 2h oxidation at 525°C on solid Al-1.3% Mg alloy in the

moist atmosphere. (x 300)

Figures 114 a,b : Surfaces of the oxide films after 30 min and 2h oxidation at 525^{o}C on solid Al-3.1% Mg alloy in the dry atmosphere. (x 400)

Figures 114 c,d : Surfaces of the oxide films after 30 min and 2h oxidation at 525^{o}C on solid Al-3.1% Mg alloy in the moist atmosphere. (x 400)

Figures 115 a,b : Surfaces of the oxide films after 30 min and 2h oxidation at 525^{o}C on solid Al-5.1% Mg alloy in the dry atmosphere. (x 400 and x 300)

Figure 115 c : Surface of the oxide film after 2h oxidation at 525^{o}C on solid Al-5.1% Mg alloy in the moist atmosphere. (x 400)

Figures 116 a,b : Surfaces of the oxide films after 30 min and 2h oxidation at 525^{o}C on solid Al-7.4% Mg alloy in the dry atmosphere. (x 400)

Figure 116 c : Surface of the oxide film after 2h oxidation at 525^{o}C on solid Al-7.4% Mg alloy in the moist atmosphere. (x 400)

Figure 117 a : Surface of the oxide film after 2h oxidation at 525^{o}C on solid Al-9.3% Mg alloy in the dry atmosphere. (x 400)

Figures 117 b,c : Surfaces of the oxide films after 60 min and 2h oxidation at 525^{o}C on solid Al-9.3% Mg alloy in the moist atmosphere. (x 400)

The characteristic feature of the SEM micrographs for solid alloys above are that (i) initial nucleation of white magnesium oxide particles in the moist atmosphere is more prolific than that in the dry atmosphere, and (ii) further

nucleation of white magnesium oxide particles during the progressive oxidation is suppressed in the moist atmosphere.

Figure 118 a : Surface of the oxide film after 2h oxidation at 725°C on liquid Al-1.3% Mg alloy in the dry atmosphere. (x 400)

Figures 118 b,c : Surfaces of the oxide films after 2h oxidation at 675°C and 725°C on liquid Al-1.3% Mg alloy in the moist atmosphere. (x 400)

Figure 119 a : Surface of the oxide film after 2h oxidation at 725°C on liquid Al-3.1% Mg alloy in the dry atmosphere. (x 400)

Figures 119 b,c : Surfaces of the oxide films after 2h oxidation at 675°C and 725°C on liquid Al-3.1% Mg alloy in the moist atmosphere. (x 400)

Figure 120 a : Surface of the oxide film after 2h oxidation at 700°C on liquid Al-5.1% Mg alloy in the dry atmosphere. (x 200)

Figures 120 b,c : Surfaces of the oxide films after 1h and 2h oxidation at 700°C on liquid Al-5.1% Mg alloy in the moist atmosphere. (x 400 and x 600)

Figure 121 a : Surface of the oxide film after 2h oxidation at 625°C, i.e. close to the liquidus temperature, on liquid Al-7.4% Mg alloy in the dry atmosphere. (x 400)

Figures 121 b,c : Surfaces of the oxide films after 1h and 2h oxidation at 625°C, i.e. close to the liquidus temperature, on liquid Al-7.4% Mg alloy in the moist atmosphere. (x 400)

Figure 122 a : Surface of the oxide film after 2h oxidation at 700°C on liquid Al-7.4% Mg alloy in the dry atmosphere. (x 400)

Figures 122 b,c : Surfaces of the oxide films after 30 min and 2h oxidation at 700°C on liquid Al-7.4% Mg alloy in the moist atmosphere. (x 200 and x 500)

Figure 123 a : Surface of the oxide film after 2h oxidation at 625°C, i.e. close to the liquidus temperature, on liquid Al-9.3% Mg alloy in the dry atmosphere. (x 400)

Figures 123 b,c : Surfaces of the oxide films after 1h and 2h oxidation at 625°C, i.e. close to the liquidus temperature, on liquid Al-9.3% Mg alloy in the moist atmosphere. (x 400)

Figure 124 a : Surface of the oxide film after 2h oxidation at 700°C on liquid Al-9.3% Mg alloy in the dry atmosphere. (x 400)

Figures 124 b,c : Surfaces of the oxide films after 1h and 2h oxidation at 700°C on liquid Al-9.3% Mg alloy in the moist atmosphere. (x 200 and x 400)

Figures 118-124 above show that the oxidised alloy surfaces are wrinkled and corrugated for liquid alloys containing low, i.e. 1,3 and 5%, and high, i.e. 7 and 9%, magnesium contents respectively during oxidation close to their respective liquidus temperatures. This increases the effective surface area for oxidation. The effect diminishes as the temperature for isothermal oxidation is raised to give much smoother surfaces, unless or until accelerated oxidation is initiated.

Figure 125 a : Surface of the oxide film after 2h oxidation at 646°C in the dry atmosphere on Al-1.3% Mg alloy with < 50% liquid in the semi-liquid state. (x 250)

Figures 125 b,c : Surfaces of the oxide films after 30 min and 2h oxidation at 646°C in the moist atmosphere on Al-1.3% Mg alloy with < 50% liquid in the semi-liquid state. (x 250)

Figure 126 a : Surface of the oxide film after 2h oxidation at 654°C in the dry atmosphere on Al-1.3% Mg alloy with > 50% liquid in the semi-liquid state. (x 250)

Figures 126 b,c : Surfaces of the oxide films after 1h and 2h oxidation at 654°C in the moist atmosphere on Al-1.3% Mg alloy with > 50% liquid in the semi-liquid state. (x 250)

Figure 127 a : Surface of the oxide film after 2h oxidation at 625°C in the dry atmosphere on Al-3.1% Mg alloy with < 50% liquid in the semi-liquid state. (x 250)

Figures 127 b,c : Surfaces of the oxide films after 1h and 2h oxidation at 625°C in the moist atmosphere on Al-3.1% Mg alloy with < 50% liquid in the semi-liquid state. (x 250)

Figure 128 a : Surface of the oxide film after 2h oxidation at 640°C in the dry atmosphere on Al-3.1% Mg alloy with > 50% liquid in the semi-liquid state. (x 250)

Figures 128 b,c : Surfaces of the oxide films after 1h and 2h oxidation at 640°C in the moist atmosphere on Al-3.1% Mg alloy with > 50% liquid in the semi-liquid state. (x 250)

Figures 129 a,b : Surfaces of the oxide films after 2h oxidation at 600°C in dry and moist atmospheres on Al-5.1% Mg alloy with < 50% liquid in the semi-liquid state. (x 250 and x 500)

Figure 129 c : Surface of the oxide film after 2h oxidation at 610°C in the moist atmosphere on Al-5.1% Mg alloy with ∿ 50% liquid in the semi-liquid state. (x 250)

Figure 130 a : Surface of the oxide film after 2h oxidation at 625°C in the dry atmosphere on Al-5.1% Mg alloy with > 50% liquid in the semi-liquid state. (x 250)

Figures 130 b,c : Surfaces of the oxide films after 1h and 2h oxidation at 625°C in the moist atmosphere on Al-5.1% Mg alloy with > 50% liquid in the semi-liquid state. (x 250)

Figures 131 a,b : Surfaces of the oxide films after 2h oxidation at 575°C in dry and in moist atmospheres on Al-7.4% Mg alloy with < 50% liquid in the semi-liquid state. (x 250)

Figure 132 a : Surface of the oxide film after 2h oxidation at 610°C in the dry atmosphere on Al-7.4% Mg alloy with > 50% liquid in the semi-liquid state. (x 250)

Figures 132 b,c ; Surfaces of the oxide films after 1h and 2h oxidation at 610°C in the moist atmosphere on Al-7.4% Mg alloy with > 50% liquid in the semi-liquid state. (x 250)

Figures 133 a,b : Surfaces of the oxide films after 2h oxidation at 550°C in dry and in moist atmospheres on Al-9.3% Mg alloy with < 50% liquid in the semi-liquid state. (x 250)

Figure 134 a : Surface of the oxide film after 2h oxidation at 600°C in the dry atmosphere on Al-9.3% Mg alloy with > 50% liquid in the semi-liquid state. (x 250)

Figures 134 b,c : Surfaces of the oxide films after 1h and 2h oxidation at 600°C in the moist atmosphere on Al-9. % Mg alloy with > 50% liquid in the semi-liquid state. (x 250)

Figures 125-134 above show that (i) the grain boundary oxidation is more

pronounced for alloys with < 50% liquid, oxidised above the solidus temperature and (ii) overall surface oxidation is higher for alloys with > 50% liquid, oxidised below the liquidus temperature.

Figures 135-147 give the SEM micrographs of the surfaces of oxide films formed on Al-Mg-Be alloys.

Figures 135 a,b : Surfaces of the oxide films formed after 3h oxidation at 525^{o}C on solid Al-8.2% Mg-0.003% Be alloy in dry and moist atmospheres. (x 5000)

Figures 136 a,b : Surfaces of the oxide films formed after 3h oxidation at 525^{o}C on solid Al-8.16% Mg-0.003% Be-0.24% Mn alloy in dry and moist atmospheres. (x 5000)

Figures 137 a,b : Surfaces of the oxide films formed after 3h oxidation at 525^{o}C on solid Al-8.13% Mg-0.003% Be-0.12% Zr alloy in dry and moist atmospheres. (x 5000)

The characteristic feature of the solid Al-Mg-Be alloys is that the oxide is protective throughout the 3h oxidation period because white tertiary magnesium particles did not appear during either the initial or subsequent oxidation in both atmospheres, as observed for solid Al-Mg binary alloys.

Figures 138 a,b : Surfaces of the oxide films formed after 3h oxidation at 675^{o}C, i.e. close to the liquidus temperature , on liquid Al-8.2% Mg-0.003% Be alloy in dry and moist atmospheres. (x 5000)

Figure 139 a : Surface of the oxide film after 3h oxidation at 700^{o}C on liquid Al-8.16% Mg-0.003% Be-0.24% Mn alloy in the dry atmosphere. (x 5000)

Figure 139 b,c : Surfaces of oxide films after 1.5h and 3h oxidation at 700°C on liquid Al-8.16% Mg-0.003% Be-0.24% Mn alloy in the moist atmosphere. (x 5000)

Figure 140 a : Surface of the oxide film after 3h oxidation at 700°C on liquid Al-8.13% Mg-0.003% Be-0.12% Zr alloy in the dry atmosphere. (x 5000)

Figures 140 b,c : Surfaces of the oxide films after 1h and 3h oxidation at 700°C on liquid Al-8.13% Mg-0.003% Be-0.12% Zr alloy in the moist atmospheres. (x 5000)

Figures 138-140 show that oxidised surfaces for Al-Mg-Be alloys are wrinkled during oxidation, close to the liquidus temperature. The effect diminishes as the temperature for isothermal oxidation is raised to give much smoother surfaces, unless or until accelerated oxidation is initiated.

Figures 141 a,b : Surfaces of oxide films after 3h oxidation at 575°C in dry and moist atmospheres on Al-8.2% Mg-0.003% Be alloy with < 50% liquid in the semi-liquid state. (x 5000)

Figures 142 a,b : Surfaces of oxide films after 3h oxidation at 610°C in dry and moist atmospheres on Al-8.2% Mg-0.003% Be alloy with > 50% liquid in the semi-liquid state. (x 5000)

Figures 143 a,b : Surfaces of oxide films after 3h oxidation at 575°C in dry and moist atmospheres on Al-8.16% Mg-0.003% Be-0.24% Mn alloy with < 50% liquid in the semi-liquid state. (x 5000)

Figures 144 a,b : Surfaces of oxide films after 3h oxidation at 610°C in dry and moist atmospheres on Al-8.16% Mg-0.003% Be-0.24% Mn alloy with > 50% liquid in the semi-liquid state. (x 5000)

Figures 145 a,b : Surfaces of oxide films after 3h oxidation at 575°C in dry and moist atmospheres on Al-8.13% Mg-0.003% Be-0.12% Zr alloy with < 50% liquid in the semi-liquid state. (x 5000)

Figure 146 a : Surface of the oxide film after 3h oxidation at 585°C in the dry atmosphere on Al-8.13% Mg-0.003% Be-0.12% Zr alloy with ∿ 50% liquid in the semi-liquid state. (x 5000)

Figures 146 b,c : Surfaces of oxide films after 1h and 3h oxidation at 585°C in the moist atmosphere on Al-8.13% Mg-0.003% Be-0.12% Zr alloy with ∿ 50% liquid in the semi-liquid state. (x 5000)

Figures 147 a,b : Surfaces of oxide films after 3h oxidation at 610°C in dry and moist atmospheres on Al-8.13% Mg-0.003% Be-0.12% Zr alloy with > 50% liquid in the semi-liquid state. (x 5000)

As for semi-liquid Al-Mg binary alloys, Figures 141-147 above also show that (i) the grain boundary oxidation is more prolific for alloys with < 50% liquid, oxidised above the solidus temperature, and (ii) the overall surface oxidation is higher for alloys with > 50% liquid, oxidised below the liquidus temperature. The characteristic feature of these alloys is that in both atmospheres the nucleation and growth of tertiary magnesium oxide is observed only during the eventual oxidation and thus the oxide formed is protective during the initial state of oxidation.

7.6. Observations by Light-Microscopy

Figures 148-150 show the pores and blisters developed under the oxide or within the alloy during breakaway oxidation for Al-Mg binary and Al-Mg-Be alloys.

Figure 148 a : Pores and blisters developed in Al-5.1% Mg alloy at 725°C during breakaway oxidation, i.e. after 90 min, in the dry atmosphere. (x 6)

Figure 148 b : Pores and blisters developed in Al-5.1% Mg alloy at 725°C during breakaway oxidation, i.e. after 60 min, in the moist atmosphere. (x 6)

Figure 149 a : Pores and blisters developed in Al-7.4% Mg alloy at 700°C during breakaway oxidation, i.e. after 2h, in the dry atmosphere. (x 6)

Figure 149 b : Pores and blisters developed in Al-7.4% Mg alloy at 700°C during breakaway oxidation, i.e. after 60 min, in the moist atmosphere. (x 6)

Figures 150 a,b : Pores and blisters developed in Al-8.13% Mg-0.003% Mg-0.12% Zr alloy at 725°C during breakaway oxidation, i.e. after 2h, in dry and in moist atmospheres. (x 6)

The pores and blisters developed faster and became larger during breakaway oxidation in the moist atmosphere than those observed in the dry atmosphere.

8. DISCUSSION

The present investigation has yielded valuable information on several aspects of the structure, chemical composition and growth kinetics of oxide films formed on solid, liquid, and semi-liquid aluminium-magnesium alloys. When combined with other information drawn from the literature, the results obtained lead to a significant advance in establishing the principles which underlie the oxidation phenomena observed for these alloys.

Before embarking on an interpretation of the results, it is first essential to assess their validity.

8.1. Critical Assessment of Experimental Techniques and Results

8.1.1. Validity of Thermogravimetric Procedures

The validity of the present results depends on the intrinsic characteristics of the microbalance employed and the degree of success in resolving the adverse effects of extraneous factors on operation of the microbalance.

(a) Balance Type

To produce results of adequate accuracy a suitable thermobalance has certain obvious attributes. For the present investigation it was anticipated from earlier work[175,188,189] that it must have a sensitivity of $\leqslant$10 μg, a loading capacity of $\geqslant$10 g, and facilities for close control of temperature and oxidising atmosphere.

The balance selected was a Sartorius microbalance, model 4410, with a sensitivity of 1 μg, a loading capacity of 25 g, and a weighing system in a sealed unit with provision for incorporating ancillary apparatus to control temperature and oxidising atmosphere as described in Section 6.3.

The accurate functioning of the balance was validated by calibration and

checks recommended by the manufacturers, undertaken immediately before the initiation of every set of experiments.

(b) Balance Sensitivity and Noise Level

The sensitivity of the balance and hence the accuracy of the readings are adversely affected by adventitious noise and its full potential can be realised only if these factors are recognised and suitable precautions taken:

(i) Vibration from Laboratory Activities

This was avoided by mounting the balance rigidly on a massive structural concrete pillar set 1.5 metres into the ground where it was stable to ±2 μg indefinitely.

(ii) Buoyancy Effect of Gases in the Oxidising Atmosphere

In a preliminary investigation, high density gases such as nitrogen or argon in the oxidising atmosphere were found to increase the noise to an unacceptable level, i.e. ±150 μg at the highest sample temperature, due to the interaction of convection currents with the balance mechanism, suspension, and crucible. This effect was minimised by replacing the nitrogen in air with helium and by locating baffles in the top of the reaction chamber to attenuate the convection noise reaching the balance mechanism.

(iii) The Effect of the Magnetic Field due to the Current in the Furnace Windings

The furnace tube was wound with "Nichrome" wire. Electromagnetic field generated within the furnace can have an adverse effect on the sensitivity of the balance by interfering with the balance poise. This was negated by winding the furnace non-inductively.

(iv) The Effect of Static Electricity Accumulated on the Silica Walls of the Reaction Chamber

Static electricity generated on the specimen chamber can exert an interfering electric force on the crucible, reducing the sensitivity of the balance. This was eliminated by winding the reaction tube with an earthed metal wire, as shown in Figure 41.

(c) The Integrity of the Vacuum System and the Purity of Gases

In designing the vacuum system and the associated systems for supplying and purifying the gases as described in Section 6.3.3, the overriding objective was to eliminate all traces of impurities in the oxidising atmosphere because of the high sensitivity of oxidation kinetics to impurities, as discussed in Sections 2.3.5. and 4.3.

The efficiency of the construction used and the measures adopted were confirmed by monitoring the weight gain of the samples both during heating to and stabilisation at test temperature in helium before commencing every test. In no case was any detectable oxidation observed.

(d) Reproducibility of Sample Preparation

The quality of surface preparation influences the oxidation of pure magnesium[125].

A preliminary investigation to evaluate the effect for aluminium-magnesium alloys showed that the oxidation rate was slightly increased by increasing surface roughness produced by different grades of silicon carbide papers. Therefore, great care was taken to maintain a reproducible high standard of surface preparation to minimise the effect on oxidation.

(e) Effect of Magnesium Evaporation

It was found that if samples were heated in vacuum to temperatures above the solidus, magnesium evaporated at a rate which increased with increasing

temperature and magnesium content as had been previously observed[182,192]. By the use of helium as an atmosphere during heating the samples and during stabilisation of the test temperature, the evaporation was eliminated for alloys with magnesium contents < 7% and reduced to low levels for alloys with magnesium contents in the range 7-9%. It was further minimised by ensuring that the samples were heated to and stabilised at the test temperatures in the shortest possible time by the use of a preliminary furnace superheat of 25°C. The combined effect of these measures was to reduce experimental error arising from magnesium evaporation to the insignificant levels given in Table 10. The mass losses given in the table are insignificant, i.e. of no greater magnitude than the signal variation due to noise.

(f) Effect of Crucible Condition

Preliminary investigation revealed that the samples reacted with untreated alumina crucibles. Virtually no crucible reaction was noted when they were preconditioned to remove adsorbed volatile substances, e.g. water vapour, prior to testing. This was accomplished by holding the crucible at 800°C in a furnace for 6 hours.

(g) Crucible Suspension Filament and Cradle

To avoid error in the oxidation results, the suspension filament and cradle were constructed of inert materials, i.e. silica and platinum respectively.

8.1.2. Estimate of Errors in the Thermogravimetric Results

(a) Mass Gain

The control of factors influencing the noise level reduced the short-term signal variation of the balance to $\leqslant \pm 0.04$ mg and to $\leqslant \pm 0.10$ mg for minimum and maximum mass gains respectively. These values are acceptable because the minimum and maximum mass gains recorded were 0.95 mg and 90 mg respectively so that the errors due to noise are within the range 0.1 - 4.2%.

(b) Sample Surface Area

Some criticism is expected on the method of assessing the effective sample surface area for the samples containing > 50% liquid at the test temperature which could not maintain a rigid geometric shape in which all of the surface area was fully exposed to the atmosphere. The empirical assessment selected, as described in Section 7.2.(a), assumed that for samples which had to be treated as liquids, the top surface and cylindrical surface of a disc were openly exposed but the bottom surface masked by the crucible was only 0.25 relatively effective. On this basis the effective surface area for a standard sample, 16 mm dia x 6 mm thick is $\pi(0.8)^2 + 2\pi(0.8)\ (0.6) + 0.25\ \pi(0.8)^2 = 5.5\ cm^3$. If all faces were fully exposed the area would be $7.0\ cm^3$ and if only the top face and cylindrical surface were exposed the area would be $5.0\ cm^3$. The maximum possible error in the procedure adopted is therefore, (5.5-7.0) 100/7 and (5.5-5.0) 100/5, i.e. -21 and +10%.

The degree of uncertainty is less than these possible errors would suggest as indicated by the experimental evidence on which the calculation is based and by the logical progression of the thermogravimetric results through the temperature above which the effective area correction was applied. However, even if the errors are greater, they are not sufficient to invalidate the observed general patterns of oxidation.

(c) Sample Temperature

Regular calibration of the thermocouple showed that it truly represented the actual temperature measured. Due to thermal convection noise in the specimen chamber, the measurements with a digital thermometer showed that the temperature variation at the thermocouple tip was within $\pm 1^{o}C$. This value is acceptable and the maximum error involved is 0.2% at the lowest test temperature of $500^{o}C$. Since the physical contact between the thermocouple and the sample was impossible, confidence that the measured temper-

ature truly represented the temperature of the sample depended on the care taken to ensure that the gap between crucible and thermocouple was very small and accurately maintained.

8.1.3. Critical Assessment of Thermal Analysis Results

The Smith method of thermal analysis is regarded as the most reliable and accurate to measure phase transformations because the furnace follows the specimen temperature thereby avoiding the influence of furnace temperature on the specimen temperature during phase transformations.

Further important features of any accurate thermal analysis are prior homogenisation of specimens, just before reaching any expected phase transformation temperature on either heating or cooling and slow traverse of the temperature range of any expected two phase region, i.e. $1^{o}C$/min, to minimise any superheating or supercooling which displaces phase transformation temperatures.

In addition, the validity of the results depends predominantly on the correct measurement of the transformation temperatures and was achieved by:

(a) the use of fine thermocouple wire, i.e. 0.25 mm diameter, to obtain rapid response to the temperature of the sample[217,218].

(b) regular calibration of the temperature measuring thermocouple[217] against the melting points of pure metals, e.g. silver, zinc and tin. The temperature measurements are considered to be accurate to within $\pm 1^{o}C$, and in fact the short term reproducibility was typically an order of magnitude better.

(c) the use of a thermocouple cold junction thermostat held at $30 \pm 0.05^{o}C$ by a fully proportional temperature controller.

(d) precise location of the thermocouple bead in the centre of every alloy sample to reduce errors associated with end effects.

Since every care was taken to observe all of the precautions described above the dominant source of error is in the residual hysteresis between values obtained on heating and cooling, so that the accuracy is better than half the difference for heating and cooling given in Table 7, i.e. $< \pm 1.5^{o}C$.

8.1.4. Critical Assessment of X-ray Diffractometer

The bulk oxidised samples were examined by diffractometry with no sample preparation, since it was difficult to obtain sufficient oxide powder for the Debye-Scherrer technique. For a pure material the diffractometer technique is insensitive to quantities of a second phase < 1%. For samples in which the oxide is attached to the metal, the sensitivity is reduced because the incident X-rays penetrate into the metallic substrate. Consequently, the additional diffraction reduces the contribution of any second phase in the oxide to the total spectrum, so that the limit of detection is raised to >1%. The combined effect of preferred orientation of the oxide in situ on the substrate, irregular oxide surfaces and penetration of X-rays into the low density metal substrate can either attenuate or amplify X-ray intensities of particular peaks in the spectra[219]. Overlapping of close energy peaks related to different phases can also contribute to a change in the true X-ray intensities.

The position of the X-ray peaks obtained from magnesium in oxide films agreed well with the standards for magnesium oxide given in the ASTM data files but the intensities of the X-ray peaks did not correspond with the standard intensities given because of the influence of the factors described above. Hence the results are regarded as a strong circumstantial evidence but not absolute proof of the exclusive presence of magnesium oxide in the oxide films.

To resolve the uncertainty, the exclusive magnesium oxide structure was

confirmed by point-by-point elemental analysis and electron diffraction of selected areas using a JEOL 100 CX TEM fitted with STEM and EDX facilities.

8.1.5. Critical Assessment of Electron Optical Observations

(a) SEM

Using this technique, the topographical features of the oxides were observed three-dimensionally with minimal sample preparation. In any particular observation the quality of surface micrographs depended on the sample preparation and the selection of a suitable accelerating voltage.

(i) Sample Preparation

In examining an electrical insulater under an electron beam, the electrons cannot leak to earth and thus the sample acquires a charge which causes the picture to deteriorate. For the oxide samples, the effect was controlled by adjusting the accelerating voltage and by providing a good conduction path to earth by making electrical contact between the sample and the stub using silver dag.

(ii) Selection of Accelerating Voltage

For the present samples, the low density alloy substrate gave rise to high beam penetration and poor electron emission which combined to give a light and hazy image with loss of topographical details. To overcome this problem, the accelerating voltage was lowered to 10 kV and the consequent reduction in resolution was accepted because it still permitted observation at magnifications of 50-500 times, used in the present work.

(b) TEM

In view of the limitations on SEM and X-ray diffraction, imposed by sample surface unevenness, X-ray absorption by the metal substrate,and the oxide orientation, the most rewarding work was carried out with the TEM. The

sample preparation method is tedious and time-consuming but the TEM has advantages, particularly over the X-ray diffractometer for the present work and hence the results obtained are comparatively reliable and accurate. The samples examined were almost pure oxide, and not oxide/metal composites as is inevitable for X-ray diffraction, so that the results obtained are relevant to the oxide itself and not distorted by contaminating signals from the substrate metal. The use of powder also removed the effect of preferred orientation. Using its high resolution and its ancillaries, i.e. STEM and EDX, the amorphous or crystalline nature of the oxide samples can be distinguished and directly correlated with corresponding electron diffraction patterns and with the elements expected as possible oxide components, thus providing a basis for chemical identification. Since the use of pure oxide samples, the full sensitivity of this technique can be exploited, i.e. the limit of detection of a second phase is 1%.

The accuracy of the chemical analysis using diffraction patterns depends on the accuracy with which the camera constant and the ring diameter are known. The measurements of diffraction rings were made using a x5 magnifying eye-piece, a pair of dividers, a metal ruler graduated in mm, and a light box. However, because the rings were thick and the centre of a spot was difficult to assess, accuracies of only ± 1 mm could be achieved which could induce errors of $\leqslant 5\%$ in ring radii.

For precise work, the camera constant was calculated for every ring of the known diffraction pattern and the average value was accepted to aid interpretation of other patterns. The error in the average value was only 0.5 - 1.5% but the error in the calculated values for interplanar spacings was 5.52 - 6.58%, because the error incurred in the ring radii measurements was $\leqslant 5\%$.

8.2. Thermodynamic Assessment of Oxidation Reactions for Aluminium-Magnesium Alloys

8.2.1. Prediction of Stability of Oxides

The relative stabilities of the anticipated oxides, i.e. MgO, $MgAl_2O_4$ and Al_2O_3, formed on binary aluminium-magnesium alloys can be assessed by plotting the notional oxygen dissociation pressure, P_{O_2}, as functions of magnesium content. For any particular composition at a given temperature, the oxide with the lowest dissociation pressure is the most stable.

For a reaction:

$$a\,A + b\,B \rightleftharpoons c\,C + d\,D \qquad \ldots\ldots\ldots\ldots\ldots\ldots (8.1)$$

equilibrium is given by

$$K = a_C^c\, a_D^d \,/\, a_A^a\, a_B^b \qquad \ldots\ldots\ldots\ldots\ldots\ldots (8.2)$$

where a_C, a_D, a_A and a_B are equilibrium activities.

For a permanent gas at elevated temperature such as oxygen which has nearly ideal behaviour, the activity is almost identical with the pressure. Thus for an oxidation reaction, the dissociation pressure can be calculated if the standard Gibbs free energy change, ΔG^θ, for the reaction and the activities of the other components are known by application of the Van't Hoff Isotherm:

$$\Delta G^\theta = - RT \ln K \qquad \ldots\ldots\ldots\ldots\ldots\ldots (8.3)$$

Critically assessed values for the Gibbs free energy of formation of MgO and of Al_2O_3 from their elemental components as functions of temperature are given by Kubaschewski and Alcock[220] as follows:

(a) $2Mg(s) + O_2(g) \rightleftharpoons 2\,MgO(s)$ $\qquad \ldots\ldots\ldots\ldots\ldots\ldots (8.4)$

$$\Delta G_a^\theta = - 1{,}206{,}766 - 24.66\ T \log T + 283.8\ T \text{ J mol}^{-1}$$

(b) $2\ Mg(l) + O_2(g) \rightleftharpoons 2\ MgO(s)$ ..... (8.5)

$\Delta G_b^{\ominus} = -1{,}215{,}126 - 2\ T \log T + 225.3\ T\ J\ mol^{-1}$

(c) $4/3\ Al(s) + O_2(g) \rightleftharpoons 2/3\ Al_2O_3(s)$ ..... (8.6)

$\Delta G_c^{\ominus} = -1{,}116{,}924 - 11.1\ T \log T + 224.2\ T\ J\ mol^{-1}$

(d) $4/3\ Al(l) + O_2(g) \rightleftharpoons 2/3\ Al_2O_3(s)$ ..... (8.7)

$\Delta G_d^{\ominus} = -1{,}130{,}718 - 10.5\ T \log T + 257\ T\ J\ mol^{-1}$

Corresponding values for the Gibbs free energy of formation of $MgAl_2O_4$ from its elemental components are not available explicitly but with some reasonable assumptions, can be derived as follows:

Gatellier and Olette[221] give the standard enthalpy change for the reaction:

(e) $MgO(s) + Al_2O_3(s) \rightleftharpoons MgAl_2O_4(s)$ ..... (8.8)

as $\Delta H_{298}^{\ominus} = -35{,}530\ J\ mol^{-1}$

The standard entropy change for the reaction can be obtained by summing the standard entropies for the reactants and products, i.e.

$$\Delta S_{298}^{\ominus} = \Delta S_{298}^{\ominus}(MgAl_2O_4) - \Delta S_{298}^{\ominus}(MgO) - \Delta S_{298}^{\ominus}(Al_2O_3)$$

Inserting values given by Kubaschewski and Alcock[220]:

$$\Delta S_{298}^{\ominus} = 80.46 - 26.75 - 50.2 = 3.5\ J\ K^{-1}mol^{-1}$$

The temperature dependence of these values is not given, but in default it is a reasonable assumption that $\Delta H_{298}^{\ominus}$ and $\Delta S_{298}^{\ominus}$ do not vary appreciably with temperature so that the temperature dependence of the Gibbs free energy change, $\Delta G^{\ominus}$, for this reaction can be obtained from the definitional relation,

$$\Delta G^{\ominus} = \Delta H_{298}^{\ominus} - T\ \Delta S_{298}^{\ominus}$$

i.e. $\Delta G_e^{\theta} = -35{,}530 - 3.5\ T\ J\ mol^{-1}$

Using this value, it is now possible to evaluate the Gibbs free energy change, ΔG_f^{θ}, for the formation of $MgAl_2O_4$ on solid aluminium-magnesium alloys.

The reaction:

(f) $1/2Mg(s) + Al(s) + O_2(g) \rightleftharpoons 1/2\ MgAl_2O_4(s)$ ..... (8.9)

is obtained by summing reactions (a), (c) and (e), i.e.

$$(f) = 1/4(a) + 3/4(c) + 1/2(e)$$

Hence $\Delta G_f^{\theta} - 1/4\ \Delta G_a^{\theta} + 3/4\ G_c^{\theta} + 1/2\ G_e^{\theta}$

$$= -1{,}157{,}150 - 14.5\ T \log T + 235.7\ T\ J\ Mol^{-1}$$

Similarly, for the formation of $MgAl_2O_4$ on liquid alloys:

(g) $1/2Mg(l) + Al(l) + O_2(g) \rightleftharpoons 1/2\ MgAl_2O_4(s)$ ..... (8.10)

$$\Delta G_g^{\theta} = -1{,}169{,}585 - 8.4\ T \log T + 245.6\ T\ J\ mol^{-1}$$

Values for the activities of aluminium and of magnesium in solid aluminium-magnesium binary alloys given by Brown and Pratt[222] are reproduced in Tables 11-13. Values for the activities of aluminium and of magnesium in liquid aluminium-magnesium binary alloys are given by Bhatt and Garg[223] and are given in Tables 14-16.

The method of calculation is illustrated for the formation of magnesium oxide on solid aluminium-magnesium alloys at 500^oC (773^oK) as follows:

The reaction is:

(a) $2Mg(s) + O_2(g) \rightleftharpoons 2MgO(s)$ ..... (8.4)

$$\Delta G_a^{\theta} = -1{,}206{,}766 - 24.66\ T \log T + 283.8\ T\ J\ mol^{-1}$$

whence $\Delta G^{\ominus}_{773} = -1{,}042{,}500 \text{ J mol}^{-1}$

$$K_{MgO} = a^2_{MgO}/a^2_{Mg} \cdot a_{O_2}$$

Assuming the MgO is pure and oxygen behaves ideally,

$$K(MgO) = 1/a^2_{Mg} \cdot P_{O_2} \qquad \ldots\ldots\ldots\ldots \quad (8.11)$$

Applying the Van't Hoff Isotherm,

$$\Delta G^{\ominus} = -RT \ln K$$

Hence at $500^{o}C$ ($773^{o}K$)

$$-1{,}042{,}500 = -19.14 \times 773 \log K$$

$$\therefore K = 2.89 \times 10^{70}$$

Substituting for this value in equation (8.11) yields:

$$P_{O_2} = 0.3452 \times 10^{-70}/a^2_{Mg} \text{ atm.}$$

Inserting the appropriate values of a_{Mg} given by Brown and Pratt[222], this equation yields the values of oxygen dissociation pressure as a function of a_{Mg} given in Table 11.

Similar calculations for equations (8.6), (8.9), (8.5), (8.7) and (8.10) yield corresponding values for the oxygen dissociation pressures for Al_2O_3 and $MgAl_2O_4$ formed on solid alloys, and MgO, Al_2O_3 and $MgAl_2O_4$ formed on liquid alloys in Tables 12-16 respectively.

Tables 11-16 have been used to plot Figures 151 and 152 which give the oxygen pressure in equilibrium with MgO, Al_2O_3 and $MgAl_2O_4$ as functions of magnesium mole fraction for solid and liquid binary aluminium-magnesium alloys.

The significance of Figures 151 and 152 is to show that the oxides MgO, Al_2O_3 and $MgAl_2O_4$ are the most stable oxides for the composition ranges given in

Table 17.

The upper limits of magnesium content for the formation of stable Al_2O_3 cannot be directly read accurately from the curves in Figures 151 and 152 but can be obtained indirectly by calculation as follows. From Figure 151 the oxygen pressure corresponding to the stability of Al_2O_3 at 500°C on solid pure or nearly pure alumina is 3520×10^{-69} atm. Inserting the value in equation (8.11) yields $a_{Mg} = 3.13 \times 10^{-3}$ atm. Interpolating the value of a_{Mg} in Table 11 yields a magnesium concentration of 0.0016. A similar calculation for the liquid alloys at 725°C using Figure 152 yields a magnesium concentration of 0.0001.

8.2.2. The Validity of the Thermodynamic Values Used to Predict the Stability of Oxides

The validity of the assessment made in Figures 151 and 152 depends on the validity of the values used for the activities of magnesium and aluminium in solid and liquid aluminium-magnesium alloys. The activities of magnesium and aluminium in solid and liquid alloys have been reported by many investigators using various experimental techniques but large discrepancies exist between the various values given. Critical assessments of existing thermodynamic values for the aluminium-magnesium systems have been made by Kubaschewski and Catterall[224], Kubaschewski[225], and Anderson[226] who emphasised the inconsistencies in the various results and the need for further work. In response to these criticisms, further investigations were made by Brown and Pratt[222], and Bhatt and Garg[223] for solid and liquid aluminium-magnesium alloys respectively. Although these results are also at variance with previous results, they can be accepted with greater confidence because the calculated activities for liquid alloys using the measured activities for solid alloys of Brown and Pratt[222] were in fair agreement with measured activities for liquid alloys of Bhatt and Garg[223].

The expression for the Gibbs free energy of formation of $MgAl_2O_4$ from its

elemental components is not entirely satisfactory since it is computed by summing the entropies of oxide components so that errors in the values are cumulative. Furthermore, the assumption of temperature independence for the entropy and enthalpy changes is not rigorously justified. However, since the entropy change is small compared with the entropy change for formation of magnesium oxide and alumina, the errors incurred should not materially influence the assessment of the relative stability of the three oxides, MgO, Al_2O_3 and $MgAl_2O_4$.

8.3. Thermodynamic Analysis of Hydrogen Absorption by Aluminium Magnesium Alloys

8.3.1. Incorporation of Hydroxyl Ions into Magnesium Oxide Lattice

If moisture is present in the atmosphere, the possibility must be considered that OH^- ions may be incorporated into the growing oxide, both influencing the oxidation kinetics and contributing to the absorption of hydrogen by the underlying metal.

Although magnesium oxide which has a simple cubic lattice is structurally incompatible with magnesium hydroxide, $Mg(OH)_2$, which has a CdI_2 type hexagonal lattice, it is possible to make a rough estimate of the extent to which OH^- ion substitution in the magnesium oxide lattice may occur by considering the relative stabilities of magnesium oxide and magnesium hydroxide.

For the reaction:

$$MgO(s) + H_2O(g) \rightleftharpoons Mg(OH)_2(s) \qquad \text{.....(8.12)}$$

the standard Gibbs free energy change is given by[220]

$$\Delta G^{\ominus} = -45{,}980 + 100.3\,T \quad J\,mol^{-1}$$

Application of the Van't Hoff Isotherm, (8.3) at 500^oC (773^oK) for reaction (8.12) yields a value for the equilibrium constant, K of 0.0073. Since

from equation (8.12),

$$K = a_{Mg(OH)_2}/a_{MgO} \cdot a_{H_2O} \quad \ldots\ldots\ldots\ldots (8.13)$$

for magnesium oxide formed on solid alloys equilibrated at 500°C in air containing 0.03 atm water vapour pressure,

$$a_{Mg(OH)_2} = 2.2\times10^{-4} \quad \ldots\ldots\ldots\ldots (8.14)$$

by a similar argument for magnesium oxide formed on liquid alloys equilibrated at 725°C (998°K) in air containing 0.03 atm water vapour pressure,

$$a_{Mg(OH)_2} = 0.03 \times 0.0015 = 4.5\times10^{-5} \quad \ldots\ldots\ldots\ldots (8.15)$$

Hence if it is structurally possible to substitute OH^- ions in the magnesium oxide lattice, a small but significant proportion may be expected. The validity of this approach is supported by the Johnson et al's[58] experimental observation that the dielectric constant for magnesium oxide is influenced by absorbed OH^- ions as described in Section 2.3.5 (b).

8.3.2. Hydrogen Absorption by the Underlying Metal

The driving force for hydrogen absorption is provided by the Gibbs free energy change for the reaction:

$$Mg(s) + H_2O(g) \rightleftharpoons MgO(s) + H_2(g) \quad \ldots\ldots\ldots\ldots (8.16)$$

for which the standard Gibbs free energy change[220] is:

$$\Delta G^{\ominus} = -364{,}078 - 31.06\ T \log T + 151.1\ T \ \text{J mol}^{-1}$$

Application of Van't Hoff Isotherm (8.3) at 500°C (773°K) for reaction (8.16) yields a value for equilibrium constant, K of 2.51×10^{21}. Since from equation (8.16)

$$K = a_{MgO} \cdot a_{H_2}/a_{Mg} \cdot a_{H_2O} \quad \ldots\ldots\ldots\ldots (8.17)$$

for magnesium oxide formed on solid alloys equilibrated at 500°C in air

containing 0.03 atm water vapour pressure,

$$P_{H_2} = 7.5 \times 10^{19} \text{ atm} \quad \ldots\ldots\ldots\ldots\ldots (8.18)$$

assuming that a_{Mg} is unity.

By a similar argument for magnesium oxide formed on liquid alloys equilibrated at 725°C (998°K) in air containing 0.03 atm water vapour pressure,

$$P_{H_2} = 3.01 \times 10^{14} \text{ atm} \quad \ldots\ldots\ldots\ldots\ldots (8.19)$$

Even though the values for aluminium-magnesium alloys are slightly lower since the activites of magnesium in the alloys is <1, these very high theoretical hydrogen pressures imply that a large quantity of hydrogen is absorbed in both solid and liquid alloys according to Henry's law, e.g. at a pressure, P_{H_2}, of 10^4 atm the solubility of hydrogen is theoretically approaching 1 $cm^2/100$ g.

8.4. Interpretation of Thermogravimetric Results

Oxidation phenomena for alloys are very complex and usually cannot be explained by applying a single idealised concept of oxidation theory. A useful discussion of experimental observations must be based on the interaction of several factors, i.e.

(i) Predictions of the thermodynamically favourable oxides.

(ii) Mechanisms of formation of the oxides actually observed, which may or may not correspond with those predicted thermodynamically.

(iii) The protective character of oxides formed.

(iv) The influence on the oxidation kinetics of alloy composition and temperature.

(v) The influence on the oxidation kinetics of impurities introduced into the oxide film from the atmosphere and from the alloy substrate.

The operation of these factors depends on physical processes including diffusion, nucleation and partition of alloy components between conjugate phases. Hence, their relative importance varies according to circumstances. For example, in solid alloy, diffusion and nucleation assume greater importance than for liquid alloy and the partition of alloying elements is particularly significant for metal within the solidus-liquidus temperature range.

In the following sections, the experimental observations for solid, liquid and semi-liquid aluminium-magnesium binary alloys and aluminium-magnesium-beryllium alloys will be interpreted using this approach.

8.4.1. Oxidation of Binary Aluminium-Magnesium Alloys in the Solid State

(a) Thermodynamic Considerations

For solid aluminium-magnesium alloys with magnesium contents < 10%, the thermodynamic calculations described in Section 8.2.1 and presented in Tables 11-13 and Figure 151 show that the only stable oxides expected at 500°C on the clean, i.e. oxide free, solid alloy surfaces are Al_2O_3 for magnesium < 0.16%, the spinel, $MgAl_2O_4$ for 0.16% < magnesium < 1.05% and MgO for magnesium > 1.05%, as presented in Table 17. Thus for the whole composition range for the alloys investigated, i.e. 1.3-9.3% Mg, the thermodynamically stable oxide is magnesium oxide.

It is a well-known fact that even with high magnesium contents, aluminium-magnesium alloys bear an air-formed amorphous alumina film of 1 or 2 nm thick which thickens as the temperature rises up to 350°C.[185,186,188,190,191] The alumina layer is thermodynamically unfavourable as evident in Figure 151, but its formation at temperatures < 350°C is explained by slow diffusion of magnesium to the oxide/alloy interface because the thermal activation is insufficient. For higher temperatures selective oxidation of

magnesium has often been reported[183,184,186,188], as would be expected.

In the present investigation, in which oxidation was truly isothermal, the alloy samples bearing the very thin initial air-formed film of amorphous alumina were heated in helium to the test temperatures and since no weight gain was detected on the very sensitive microbalance before oxygen was admitted, it can be reasonably assumed that the initial air-formed alumina film did not develop during heating through the temperature range 20-350°C. Subsequently, as the temperature exceeded 350°C and magnesium became accessible to the oxide/alloy interface through increased diffusivity[227], an approach to thermodynamic equilibrium becomes possible through the reduction of alumina by one of the following reaction schemes:

$$3\,Mg\,(s) + Al_2O_3\,(s) \rightleftharpoons 3\,MgO\,(s) + 2\,Al\,(s) \quad \ldots\ldots\ldots\ldots (8.20)$$

$$\Delta G^{\theta} = -1,34,763 - 20.34T \log T + 89.4T \ J mol^{-1}$$

$$\Delta G^{\theta}_{500} = -111.06 \ kJ \ mol^{-1}$$

$$3/4\,Mg + Al_2O_3 \rightleftharpoons 3/4\,Mg\,Al_2O_4 + 1/2\,Al \quad \ldots\ldots\ldots\ldots (8.21)$$

$$\Delta G^{\theta} = -60,338 - 5.08T \log T + 19.7T$$

$$\Delta G^{\theta}_{500} = -56.45 \ kJ \ mol^{-1}$$

The free energies for reactions (8.20) and (8.21) were obtained by combining the values for reactions (8.4), (8.6) and (8.8).

Since reactions (8.20) and (8.21) occur at temperatures > 350°C, the amorphous alumina film is expected to be crystalline[191] during the reaction but even if it was amorphous, the effect on the free energy changes for reactions (8.20) and (8.21) does not change the argument.

However, due to the presence of the very thin air-formed film of alumina

during heating of samples to test temperatures, reaction (8.20) is the more favourable and would have occurred while the alloy was heated to and held at the test temperature in helium. Thus prior to the isothermal oxidation, the alloy samples were expected to be covered not with an alumina film but with a very thin film of primary magnesium oxide formed by reaction (8.20).

When oxidation was initiated by admitting oxygen, the primary magnesium oxide film was exposed to oxygen and developed by the growth of secondary magnesium oxide by reaction (8.4). In areas where the film remained coherent the growth interface must have been the outer surface of the oxide because, as discussed in Section 2.3.5(a), the Mg^{2+} cations are the more mobile species in magnesium oxide, and the rate of growth was controlled by diffusion of the reacting species, i.e. Mg^{2+} ions, through the primary oxide layer. In other areas where the oxide film was disrupted, prior to or during oxidation, the growth occurred at the oxide/alloy interface[186] as separate tertiary magnesium oxide. The probable growth mechanisms are discussed later.

As expected from the above discussion, magnesium oxide was the only oxide species identified by TEM with electron diffraction and EDX techniques during the 2h period of oxidation for any of the alloys in the composition range 1-10% magnesium. The TEM and electron diffraction evidence for this observation was very similar for all of the alloys irrespective of the oxidation temperature in the range 500-625^{o}C. It is illustrated for the aluminium-3% and 7% magnesium alloys oxidised at 525^{o}C under moist atmospheres in Figure 85 and under dry atmospheres in Figure 86 respectively. The related electron diffraction patterns illustrated in Figures 85 and 86 could be matched, as explained in Section 6.4.3(c), only to magnesium oxide. In confirmation, the X-ray diffraction spectra obtained, as illustrated in Figures 101-102 could be matched only to spectra derived from d-spacings given in the ASTM powder diffraction data files for crystalline magnesium

oxide and for the parent metal. These findings confirm some earlier reported results[175,185,187,191].

In other earlier work the formation of $MgAl_2O_4$ spinel has been reported[169, 190,192] on aluminium-magnesium alloys. This observation has given rise to some confused interpretation. For example, Ritchie et al[190] used a thermodynamic argument to suggest that $MgAl_2O_4$ is the stable oxide for an aluminium-1.2% magnesium alloy but the argument is totally fallacious since they disregarded the effect of activities of the alloy components, as illustrated in Tables 11-13, and a correct argument leads to the conclusion that the stable oxide is in fact magnesium oxide. The occasional observation of $MgAl_2O_4$ must therefore be ascribed to kinetics and not thermodynamic factors; notably the reduction of the magnesium content at the alloy surface either by slow magnesium diffusion at low temperature or by depletion of the magnesium content of the alloy. This is confirmed by close examination of experimental procedures used in earlier work in which the appearance of spinel $MgAl_2O_4$ was reported.

If the alloys are heated to the test temperature in an oxidising atmosphere, i.e. non-isothermal condition, the growth of the air-formed alumina film is not restricted, so that a fairly thick layer of alumina is expected when the temperature reaches 350°C. As the temperature rises further and the magnesium becomes mobile, two reaction schemes are possible:

(a) Magnesium diffuses to oxide/alloy interface to react with the amorphous or crystalline alumina to form $MgAl_2O_4$ spinel according to reaction (8.21) because for reaction (8.20) to occur, the greater bulk of alumina formed has a correspondingly greater requirement for magnesium:

$$3\,Mg\,(s) + 4\,Al_2O_3\,(s) \rightleftharpoons 3\,Mg\,Al_2O_4 + 2Al\,(s) \quad \ldots\ldots\ldots\ldots \quad (8.21)$$

(b) Magnesium concentrated at the oxide/alloy interface diffuses through

the unreduced alumina layer, if remains after reaction (8.21), to the oxide/atmosphere interface forming secondary magnesium oxide overlying the alumina film, according to reaction (8.4). The secondary magnesium oxide formed in this manner eventually reacts with the underlying alumina layer to give $MgAl_2O_4$ spinel:

$$MgO\ (s) + Al_2O_3\ (s) \rightleftharpoons MgAl_2O_4\ (s) \quad \ldots\ldots\ldots\ldots\ (8.8)$$

Most investigators[175,186-188,191] found only an magnesium oxide film during oxidation at temperatures > 350°C, as described in Section 4.3.1, even for non-isothermal conditions. These results reveal that the formation of $MgAl_2O_4$ spinel under reaction schemes (8.21) and (8.8) above is usually suppressed. This can be ascribed to the high activation energy required for the initiation of these reactions. However, on some occasions[190,192] under non-isothermal conditions, the alloy samples were in a very fine state of division, e.g. 0.1-0.5μm, with magnesium contents being < 5% and hence the magnesium content of the alloy was rapidly depleted by selective oxidation so that magnesium activity was reduced to a very low level in a short period of oxidation stabilising $MgAl_2O_4$ spinel. On other occasions[169] the alloy samples used had low initial magnesium activity, i.e. 0.05-0.1% mg, so that the formation of thermodynamically favourable Al_2O_3 would have led to the enhancement of magnesium activity in the alloy for the stability of $MgAl_2O_4$ as predicted from Figure 151.

(b) Protective Character of the Magnesium Oxide Layer Formed on Solid Alloys

When formed on pure solid magnesium, magnesium oxide is non-protective[228] as anticipated by the oxide/metal volume ratio[139] of 0.81 calculated using molar volumes of 11.32 cm^3 and 13.98 cm^3 for magnesium oxide and solid magnesium respectively. However, this assessment does not apply to magnesium oxide formed on aluminium-magnesium alloys because the atomic

volume of the alloy substrate is different.

The atomic volume of pure solid aluminium is 9.98 cm^3. The corresponding value for a solid aluminium-5.1% magnesium alloy can be calculated since it was found that the addition of 5.1% magnesium 99.99% pure aluminium reduces the density from 2.780 to 2.642† g cm^{-3}. The atomic volume of the alloy is therefore:

$$\frac{N_{Al} \cdot M_{Al} + N_{Mg} \cdot M_{Mg}}{\rho \text{ alloy}}$$

$$= \frac{0.949 \times 26.97 + 0.051 \times 24.32}{2.642}$$

$$= 10.16 \text{ cm.}$$

This yields a magnesium oxide/alloy volume ratio of 1.11. By similar calculation, the volume ratio for aluminium-9.3% magnesium alloy is about 1.08 because the density of the alloy is 2.541† g cm^{-3}. These volume ratios are just greater than unity and provide an essential, but not a sufficient, criterion for a protective oxide. Other criteria must also be satisfied if the oxide is to be protective, particularly the ability of the oxide to withstand the stress system inevitably developed in a growing oxide layer by the solid substrate, as explained in Section 2.5.3.

(c) Influence of Temperature, Magnesium Content and Atmospheric Moisture on the Oxidation Kinetics of Solid Alloys

The first step is to examine the thermogravimetric results for the aluminium-magnesium binary alloys, given in Figures 51-60, to assess possible oxidation rate laws.

Non-protective oxide films are characterised by linear or accelerating growth laws, e.g.

$$x = Kt \qquad \text{.....(2.52)}$$

† Measured on samples used in this investigation.

Protective films are characterised by growth laws in which $d\Delta m/dt$ diminishes progressively with time. For oxidation completely controlled by diffusion of reacting species through a coherent uniform film according to the Wagner model, the growth law is simply parabolic, i.e.

$$x^2 = Kt \qquad \text{.....(2.49)}$$

and a convenient method of assessing the application of this law is by replotting the results given in Figures 51-60 as (mass gain)^2 versus time, i.e. Δm^2 v t.

Examination and analysis of the thermogravimetric results given in Figures 51-60 reveal two distinct modes of oxidation for solid alloys, i.e.

Mode A : Oxidation gradually diminishing as oxidation proceeds.

Mode B : Oxidation temporarily diminishing and later transforming to either a steady or an accelerating rate.

The distinction between these two modes of oxidation is evident in the response to replotting the results as Δm^2 v t, as shown in Figures 63-72. In such a plot, results for a protective film on the Wagner model would, of course, yield a linear plot. Mode A oxidation is characterised by a Δm^2 v t plot which is generally concave with respect to time axis, implying that the film becomes inherently more protective as oxidation proceeds. In contrast, mode B oxidation is characterised by a Δm^2 v t plot which is generally convex with respect to time axis, implying that the film becomes inherently less protective as oxidation proceeds.

The tendency towards mode A or mode B oxidation followed the apparently logical pattern below:

Temperature ^{o}C	Atmosphere	1% Mg	3% Mg	5% Mg	7% Mg	9% Mg
500	dry	A	A	A	A	A
525	dry	A	A	B	B	B
550	dry	A	B	B	B	-
575	dry	B	B	B	-	-
600	dry	B	B	-	-	-
625	dry	B	-	-	-	-
500	moist	A	A	A	A	A
525	moist	A	A	A	A	A
550	moist	A	A	A	A	-
575	moist	A	A	A	-	-
600	moist	A	A	-	-	-
625	moist	A	-	-	-	-

This shows that for the dry atmospheres, mode A oxidation is favoured by low temperature and low magnesium content but for the moist atmospheres mode A oxidation occurred irrespective of temperature or magnesium content.

There are two further distinctions between the corresponding oxidation kinetics in moist and in dry atmospheres for all of the aluminium-1 to 9% magnesium alloys, as illustrated for the aluminium-3 and 7% magnesium alloys by the results extracted from Figures 53-54 and 57-58 and assembled in Figures 61 and 62 respectively.

(i) The initial oxidation rate in moist atmospheres was always faster than the corresponding rate in dry atmospheres.

(ii) Subsequently the relative rates changed so that ultimately, oxidation in moist atmospheres was the slower process. Thus for any given prescribed temperature and magnesium content there was a critical time, t_c, indicated on the Figures 61 and 62 for which the total mass of

oxide was the same. The value for this critical time diminished with increasing temperature and increasing magnesium content. For the lowest temperatures investigated, the total time of oxidation, i.e. 2h, was less than the critical time, so that the total mass of oxide in moist atmospheres is higher than that in dry atmospheres, as apparent from Figures 61 and 62.

(d) Interpretation of Oxidation Kinetics for Solid Alloys

The relationships between mass gain and time do not conform with expressions describing standard simple oxidation mechanisms and the oxidation process must therefore be due to a combination of effects which can explain inter alia the progressively more protective character of the oxide film formed in mode A oxidation and the progressively less protective character of the film formed in mode B oxidation. A useful approach is to examine the limitations of some of the assumptions implicit in the Wagner theory of parabolic oxidation. Three factors merit particular attention:

(1) The influence of grain boundaries in the oxide.
(2) Changes in the morphology or integrity of the oxide film and the formation of new nuclei.
(3) Variability in the defect structure of the oxide film.

(1) The Wagner theory neglects the influence of grain boundaries on the diffusion of the reacting species through the oxide film. The activation energy for diffusion at the grain boundaries is, of course, lower than that for diffusion in the lattice so that diffusion at the boundaries is more rapid and less temperature-dependant. Thus for polycrystals, grain boundary diffusion can become the dominant transport mechanism at low temperatures. In magnesium oxide, the predominant diffusing species is Mg^{2+} and it has been confirmed experimentally that Mg^{2+} ions do indeed diffuse much more rapidly through the grain boundaries than through the

lattice[96,227]. The grain size of the initially-formed oxide films observed on the aluminium magnesium alloys in the present work was very small, e.g. for the aluminium-3% magnesium alloy oxidised at 525°C for 30 min in the moist atmosphere the grain size was of the order 2×10^8 mm^{-2}. As oxidation continued, the grain size increased, as illustrated by the sequence of TEM micrographs given in Figures 85-86 and by the development of spots in the concentric rings of the corresponding electron diffraction patterns. The diminishing grain boundary area alters the balance of diffusion via the grain boundaries and via the lattice so that the overall apparent diffusivity diminishes as oxidation progresses. Thus if oxidation is controlled by diffusion through a uniform film undergoing grain growth, the relationship between mass gain and time is displaced from a parabolic function in a direction indicating the progressively more protective nature of the film. Such an argument forms the basis of an explanation for mode A oxidation.

(2) As oxidation proceeds, the morphology of a real oxide can sometimes evolve in a manner permitting the growth of oxide in excess of that expected from a parabolic oxidation law. In the present work, new nuclei form within the oxide film during the course of oxidation, evident as white particles on the dark groundmass in the SEM micrographs given in Figures 113-117. Although the nuclei have a very different appearance from the groundmass, they are of the same chemical species as the original oxide film, i.e. magnesium oxide, since no evidence of other species could be discerned in either electron diffraction patterns or X-ray analysis, as illustrated in Figures 85-86 and 101-102 respectively. The nucleation sites cannot be associated with the grain boundaries since they are distributed on a much coarser scale, e.g. of the order of 2×10^3 mm^{-2} for the aluminium-3% magnesium alloy oxidised at 525°C for 30 min in the moist atmosphere. The nuclei grow as oxidation proceeds, developing into

nodules overlying the oxide film, as illustrated in Figures 113-117, augmenting the mass of oxide formed under diffusion control in the continuous film. This excess oxide will be referred to as tertiary magensium oxide, as introduced in Section 8.4.1(a). The formation of new nuclei within an oxide film is often associated with cracking in the film and this may indeed be true in the present work, but no clear evidence was found.

(3) The spontaneous formation of Schottky disorder in magnesium oxide can be written;

$$MgO = Mg_{(1-\delta)}O_{(1-\delta)} + \delta(Mg^{2+}\square) + \delta(O^{2-}\square) \quad .....(8.22)$$

for which

$$K = n(Mg^{2+}\square).n(O^{2-}\square) \quad .....(8.23)$$

In the ideal stoichiometric oxide, the cation and anion vacancy populations are equal and are determined by the oxygen potential through the reaction:

$$1/2\ O_2 = MgO + (Mg^{2+}\square) + 2(e\square) \quad .....(8.24)$$

for which

$$K = n(Mg^{2+}\square).n(e\square)/P^{1/2} \quad .....(8.25)$$

In the real oxide, the cation or anion population can be varied by the introduction of impurities, because they differ in valency from the host ions or because they introduce donor or acceptor levels into the gap between the valence and conduction bands or because they reduce the gap between the valence and conduction bands. Impurities which raise the population of anion vacancies decrease the population of cation vacancies according to equation (8.23) and vice versa. These effects have been shown by comparing the activation energies for self-diffusion and conductivity in doped samples, applying the Nernst-Einstein equation[47]. The oxide is so

sensitive to such impurities that even the purest available bulk samples exhibit extrinsic cationic character at temperatures of interest in the present work, i.e. $<1000^{o}C$[47,230]. The defect structure of an oxide film growing on an aluminium-magnesium alloy is further complicated by the large gradient in oxygen potential across it so that there are gradients in both cation and anion populations between the oxide/atmosphere and oxide/metal interfaces.

The hydroxyl ion, OH^- is an impurity known to enhance the extrinsic cationic character of the bulk oxide[58]. It is introduced from moist atmospheres by the reaction:

$$O^{2-} + H_2O = 2OH^- \quad \text{.....(2.40)}$$

reducing the anion valency and hence increasing the population of cation vacancy defects to fulfil the requirement for electroneutrality.

The population of OH^- ions in the oxide in equilibrium with a given water vapour pressure can be estimated from the Gibbs free energy for the hydration of magnesium oxide:

$$MgO\ (s) + H_2O\ (g) = Mg(OH)_2\ (s) \quad \text{.....(8.12)}$$

which is given by:

$$\Delta G^{o} = -45{,}980 + 100.3T \ J\ mol^{-1}\ (220)$$

Application of the Van't Hoff isotherm, as described in Section 8.3.1, yields an estimate for the population of OH^- ions in magnesium oxide equilibrated with water vapour at a pressure of 3040Pa (0.03 atm) in the temperature range 500-725°C of about 10^{-4} atm which is significant compared with defect populations common in oxides.

For a magnesium oxide film growing on the metal in the moist atmosphere, OH^- ions enter at the oxide/atmosphere interface and migrate towards the

very low oxygen potential at the oxide/metal interface where they are eliminated due to the consumption of cation vacancies by Mg^{2+} ions injected from the alloy to fulfil the requirement for electroneutrality by reaction[230,231]:

$$Mg(alloy) + Mg^{2+}.\ 2OH^- + (Mg^{2+}\square) = 2MgO + 2H \quad .....(8.26)$$

Thus the enhanced cationic character of the oxide film is not uniform but is predominant towards the oxide/atmosphere interface.

The above considerations can be applied to account for the oxidation kinetics observed in the present work as follows:

(1) Mode A oxidation is observed when the nucleation of tertiary magnesium oxide is largely confined to the start of oxidation so that the dominant factor is the diminishing overall diffusivity through the progressive reduction of grain boundary area by grain growth.

(2) Mode B oxidation is observed when tertiary magnesium oxide nucleates continuously throughout oxidation so that the growth of oxide on the nuclei is dominant over the diffusion-controlled growth of the continuous film.

(3) The faster initial oxidation rate in the moist atmosphere can be explained by (i) the more rapid diffusion of the mobile Mg^{2+} ions due to the enhanced cationic character of the oxide while the film is thin, an effect which diminishes as the film thickens and the oxide/atmosphere interface recedes from the metal surface, and (ii) more prolific initial nucleation of tertiary magnesium oxide.

(4) The slower ultimate oxidation rate in the moist atmosphere is due to an effect on the nucleation of tertiary magnesium oxide. Comparison of Figures 113(a), (b) and 114(a), (b) with Figures 113(c), (d) and 114(c), (d) shows that although the initial nucleation of tertiary

magnesium oxide is more prolific in the moist atmosphere while the oxide film is thin, it is subsequently suppressed as the film thickens. The role of OH^- ions in stimulating this effect is not clear but there are several possible factors which would repay investigation, e.g. (i) a favourable effect on the physical characteristics of the oxide, such as plasticity[152], (ii) rapid regrowth of oxide to repair cracks which might otherwise spread to become nucleation sites, (iii) an influence on the film growth mechanism, i.e. to move the growth interface towards the oxide/atmosphere interface,through the change in the relative mobilities of cations and anions.

8.4.2. Oxidation of Binary Aluminium-magnesium Alloys in the Liquid State

(a) Thermodynamic Considerations

For liquid aluminium-magnesium alloys, the information presented in Tables 14-16 and Figure 152 show that the stable oxides expected on the clean, oxide-free liquid aluminium containing up to 10% magnesium alloy surfaces at 725°C are Al_2O_3 for magnesium < 0.01%, the spinel $MgAl_2O_4$ for 0.01% < magnesium < 1.5%, and MgO for magnesium > 1.5%, as presented in Table 17.

In the present work, only MgO was found, although at 725°C the aluminium-1.3% magnesium alloy actually falls in the composition range for which $MgAl_2O_4$ is the thermodynamically stable oxide. The presence of only MgO is evident from the results of TEM with electron diffraction and EDX techniques, and from the X-ray diffraction spectra, as illustrated in Figures 87-89 and 103-104 respectively for all of the alloys in the composition range 1.3-9.3% magnesium irrespective of the atmosphere. By analogy with other systems, e.g. iron-chromium[37] and nickel-chromium[37,109], the presence of MgO on the 1.3% magnesium alloy can be ascribed to difficulty

in direct nucleation of the complex spinel structure at the liquid alloy surface. The mechanism of formation of MgO is as described in Section 8.4.1(a).

It is true that in other work, the spinel has been identified as a component of the oxide formed on liquid aluminium-magnesium alloys but only where the experimental techniques employed did not truly represent isothermal oxidation of alloy of the nominal composition. Cochran et al[85] and Belitskus[198] found the spinel in the oxide formed on alloys with magnesium contents in the range 1-10% and 4-4.5% respectively because the magnesium contents of the alloys had been exhausted by very prolonged oxidation, i.e. from 10 to 100h. Haginoya and Fukusako[199] also found the spinel in tests where samples had been preheated in the oxidising atmosphere so that, for the reasons given in Section 8.4.1(a), a thick Al_2O_3 film would be expected to form at low temperatures on the alloy surface yielding the spinel by reaction (8.21) and (8.8) during heating to and subsequent oxidation at the test temperature.

(b) Protective Character of the Magnesium Oxide Layer Formed on Liquid Alloys

The TEM micrographs and corresponding electron diffraction patterns given in Figures 87-89 show that both amorphous and crystalline forms of magnesium oxide were observed. The initial oxidation product was always amorphous magnesium oxide and when it was observed, the crystalline form appeared later as a transformation product on the alloys with high magnesium contents. The amorphous form was observed only on the liquid alloy and its existence has been confirmed independently[85,198,199]. It is well-known that oxide films grow epitaxially on the ordered structures of solid metals but the mobile random structure of a liquid metal surface has a disordering influence, which according to the present results is sufficient to impart a metastable amorphous structure to the initial oxide

growing upon it. If conditions permit, this eventually transforms to the stable crystalline form.

Amorphous magnesium oxide is expected to be more protective than the crystalline oxide. It is known that in amorphous materials, the charge carriers have low mobility compared to that in crystalline materials because they are bound to the localised energy states which exist within the mobility gap due to disorder in the material[232-234]. This requires a higher activation energy for conductivity than that for crystalline materials. The effect is to reduce the diffusivity of the mobile Mg^{2+} ions by increasing the energy for the electron flow required to preserve the electroneutrality. A further important factor is the absence of grain boundaries which act as preferred diffusion paths in crystalline materials.

The density of the liquid alloy is about 12% lower than that of the solid alloy[235] and therefore the oxide/metal volume ratio is reduced from 1.11 to 0.98 for 5.1% magnesium alloys and from 1.08 to 0.95 for 9.3% magnesium alloys, so that stresses due to mismatch of volume is fairly eliminated. Furthermore, since the liquid substrate cannot sustain shear, stresses imposed in other ways can be relaxed by local changes in the shape of the alloy surface.

(c) Influence of Temperature, Magnesium Content and Atmospheric Moisture on the Oxidation Kinetics of Liquid Alloys

Examination and analysis of the thermogravimetric results given in Figures 51-60 indicate two distinct modes of oxidation for the liquid alloys, i.e.

Mode A : Oxidation gradually diminishing as oxidation proceeds.

Mode C : Oxidation diminishing at first but transforming to an accelerated rate after an incubation period.

As for the solid alloys, mode A oxidation is identified by the concavity

of parabolic plots, i.e. Δm^2 v t, with respect to time axis, as illustrated in Figures 63-72, obtained by replotting the information given in Figures 51-60. It is apparent that little useful information can be extracted from the parabolic plots for the complex mode C oxidation.

The tendency towards mode A or mode C oxidation followed the logical pattern below:

Temperature ^{o}C	Atmosphere	1% Mg	3% Mg	5% Mg	7% Mg	9% Mg
625	dry	-	-	-	C	C
650	dry	-	A	C	C	C
675	dry	A	A	C	C	C
700	dry	A	A	C	C	C
725	dry	A	A	C	C	C
625	moist	-	-	-	C	C
650	moist	-	A	C	C	C
675	moist	A	A	C	C	C
700	moist	A	C	C	C	C
725	moist	A	C	C	C	C

This shows that mode C oxidation is favoured by high temperatures, high magnesium contents and to a lesser extent a moist atmosphere.

A curious feature of the oxidation kinetics for the liquid alloys was an *inverse* relationship between oxidation rate and temperature for a temperature range of about 10-75^{o}C above the liquidus temperature, as illustrated in Figures 51-60 above which the normal direct relationship prevailed.

The oxidation rate in the moist atmosphere was always faster throughout the entire oxidation period, i.e. 2h, than that in the dry atmosphere as illustrated in Figures 51-60.

(d) Interpretation of Oxidation Kinetics for Liquid Alloys

As for the corresponding solid alloys, no simple oxidation law can be fitted to the results, so that the oxidation mechanism is again complex. The results for the liquid alloys differed from those for the corresponding solids in several essential aspects:

(i) In mode A oxidation, a film of amorphous magnesium oxide was present on the metal surface during the whole period of oxidation, as illustrated by the TEM micrographs and corresponding featureless electron diffraction patterns for the aluminium-3% magnesium alloy given in Figure 87 and referred to corresponding points on the mass gain/time curve given in Figure 98, extracted from Figure 53.

(ii) In mode C oxidation, the magnesium oxide film was initially amorphous but after an incubation period the film crystallised at a point corresponding with the transition to the accelerated oxidation rate. This is illustrated by the sequences of TEM micrographs and corresponding electron diffraction patterns for aluminium-5% and 9% magnesium alloys given in Figures 88-89 which are referred to the corresponding points on the mode C mass gain/time curves given in Figures 99-100, extracted from Figures 56 and 59 respectively. The incubation period decreased with surface corrugation,increasing magnesium content, increasing temperature, and moisture in the atmosphere.

(iii)For all of the alloys an inverse relationship between oxidation rate and mass gain was observed in the temperature range 10-75^{o}C above the liquidus temperatures, as illustrated in Figures 51-60.

(iv) At temperatures just above the liquidus temnerature, all of the oxidised alloys exhibited undulating surfaces† which developed at the start of oxidation increasing the effective area of the alloy surface.

† Formed during oxidation and not on cooling. This was confirmed by observation.

For the alloys with lower magnesium contents, i.e. 1%, 3% and 5%, the effect was evident as surface wrinkling, as illustrated by the SEM micrographs given in Figures 118 and 119(a), (b) but for the alloys with the higher magnesium contents, i.e. 7% and 9%, the effect was more pronounced and deep corrugations were apparent, as illustrated by the SEM micrographs given in Figures 121 and 123. The surface became progressively smoother as the temperature for isothermal oxidation was raised within the temperatures where the inverse relationship between temperature and mass gain applied and were level at temperatures where the relationship was normal, unless or until accelerated oxidation was initiated.

(v) Several kinds of macroscopic defects were observed during the accelerated oxidation phase in mode C oxidation, i.e. macroscopic cracks as apparent from the SEM micrographs given in Figures 120(a) and 122(b) pores and blisters which developed both at the oxide/metal interface and within the metal, as illustrated in Figures 148-149, for the higher temperatures, i.e. $\geq 700^{o}C$, leading to "cauliflower" growths.

(vi) The effect of the moist atmosphere was to increase the oxidation rate throughout the entire oxidation period in contrast with the corresponding effect for the solid alloys, where the increased rate was confined to the initial period.

The concepts that have been introduced concerning the nature, topography and character of the oxide film and its liquid substrate permit a fairly detailed interpretation of the oxidation kinetics observed for the liquid alloys.

The initially-formed film on the liquid metal is always amorphous because it is epitaxial upon a mobile *random* structure. Moreover, it is magnesium

oxide for the complete range of magnesium compositions investigated because of the difficulty in nucleating the spinel, $MgAl_2O_4$ even for a magnesium content just below the critical composition for the thermodynamic stability of magnesium oxide. While the oxide remains amorphous it forms a protective film because of the low electron mobility, which inhibits the selective diffusion of Mg^{2+} ions.

Where the amorphous film persists during the whole of the oxidation period as for the alloys of low magnesium content, mode A oxidation is observed. This kinetic behaviour is analogous with mode A oxidation for solid alloys but with the difference that allowing for the temperature difference, the amorphous film on liquid alloys is more protective than the microcrystalline film on the corresponding solids. No explanation can be offered for the increasingly protective character of the film as oxidation proceeds as is possible for the solid alloys because there is no measureable characteristic of the amorphous oxide on which to base arguments.

Where the amorphous film crystallises after an incubation period, as it does for alloys with $\geq$ 5% magnesium, the onset of crystallisation is associated with an acceleration of the oxidation rate. The evidence from the SEM and optical micrographs given in Figures 120(a), 122(b) and 148-149 respectively show that the effect of crystallisation is to disrupt the oxide film[98], initiating blistering and cracking. From then onwards the oxide grows in an irregular manner from preferred growth centres[197] rather than by the uniform growth normal to the substrate which would occur under diffusion control. Once irregular oxide growth is established, the growth stresses within the oxide are irregular so that the disruption of the oxide film is self-sustaining and rapid oxidation continues.

The effects of the irregular growth of oxide and the consequent disruption of the oxide film are difficult to analyse, especially because, unlike the solid, the liquid metal cannot support shear stresses imposed on it and

is able to accommodate topographically to the growing oxide. Moreover, the liquid metal can exude through cracks developed in the film by growth stresses, thereby becoming exposed to oxidation leading, for example, to the "cauliflower" growths observed at higher temperatures, as illustrated in Figures 120, 122 and 124. Even for regular oxide growth, it is difficult to ascertain the precise nature of the stresses within an oxide[109]. Thus several features of the oxide cannot at present be explained with certainty. These include:

(i) The development of pores and blisters both at the oxide/metal interface and within the metal.

(ii) "Cauliflower" growths of oxide at higher temperatures, i.e. $\geq 700^{o}C$.

(iii) Wrinkling and corrugation of the surface during oxidation.

However, it is possible to advance a logical, though speculative explanation for the general nature of the observed effects, based on the mechanisms available for the relief of stresses in the growing oxide.

For alloys of low magnesium content at temperatures not far above the liquidus temperature for which the oxide remains amorphous and which exhibit mode A oxidation, the initial growth stresses can apparently be relieved by wrinkling of the surface after a few minutes of oxidation without disrupting the oxide film. At higher temperatures, the wrinkling is not observed and the protective nature of the film is maintained, suggesting that the stresses can be relaxed by plastic deformation of the metal.

In comparison, for alloys of high magnesium content at temperatures not far above the liquidus, the immediate onset of crystallisation further increases the growth stresses to a higher level which is relieved first by the formation of deep corrugations which promote early film rupture.

Hence, the effect of both crystallisation and surface corrugations is to cause a short incubation period before accelerated oxidation commences. At higher temperatures, the early crystallisation or the development of surface corrugations do not occur, presumably because oxide film is more plastic, so that the incubation period before film rupture is extended.

Generally, similar effects are observed for oxidation in the moist atmosphere but with higher rates of oxidation throughout, shorter incubation times and greater disturbance to the oxide film as manifest by deeper corrugations, larger pores and blisters and larger "cauliflower" growths as illustrated in Figures 121 and 123, 148-149, and 120, 122 and 124 respectively. The only conceivable explanations are based on the effect of OH^- ion injection into the film and on the enhanced plasticity of the oxide film at higher liquid temperatures. The injection of OH^- ions promotes:

(i) acceleration of Mg^{2+} ion migration, as described in Section 8.4.1(d).

(ii) expansion of pores and blisters under the oxide or within the alloy by hydrogen formed, equation (8.19), by the reduction of the migrating OH^- ions on reaching the low oxygen potential at the alloy surface, as described earlier in Section 8.4.1(d):

$$Mg(alloy) + Mg^{2+}.2OH^- + (Mg^{2+}\square) = 2MgO + 2H \quad .....(8.26)$$

During both mode A oxidation and the incubation period, stresses imposed on the oxide film in the dry atmosphere are apparently not raised above the critical fracture stress due both to the enhanced plasticity of the oxide at higher temperatures and to the lower stress constraints imposed by the liquid substrate. This is supported by the SEM micrographs given in Figures 118-119 which show that tertiary magnesium oxide, assumed to

develop via cracks, is not observed in the dry atmosphere. The effect is to hinder the continuous cracking and hence the nucleation of tertiary magnesium oxide, as observed on solid alloys. This explains why the alloys exhibit lower oxidation rate in the dry atmosphere than that observed in the moist atmosphere from which OH^- ions are injected. The delayed breakaway oxidation and lower oxidation rate during breakaway in the dry atmosphere could perhaps be due to the combined effect of both OH^- ion injection and expansion of pores and blisters in the moist atmosphere.

8.4.3. Oxidation of Binary Aluminium-Magnesium Alloys in the Semi-Liquid State

The complex nature of the oxidation of aluminium-magnesium alloys in either the solid or liquid state is further complicated in the semi-liquid state, where both phases are present. The additional features are:

(i) The solid and liquid fractions of the surface may be expected to oxidise with some of their own particular characteristics.

(ii) The oxide formed passes over multiple discontinuities between the liquid and solid phases.

(iii) The magnesium content is partitioned between the solid and liquid phases by selective liquation according to the phase equilibrium diagram given in Figure 44.

(a) Thermodynamic Considerations

Although the partition of magnesium by selective liquation gives widely different magnesium contents in the solid and liquid fractions of the alloy, the activity of magnesium in both the phases is the same because they are in equilibrium. No attempt was made to evaluate quantitatively the stability ranges for the potential oxides as was performed for the single phase solid and liquid alloys because no precise information

is available. However, it is logical to assume that the critical magnesium compositions for the formation of Al_2O_3, spinel $MgAl_2O_4$, and MgO are intermediate between those for the wholly solid and liquid alloys given in Table 17, so that MgO is thermodynamically favoured in the semi-liquid state. Moreover, since only MgO was found as the oxidation product on all of the alloys in both wholly solid and liquid states, it was also expected that only MgO would be formed on both solid and liquid fractions in the semi-liquid state and this is confirmed by the results of TEM with electron diffraction and EDX techniques given in Figures 90-92 and by the X-ray diffraction spectra given in Figures 105-108.

(b) Protective Character of the Magnesium Oxide Layer Formed on Semi-Liquid Alloys

Since the initial oxide film formed on the wholly liquid alloys was amorphous and that on the wholly solid was crystalline, it was expected that the oxide formed on the semi-liquid alloys would be a composite. The TEM micrographs and the corresponding electron diffraction patterns given in Figures 90-91 confirm this expectation. As oxidation proceeded, the whole film crystallised in a very short period, as illustrated by the sequences of TEM micrographs and electron diffraction patterns given in Figures 90-92. Thus the effect of composite character of the oxide film is that crystalline nuclei are available in the oxide over the solid phase to promote easy crystallisation of the protective amorphous film formed over the liquid phase. The effectiveness of the nuclei depends on the relative proportions of solid and liquid phases. The table below shows the maximum period for which amorphous magnesium oxide could be detected by electron diffraction during oxidation of all of the alloys in the moist atmosphere, arranged according to whether the liquid fraction was less or greater than 50%.

Nominal wt% Mg	Liquid Fraction	
	< 50%	> 50%
1	∿ 10 min at 646°C	∿ 30 min at 654°C
3	∿ 10 min at 625°C	∿ 25 min at 640°C
5	∿ 5 min at 600°C	∿ 10 min at 625°C
7	0 min at 575°C	0 min at 610°C
9	0 min at 550°C	0 min at 600°C

Unfortunately, the significance of this information was not appreciated until a late stage of the investigation and sufficient information is not available for a corresponding table for the dry atmosphere.

(c) Influence of Temperature, Magnesium Content and Atmospheric Moisture on the Oxidation Kinetics of Semi-Liquid Alloys

Examination and analysis of the thermogravimetric results given in Figures 51-60 indicate two distinct modes of oxidation for the semi-liquid alloys, i.e.

Mode A : Oxidation gradually diminishing as oxidation proceeds.

Mode B : Oxidation temporarily diminishing and later transforming to either a steady or an accelerating rate.

As for solid alloys, mode A and mode B oxidation were identified respectively by concavity and convexity of the parabolic plots, i.e. Δm^2 v t, with respect to time axis given in Figures 63-72, obtained by replotting the information given in Figures 51-60.

The tendency towards mode A or mode B oxidation followed the pattern below:

Temperature °C	Atmosphere	1% Mg	3% Mg	5% Mg	7% Mg	9% Mg
550	dry	-	-	-	-	B
575	dry	-	-	-	B	B´
600	dry	-	-	B	B´	B´
610	dry	-	-	B	B´	-
615	dry	-	-	B	-	-
625	dry	-	B	A	-	-
632	dry	-	A	-	-	-
640	dry	-	A	-	-	-
646	dry	B	-	-	-	-
650	dry	A	-	-	-	-
654	dry	A	-	-	-	-
550	moist	-	-	-	-	B
575	moist	-	-	-	B	B´
600	moist	-	-	A	B´	B´
610	moist	-	-	B	B´	-
615	moist	-	-	B	-	-
625	moist	-	A	B	-	-
632	moist	-	A	-	-	-
640	moist	-	B	-	-	-
646	moist	A	-	-	-	-
650	moist	A	-	-	-	-
654	moist	A	-	-	-	-

In all cases, the oxidation rates for the semi-liquid alloys were much faster than would be expected from the results for either the wholly solid or the wholly liquid alloys, taking account of the relative proportions of solid and liquid present. In fact for alloys with magnesium contents > 3%, the initial oxidation rate was usually faster than for the wholly liquid alloys.

The table above shows that influences of temperature, magnesium content and moisture in the atmosphere are more complicated than for either the wholly liquid or the wholly solid alloys and are in fact inseparable. However, in the dry atmosphere the tendency towards mode B oxidation is associated with lower temperatures and higher magnesium contents. In the moist atmosphere, the oxidation rates were usually increased and the tendency towards mode A oxidation is associated with lower temperatures and lower magnesium contents.

(d) Interpretation of Oxidation Kinetics for Semi-Liquid Alloys

The nature of the magnesium oxide film formed on semi-liquid alloys, as discussed in Section (b) above, permits a fairly complete explanation of most of the features of the results obtained.

In the interpretation, it is convenient to discuss the oxidation mechanism for two conditions, (i) when the proportion of solid phase predominates, i.e.< 50% liquid and (ii) when the proportion of liquid phase predominates, i.e.> 50% liquid. This is the critical proportion of liquid which determines whether or not the material is cohesive. For a liquid fraction of < 50% the material is cohesive and the total oxidation is the sum of the separate contributions from oxidation of the solid grains and of the liquid regions enriched in magnesium around the grain boundaries. For a liquid fraction of >50%, the material is unable to support its own mass and the oxidation is essentially that for a liquid but modified by the influence of the entrained solid particles. The solid particles have two significant effects, they act as disruptive stress raisers where they impinge on the oxide film and they provide the oxide nuclei which promote rapid crystallisation of the protective amorphous film. This is analogous with Cochran et al's observation[85] that seeding an oxide film on wholly liquid metal with magnesium oxide crystals produced the same effect.

The characteristic features of all of the alloys oxidised in the semi-liquid state are:

(i) if the liquid fraction is < 50%, the liquid phase which adopts the oxidation kinetics of wholly liquid alloys, is mostly confined to the grain boundaries and the solid phase which adopts the oxidation kinetics of wholly solid alloys, is mostly confined to the grains. Since the solid phase occupies a large area of the alloy sample represented by solid grains, the alloys exhibit oxidation kinetics similar to those for wholly solid alloys in a particular atmosphere but with comparatively faster oxidation rates due to the influence of magnesium enriched liquid grain boundaries. Moreover, as observed for wholly solid alloys, the oxidation rate is initially faster in the moist atmosphere but as the oxidation proceeds the oxidation rate in the dry atmosphere becomes faster, so that the overall oxidation after 2h is higher in the dry atmosphere in comparison with that in the moist atmosphere. The factors which determine mode A or mode B oxidation are essentially similar to those for the wholly solid alloys as discussed in Section 8.4.1(d).

(ii) if the liquid fraction is >50%, the alloy can be assumed as liquid in which solid particles are suspended, so that the oxidation kinetics are similar to those for wholly liquid alloys in a particular atmosphere but with comparatively faster oxidation rates due to the presence of disruptive solid particles with crystalline magnesium oxide as described above. Moreover, as observed for wholly liquid alloys, the oxidation rate is always faster in the moist atmosphere than that observed in the dry atmosphere. The factors which determine mode A or mode B oxidation are essentially similar to those which determine mode A or mode C oxidation in the wholly liquid alloys as discussed in Section 8.4.2(d).

(iii) if the liquid fraction is ∿ 50%, the alloy most likely oxidises with characteristics of wholly liquid alloys.

For convenience, the alloys are considered in three groups,(i) alloys with 1% and 3% magnesium, (ii) the alloy with 5% magnesium, and (iii) alloys with 7% and 9% magnesium.

Al-1% and 3% Mg alloys

The oxidation rate for these alloys was directly proportional to the temperature throughout the semi-liquid range in both dry and moist atmospheres, so that the highest oxidation was observed at the highest semi-liquid temperature. The alloys changed their mode of oxidation from B to A in the dry atmosphere and from A to B in the moist atmosphere when the liquid phase in the alloy changed from < 50% to > 50% because they adopted the oxidation character of the major phase.

Hence, the alloy samples oxidised yielding < 50% liquid exhibited mode B and mode A oxidation in the dry and in the moist atmospheres respectively. This observation is supported by the TEM micrographs and corresponding electron diffraction patterns given in Figure 90 and by the SEM micrographs given in Figures 125 and 127, i.e:

(i) in the dry atmosphere, the dominant feature of the oxide is continuous nucleation of tertiary magnesium oxide which developed densely over all the grains, as illustrated in Figures 125(a) and 127(a) with only a minor influence of grain growth, as illustrated in Figure 90, and the alloys exhibited mode B oxidation.

(ii) in the moist atmosphere, the dominant feature is grain growth of the oxide, as illustrated in Figure 90, since no tertiary magnesium oxide is apparent over the solid grains of the alloy, as illustrated in Figures 125(b), (c) and 127(b), (c), so that the alloys exhibited

mode A oxidation.

Although it is clear from the SEM micrographs given in Figures 125 and 127 that the liquid grain boundary oxidation is more pronounced in the moist atmosphere, this effect did not promote a higher overall oxidation rate in the moist atmosphere because the area occupied by the grain boundaries is less than that by the solid grains.

Alloy sample yielding > 50% liquid exhibited mode A oxidation in both dry and moist atmospheres for the aluminium-1% magnesium alloy but mode A and mode B oxidation in the dry and moist atmospheres respectively for the aluminium-3% magnesium alloy. These observations are supported by the TEM micrographs and corresponding electron diffraction patterns given in Figure 91, by the table given on page 149 and by the SEM micrographs given in Figures 126 and 128, i.e:

(i) *in the dry atmosphere, the dominant feature of the oxide is grain* growth, as illustrated in Figure 91 without cracking but with wrinkling, as illustrated in Figures 126(a) and 128(a), so that mode A oxidation prevailed.

(ii) in the moist atmosphere, the dominant feature of the oxide on the aluminium-1% magnesium alloy is grain growth as illustrated in Figure 91 without cracking but with wrinkling, as illustrated in Figures 126(b) and (c), so that mode A oxidation prevailed, whereas for the aluminium-3% magnesium alloy, extensive cracking of the oxide, as illustrated in Figure 128(c), over-rode the influence of grain growth as illustrated in Figure 91, so that mode B oxidation prevailed.

Although it was expected that suspended solid particles with crystalline magnesium oxide might generate disruptive stresses in the oxide layer, the SEM micrographs given in Figures 126 and 128(a) show that for the aluminium -1% magnesium alloys in both atmospheres and for the aluminium-3% magnesium

alloys in the dry atmosphere, the stresses are relieved by wrinkling without cracking the oxide film. This may apparently be due to the enhanced plasticity of oxide film, promoted both by higher temperatures and by the formation of a thin oxide layer, in contrast with the oxide formed on alloys of high magnesium content.

Al-5% Mg alloy

This alloy also changed its mode of oxidation from B to A in the dry atmosphere and from A to B in the moist atmosphere. Although the oxidation rate in the dry atmosphere showed a direct relationship with temperature as for the other magnesium-containing alloys, the exceptional feature in the moist atmosphere is that the alloy exhibited the highest oxidation when the liquid fraction of the sample was $\sim$ 50%. This behaviour can be ascribed to the poor mechanical strength of oxide arising from the composite character of oxide film at this critical liquid proportion in the moist atmosphere. The effect is to offer poor protection to the alloy as apparent from the SEM micrographs given in Figure 129(c) which shows that the alloy has lost its integrity due to intergranular oxidation and disintegration.

Alloy samples yielding < 50% liquid exhibited mode B and mode A oxidation in the dry and moist atmospheres respectively. This is supported by the TEM micrographs with corresponding electron diffraction patterns given in Figure 90 and by the SEM micrographs given in Figures 129(a) and (b), i.e:

(i) in the dry atmosphere, the dominant feature is the nucleation of tertiary magnesium oxide as illustrated by Figure 129(a) and hence the grain growth has a minor influence.

(ii) in the moist atmosphere the dominant feature is the grain growth, as illustrated by Figure 90,since a dense distribution of tertiary magnesium was not observed. Wrinkling appeared in place of cracking

of the oxide, as illustrated by Figure 129(b).

Samples yielding > 50% liquid exhibited mode A and mode B oxidation in the dry and moist atmospheres respectively. Supporting evidence is provided by the TEM micrographs with corresponding electron diffraction patterns given in Figure 91 and by the SEM micrographs given in Figure 130, i.e:

(i) in the dry atmosphere, grain growth is the dominant feature since the stresses imposed on the oxide layer both by the suspended solid particles and by crystallisation of oxide, are relieved by corrugation of the oxide without cracking, as illustrated in Figure 130(a).

(ii) in the moist atmosphere, the dominant feature is the disruption of the oxide film by continuous cracking followed by tertiary magnesium oxide due to the disruptive effect of the suspended solid particles, as illustrated by Figures 130(b) and (c).

Al-7% and 9% Mg alloys

These alloys also exhibited a direct relationship between oxidation rate and temperature in both dry and moist atmospheres and hence the highest oxidation was observed at the highest semi-liquid temperature. The special feature on these alloys is that they changed their mode of oxidation from B to B´ in both atmospheres. The distinction between mode B and mode B´ oxidation is that mode B´ oxidation exhibits a very much higher initial oxidation rate which eventually accelerates still further.

Samples yielding < 50% liquid exhibited mode B oxidation in both atmospheres. Mode B oxidation observed on these alloys in the dry atmosphere is supported by the TEM micrographs and corresponding electron diffraction patterns given in Figure 92 illustrating grain growth of the oxide and by the SEM

micrographs given in Figures 131 and 133 illustrating the dense distribution and growth of tertiary magnesium oxide covering the entire alloy surface which is the major influence on oxidation. However, in the moist atmosphere, mode B oxidation was observed on these alloys instead of mode A oxidation, as observed for wholly solid alloys. This can be attributed to the formation of tertiary magnesium oxide both by severe grain boundary oxidation and by oxidation within the grains, because of the failure of oxide layer which thickened rapidly at these low temperatures in contrast with the oxide formed on alloys of low magnesium content. This observation is supported by the SEM micrographs, as illustrated in Figures 131(b) and 133(b).

Samples yielding > 50% liquid exhibited mode B´ oxidation in both atmospheres. The reason for the overall rapid oxidation in both atmospheres can be explained by:

(i) the formation of a thick crystalline layer of magnesium oxide on both the solid and liquid phases with the onset of oxidation, as illustrated by the TEM micrographs and the corresponding electron diffraction patterns given in Figure 92 and by the table given on page 149.

(ii) disruption by solid particles suspended within the alloy, as illustrated by the SEM micrographs given in Figures 132 and 134.

The effects are to generate stresses which continuously disrupt the oxide film, so that the grain growth illustrated by Figure 92 has a reduced influence on oxidation. The stresses generated cannot be accommodated in the film by wrinkling as observed for the alloys of low magnesium content because the oxide is so much thicker and also because it has a relatively low plasticity at low temperatures.

8.4.4. Oxidation of Aluminium-Magnesium Alloys Containing Beryllium with and without Manganese or Zirconium

(a) Alloys in the Solid State

(1) Thermodynamic Considerations

On first consideration, it might be expected that if sufficient beryllium is present in aluminium-magnesium alloys, during oxidation it would oxidise preferentially to form a BeO layer on the alloy surface because (i) the free energy for the formation of BeO is more negative than that for the formation of MgO[193], and (ii) the high diffusivity of beryllium in both aluminium-magnesium alloys and its own oxide due to its small atomic and ionic radii compared with those of aluminium and magnesium[107].

However, if the beryllium content in the aluminium-magnesium alloy is insufficient to produce BeO on the alloy surface, other possible oxide phases that can be expected on alloys in the Al-Mg-Be-Mn-Zr system include Al_2O_3, $MgAl_2O_4$, MgO, MnO and ZrO_2. The formation of MnO and ZrO_2 is unlikely because their free energies of formation are less than those for the other oxides and because the relatively large ionic radii[47,107] imply slower diffusion through other oxides.

The activities of aluminium and of magnesium in aluminium-magnesium alloys are probably not significantly influenced by the very small additions of beryllium, manganese and zirconium present. Thus, the critical magnesium compositions for the formation of oxides on solid aluminium-magnesium binary alloys, given in Table 17 and in Figure 151 apply also to the solid aluminium-magnesium alloys with small additions of beryllium, beryllium+manganese or beryllium+zirconium. On this basis, if the beryllium content in the alloy is insufficient to produce beryllium oxide, the only thermodynamically favourable oxide on the alloys examined in the present work, i.e. Al-Mg-Be, Al-Mg-Be-Mn and Al-Mg-Be-Zr alloys containing 8% magnesium, is MgO. The

expectation of MgO is confirmed by the results of TEM with electron diffraction and EDX techniques, illustrated in Figure 93, and by the X-ray diffraction spectra, illustrated in Figure 109, for all of the alloys in the temperature range 500-550^{o}C irrespective of the atmosphere. The mechanism of formation of MgO is as described in Section 8.4.1(a).

The formation of BeO seems very unlikely due to very low beryllium activities, i.e. 0.003%, in the present alloys and is supported by the identification of only MgO for all of the alloys, confirming the results reported earlier by Whitaker and Heath[193] who showed using electron diffraction studies that films formed on aluminium-10% magnesium alloys were only MgO if the beryllium content in the alloy was < 0.004%.

(2) Protective Character of the Magnesium Oxide Layer Formed on Solid Al-Mg-Be Alloys

Earlier, Field et al[186] and Hine and Guminski[59], attributed the protective character of oxide films formed on aluminium-magnesium-beryllium alloys to the formation of a protective beryllium oxide layer on the basis of the high oxide/metal volume ratio for pure beryllium, i.e. BeO/Be=7.56/4.5=1.68[193]. It is, of course, fallacious to apply this criteria to beryllium oxide formed on aluminium-magnesium alloys where the volume ratio is much less than unity, e.g. for Al-5% Mg-Be alloy it is 7.56/10.16=0.744. This implies a tensile stress in the oxide and hence it would be non-protective. In addition, if beryllium oxide were to be regarded as protective, an increase of beryllium content in the aluminium-magnesium alloy should confer an increasing protective character to the oxide because the increase of beryllium in the alloy would, of course, lead to the establishment of a more complete beryllium oxide layer on the alloy surface. In fact, the reverse effect has been observed by Whitaker and Heath[193], i.e. the oxide formed on an aluminium-10% magnesium-0.035%

beryllium alloy is less protective than that formed on an aluminium-10% magnesium-0.004% beryllium alloy and this was ascribed to an effect on the mechanical strength (toughness) of oxide film consisting of beryllium oxide or magnesium oxide, or both.

The above argument can be extended to explain the protective character of magnesium oxide formed on the aluminium-8% magnesium-0.003% beryllium alloys in the present work. As discussed in Section 8.4.1(b), magnesium oxide formed on aluminium-magnesium binary alloys is protective according to metal/oxide volume ratio but its integrity was breached under the influence of stresses generated during oxidation. In contrast, the protective character of magnesium oxide film formed on the aluminium-8% magnesium-0.003% beryllium alloy is maintained even with the application of oxidation stresses due to the exceptionally high toughness[193] conferred on the oxide by beryllium absorbed from the alloy.

(3) Influence of Temperature, Manganese or Zirconium Additions, Atmospheric Moisture on the Oxidation Kinetics of Solid Al-Mg-Be Alloys

Examination and analysis of the thermogravimetric results given in Figures 73-78 indicate only one mode of oxidation for solid alloys, irrespective of temperature,manganese or zirconium additions, and atmosphere, i.e.

Mode A : Oxidation gradually diminishing as oxidation proceeds,

identified as before by concavity of parabolic plots with respect to the time axis, as illustrated in Figures 79-84, obtained by replotting the information given in Figures 73-78.

However, oxidation was always higher in the moist atmosphere than that in the dry atmosphere, as illustrated in Figures 73-78.

Another distinct feature of the oxidation kinetics was the effect of the

small additions of manganese or zirconium to aluminium-magnesium-beryllium alloys. Although, there is no clear distinction between the oxidation kinetics at low temperatures, e.g. 500^{o}C, manganese and zirconium promote higher oxidation than when beryllium alone was present in the alloy at the higher temperatures, i.e. 525-550^{o}C, as illustrated in Figures 73-78.

(4) Interpretation of Oxidation Kinetics for Solid Al-Mg-Be Alloys

The mode A oxidation observed on all of the alloys in both dry and moist atmospheres can be explained by the diminishing overall diffusivity through the progressive reduction of grain boundary area by grain growth as explained earlier in Section 8.4.1(d). This is illustrated by the TEM micrographs given in Figure 93. It is noteworthy that no initial or subsequent nucleation of tertiary magnesium oxide particles were observed as for solid aluminium-magnesium binary alloys. (Note: the white areas, illustrated in Figures 135-137 are not, in fact, particles of tertiary magnesium oxide but areas indicating partial detachment of the coherent film from the substrate).

The faster oxidation rate observed on alloys with manganese or zirconium can be explained by an increase of cation vacancy population due to enhanced extrinsic character of the oxide by the injection of Mn^{4+} or Zn^{4+} ions as described for solid aluminium-magnesium binary alloys in Section 2.3.5(b), because no disruptive effects due to cracks promoting nucleation of tertiary magnesium oxide were observed in the oxide films as evident from the SEM micrographs given in Figures 135-137. The effects of manganese and zirconium in these alloys can be assumed to be broadly similar because the alloys with either manganese or zirconium exhibited generally similar oxidation kinetics.

Unfortunately, the beryllium, manganese or zirconium in the oxide film

which causes these effects, could not be detected by the available X-ray diffraction, and TEM with electron diffraction and EDX techniques, as illustrated respectively in Figure 109 and Figure 93. This implies that these elements are present in the oxide at concentrations below the level of detection by above techniques, i.e.< 1%.

The initial faster oxidation rate and the eventual similar oxidation rate in the moist atmosphere in comparison with the dry atmosphere, i.e. higher oxidation throughout, can be explained by the more rapid diffusion of the mobile Mg^{2+} ions due to the enhanced cationic character of the oxide while the film is thin, an effect which diminishes to exhibit similar oxidation rates in both atmospheres as the film thickens and the oxide/atmosphere interface recedes from the alloy surface.

As illustrated in Figures 135-137, no tertiary magnesium oxide particles were observed during the progressive *oxidation in the dry atmosphere*, as were observed for solid aluminium-magnesium binary alloys; hence the eventual oxidation rate in the dry atmosphere is similar to that in the moist atmosphere.

(b) Alloys in the Liquid State

(1) Thermodynamic Considerations

By the same argument, as advanced for the solid alloys in Section 8.4.4.a (1), the thermodynamically favourable oxides on liquid alloys in the Al-Mg-Be-Mn-Zr system are expected to be Al_2O_3, $MgAl_2O_4$ and MgO. Reference to Table 17 and Figure 152 shows that the oxide expected on Al-Mg-Be, Al-Mg-Be-Mn, and Al-Mg-Be-Zr alloys containing 8% magnesium is MgO. This is confirmed by the results of TEM with electron diffraction and EDX techniques, as illustrated in Figures 94-95 and by the X-ray diffraction spectra as illustrated in Figure 110. The mechanism of formation of MgO is as described in Section 8.4.1(a).

(2) Protective Character of the Magnesium Oxide Layer Formed on Liquid Al-Mg-Be Alloys

The TEM micrographs and corresponding electron diffraction patterns given in Figures 94-95 show that both amorphous and crystalline forms of magnesium oxide were observed. The initial oxidation product was always amorphous and when it was observed, the crystalline form appeared later as the transformation product.

The amorphous magnesium oxide film is more protective than its crystalline form, according to the discussion in Section 8.4.2(b). Since the presence of beryllium in the alloy is expected to toughen the oxide[193], the amorphous magnesium oxide film formed on these alloys is more protective than that formed on corresponding aluminium-magnesium binary alloys. By similar argument, the crystalline magnesium oxide film formed is also more protective than that formed on aluminium-magnesium binary alloys.

A quantitative test was carried out to illustrate the relative mechanical strengths of the oxides formed on the liquid aluminium-8% magnesium-0.003% beryllium alloy and the aluminium-8% magnesium binary alloy (without beryllium), confirming that the oxide film on the aluminium-8% magnesium-0.003% beryllium alloy is much tougher than that formed on aluminium-8% magnesium binary alloy. In this test, a standard sample from both alloys was oxidised under the same experimental conditions using the microbalance. After about 20 min oxidation at 675^{o}C, i.e. before breakaway oxidation of the aluminium-8% magnesium alloy, the oxidised samples were transferred on to a preheated asbestos sheet. During the transfer of the aluminium-8% magnesium alloy sample, the protected oxide cracked in several places and the liquid metal exuded via the cracks. In contrast, during the same process the oxide covering the aluminium-8% magnesium-0.003% beryllium sample remained uncracked protecting the liquid metal

inside and moreover, the sample could be rolled over the asbestos sheet several times during which the oxide enveloped the liquid without any cracking. The aluminium-8% magnesium-0.003% beryllium samples with oxide films formed after 1,2, and 3h oxidation, i.e. before breakaway oxidation, were also tested in similar manner and showed the same effect.

The overall protective character of both amorphous and crystalline magnesium oxide films formed on the alloys containing manganese or zirconium, depends on the ability of these elements to degrade the high mechanical strength of oxide rendered by beryllium absorbed from the alloy.

(3) Influence of Temperature, Manganese or Zirconium Additions, Atmospheric Moisture on the Oxidation Kinetics of Liquid Al-Mg-Be Alloys

The examination and analysis of the thermogravimetric results *given in* Figures 73-78, indicate two distinct modes of oxidation for liquid alloys, i.e.

Mode A : Oxidation gradually diminishing as oxidation proceeds.

Mode C : Oxidation diminishing at first but transforming to an accelerating rate after an incubation period

As before, mode A oxidation is identified by the concavity of parabolic plots with respect to the time axis, whereas mode B oxidation is identified by concavity and convexity of parabolic plots respectively during incubation and breakaway oxidation. These plots are illustrated in Figures 79-84, obtained by replotting the information given in Figures 73-78.

The tendency towards mode A or mode C oxidation followed the pattern below:

Temperature ^{o}C	Atmosphere	Be	Be+Mn	Be+Zr
625	dry	A	A	A
650	dry	A	A	A
675	dry	A	A	A
700	dry	A	C	C
725	dry	C	C	C
625	moist	A	A	A
650	moist	A	A	A
675	moist	A	A	C
700	moist	C	C	C
725	moist	C	C	C

This shows that mode A is the more probable mode of oxidation while mode C oxidation is favoured by high temperature, the presence of manganese or zirconium in the alloy and to a lesser extent a moist atmosphere.

The oxidation kinetics are always higher, (i) for alloys with manganese or zirconium irrespective of mode of oxidation and of atmosphere as illustrated in Figures 73-78; zirconium is more effective than manganese in this respect, and (ii) for alloys oxidised in the moist atmosphere.

Moreover, as for liquid aluminium-magnesium binary alloys, the oxidation rate exhibited an *inverse* relationship with temperature for a range of about 55-80^{o}C, above the liquidus temperature, as illustrated by Figures 73-78.

(4) Interpretation of Oxidation Kinetics for Liquid Al-Mg-Be Alloys

As for aluminium-magnesium binary alloys, mode A oxidation can be explained by the initial formation of amorphous magnesium oxide which gradually transforms to its crystalline form as oxidation proceeds, illustrated by

the sequence of TEM micrographs and corresponding electron diffraction patterns given in Figure 94. Although no explanation can be advanced for the concavity of the parabolic plots while the film is amorphous, the concavity when the film is crystalline is explained by grain growth of the oxide, as illustrated in Figure 94. The exceptional feature of these alloys is that crystallisation does not trigger breakaway oxidation at lower temperatures and thus the alloys exhibited mode A oxidation, as apparent from the SEM micrographs given in Figure 138 which shows only wrinkling of the oxide without cracking or nucleation of tertiary magnesium oxide during the 3h period of oxidation. This can be ascribed to the enhanced mechanical strength of the oxide in comparison with the aluminium-magnesium binary alloys.

The inverse relationship of oxidation rate with temperature above the liquidus temperature can be explained by wrinkling of the oxide film, evident from the SEM micrographs given in Figure 138, as discussed in Section 8.4.2(d).

In mode C oxidation, the incubation period before breakaway oxidation commences can be explained by the existence of either or both amorphous and crystalline magnesium oxide, as explained for mode A oxidation. This is illustrated by the TEM micrographs with corresponding electron diffraction patterns given in Figure 94. Breakaway oxidation can be explained by cracking of the oxide film with the subsequent development of tertiary magnesium oxide with pores and blisters in the alloy leading to "cauliflower" growths, as explained for liquid aluminium-magnesium binary alloys in Section 8.4.2(d). This is illustrated by the Optical and SEM micrographs given in Figures 150 and 139-140 respectively.

Manganese or zirconium in the alloy increases the oxidation rate in mode A and promotes mode C oxidation and early breakaway, as illustrated in

Figures 73-78. This may be due to the combined effect of (i) enhanced diffusivity promoted by the injection of Mn^{2+}, Mn^{4+} or Zr^{4+} ions into the oxide[53,56], as explained in Section 7.3.5(b), and (ii) degradation of the mechanical strength of the oxide by the presence of Mn^{2+}, Mn^{4+} or Zr^{4+} ions of large ionic radii[47,107] in the oxide causing stresses; zirconium is more effective than manganese in this respect. However, as observed for solid alloys, the above effect is not sufficient to promote cracking of the oxide at the lower temperatures, so that the alloys exhibited mode A oxidation.

The higher oxidation observed in the moist atmosphere for mode A oxidation is explained by the argument advanced for mode A oxidation for solid aluminium-magnesium-beryllium alloys in Section 8.4.4.a(4). The higher oxidation with shorter incubation times, greater disturbance to oxide films and larger "cauliflower" growths observed for mode C oxidation in the moist atmosphere can be explained by effects due to injection of OH^- ions into the oxide film, as explained for liquid aluminium-magnesium binary alloys in Section 8.4.2(d). This is evident by examination of the SEM micrographs given in Figures 139-140 and of the optical micrographs given in Figure 150.

(c) Alloys in the Semi-Liquid State

(1) Thermodynamic Considerations

Again, it is logical to assume that the only thermodynamically favourable oxide expected on Al-8% Mg-0.003% Be alloys is MgO. This is confirmed by the results of TEM with electron diffraction and EDX techniques and by the X-ray diffraction spectra given respectively in Figures 96-97 and 111-112.

(2) Protective Character of the Magnesium Oxide Layer Formed on Semi-Liquid Al-Mg-Be Alloys

The arguments follow the same themes as discussed in Section 8.4.3(b) for semi-liquid aluminium-magnesium binary alloys, i.e. the oxide is expected to be a composite of amorphous and crystalline magnesium oxide. This is evident from the TEM micrographs and corresponding electron diffraction patterns given in Figures 96-97. As oxidation proceeded, the whole film crystallised in a short period, as indicated in the table below which applies to the aluminium-8% magnesium-0.003% beryllium alloy.

Atmosphere	Liquid Fraction	
	< 50%	> 50%
Dry	∿ 8 min at 575°C	∿ 30 min at 610°C
Moist	∿ 5 min at 575°C	∿ 20 min at 610°C

Thus, it is clear from the table that the effectiveness of crystalline nuclei on solid fractions in promoting the crystallisation of amorphous oxide is dependent on the relative proportions of solid and liquid phases and on the atmosphere. The wholly liquid alloys containing beryllium differ from the corresponding aluminium-magnesium binary alloys in that the crystalline magnesium oxide formed on wholly liquid aluminium-magnesium-beryllium alloys is protective due to the high mechanical strength of the oxide. Thus it is reasonable to assume that the crystallisation of the films formed on these alloys alone does not disrupt the oxide film unless other factors such as discontinuities at the solid/liquid interfaces and the formation of blisters in the alloy, particularly at these interfaces[185] play a significant role simultaneously.

(3) Influence of Temperature, Manganese or Zirconium Additions, Atmospheric Moisture on the Oxidation Kinetics of Semi-Liquid Al-Mg-Be Alloys

Examination and analysis of the thermodynamic results given in Figures 73-78 indicate two distinct modes of oxidation for the semi-liquid alloys, i.e.

Mode A : Oxidation gradually diminishing as oxidation proceeds.

Mode B : Oxidation temporarily diminishing and later transforming to either a steady or an accelerating rate

Mode A and mode B oxidation were identified respectively by concavity and convexity of parabolic plots with respect to the time axis given in Figures 79-84, obtained by replotting the information given in Figures 73-78.

The tendency towards mode A or mode B oxidation followed the pattern below:

Temperature ^{o}C	Atmosphere	Be	Be+Mn	Be+Zr
575	dry	A	A	A
600	dry	A	A	B
610	dry	A	B	B
575	moist	A	A	B
600	moist	A	B	B
610	moist	B	B	B

This reveals that mode B oxidation is favoured by high temperature, the presence of manganese or zirconium and the moisture in the atmosphere.

The other distinctive feature is that oxidation is always higher (i) for alloys with manganese or zirconium, as illustrated in Figures 73-78; zirconium has a greater stimulus in this respect,and (ii) for alloys

oxidised in the moist atmosphere.

(4) Interpretation of Oxidation Kinetics for Semi-Liquid Al-Mg-Be Alloys

Following the explanation in Section 8.4.3(d) for semi-liquid Al-Mg binary alloys, it is expected that if the liquid fraction of these alloys is < 50% or > 50%, they adopt oxidation behaviour similar to wholly solid or wholly liquid alloys respectively in a particular atmosphere. The factors which determine mode A oxidation are essentially similar to those for wholly solid alloys, as explained in Section 8.4.4.a(4). Mode B oxidation can be explained by the initial formation of a protective coherent film, i.e. without any nucleation of tertiary magnesium oxide particles, which during eventual oxidation promotes the nucleation and growth of tertiary magnesium oxide which is the major influence on eventual oxidation.

The higher oxidation observed in the moist atmosphere for all of the alloys having a liquid fraction (i) < 50%, is due to the injection of OH^- ions into the oxide, as explained for wholly solid Al-Mg-Be alloys in Section 8.4.4.a(4), and (ii) > 50%, is due to the injection of OH^- ions with consequent effects, as explained for wholly liquid alloys in Section 8.4.4.b(4).

For convenience, the alloys are considered in three groups, (i) the alloy without manganese and zirconium, (ii) the alloy with 0.24% manganese, and (iii) the alloy with 0.12% zirconium.

Al-8% Mg -0.003% Be alloy

The oxidation rate for this alloy was directly proportional to the temperature in both dry and moist atmospheres, so that the highest oxidation was observed at the highest semi-liquid temperature.

Alloy samples oxidised yielding < 50% liquid exhibited mode A oxidation in both atmospheres because the dominant feature is grain growth of the oxide, since neither cracking nor tertiary magnesium oxide is observed even along magnesium enriched grain boundaries of the samples, as manifest from the TEM micrographs with corresponding electron diffraction patterns given in Figure 96 and from the SEM micrographs given in Figure 141. This is because the oxide is tougher than that formed on the corresponding aluminium-magnesium binary alloys.

Samples oxidised yielding > 50% liquid exhibited mode A and mode B oxidation in the dry and moist atmospheres respectively. This is evident from the TEM micrographs and corresponding electron diffraction patterns given in Figure 97 and from the SEM micrographs given in Figure 142, i.e. in the dry atmosphere, the dominant feature is grain growth, since only wrinkling of the oxide is observed instead of cracking and of tertiary magnesium oxide, while in the moist atmosphere the dominant feature is cracking of the oxide nucleating tertiary magnesium oxide.

Al-8% Mg -0.003% Be -0.24% Mn alloy

This alloy also exhibited a direct relationship between oxidation rates and temperature in both dry and moist atmospheres, so that the highest oxidation was observed at the highest semi-liquid temperature.

Samples yielding < 50% liquid exhibited mode A oxidation in both atmospheres because the dominant feature is grain growth, since little or no tertiary magnesium oxide is observed respectively in moist and dry atmospheres. This is illustrated by the TEM micrographs and corresponding electron diffraction patterns given in Figure 96 and by the SEM micrographs given in Figure 143.

Samples yielding > 50% liquid exhibited mode B oxidation in both atmospheres because the dominant feature is the formation of tertiary magnesium

oxide densely over the sample, as illustrated by the SEM micrographs given in Figure 144, so that grain growth as illustrated in Figure 97 has a minor influence on oxidation kinetics.

The role of manganese in stimulating oxidation can be ascribed to the degradation of the mechanical strength of oxide throughout the semi-liquid range, as explained in Section 8.4.4.b(4) for wholly liquid alloys; the tertiary magnesium oxide, assumed to nucleate via cracks, was observed both in the grains and along the grain boundaries which did not appear for alloys with beryllium alone as evident from a comparison of the SEM micrographs given in Figures 141-142 with Figures 143-144.

Al-8% Mg -0.003% Be -0.12% Zr alloy

An exceptional feature of this alloy is that it exhibited the highest oxidation in both atmospheres when the liquid fraction in the sample is $\sim$ 50%. This behaviour can be attributed to the poor mechanical strength of the oxide arising from its composite character, as illustrated by the SEM micrographs given in Figure 146 which show the appearance of a weak friable oxide film with a dense distribution of tertiary magnesium oxide from the beginning of oxidation.

Samples yielding < 50% liquid exhibited mode A and mode B oxidation in dry and moist atmospheres respectively. This is because in the dry atmosphere, the dominant feature is grain growth of the oxide, since little tertiary magnesium oxide was observed over the sample, as illustrated by the SEM micrograph given in 145(a). In the moist atmosphere, the dominant feature is a dense distribution of tertiary magnesium oxide over the sample over-riding the effect of grain growth, as illustrated by the SEM micrograph given in Figure 145(b).

Samples yielding > 50% liquid exhibited mode B oxidation in both atmospheres which can be explained in the same way as mode B oxidation for the

same alloy with < 50% liquid in the moist atmosphere, as evident from the SEM micrographs given in Figure 147.

It appears that the presence of zirconium in the alloy is detrimental to the mechanical strength of the oxide throughout the semi-liquid range, as explained in Section 8.4.4.b(4) for wholly liquid alloys, so that the alloy exhibited higher oxidation rates than those with and without manganese. This is manifest by a dense distribution of tertiary magnesium oxide over the samples, as illustrated by the SEM micrographs given in Figures 145-147 in contrast with the corresponding micrographs for alloys with and without manganese, given in Figures 143-144 and 141-142 respectively.

CONCLUSIONS

1. Magnesium oxide, MgO, is the only oxidation product formed in moist oxygen/helium mixtures on binary aluminium-magnesium alloys in the temperature range 500-725^{o}C.

2. The solid alloys form crystalline MgO films which may or may not be protective. Protective films are favoured by low temperature, low magnesium content and moist atmospheres. The loss of protection is due to disruption of the film by continuous nucleation and growth of new MgO nuclei within the initially-formed coherent film.

3. The liquid alloys initially form amorphous MgO films which are always protective. The onset of crystallisation after an induction period disrupts the film and induces breakaway oxidation. Susceptibility to crystallisation is promoted by high magnesium content, high temperatures and moist atmospheres. A curious feature is an inverse relationship between oxidation rate and temperature just above the liquidus temperatures due to the development of an undulating morphology induced by growth stresses.

4. Semi-liquid alloys with > 50% solid phase adopt oxidation kinetics similar to those of wholly solid alloys but the oxidation rates are always faster than those for wholly solid alloys due to preferential oxidation of magnesium-enriched liquid fractions along grain boundaries.

5. Semi-liquid alloys with > 50% liquid phase adopt oxidation kinetics similar to those of wholly liquid alloys but the protective amorphous film formed on the liquid phase crystallises almost immediately on nuclei pre-existing on the solid phase particles promoting rapid initial oxidation.

6. In general, moisture in the atmosphere accelerates the inherent oxidation rate but this effect can be over-ridden on solid alloys by reduced susceptibility to film diruption.

7. The effect of beryllium additions is to reduce the oxidation rate markedly by increasing the mechanical strength of the oxide film. In particular, it delays breakaway oxidation on wholly liquid alloys.

8. Small manganese or zirconium additions to aluminium-magnesium-beryllium alloys to some extent offset the beneficial effect of beryllium additions by degrading the mechanical strength of the oxide film.

10. INDUSTRIAL APPLICATIONS AND SUGGESTIONS FOR FURTHER WORK

10.1 Industrial Applications

Some of the observations made in the present investigation have an industrial significance in suggesting the most effective approach to commercial melting practice to minimise dross formation.

Figures 51-60 show that the most rapid initial oxidation rates are experienced (i) for Al-1, 3 and 5% magnesium alloys, when the alloys are semi-liquid with > 50% liquid phase, i.e. at temperatures approaching the liquidus temperatures, and (ii) for aluminium-7 and 9% magnesium alloys when the alloys are semi-liquid with > 50% liquid phase and are wholly liquid but just above the liquidus temperatures, i.e. at temperatures just below and above the liquidus temperatures. It has further been shown that slow heating rates up to 350^{o}C can lead to the development of thick alumina layers on the solid alloy surfaces increasing the probability of subsequent formation of $MgAl_2O_4$ spinel causing catastrophic oxidation. It is, therefore, advantageous to melt secondary metal as rapidly as possible from room temperature to reduce the exposure period in these detrimental temperature ranges, particularly if the section is thin, e.g. as for can stock. Since oxidation in a moist atmosphere is always initially higher for the temperatures investigated, i.e. 500-725^{o}C, an even better method is to melt the metal out of contact with air which almost invariably contains moisture. It is probably for these reasons that submerging the scrap metal beneath the surface of the liquid metal once a molten metal pool is available, has been found empirically successful in controlling dross formation.

Figures 51-60 also reveal that when the alloys are wholly molten, the initial oxidation often reverts to a much lower value with a long incubation period before breakaway. It is, therefore, beneficial to melt the

metal rapidly and hold it before casting at a temperature selected to maximise the incubation period before rapid oxidation by breakaway ensues. As Figures 51-60 show, the safest holding temperatures for aluminium-1,3, 5,7 and 9% magnesium alloys are 700-725^{o}C, 700-725^{o}C, 675-700^{o}C, 675^{o}C and 675^{o}C respectively.

The oxidation behaviour of aluminium-8% magnesium-0.003% beryllium alloys with or without manganese or zirconium are broadly similar to that of an aluminium-3% magnesium binary alloy. Hence in principle it would be useful to adopt the same melting procedure prescribed for binary alloys without beryllium, the safest holding temperatures being 675-700^{o}C as shown in Figures 73-78. Unfortunately, the use of beryllium is prohibited in most countries due to its toxicity.

10.2 Suggestions for Further Work

There are many areas in the oxidation of aluminium-magnesium alloys which require further investigation. Further work should be focused on:

(1) Measurements of the plasticity and the mechanical properties of the oxides formed.

(2) Investigation of the mechanisms of surface wrinkling and corrugation, "cauliflower" growths of oxide, and blistering and pore formation in the liquid substrate.

(3) Evaluation of isothermal oxidation kinetics as a function of heating rates to simulate melting in a real furnace.

(4) Measurements of diffusion coefficients for Mg^{2+} and O^{2-} ion species in a growing magnesium oxide film on aluminium-magnesium alloys in both dry and moist atmospheres to determine the positions of growth interfaces.

(5) Investigation of possible alternatives to beryllium to improve the mechanical strength of the magnesium oxide films.

(6) Application of sensitive microbalance techniques to measure isothermal oxidation in aggressive environments containing additives such as chlorides, fluorides, sulphur dioxide and hydrogen sulphide.

------oOo------

REFERENCES

1. E.A. Starke, Material Sci. and Eng., 29 (1977) 99.
2. Battelle Memorial Institute, "Magnesium Losses in Aluminium Industry", Columbus, Ohio, Dec. (1975).
3. S.J. Walton, Sales Dept., Magnesium Elektron Ltd., P.O. Box 8, Swinton, Manchester.
4. G.J. Binczewski, Light Metal Age, Oct. (1978) 24.
5. R. Jay and A. Cibula, Foundry Trade J., Oct. (1956) 407.
6. L. David, Light Metal Age, Jan. (1955).
7. D.G. Ives, "Chemical Thermodynamics", Mcdonald, London, 1971.
8. N. Birks, and G.H. Meier, "Introduction to High Temperature Oxidation of Metals", Edward Arnold, London, 1983.
9. L.I. Osipow, "Surface Chemistry - Theory and Industrial Application", Reinhold, New York, 1963.
10. J. Oudar, "Physics and Chemistry of Surfaces", Blackie and Sons, Glasgow, 1975.
11. D.M. Young and A.D. Crowell, "Physical Adsorption of Gases", Butterworths, London, 1962.
12. D.O. Hayward and B.M. Trapnell, "Chemisorption", Butterworths, London, 1964.
13. G. Ehrlich, J. Phys. Chem. Solids, 1 (1956) 1.
14. R. Gomer, "Field Emission and Field Ionization", Harvard University Press, Cambridge, Mass. 1961.
15. A.U. Macrae, "Techniques for Studying Clean Surfaces", Surfaces and Interfaces, 1, ed. Burke, Reed and Weiss, New York, Syracuse Univ. Press, 1967.
16. G. Wedler, "Chemisorption - An Experimental Approach", translated by D.F. Klemperer, Butterworths, London, 1976.
17. H.E. Farnsworth and J. Tuul, J. Chem. Solids, 1 (1958) 48.
18. L.H. Germer and A.U. Macrae, J. Chem. Phys., 36 (1962) 1955.
19. A.U. Macrae, Surf. Sci., 1 (1964) 319.
20. H. Richter and U. Gerhardt, Phys. Rev. Lett., 51 (1983) 1570.
21. D.O. Hayward, "Chemisorption and Reactions on Metallic Films", Vol. 1, ed. J. Anderson, London, Academic Press, 1971.
22. T.A.H. Lanyon and B.M. Trapnell, Proc. Roy. Soc., (A) 227 (1955) 387.
23. C.T. Kirk and E.E. Huber, Surf. Sci., 9 (1968) 217.

24. J.W. May, Surf. Sci., 18 (1969) 431.

25. F.P. Fehlner and N.F. Mott, Oxid. Metals, 2 (1970) 59.

26. J. Bardolle and J. Benard, C.R. Acad. Sci., 232 (1951) 231.

27. F. Gronlund, J. Chim. Phys. 53 (1956) 660.

28. R.K. Hart and J.K. Maurin, Surf. Sci., 20 (1970) 285.

29. B.E. Hayden, D.F. Klemperer, C. Allen and P. Tucker, Supply. Proc. Int. Conf. Solid Surf. 4th, (1980) 453.

30. J. Benard, Metallurgical Rev., 9 (1964) 473.

31. F.W. Young, Acta Met., 8 (1960) 117.

32. W.H. Orr, "Oxide Nucleation and Growth", Thesis, Cornell University, U.S.A., 1962.

33. D. Hull, "Introduction to Dislocations", Pergamon Press, London, 1975.

34. P. Kofstad, "High Temp. Oxidation of Metals", John Wiley, New York, 1972.

35. F.A. Kroger, "The Chemistry of Imperfect Crystals", North-Holland Pub. Amsterdam, Vol. (1-4), 1974.

36. Z.M. Jarzebski, "Oxide Semiconductors", Pergamon Press, London, (1975) 66.

37. L.L. Shreir, "Corrosion", George Newnes, London, Vol. 1, 1976.

38. F.A. Kroger and J. Vink, "Solid State Physics", ed. F. Seitz and D. Turnbell, Academic Press, New York, (1956) 307.

39. W. Schottky. Z. Phys. Chem., (B) 29 (1935) 335.

40. W. Jost, Trans. Faraday Soc., 34 (1938) 860.

41. J. Frenkel, Z. Phys., 35 (1926) 652.

42. D. Wadsley, Advan. Chem. Ser., 39 (1963) 23.

43. J.S. Anderson, Pro. NPL Sympos., No. 9, 1958.

44. C. Wagner and K. Grunewald, Z. Phys. Chem., (B) 40 (1938) 455.

45. C. Wagner, Z. Phys. Chem., (B) 22 (1933) 181.

46. S.P. Mitoff, J. Chem. Phys., 36 (1962) 1383.

47. M.O. Davies, J. Chem. Phys., 38 (1963) 2047.

48. H. Schmalzried, J. Chem. Phys., 33 (1960) 940.

49. G.H. Reiling and E.B. Hensley, Phys. Rev., 112 (1958) 1106.

50. D.R. Sempolinski, W.D. Kingery and L. Tuller, J. Amer. Cer. Soc., 63 (1980) 669.

51. R. Lindner and G.D. Parfitt, J. Chem. Phys., 26 (1957) 182.

52. Y. Oishi and W.D. Kingery, J. Chem. Phys., 33 (1960) 905.

53. W. Weigelt and G. Haase, Ber. Deut. Keram. Ges. 31 (1954) 45.

54. A. Lempicki, Proc. Phys. Soc. (London), (B) 66 (1953) 281.

55. J. Lewis and A. Wright, High Temp., 5 (1967) 454.

56. A.M. Glass, J. Chem. Phys., 46 (1967) 2076.

57. A.M. Glass and T.M. Searle, J. Chem. Phys., 46 (1967) 2092.

58. H.B. Johnsen, O.W. Johnsen and I.B. Cutler, J. Amer. Cer. Soc., 49 (1966) 390.

59. R.A. Hine and R.D. Guminski, J. Inst. Metals, 89 (1960-61) 417.

60. M. Whitaker, Foundry Trade J., Aug. (1953) 195.

61. C.F. Cline and H.W. Newkirk, J. Chem. Phys., 49 (1968) 3496.

62. J. De Bruin, G.M. Watson and C.M. Blood, J. Appl. Phys., 37 (1966) 4543.

63. R.H. Condit and Y. Hashimoto, J. Amer. Cer. Soc., 15 (1967) 425.

64. S.B. Austerman and W. Wagner, J. Amer. Cer. Soc., 49 (1966) 94.

65. C.F. Cline, J. Carlberg and H.W. Newkirk, J. Amer. Cer. Soc., 50 (1967) 55.

66. B. Holt, J. Nucl. Mat., 11 (1961) 107.

67. K. Wefers and G.M. Bell, Alcoa Technical Paper, No. 19, 1972.

68. M.S. Hunter and P. Fowle, J. Electrochem. Soc., 103 (1956) 482.

69. R. Dholiwar, "Oxidation of Pure Liquid Aluminium", Ph.D. Thesis, Brunel University, London, 1984.

70. W.E. Verwey, J. Chem. Phys., 3 (1935) 592.

71. J. Cohen, Bull. Amer. Cer. Soc., 38 (1959) 441.

72. J. Pappis and W.D. Kingery, J. Amer. Cer. Soc., 44 (1961) 459.

73. P.J. Harrop and R.H. Creamer, Brit. J. Appl. Phys., 14 (1963) 335.

74. J.A. Champion, Brit. J. Appl. Phys., 15 (1964) 633.

75. M.O. Davies, NASA TN D-2765, 1965.

76. H. Schmalzried, Z. Physik. Chem., 38 (1963) 87.

77. D. Peters, J. Phys. Chem. Solids, 27 (1966) 1560.

78. J. Matsumura, Can. J. Phys., 44 (1966) 1685.

79. J.W. Verwey and E.L. Heilmann, J. Chem. Phys., 15 (1947) 174.

80. E. Sonder, J. Amer. Cer. Soc., 66 (1983) 50.

81. P.R. Reddy and A.R. Cooper, J. Amer. Cer. Soc., 64 (1981) 368.

82. K. Ando and Y. Oishi, J. Chem. Phys., 61 (1974) 625.

83. R. Lindner and A. Akerstrom, Z. Physik. Chem., NF6, (1956) 162.

84. J.L. Bates and J.E. Garnier, J. Amer. Cer. Soc., 64 (1981) C-138.

85. C.N. Cochran, D.L. Belitskus and D.L. Kinosz, Met. Trans., (B) 8 (1977) 323.

86. P. Shewmon, "Diffusion in Solids", McGraw Hill, New York, 1963.

87. J. Stark, "Solid State Diffusion", John Wiley, London, 1976.

88. C.P. Flynn, Point Defects and Diffusion, Clarendon Press, Oxford, 1972.

89. J. Crank, "The Mathematics of Diffusion", Oxford Univ. Press, 1975.

90. R. Barrer, "Diffusion in and Through Solids", Cambridge Univ. Press, 1951.

91. A. Fick, Ann. Phys. Lpz., 170 (1855) 59.

92. A. Atkinson and R.I. Taylor, Phil. Mag., (A) 39 (1979) 581.

93. A. Atkinson, R.I. Taylor, and A.E. Hughes, Phil. Mag., (A) 45 (1982) 823.

94. A. Atkinson and R.I. Taylor, Phil. Mag., (A) 43 (1981) 979.

95. A. Atkinson, Rev. Mod. Phys., 57 (1985) 437.

96. D. McLean, "Grain Boundaries in Metals", Clarendon Press, Oxford, 1957.

97. J. Stringer, "Defects and Transport in Oxides", ed. S. Seltzer and I. Jaffe, Plenum Press, New York, (1974) 495.

98. B. Cox, *J. Electrochem. Soc.*, *108* (1961) 24.

99. H.M. Hindam and W.W. Smeltzer, Oxid. Metals, 14 (1980) 337.

100. L.B. Pfeil, J. Iron Ste. Inst., 119 (1929) 501.

101. B.C. Harding, D.M. Price, and A.J. Mortlock, Phil. Mag., 23 (1971) 399.

102. L.H. Rovner, Ph. D. Thesis, Cornell University, U.S.A. 1966.

103. D.R. McKerrzie, A.W. Searcy, J.B. Holt and R.H. Condit, J. Amer. Cer. Soc., 54 (1971) 188.

104. H. Murata, S.C. Choi, K. Koumoto and H. Yanagida, J. Mat. Sci. 20(1985) 4507.

105. J. Rabier and M.P. Puls, Radiation Effects, 75 (1983) 193.

106. A.J. Mortlock, Nat. Bureau Stand., Pub. No. 296, Aug. (1968) 85.

107. B.J. Wuensch and T. Vasilos, Nat. Bureau Stand., Pub. No. 296, Aug. (1968) 95.

108. B.J. Wuensch and T. Vasilos, J. Ame. Cer. Soc., 49 (1966) 433.

109. O. Kubaschewski and B.E. Hopkins, "Oxidation of Metals and Alloys", Butterworths, London, 1967.

110. K. Hauffe, "Oxidation of Metals", Plenum Press, New York, 1965.

111. W.W. Smeltzer and J. Young, Prog. Solid State Chem., 10 (1975) 17.

112. H. Svec and J. Apel, J. Electrochem. Soc., 104 (1957) 346.

113. M.S. Cohen, Acta Met., 8 (1960) 356.

114. B. Lustman and R.F. Mehl, Trans. A.I.M.E., 143 (1941) 246.

115. R.K. Hart, Proc. Roy. Soc., (A) 68 (1956) 236.

116. O. Kubaschewski and D.M. Brasher, Trans. Faraday Soc. 55 (1959) 1200.

117. M. Roberts, Trans. Faraday Soc., 57 (1961) 99.

118. D.A. Vermilyea, Acta Met., 6 (1958) 166.

119. N.F. Mott, Trans, Faraday Soc., 43 (1947) 429.

120. N. Cabrera, Phil. Mag., 40 (1949) 175.

121. N. Cabrera and N.F. Mott, Rep. Prog. Phys., 12 (1948-49) 163.

122. A.T. Fromhold, "Theory of Metal Oxidation", North Holland Pub., Amsterdam, 1976.

123. C. Wagner, Z. Phys. Chem., (B) 21 (1933) 25.

124. T.P. Hoar and L.E. Price, Trans. Faraday Soc., 34 (1938) 867.

125. S.J. Gregg, and W.B. Jepson, J. Inst. Metals, 87 (1958-59) 187.

126. P. Kofstad and S. Espeik, J. Electrochem. Soc., 112 (1965) 153.

127. D.W.Aylmore, S.J. Gregg and W.B. Jepson, J. Electrochem. Soc., 106 (1959) 1010.

128. J. Loriers, Compt. rend., 231 (1950) 522.

129. W.W. Webb, J.T. Norton and C. Wagner, J. Electrochem. Soc., 103 (1956) 107.

130. E.W. Haycock, J. Electrochem. Soc., 106 (1959) 771.

131. D.A. Vermilyea, Acta Met., 5 (1957) 492.

132. W.W. Smeltzer and M.T. Simnad, Acta. Met., 5 (1957) 320.

133. D. Cubicciotti, J. Am. Chem. Soc., 74 (1952) 1200.

134. K.S. Khanna and J.B. Gnanamoorthy, Oxid. Metals, 18 (1982) 315.

135. U.R. Evans, Trans. Electrochem. Soc., 91 (1947) 547.

136. U.R. Evans, Inst. Met. Symp. On Internal Stresses in Metals and Alloys, London, (1947) 219.

137. R.E. Pawel and J.J. Campbell, Acta Met. 14 (1966) 1827.

138. J. Stringer, Corrosion Sci., 10 (1970) 513.

139. B.B. Pilling and R.E. Bedworth, J. Inst. Metals, 29 (1923) 529.

140. B. Borie, Acta Crystallog., 13 (1960) 542.

141. O. Richmond, W.C. Leslie and H.A. Wriedt, Trans. ASM, 57 (1964) 294.

142. W. Jaenicke and S. Leistikow, Z. Phys. Chem., 15 (1958) 175.

143. W. Jaenicke, S. Leistikow and A. Stadler, J. Electrochem. Soc., 111 (1964) 1031.

144. G.B. Gibbs and R. Hales, Corrosion Sci., 17 (1977) 487.

145. P. Hancock and C.R. Hurst, "Mechanical Properties of Oxide Films at Elevated Temp.", ed. W. Stachle and G. Fontana, Plenum Press, New York, 4 (1974) 1.

146. F.N. Rhines and J.S. Wolf, Met. Trans., 1 (1970) 1701.

147. R.F. Tylecote, J. Inst. Metals, 78 (1960) 301.

148. D.P. Whittle and J. Stringer, Phil. Trans. Roy. Soc. London, (A) 295 (1980) 309.

149. I.M. Allam, D.P. Whittle and J. Stringer, Oxid. Metals, 13 (1979) 381.

150. A.W. Funkenbusch, J.G. Sheggil and N.S. Bornstein, Met. Trans., 16 (1985) 1164.

151. D.J. Stephenson and J.R. Nicholls, Personnel Communication, School of Industrial Science, Cranfield Ins. of Tech., Cranfield, Bedford,1985.

152. D.L. Douglass, Oxid. Metals, 1 (1969) 127.

153. R.M. Spriggs and T. Vasilos, J. Amer. Cer. Soc., 47 (1964) 47.

154. B.W. Dunnington, F.H. Beck and M.G. Fontana, Corrosion, 8 (1952) 2.

155. G.W. Groves, Proc. Brit. Cer. Soc., 15 (1970) 103.

156. H. Hensler and G.V. Cullen, J. Amer. Cer. Soc., 50 (1967) 584.

157. J. Stringer, J. Less Common Met., 16 (1968) 55.

158. J.D. Noden, C.J. Knights and M.W. Thomas, Brit. Corros. J., 3 (1968) 47.

159. C. Roy and B. Burgess, Oxid. Metals, 2 (1970) 235.

160. R.B. Jones and G. Willoughby, Personnel Communication to Noden et al (ref. 158), 1966.

161. J.C. Grosskreutz and M.B. McNeil, J. Appl. Phys., 40 (1969) 355.

162. J. Moreau and J. Benard, "L'Oxidation des Metaux", Gauthier - Villars, Paris, 1 (1962) 318.

163. N. Birks and H. Rickert, J. Inst. Metals., 91 (1961-62) 308.

164. J. Stringer, Metallurgical Rev., 11 (1966) 113.

165. J.W. Verwey, W. Haayman, C. Romeijn, Chem. Weekbl 44 (1948) 705.

166. C. Wagner and K.E. Zimens, Acta Chem. Scand., 1 (1947) 547.

167. K. Hauffe and A.L. Vierk, Z. Phys. Chem., (B) 196 (1950) 160.

168. E. Koch and C. Wagner, Z. Phys. Chem., (B) 38 (1937) 295.

169. H.P. Leighly and A. Alam, J. Phys. F: Met. Phys., 4 (1984) 1573.

170. E.A. Gulbransen, Adv. Cataly., 5 (1953) 119.

171. E.A. Gulbransen and Y. Wysong, J. Phys. Colloid. Chem., 51 (1947) 1087.

172. W.W. Smeltzer, J. Electrochem. Soc., 103 (1956) 209.

173. D.W. Aylmore, S.J. Gregg and W.B. Jepson, J. Inst. Metals, 88 (1959) 205.

174. P.E. Blackburn and E.A. Gulbransen, J. Electrochem. Soc., 107 (1960) 944.

175. C.N. Cochran and W.C. Sleppy, J. Electrochem. Soc., 108 (1961) 322.

176. A.F. Beck, M.A. Heine, E.J. Caule and J. Pryor, Corrosion Sci. 7 (1967) 1.

177. R.E. Honig, Review of RCA Laboratory, Princeton, New Jersey, (1957) 195.

178. Y. Suzuki, Bull. Inst. Phys. Chem. Res. (Japan), 15 (1936) 147.

179. E.A. Gulbransen, Trans. Electrochem. Soc., 87 (1945) 589.

180. T.E. Leontis and F.N. Rhines, Trans. A.I.M.E., 166 (1946) 265.

181. J.E. Castle, S.J. Gregg and W.B. Jepson, J. Electrochem. Soc., 109 (1962) 1018.

182. C.E. Nelson, Metals Tech., Oct. (1943) 77.

183. S. Dobinski and M. Niesluehowski, Nature, 144 (1939) 510.

184. W.W. Smeltzer, J. Electrochem. Soc., 105 (1958) 67.

185. L. De. Brouckere, J. Inst. Metals, 71 (1945) 131.

186. D.J. Field, G.M. Scamans and E.P. Butler, Proc. 2nd Int. Conf. on Al-Li Alloys, California, (1983) 393.

187. D.J. Field, E.P. Butler and G.M. Scamans, Proc. 1st. Int. Conf. on Al-Li Alloys, Georgia, (1980) 325.

188. K. Wefers, Aluminium, 57 (1981) 722.

189. C. Lea and J. Ball, Appl. Surf. Sci., 17 (1984) 344.

190. I.M. Ritchie, J.V. Sanders, and P.L. Weiekhard, Oxid. Metals, 3 (1971) 91.

191. A.J. Brock and M.A. Heine, J. Electrochem. Soc., 119 (1972) 1123.

192. G.M. Scamans and E.P. Butler, Met. Trans., (A) 6 (1975) 2055.

193. M. Whitaker and A.R. Heath, J. Inst. Metals, 82 (1953-54) 107.

194. D.J. Field, E.P. Butler and G.M. Scamans, unpublished work, Proc. Conf. Modern Metallography, Birmingham, 1978.

195. M. Drouzy and C. Mascre, Metallurgical Rev., 131 (1969) 25.

196. S. Balicki, Prace. Inst. Hutniczych., 10 (1958) 208.

197. W. Thiele, Aluminium, 38 (1962) 780.

198. D.L. Belitskus, Oxid. Metals, 8 (1974) 303.

199. I. Haginoya and T. Fususako, J. Japan Inst. Light Met., 24 (1974) 364.

200. D.E.J. Talbot, Int. Met. Rev., 20 (1975) 166.

201. D.J. Stephenson, "The Absorption of Hydrogen from Humid Atmospheres by Al and Al-Mg Alloys", Ph.D. Thesis, Brunel University, London, 1978.

202. A. Griror'Eva and V.A. Danilkin, Tsvetn. Met., 1 (1984) 87.

203. R. Eborall and C.E. Ransley, J. Inst. Metals, 71 (1945) 525.

204. C.E. Ransley and H. Neufeld, J. Inst. Metals, 74 (1948) 599.

205. R.A. Swalin, "Thermodynamics of Solids", John Wiley, New York, 1962.

206. L.M. Foster, A. Gillespie, T. Jack and W. Hill, Nucleonics, 21 (1963) 53.

207. D.E.J. Talbot and D.A. Granger, J. Inst. Metals, 92 (1963-64) 290.

208. C.E. Ransley and D.E.J. Talbot, J. Inst. Metals, 88 (1959-60) 150.

209 A.J. Swain, J. Inst. Metals, 80 (1951-52) 125.

210. G.M. Scamans and A.S. Rehal, J. Mat. Sci., 14 (1979) 2459.

211. H. Kostron, Z. Metallkunde, 43 (1952) 269, 373.

212. C.S. Tuck, Proc. 2nd Int. Conf. on Hydrogen Effects in Metals, Wyoming, (1980) 503.

213. L. Montgrain, G.M. Scamans and P.R. Swann, Pro. 3rd Tewkesbury, Sympo. Fract. proce., Melbourne, (1974) 194.

214. T. Malis and M.C. Charturvedi, J. Mat. Sci., 17 (1982) 1479.

215. G. Raynor, "Annotated Equilibrium Diagram Series", Inst. Metals, No. 5, 1945.

216. C.S. Smith, Trans. A.I.M.E., 137 (1940) 236.

217. G. Kollie, L. Horton, R. Car, B. Herskovitz and A. Mossman, Rev. Sci. Instrum., 46 (1975) 1447.

218. W. Kardos, Chem. Eng., Aug. (1977) 79.

219. H. Klug and L. Alexander, "X-ray Diffraction Procedures", John Wiley, New York, 1962.

220. O. Kubaschewski and O.B. Alcock, "Metallurgical Thermochemistry", Pergamon Press, New York, 1979.

221. C. Gatellier and M. Olette, C.r. Acad. Sci., 266 (1968) 1133.

222. J.A. Brown and J.N. Pratt, Met., Trans., 1 (1970) 2743.

223. Y.B. Bhatt and S.P. Garg, Met. Trans, (B) 7 (1976) 271.

224. O. Kubaschewski and J.A. Catterall, "Thermodynamic Properties of Alloys", Pergamon Press, London, 1956.

225. O. Kubaschewski, DCS report, No. 2, 1968.

226. P.D. Anderson, "Selected Values of Thermodynamic Properties of Metals and Alloys", ed. R. Hultgren, University of California, Berkeley, 1958.

227. C. Lea and C. Molinari, J. Mat. Sci., 19 (1984) 2336.

228. P.D. Dankov and P.V. Chuarev, Dokl. Akad. Nauk. SSSR, 73 (1950) 1221.

229. P. Tasker, J. Amer. Cer. Soc., 68 (1985) 74.

230. W.J. Moore, "Physical Chemistry", Longman, London, (1970) 338.

231. M.R. Tahbaz, "Absorption of Hydrogen by Solid Aluminium-Magnesium Alloys from Humid Atmosphere", M. Phil. Thesis, Brunel University, London, 1977.

232. N.F. Mott and A. Davis, "Electronic Processes in Non-Crystalline Materials", Clarendon Press, Oxford, 1979.

233. W.S. Abeysuriya, "Electrical and Optical Properties of CO-Evaporated SiO_x/Ge Films", Ph.D Thesis, Brunel University, London, 1986.

234. R. Chittick, J. Non-Cryst. Solids, 3 (1970) 255.

235. C.J. Smithells, "Metals Reference Book", Butterworths, London, 1983.

236. G. Humpston, "The Constitution of Some Ternary Au-Based Solder Alloys", Ph.D Thesis, Brunel University, London, 1985.

237. J. Goldstein and H. Yakawitz, "Practical Scanning Electron Microscopy", Plenum Press, New York, 1975.

238. W.S. Hearle, T.J. Sparrow and P.M. Cross, "The Use of Scanning Electron Microscope", Pergamon Press, New York, 1972.

239. D. Chescoe and P.J.Goodhew, "The Operation of Transmission Electron Microscope", Oxford Univ. Press, Oxford, 1984.

240. G. Thomas, "Transmission Electron Microscopy of Metals", John Wiley, New York, 1966.

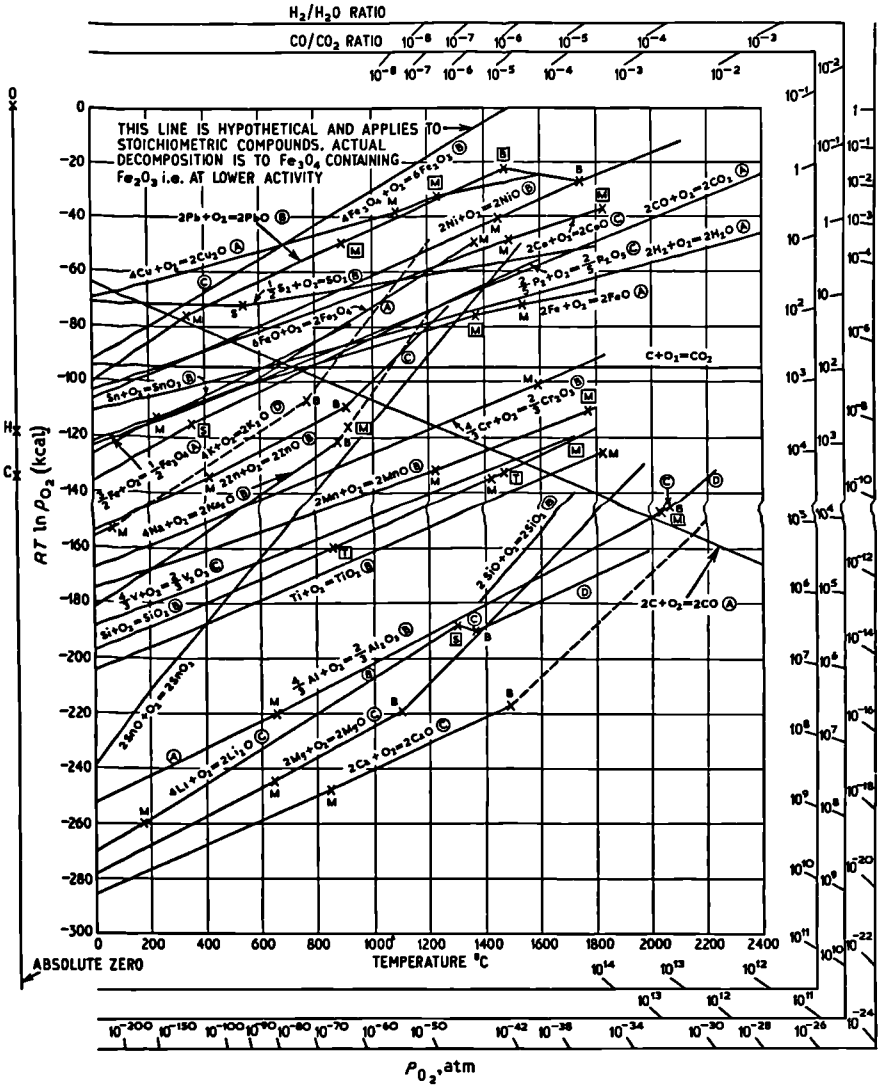

KEY (A) (B) (C) (D) suggested accuracies: ±1 kcal; ±3 kcal; ±10 kcal; ± >10 kcal

M, [M]: melting point, metal, oxide, resp.
B, [B]: boiling point, metal, oxide, resp.
S, [S]: sublimation point, metal, oxide, resp.
T, [T]: transition point, metal, oxide, resp.

Note: 1 kcal ≈ 4·2 kJ

Figure 1. Oxygen potential diagram for formation of oxides.

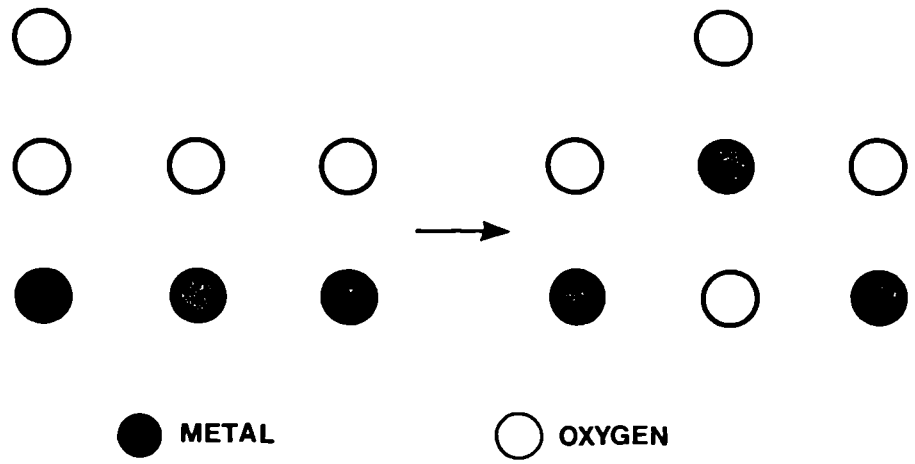

Figure 2. Model of place exchange mechanism during chemisorption of oxygen.

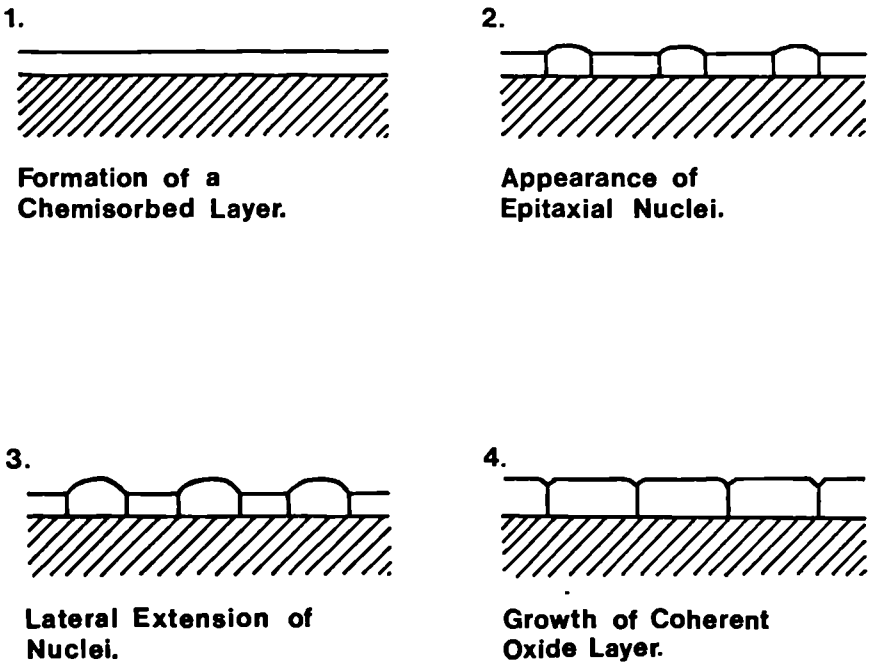

Figure 3. Initial stages of oxidation leading to the formation of a compact layer.

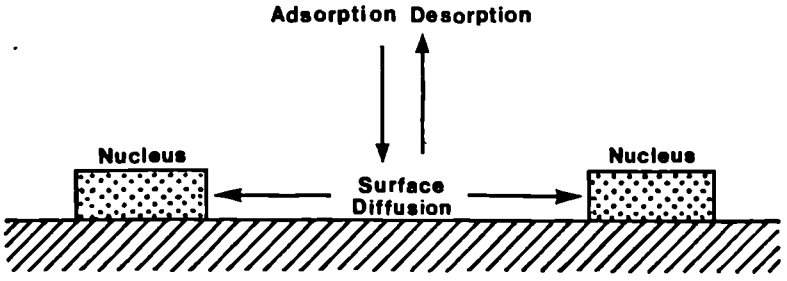

Figure 4. Growth of oxide nuclei.

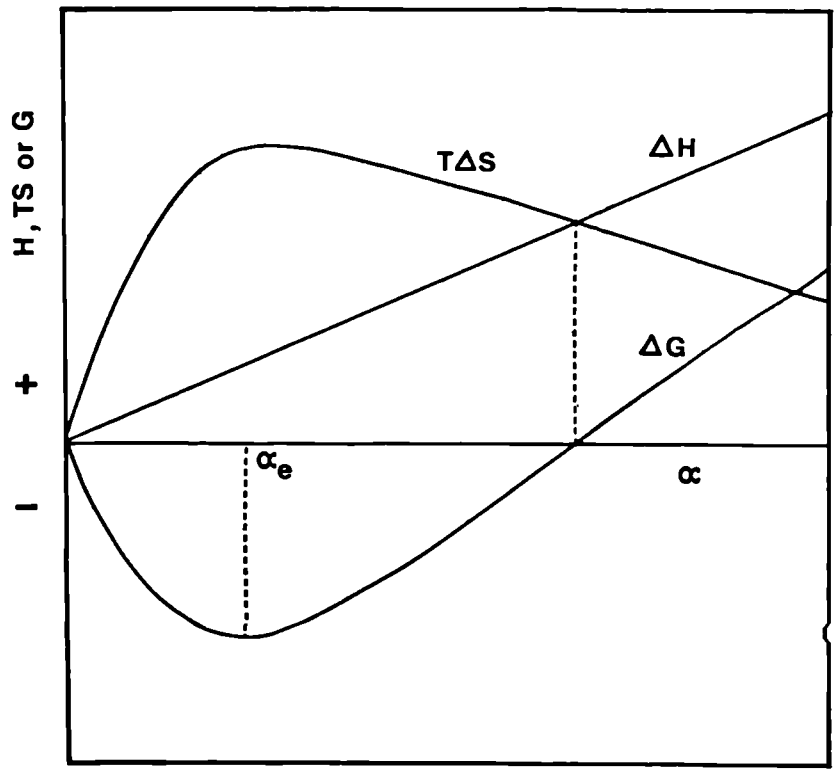

Figure 5. Thermodynamic functions G, H and TS as functions of non-stoichiometry, α.

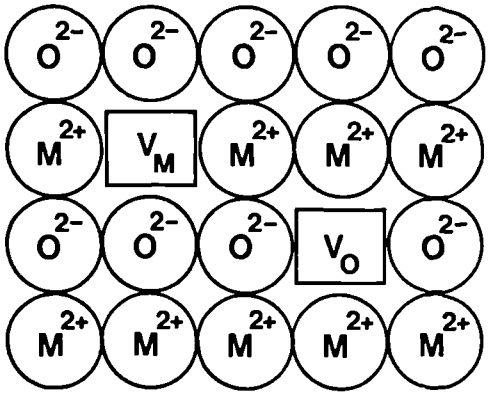

Figure 6. Schematic illustration of Schottky defect structure in an oxide, MO, with equivalent concentrations of doubly charged vacancies of cations, (V_m), and anions (V_o) of about equal size.

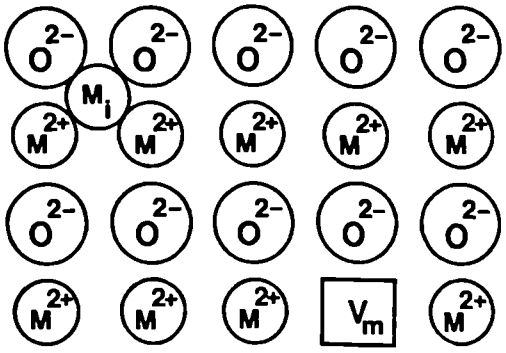

Figure 7. Schematic illustration of Frenkel defect structure in an oxide, MO, with doubly charged cation vacancies, (V_m), and interstitial ions, (M_i), of different sizes.

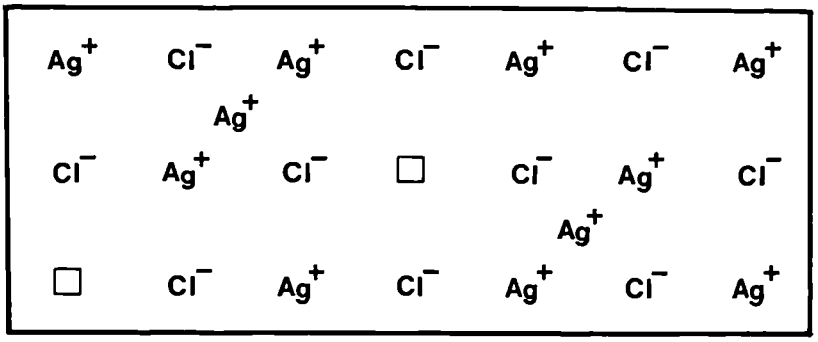

Figure 8. Frenkel defects in an ionic compound, AgCl, in which cations are the most mobile species via cation vacancies.

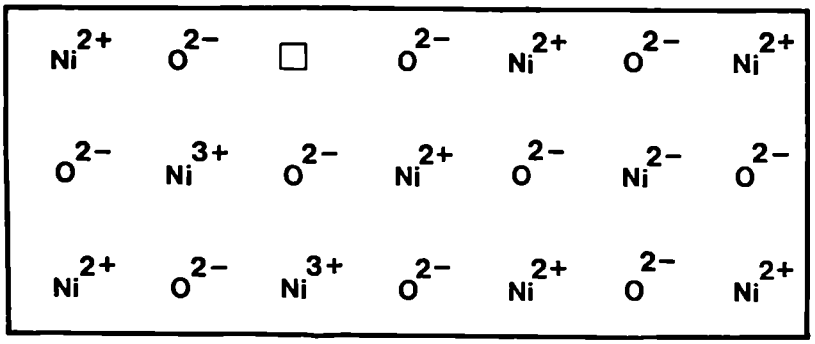

Figure 9. Defects in a p-type oxide with cation vacancies, exemplified by NiO.

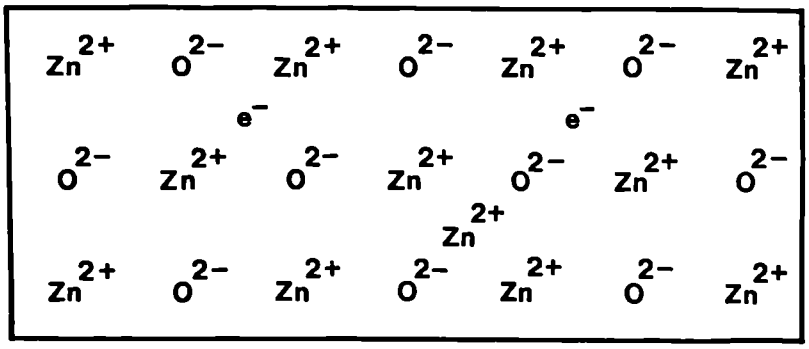

Figure 10. Defects in an n-type oxide with cation interstitials, exemplified by ZnO.

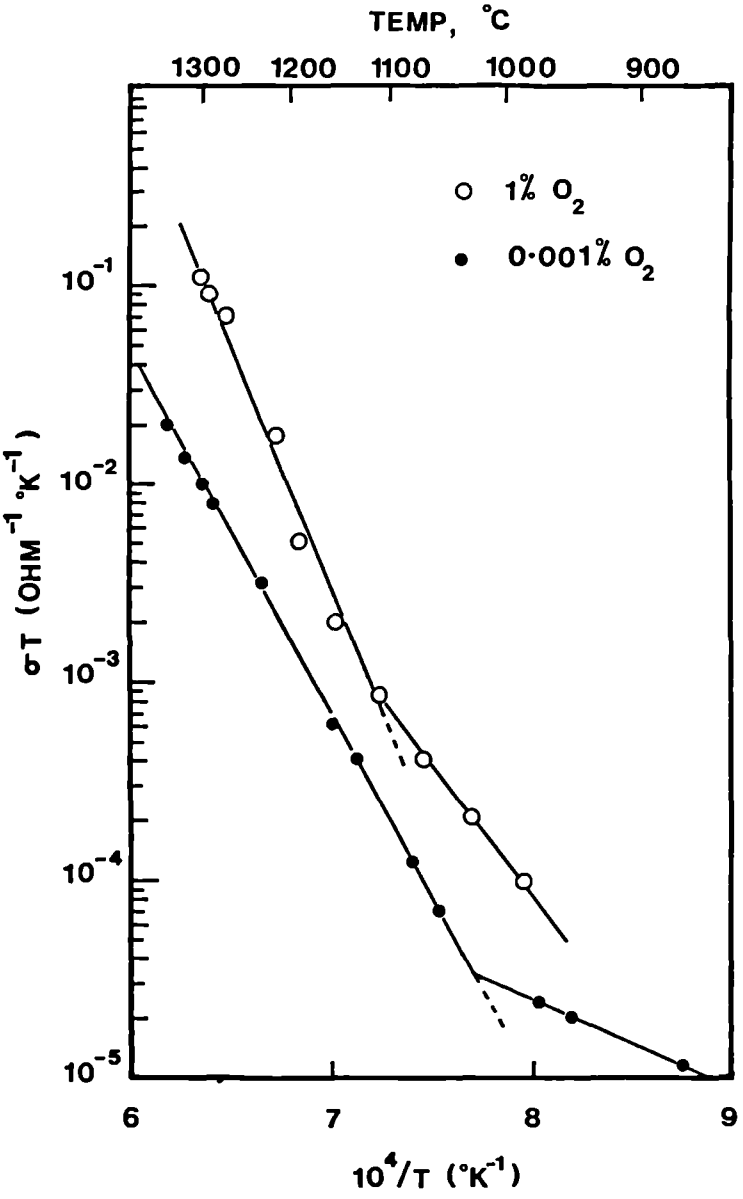

Figure 11. Intrinsic and Extrinsic conductivity of pure MgO in argon containing 0.001% and 1% oxygen[47].

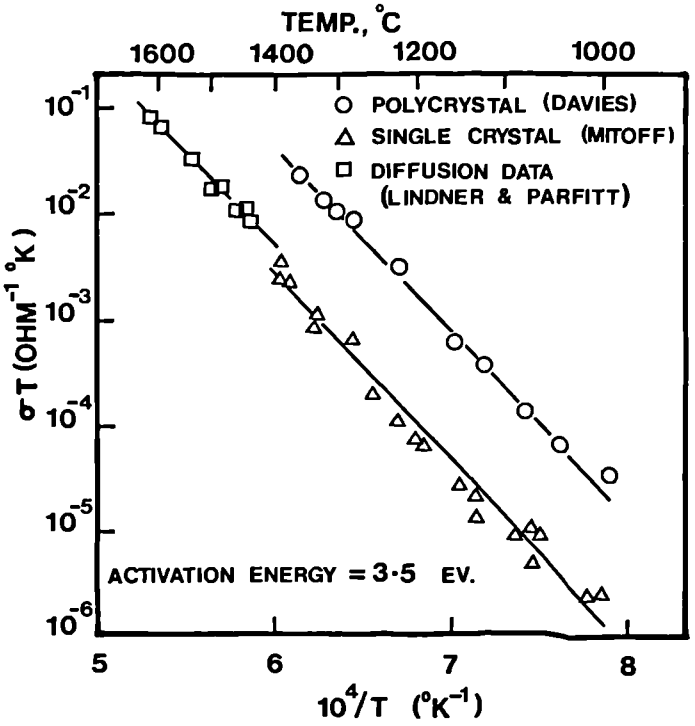

Figure 12. Evidence for ionic conductivity in MgO with respect to Mg^{2+} ion diffusion(47).

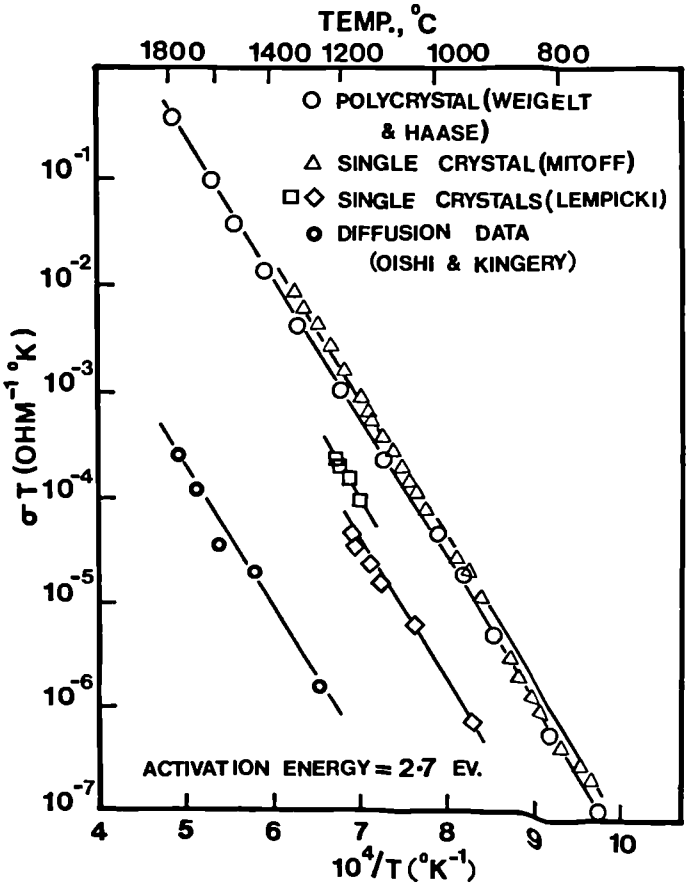

Figure 13. Evidence for ionic conductivity in MgO with respect to O^{2-} ion diffusion(47).

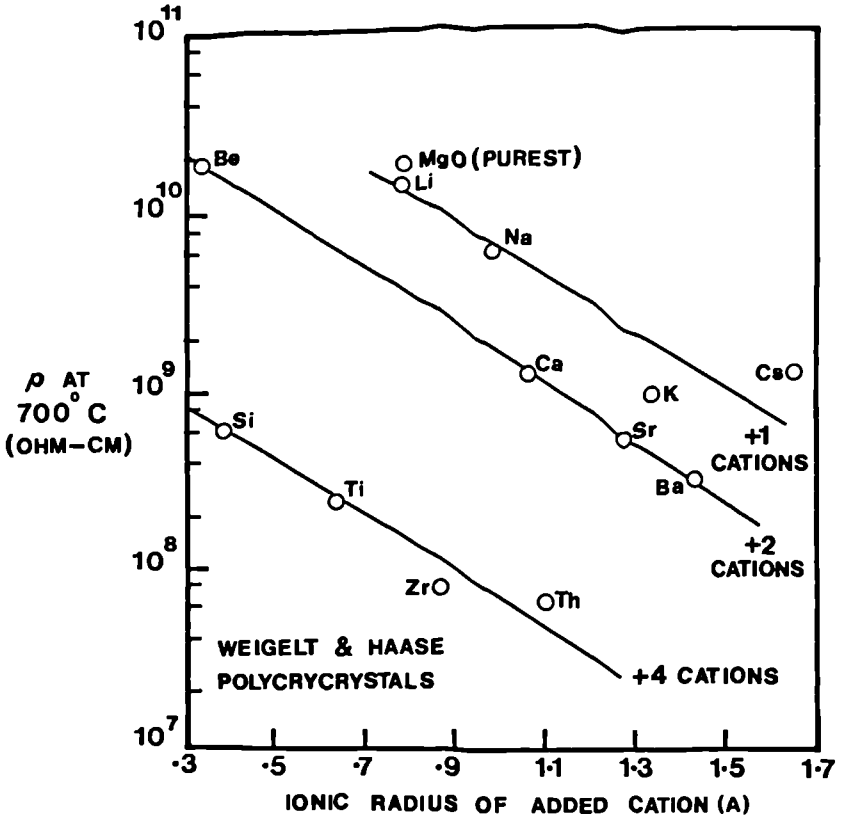

Figure 14. Influence of ionic radius and valency of impurities on the electrical conductivity of pure MgO[53].

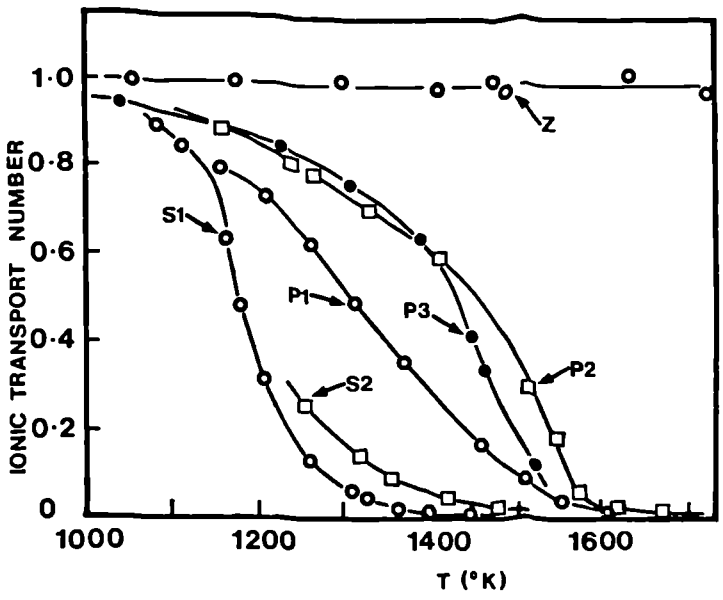

Figure 15. Ionic transference number as a function of temperature in Al_2O_3; curves S and P represent single crystal and polycrystalline Al_2O_3 respectively while line Z represents the results obtained for polycrystalline zirconia.

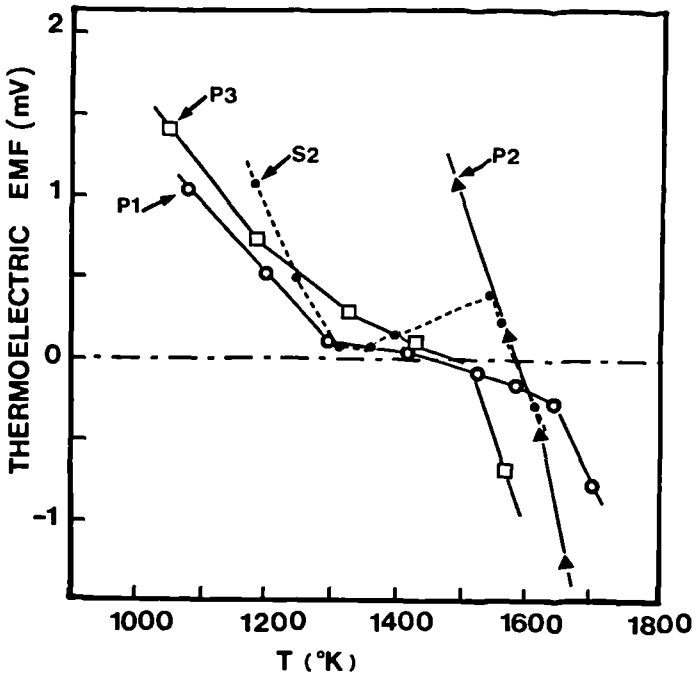

Figure 16. Thermoelectric EMF as a function of temperature[78]. The change of sign indicates a change in diffusing species from Al^{3+} ions at low temperature to electrons at higher temperature with corresponding change from ionic to electronic conductivity.

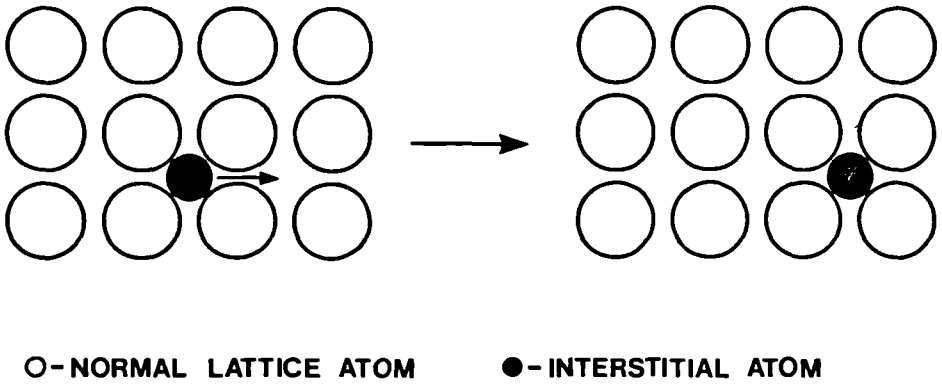

Figure 17(a). Schematic illustration of interstitial diffusion in solids.

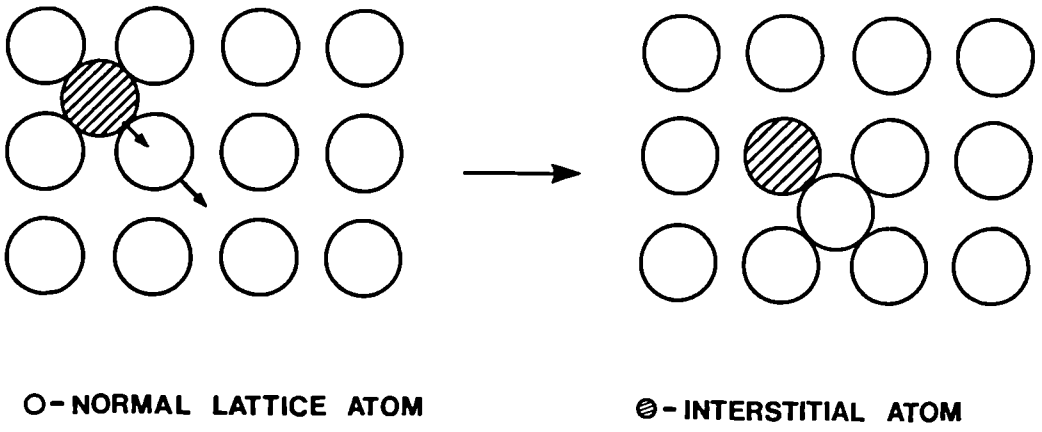

Figure 17(b). Schematic illustration of interstitialcy diffusion in solids.

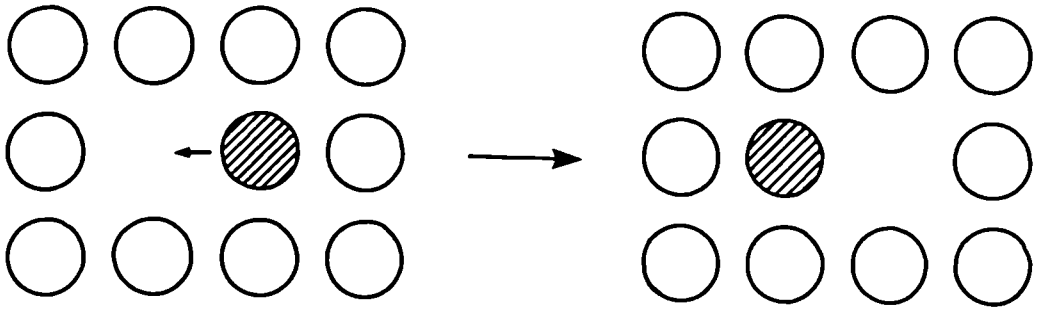

Figure 17(c). Schematic illustration of vacancy diffusion in solids; A normal lattice atom diffuses to a neighbouring lattice vacancy and thus the direction of vacancy movement is opposite to that of atom movement.

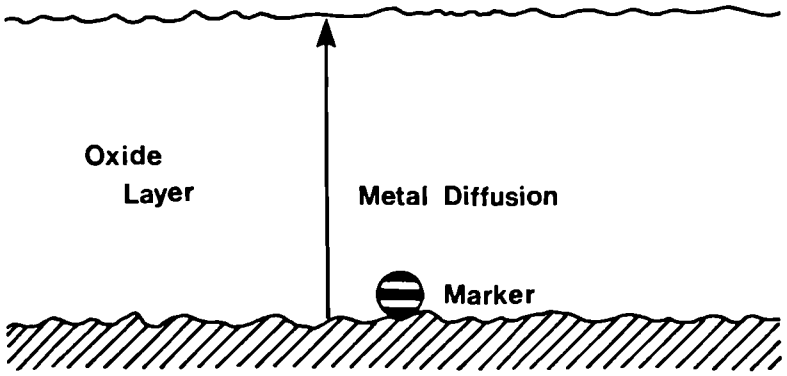

a) Metal diffusion predominant.

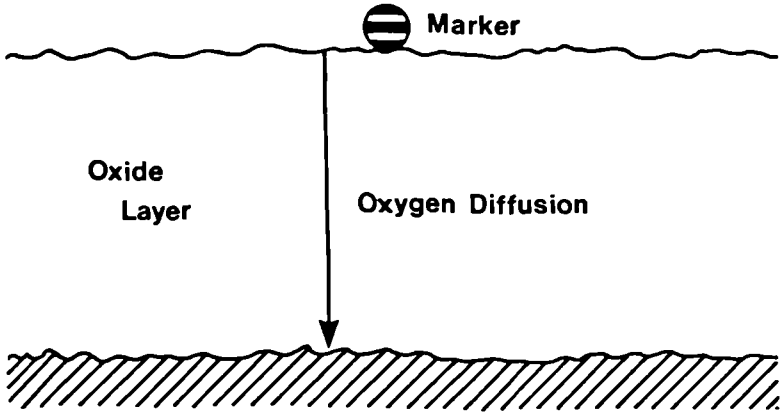

b) Oxygen diffusion predominant.

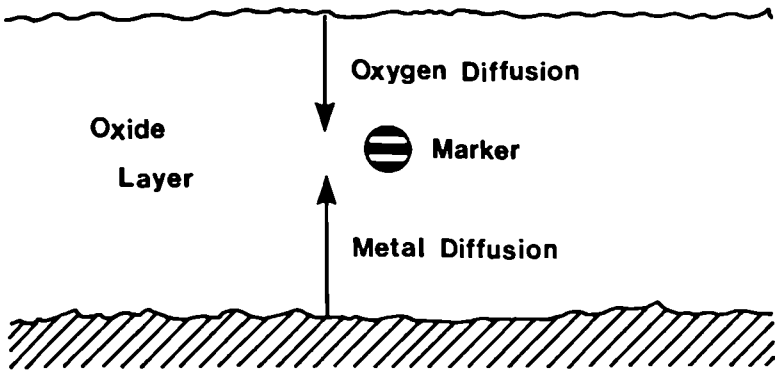

c) Simultaneous metal and oxygen diffsion.

Figure 18. Ideal location of inert markers after diffusion-controlled parabolic growth of an oxide film[99,100].

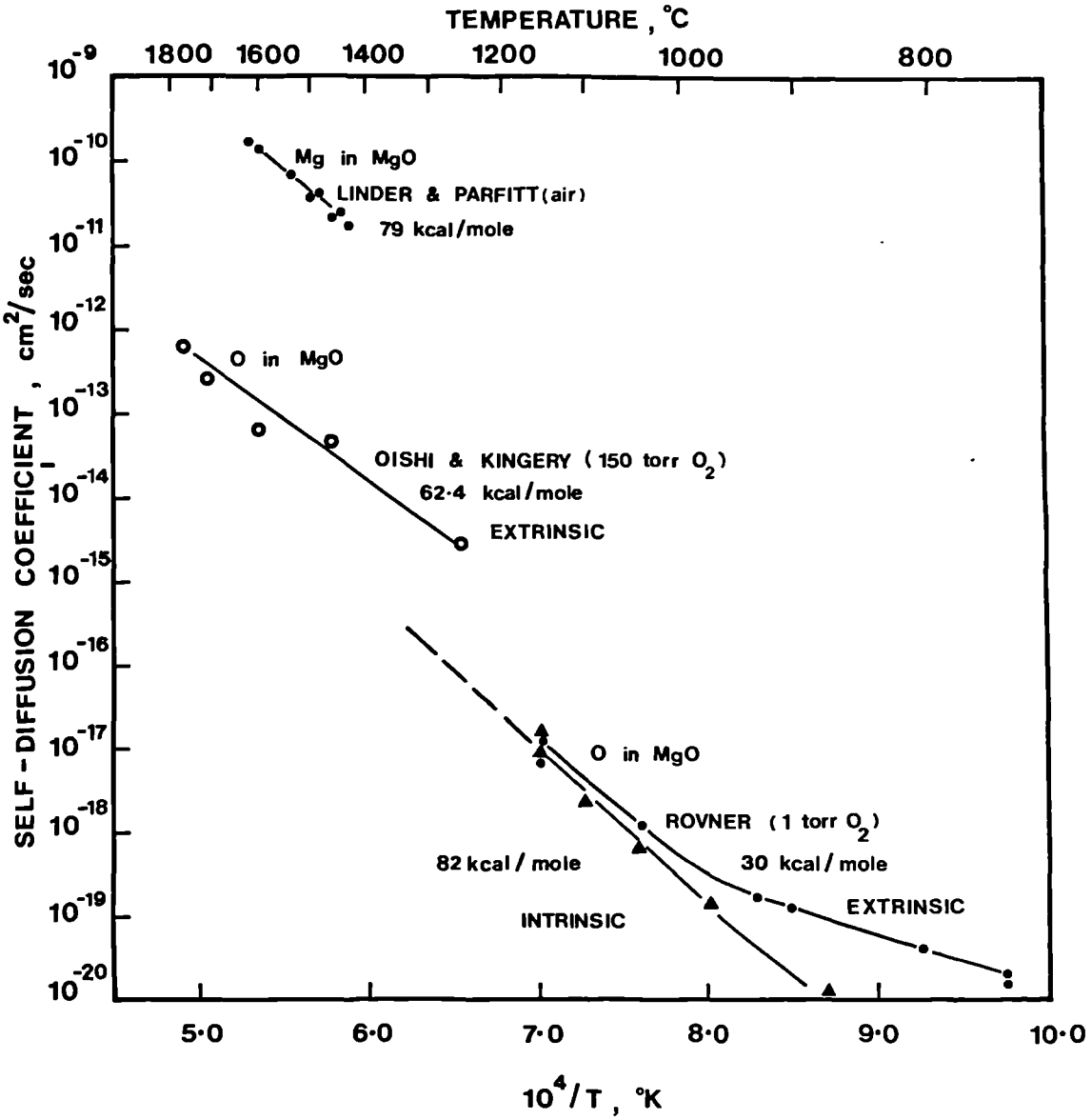

Figure 19. Self-diffusion of magnesium[51] and of oxygen[52,102], in magnesium oxide.

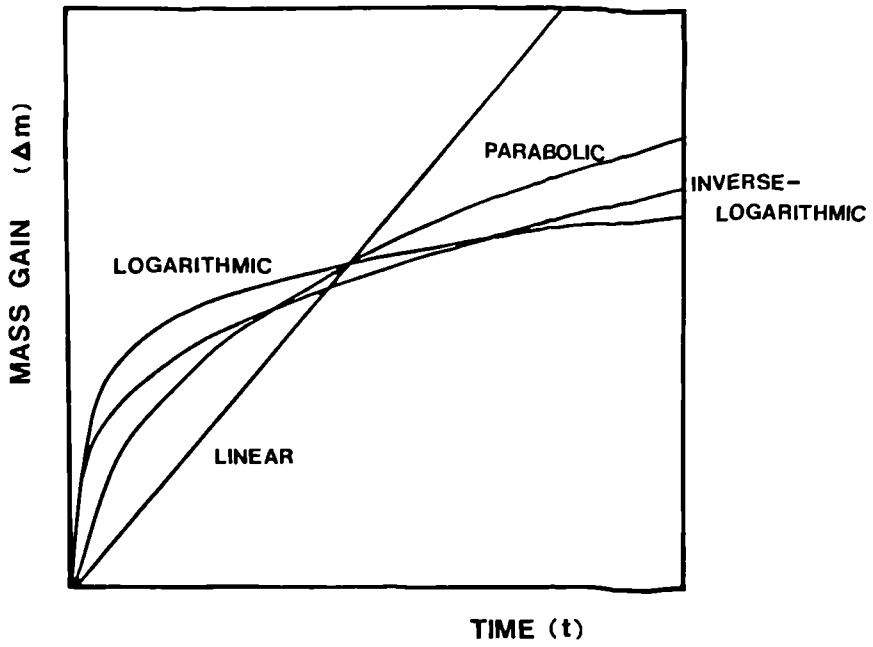

Figure 20. Common oxidation rate laws

(i) $\Delta m = K_1 t$ ..... linear law

(ii) $(\Delta m)^2 = K_2 t$ ..... parabolic law

(iii) $\Delta m = K_4 \log (at+t_o)$.. logarithmic law

(iv) $\frac{1}{\Delta m} = A - K_5 \log t$ ..... inverse-log law

(Δm = mass gain; t = time)

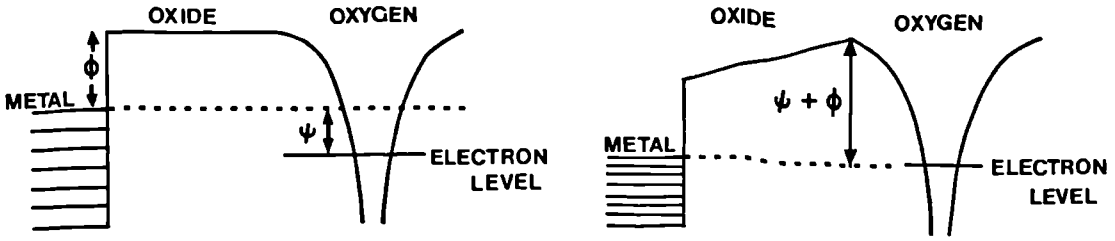

Figure 21. Electron energy levels in a metal, in its oxide, and in oxygen (a) before, and (b) after exchange of electrons for equilibrium[119].

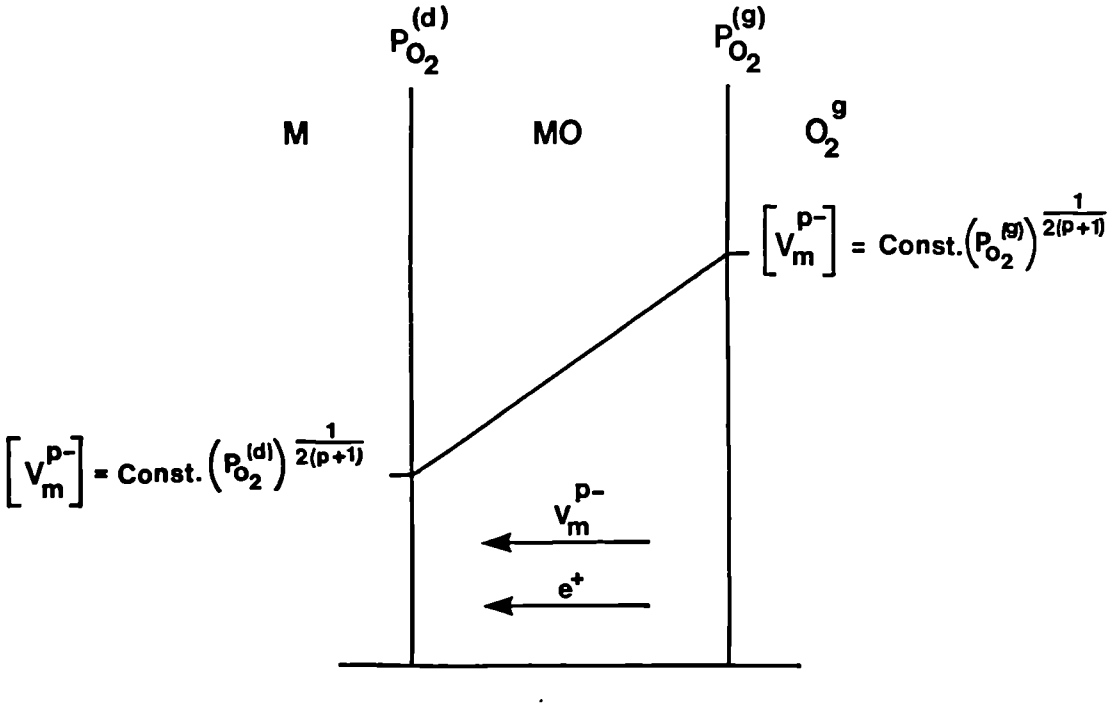

Figure 22. Schematic representation of concentration gradient of metal ion vacancies and transport process in a p-type oxide containing a predominance of cation vacancies, i.e. metal deficient oxide

MO = Oxide

V_m^{p-} = Metal ion vacancy with a charge p.

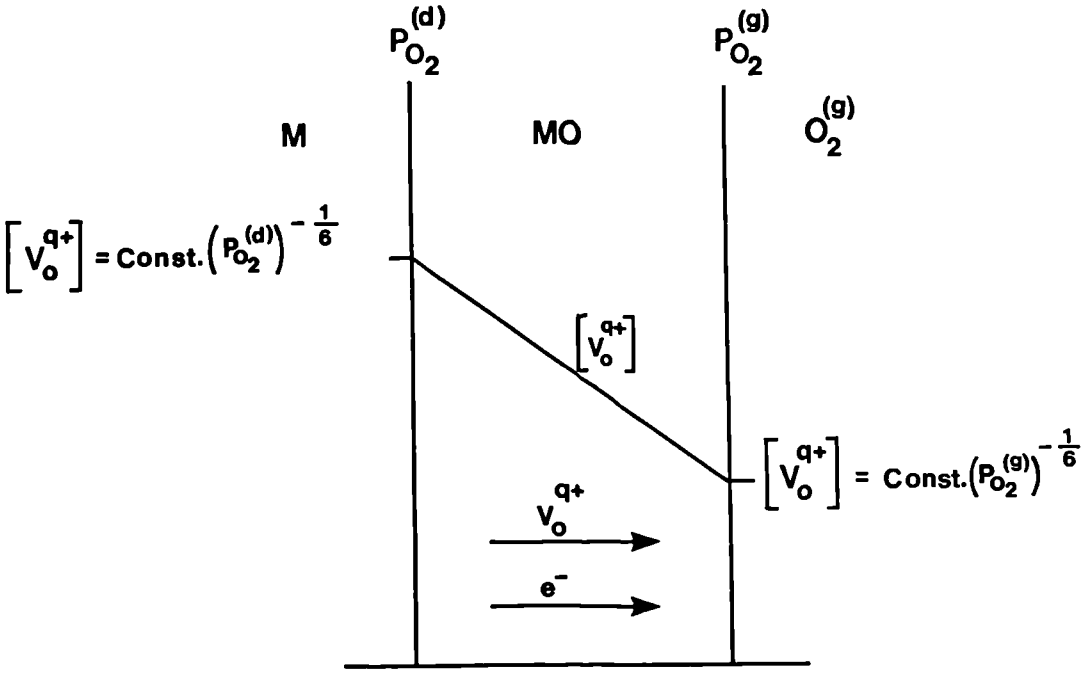

Figure 23. Schematic representation of concentration gradient of oxygen ion vacancies and transport process in an n-type oxide containing a predominance of anion vacancies, i.e. oxygen deficient oxide.

MO = Oxide

V_O^{q+} = Oxygen ion vacancy with a charge q.

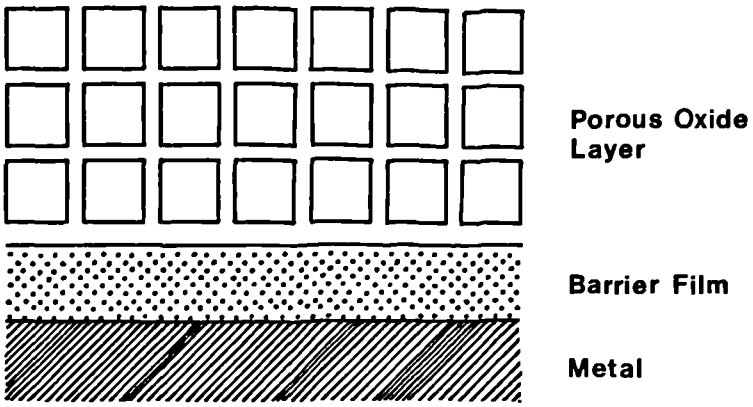

Figure 24. Cross-section of a metal specimen during linear oxidation. The thickness of the barrier film is effectively constant while the thickness of the outer layer which is permiable to gaseous oxygen, increases.

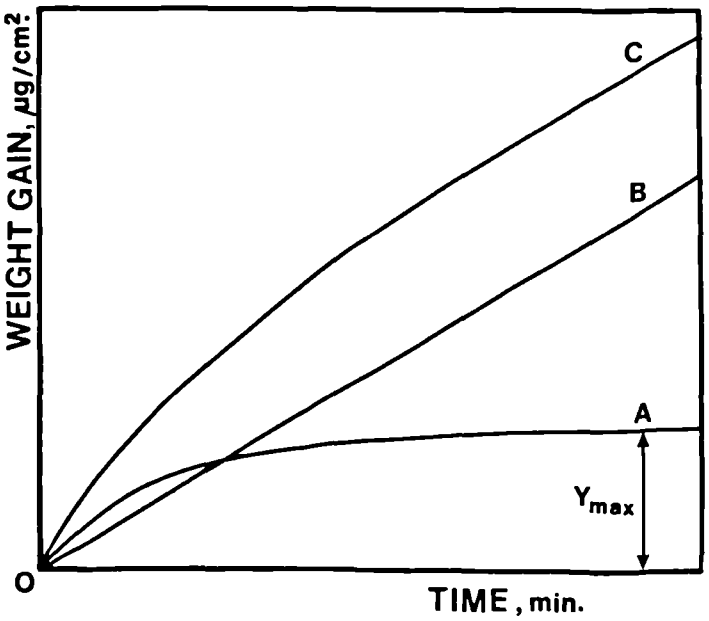

Figure 25. Kinetic interpretation of paralinear oxidation. Curves A and B correspond with the growth of an inner compact layer and an outer porous layer respectively. Curve C represents the total mass gain and is the algebraic sum of curves A and B.

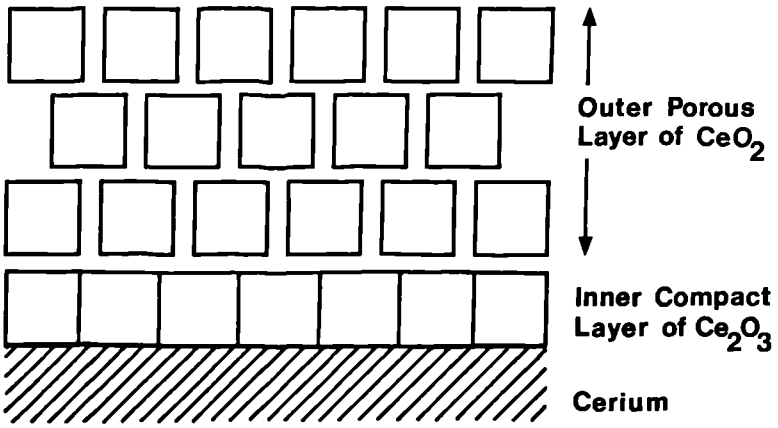

Figure 26. Cross-section of a cerium sample during paralinear oxidation. In this model, the compact layer of Ce_2O_3 which thickens at a parabolic rate, continuously transforms or oxidises at a constant rate to an outer-porous layer of CeO_2.

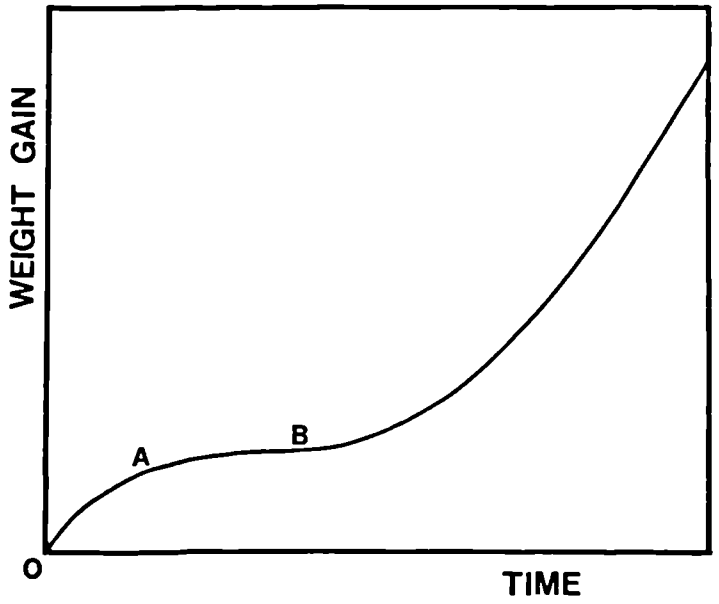

Figure 27. Illustration of breakaway oxidation.
OB = initial oxidation during which oxidation rate decreases with time.
AB = induction period.
B = onset of breakaway kinetics during which oxidation rate increases with time.

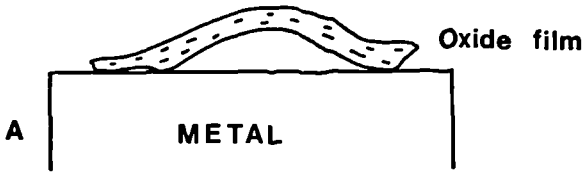

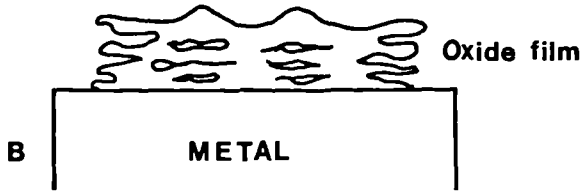

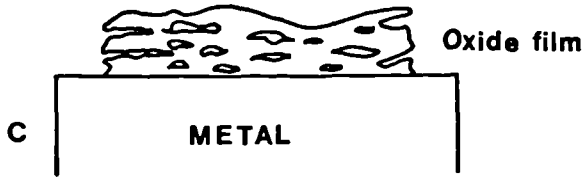

Blistering.

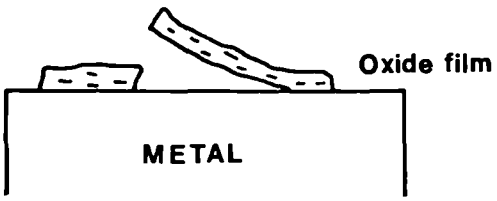

Flaking.

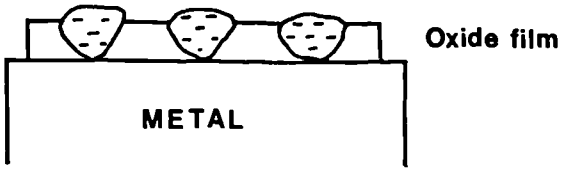

Shear Cracking.

Figure 28. Mechanisms of scale fracture, indicating compressive growth stresses in the oxide.

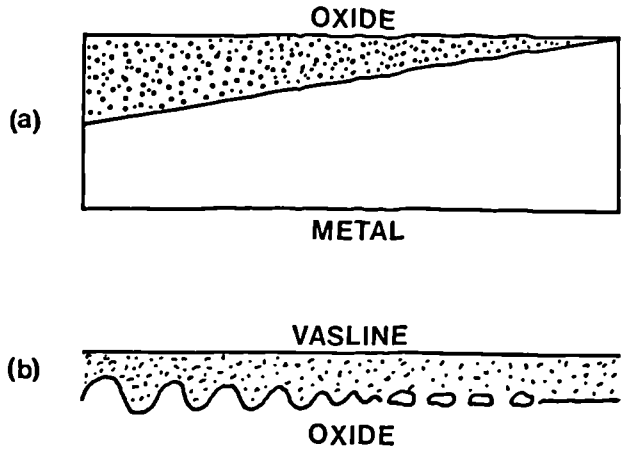

Figure 29. Wedge-shaped film of nickel oxide[136].
(a) as formed on the metal.
(b) after dissolution of the metal substrate; thicker parts of the film have wrinkled due to the relaxation of compressive growth stresses. At intermediate thicknesses the film has fractured and curled up indicating a stress gradient.

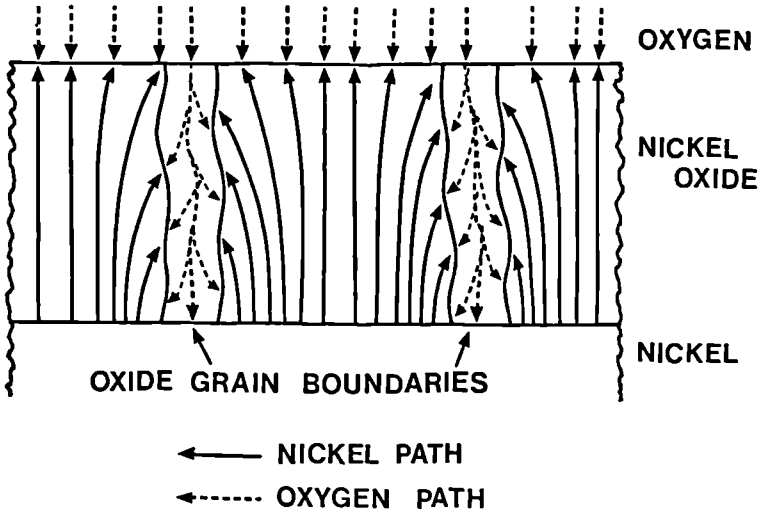

Figure 30. Schematic diagram showing diffusion paths of nickel and oxygen during the development of nickel oxide[146].

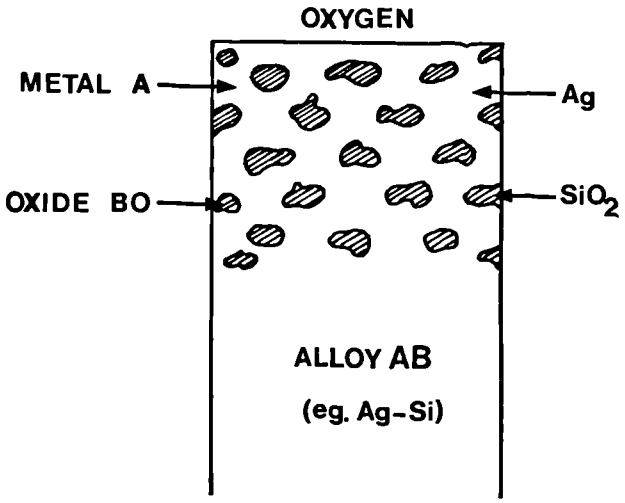

Figure 31. Internal oxidation for a binary alloy, AB, where the minor element B oxidises.

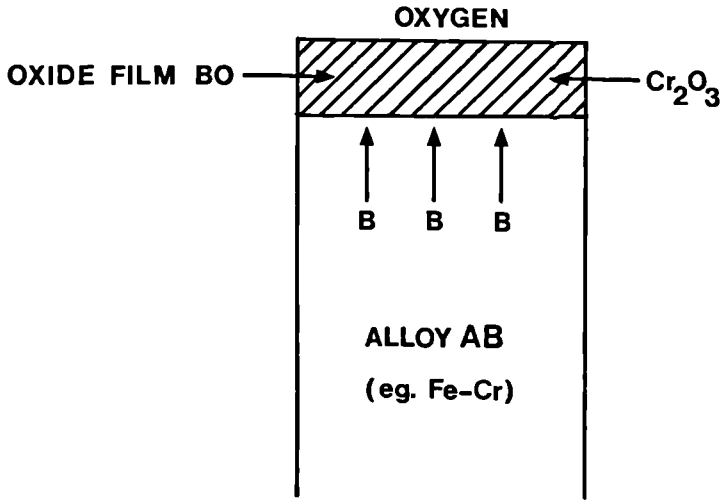

Figure 32. External oxidation for a binary alloy, AB, where the minor element B is selectively oxidised.

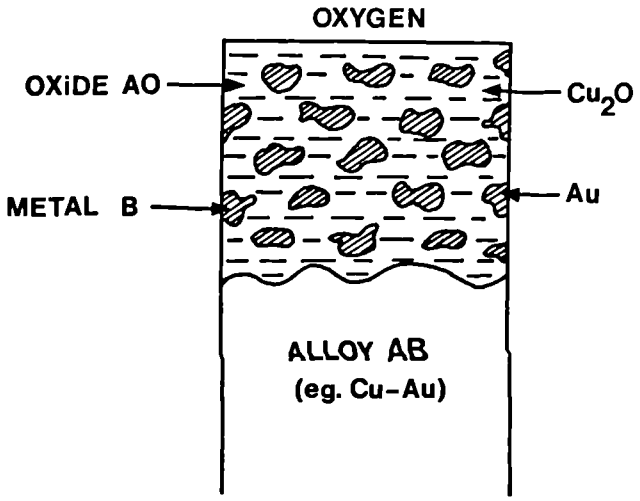

Figure 33. Internal oxidation for a binary alloy, AB, where the host element A oxidises.

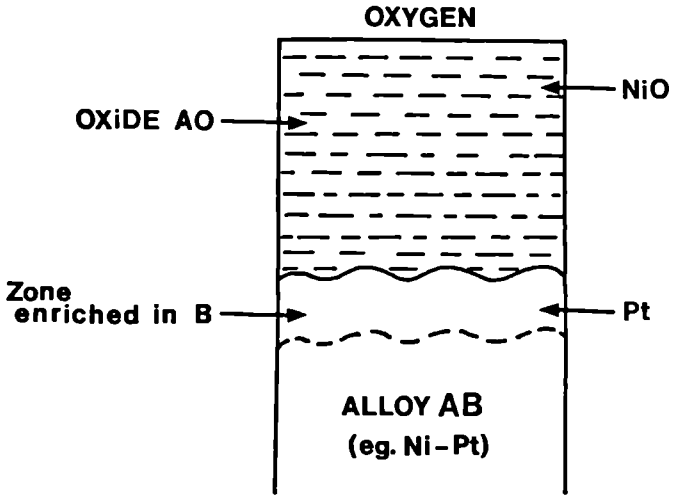

Figure 34. External oxidation for a binary alloy,AB, where the host element A is selectively oxidised producing a layer enriched with element B at the oxide/alloy interface.

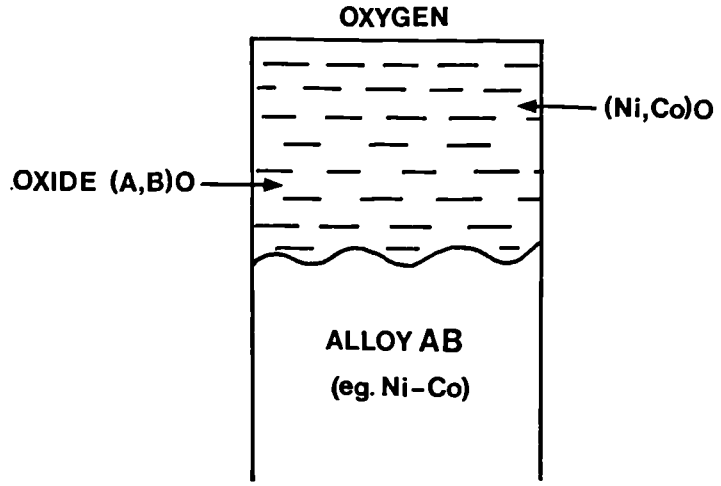

Figure 35. Oxidation of a binary alloy, AB, for which the oxides of both the elements are completely miscible.

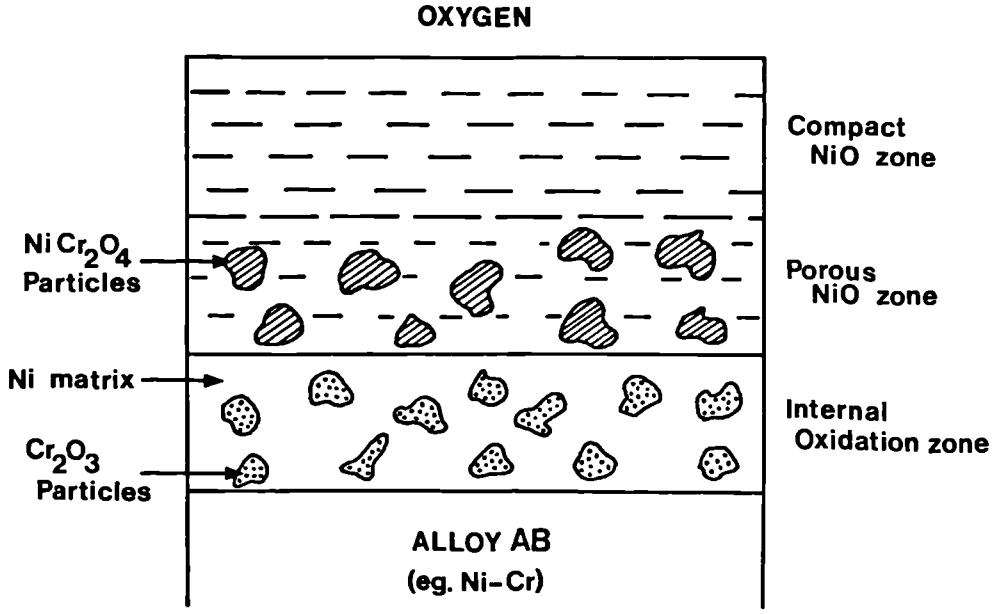

Figure 36. Oxidation of a binary alloy, AB, illustrating external oxidation of the host element, internal oxidation of the minor element, and simultaneous formation of an intermediate double oxide layer, e.g. Ni-10% Cr alloy[163].

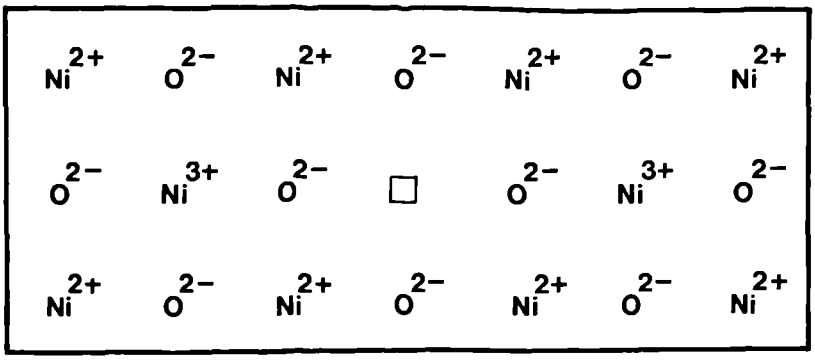

Nickel Oxide (NiO)

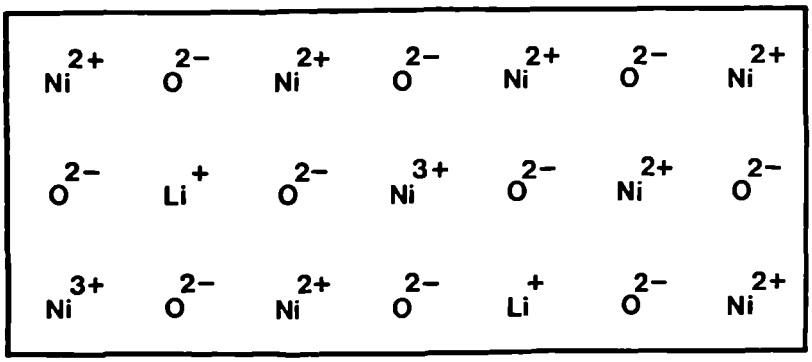

NiO + Lithium Oxide (LiO)

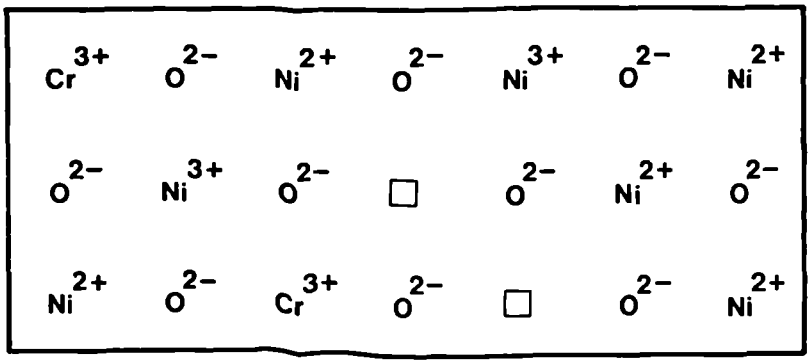

NiO + Chromium Oxide (Cr_2O_3)

Figure 37. Effect of Li_2O[165] and Cr_2O_3[166] on the defect structure of p-type NiO with cation vacancies.

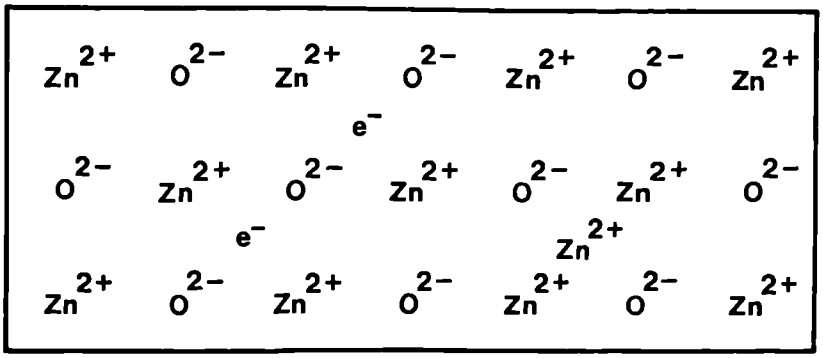

Zinc Oxide (ZnO)

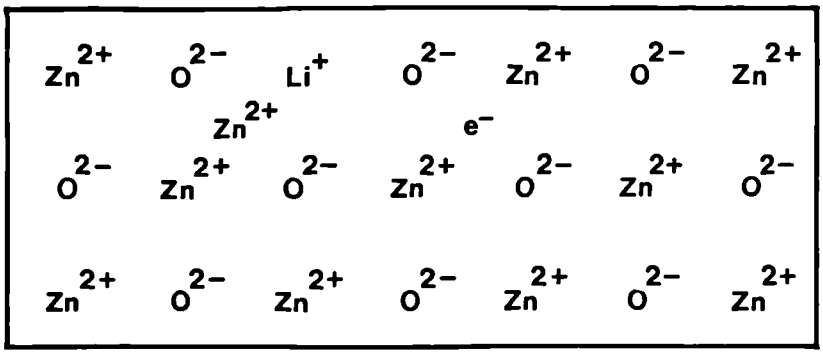

ZnO + Lithium Oxide (LiO)

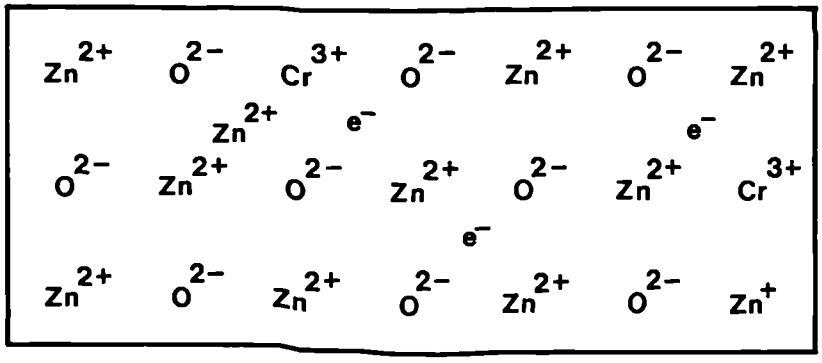

ZnO + Chromium Oxide (Cr_2O_3)

Figure 38. Effect of Li_2O[167] and Cr_2O_3[166] on the defect structure of n-type ZnO with cation interstitials.

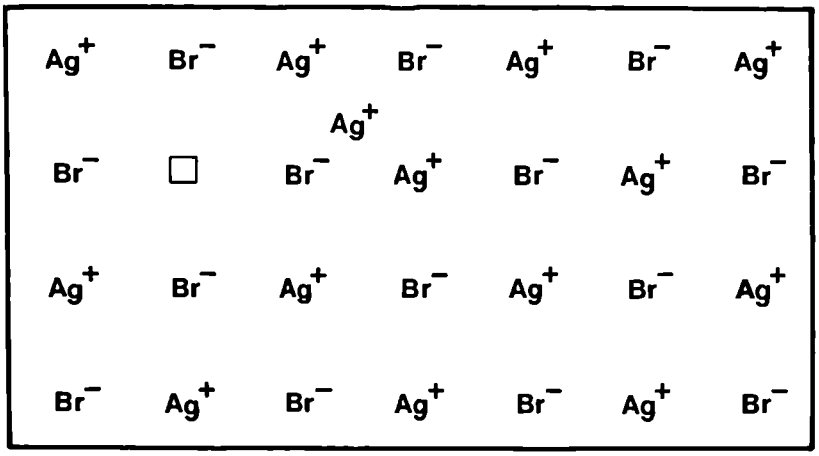

Silver Bromide (AgBr)

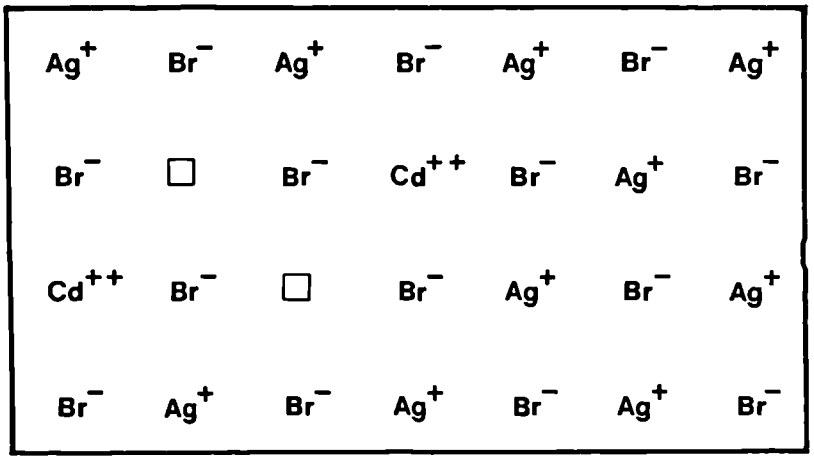

AgBr + Cadmium Bromide (CdBr)

Figure 39. Effect of CdBr[168] on the defect structure of ionic compound, AgBr, with mobile cation vacancies.

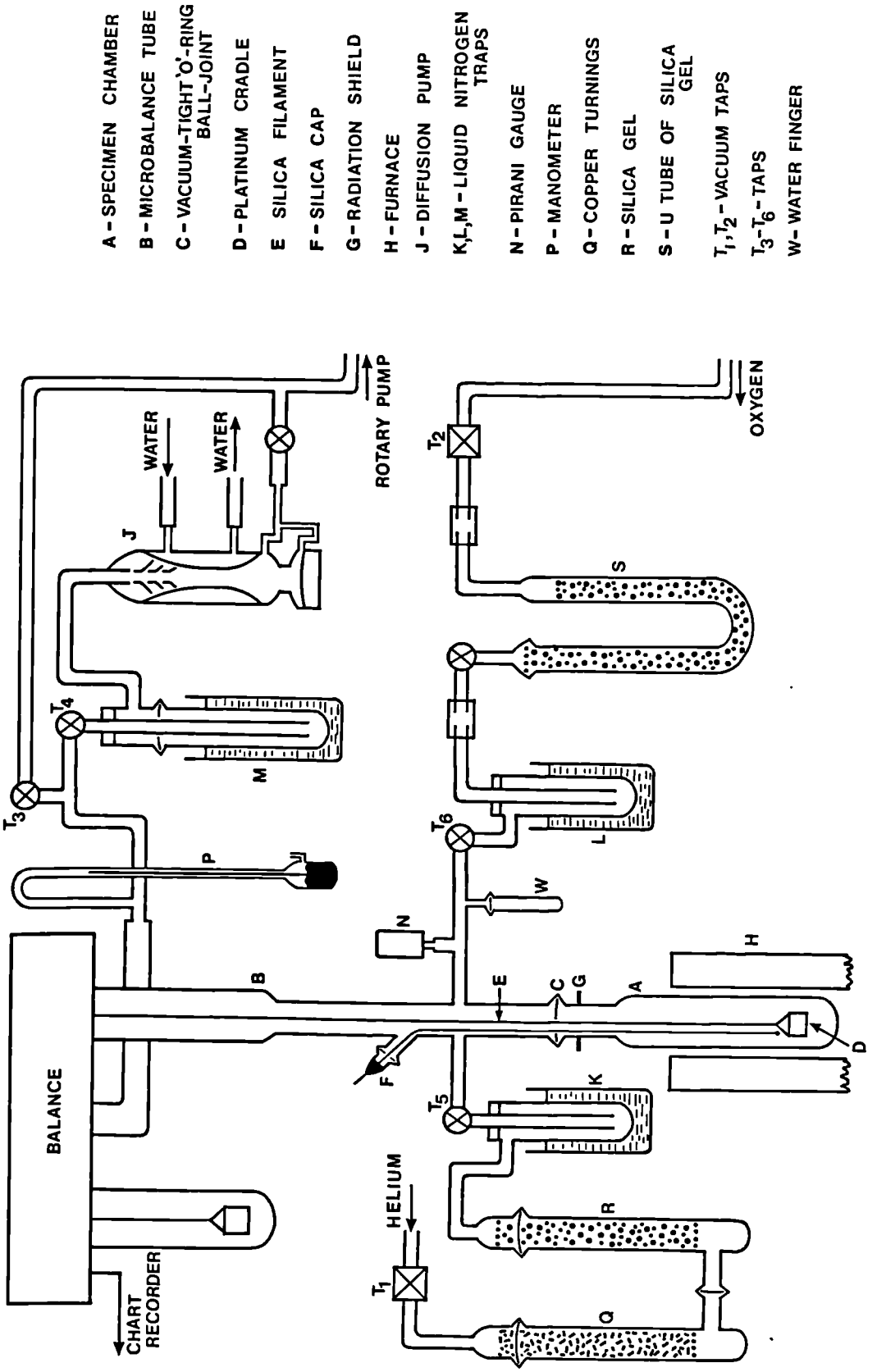

Figure 40. Schematic diagram of thermogravimetric equipment and ancillaries (arrangement for oxidation in the dry atmosphere).

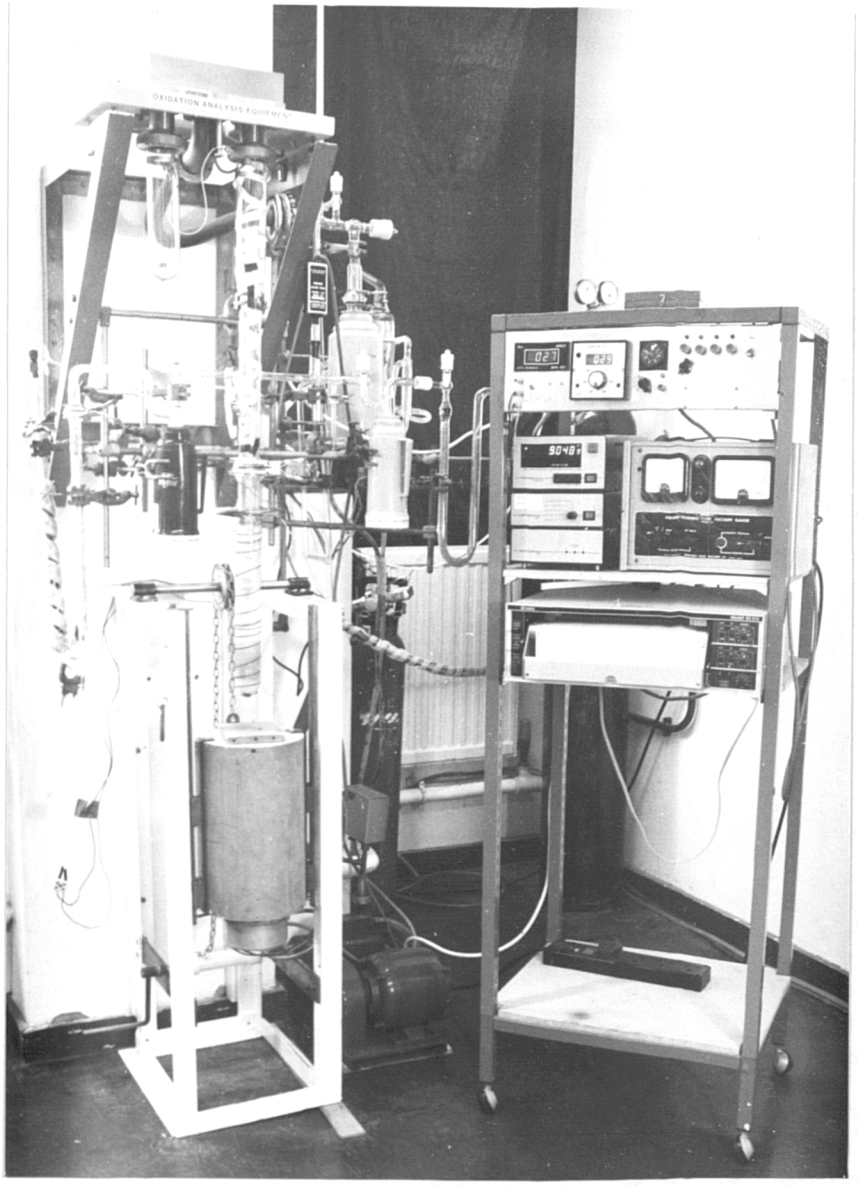

Figure 41. Complete thermogravimetric equipment.

Figure 42. Ancillary recording system for microbalance.

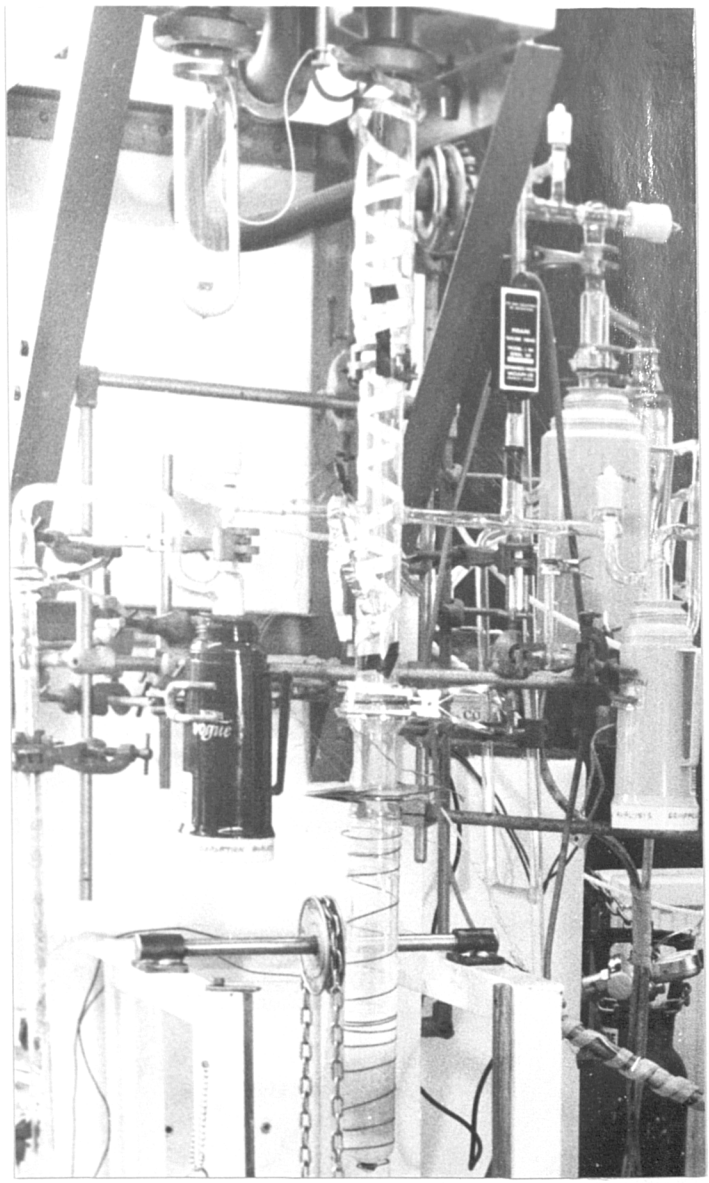

Figure 43. Specimen chamber attached to microbalance.

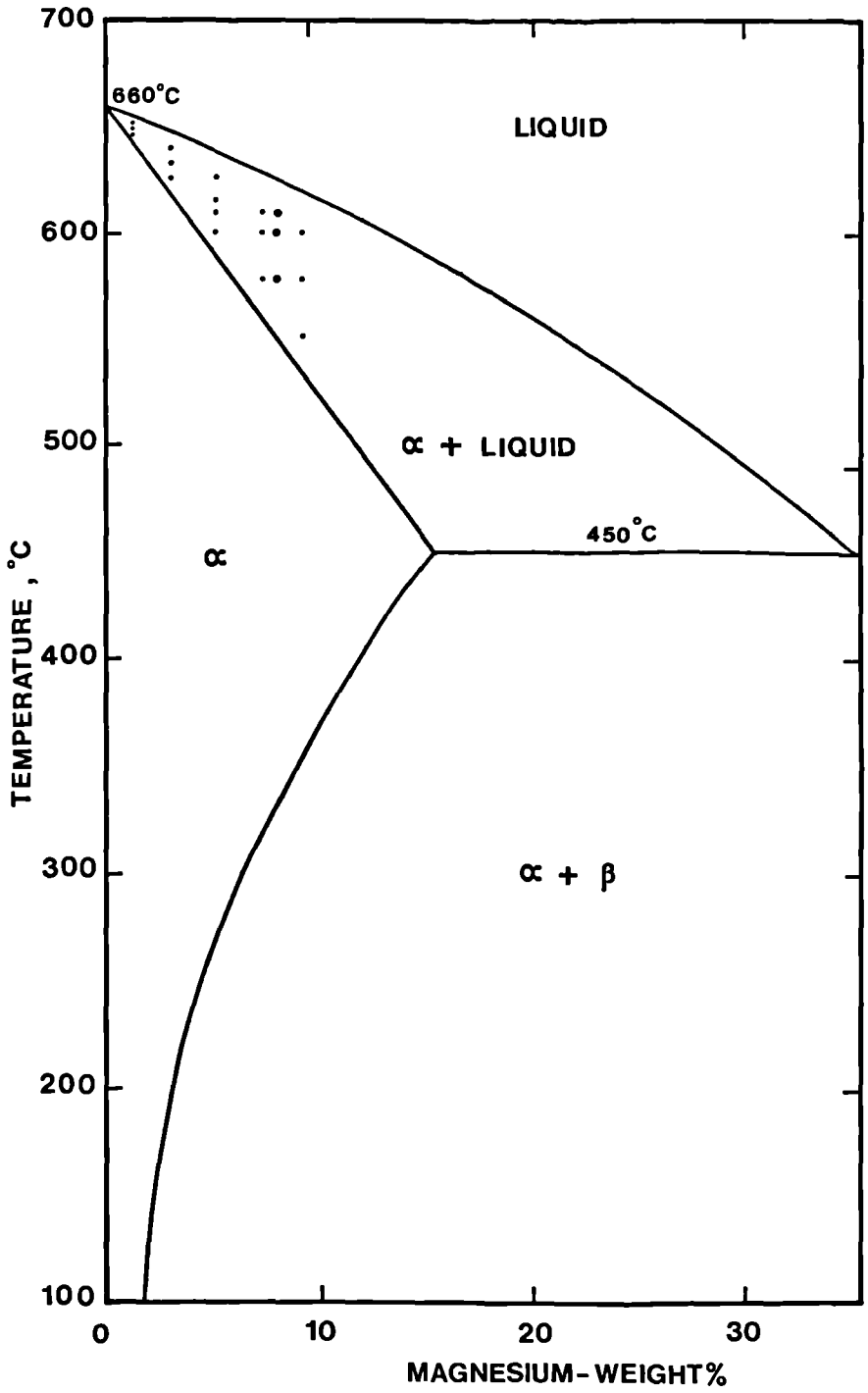

Figure 44. Test temperatures for thermogravimetric oxidation measurements superimposed on part of the Al-Mg binary phase equilibrium diagram.

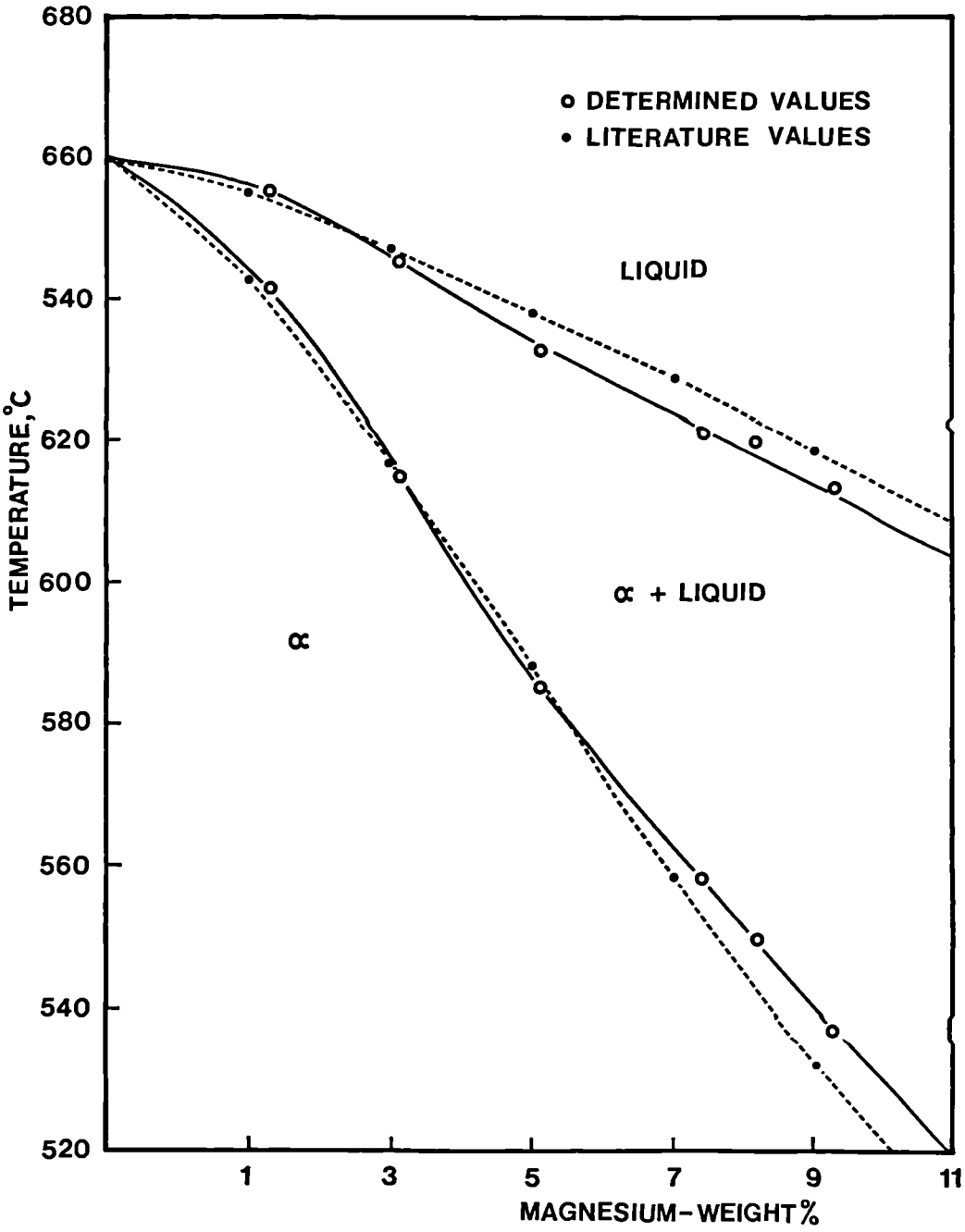

Figure 45. Partial phase equilibrium diagram for the Al-Mg system, determined using STA technique. Note the comparison of experimental solidus and liquidus temperatures with literature values.

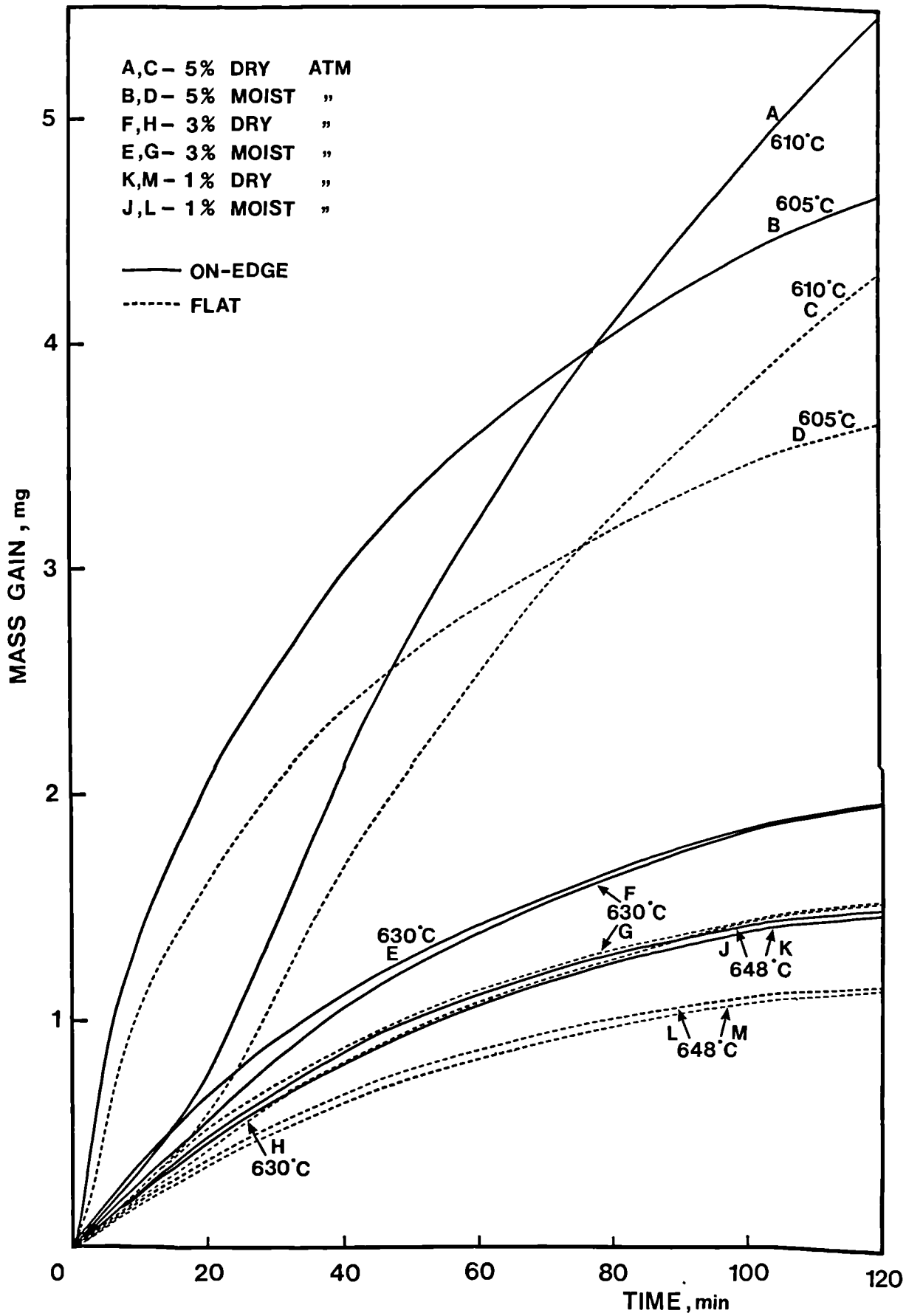

Figure 46. Total mass gain as a function of time for Al-1.3, 3.1 and 5.1% Mg alloys oxidised both flat and on edge in the crucible yielding ∿ 50% liquid fraction in dry and moist atmospheres.

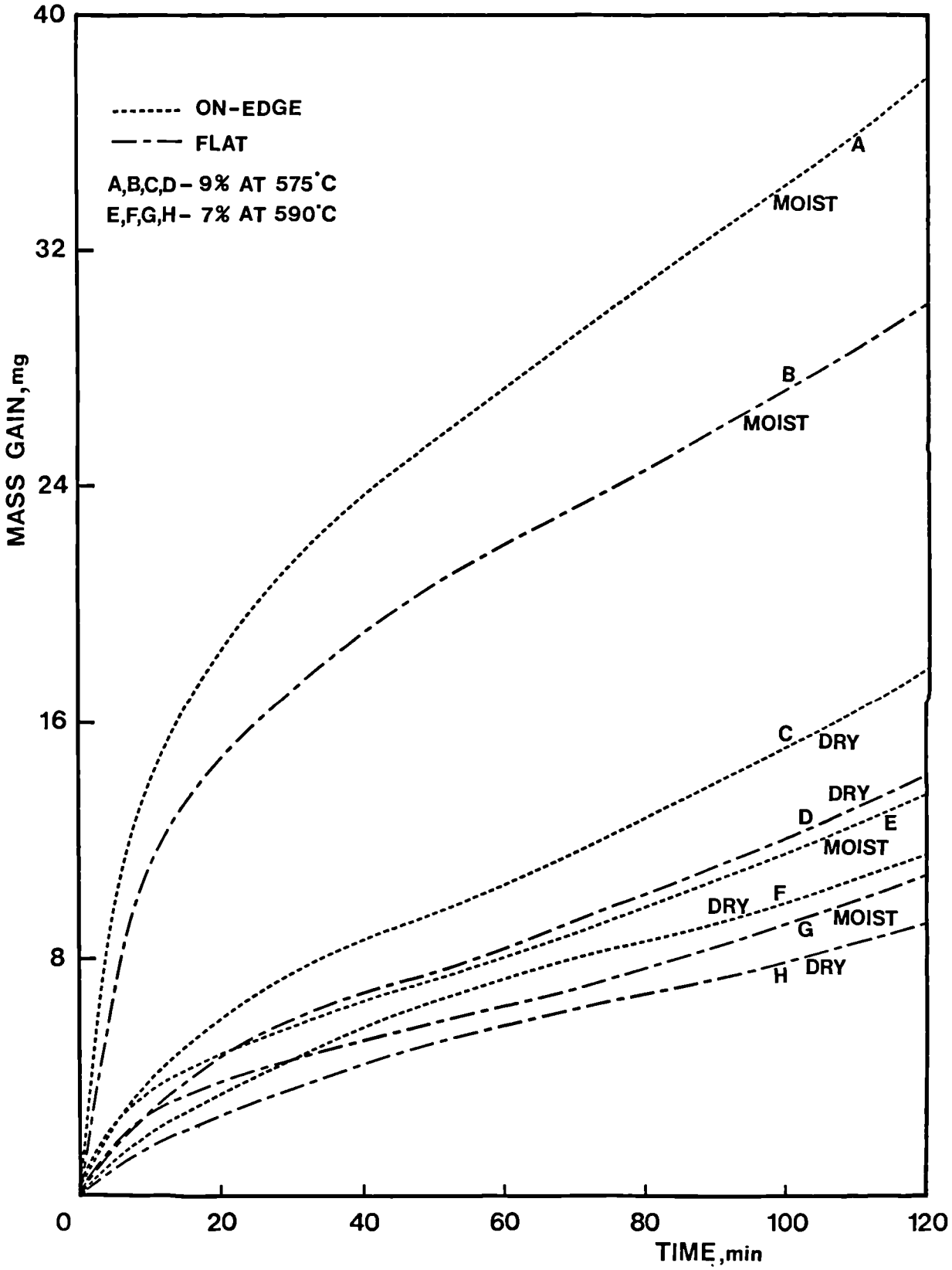

Figure 47. Total mass gain as a function of time for Al-7.4 and 9.3% Mg alloys oxidised both flat and on edge in the crucible, yielding ∿ 50% liquid fraction in dry and moist atmospheres.

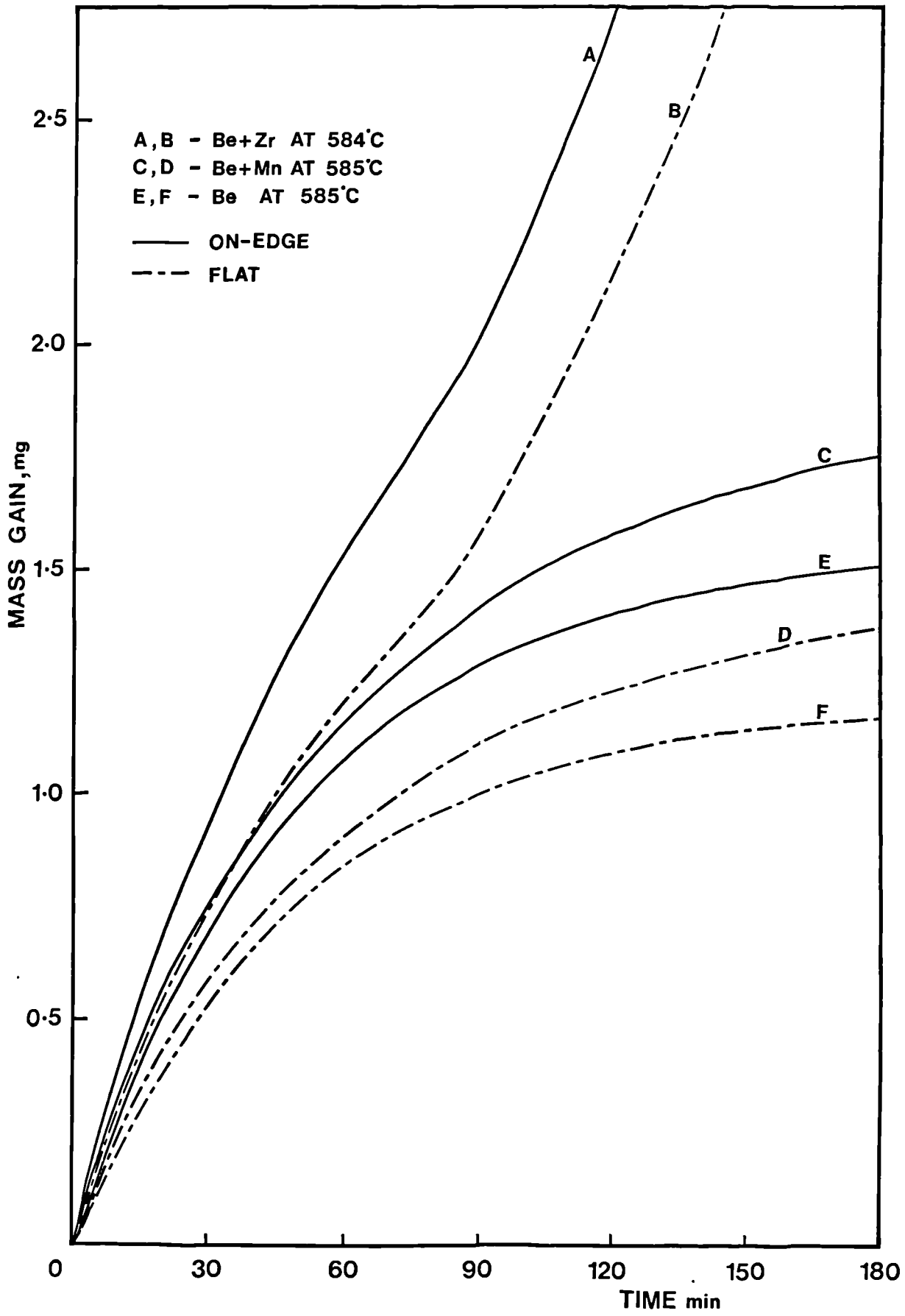

Figure 48. Total mass gain as a function of time for Al-8.2% Mg-0.003% Be, Al-8.16% Mg-0.003% Be-0.24% Mn, and Al-8.13% Mg-0.003% Be-0.12% Zr alloys oxidised both flat and on edge in the crucible, yielding ∿ 50% liquid fraction in the dry atmosphere.

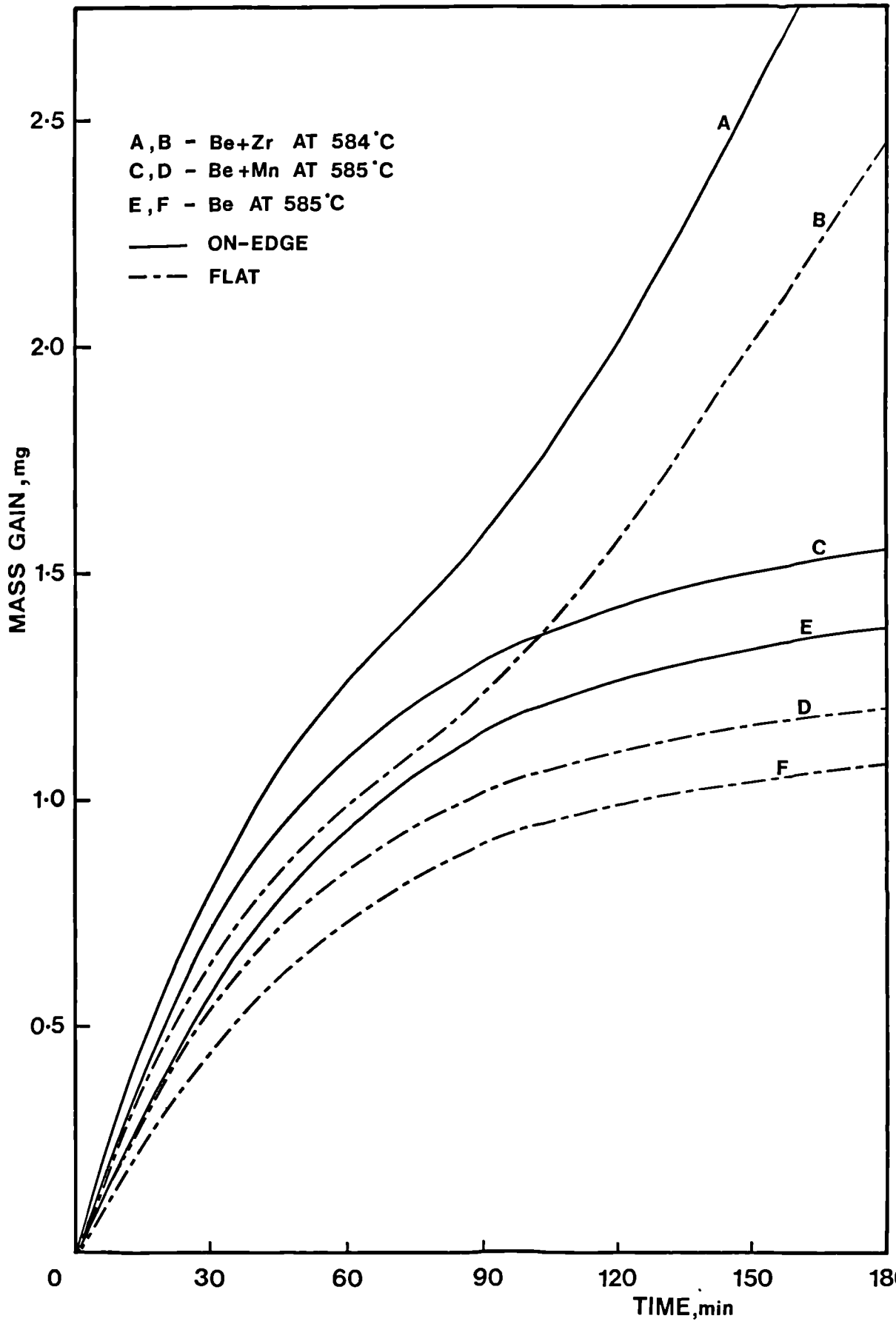

Figure 49. Total mass gain as a function of time for Al-8.2% Mg-0.003% Be, Al-8.16% Mg-0.003% Be-0.24% Mn, and Al-8.13% Mg-0.003% Be-0.12% Zr alloys oxidised both flat and on edge in the crucible, yielding ∿ 50% liquid fraction in the moist atmosphere.

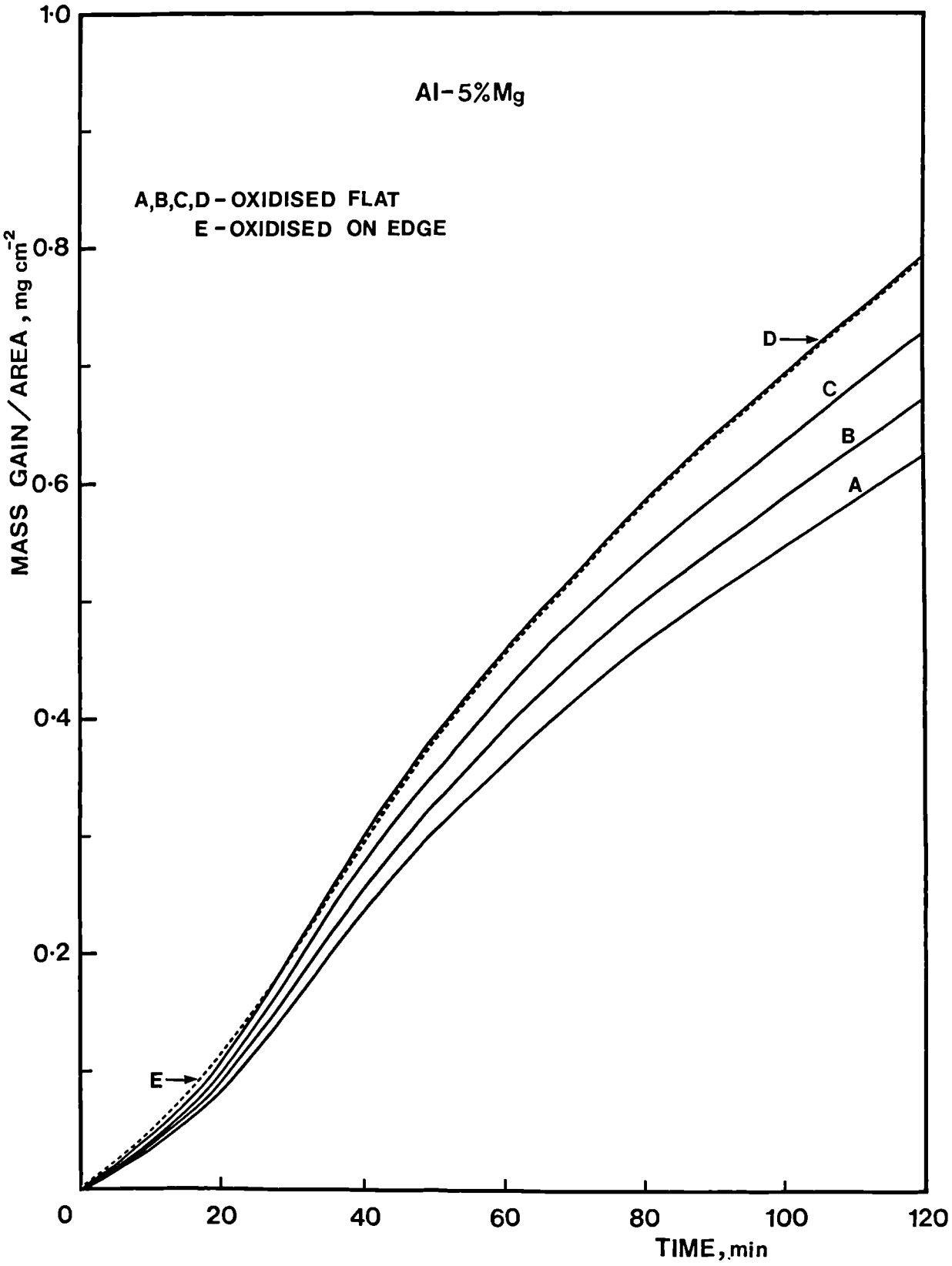

Figure 50. Mass gain-time curves for Al-5.1% Mg alloy oxidised flat in the dry atmosphere at 610°C, corrected for effective surface area.

A - Accounting for the whole bottom surface.
B - Accounting for 75% of the bottom surface.
C - Accounting for 50% of the bottom surface.
D - Accounting for 25% of the bottom surface.

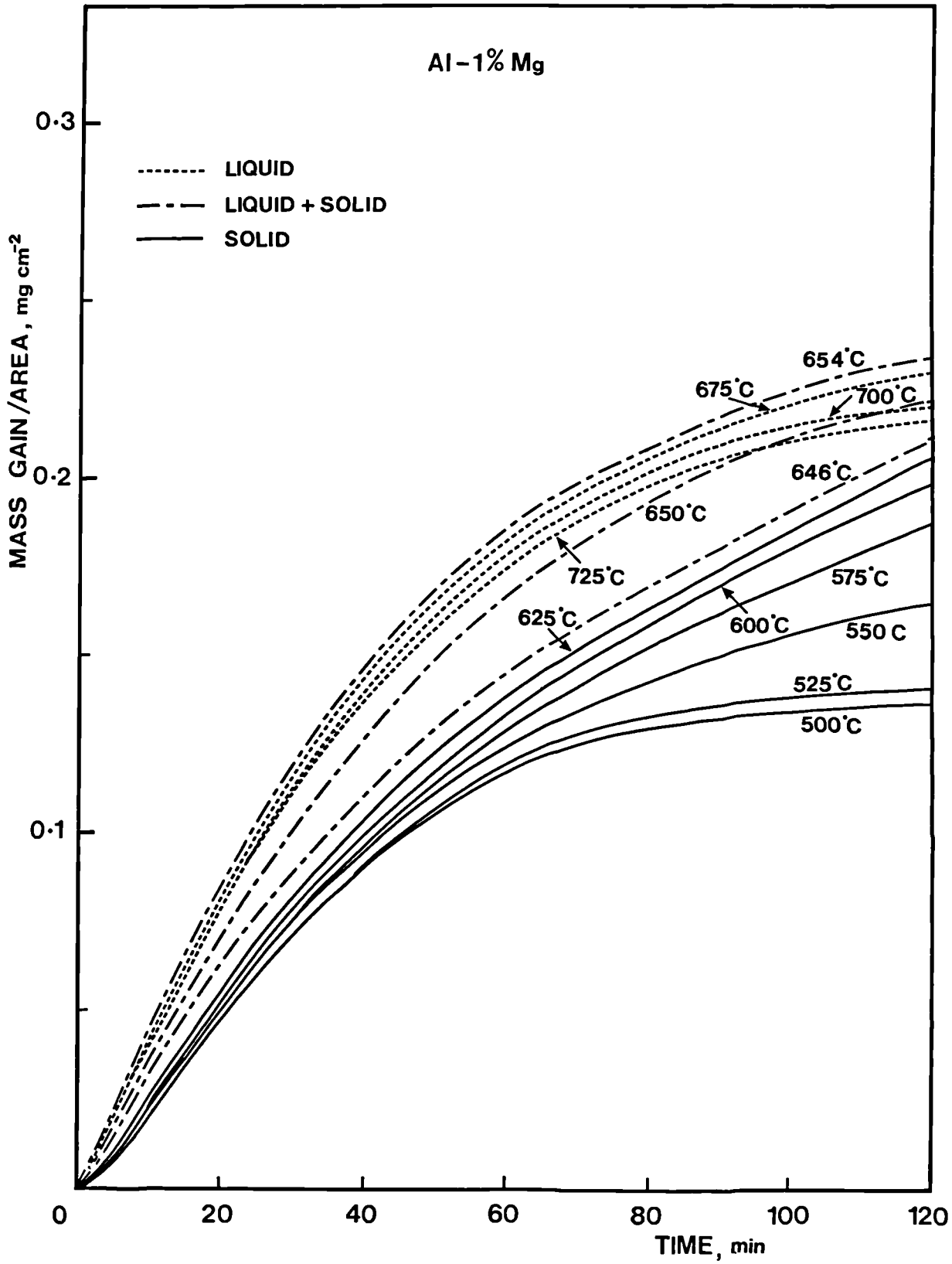

Figure 51. Mass gain as a function of time for Al-1.3% Mg alloy exposed to the dry atmosphere in the temperature range 500-725^{o}C.

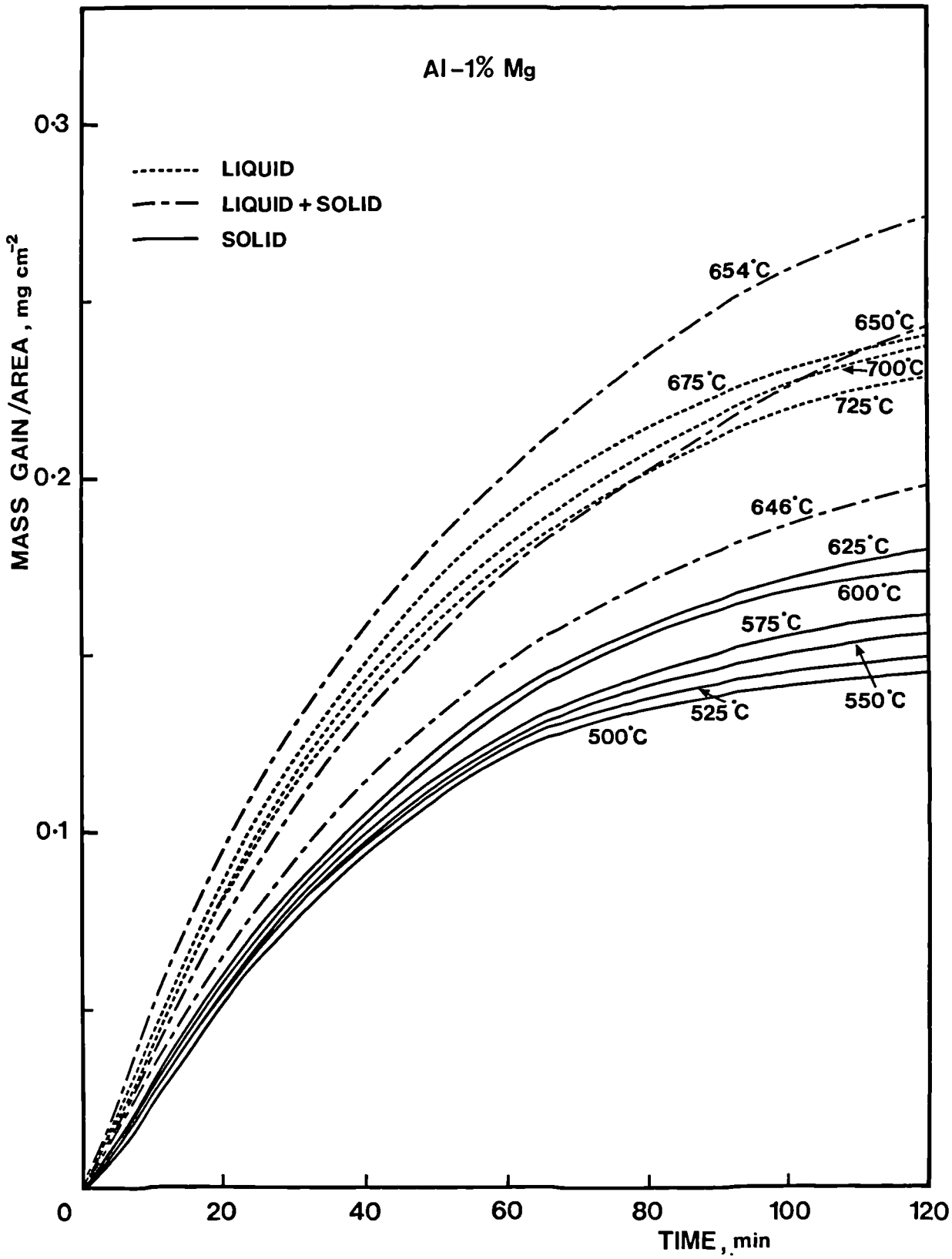

Figure 52. Mass gain as a function of time for Al-1.3% Mg alloy exposed to the moist atmosphere in the temperature range 500-725^{o}C.

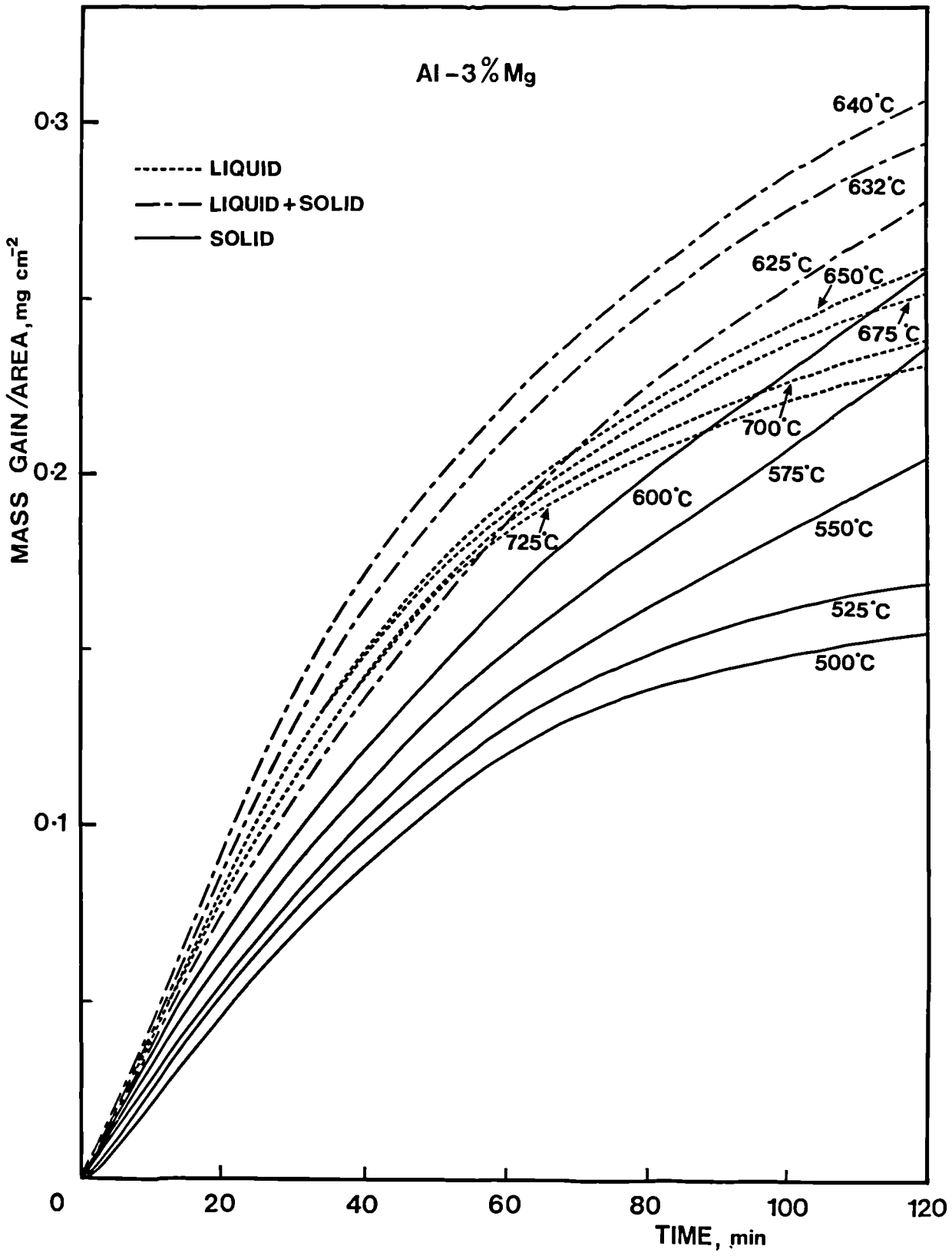

Figure 53. Mass gain as a function of time for Al-3.1% Mg alloy exposed to the dry atmosphere in the temperature range 500-725°C.

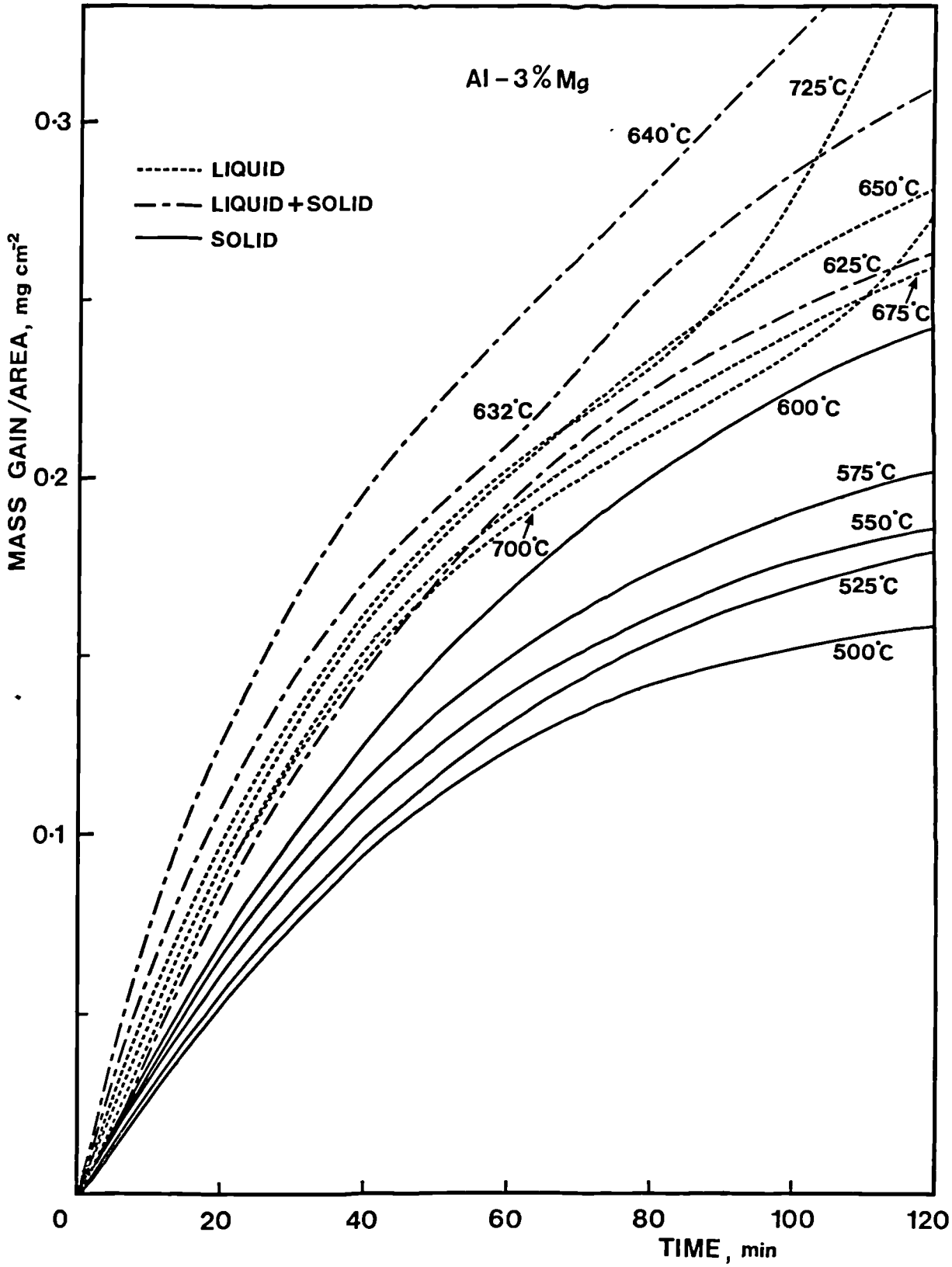

Figure 54. Mass gain as a function of time for Al-3.1% Mg alloy exposed to the moist atmosphere in the temperature range 500-725°C.

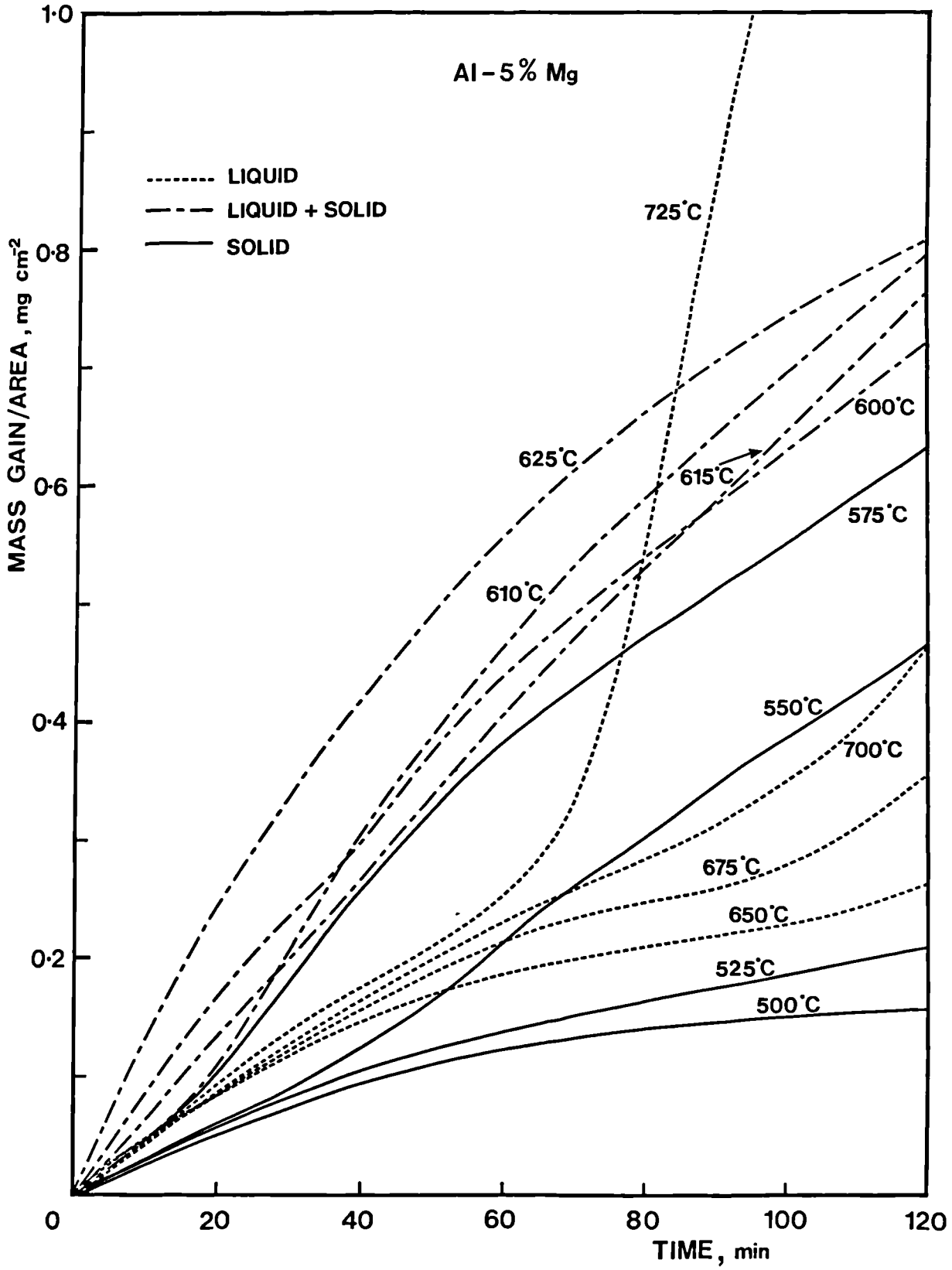

Figure 55. Mass gain as a function of time for Al-5.1% Mg alloy exposed to the dry atmosphere in the temperature range 500-725°C.

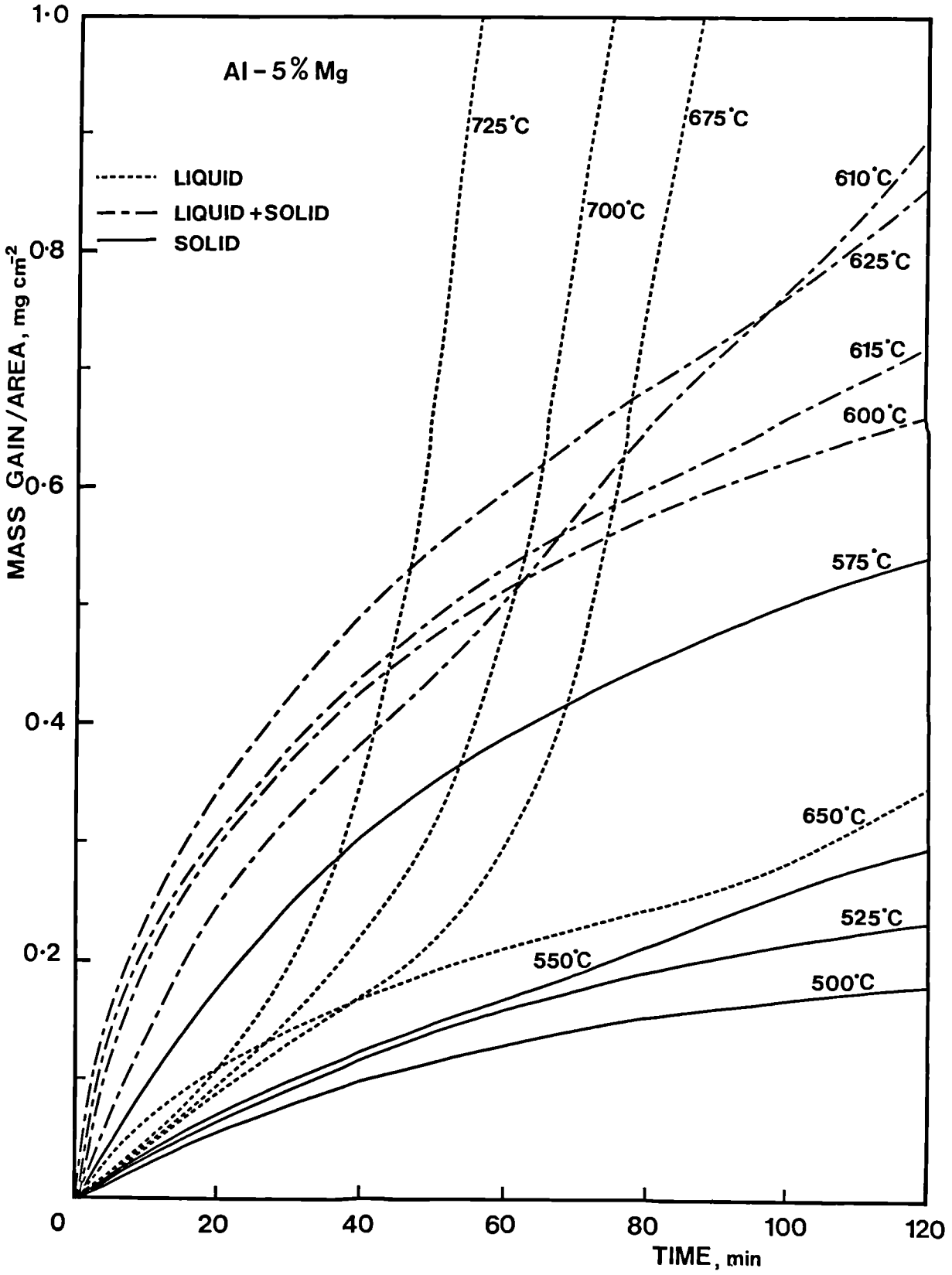

Figure 56. Mass gain as a function of time for Al-5.1% Mg alloy exposed to the moist atmosphere in the temperature range 500-725°C.

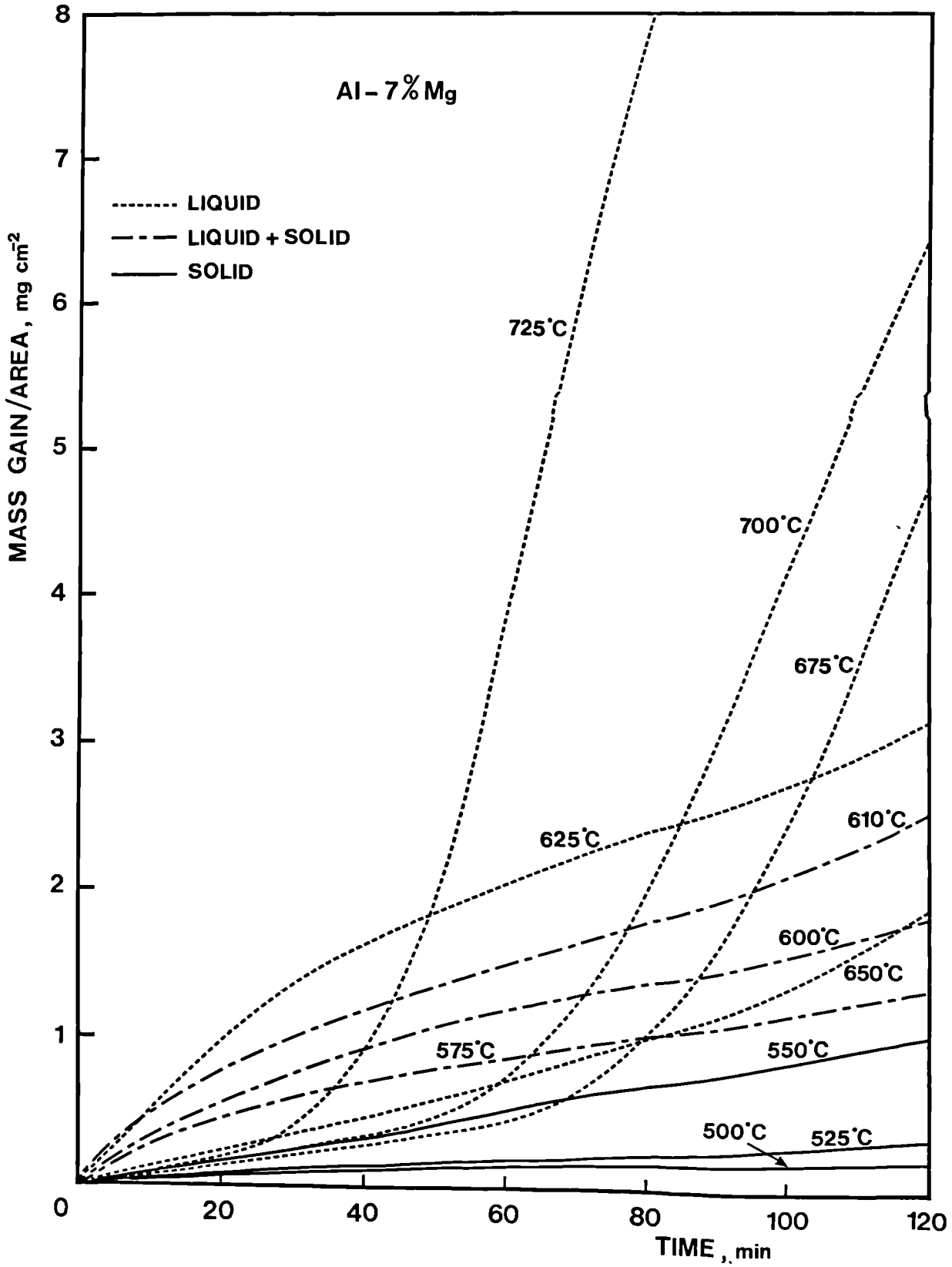

Figure 57. Mass gain as a function of time for Al-7.4% Mg alloy exposed to the dry atmosphere in the temperature range 500-725°C.

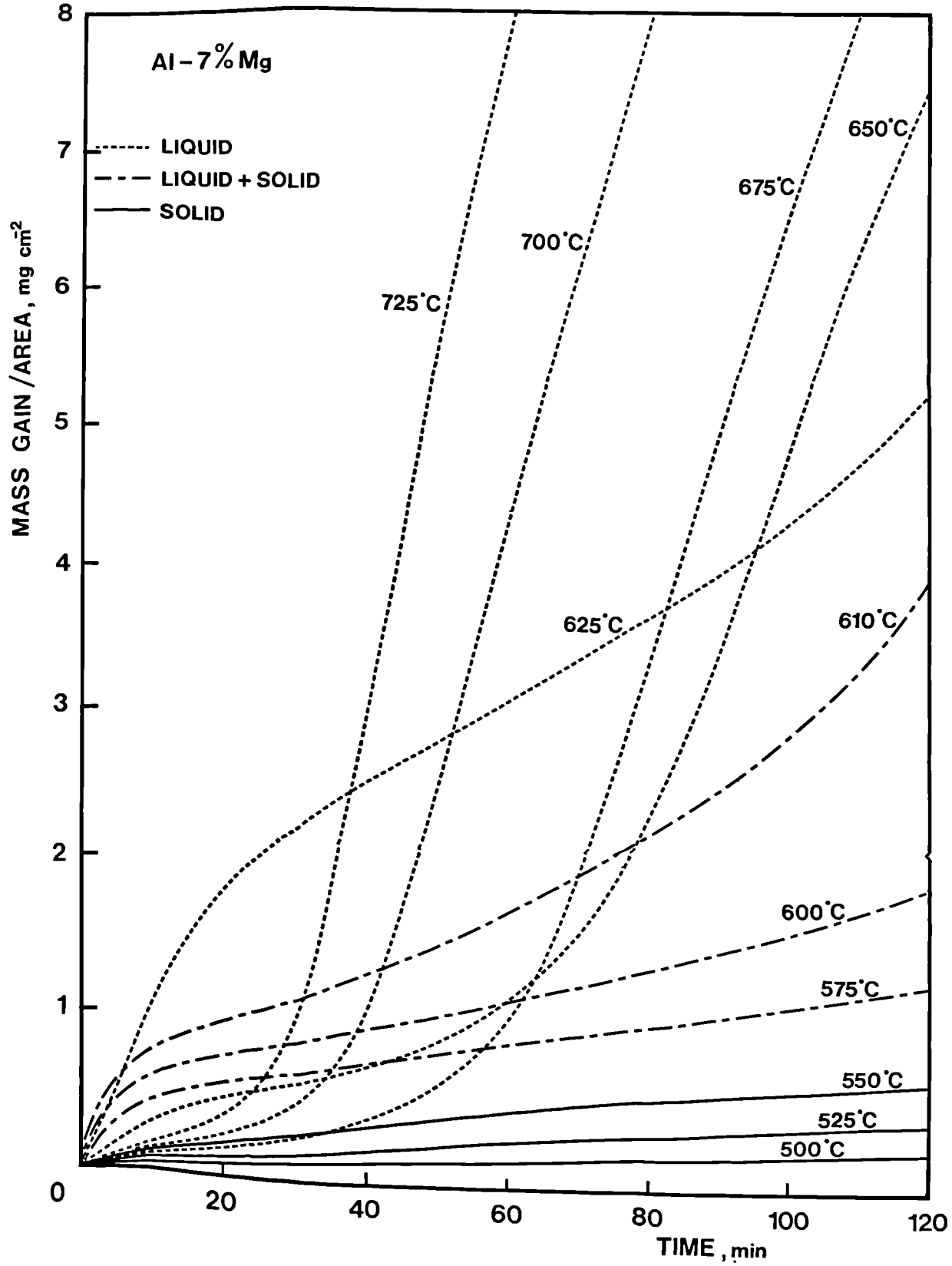

Figure 58. Mass gain as a function of time for Al-7.4% Mg alloy exposed to the moist atmosphere in the temperature range 500-725°C.

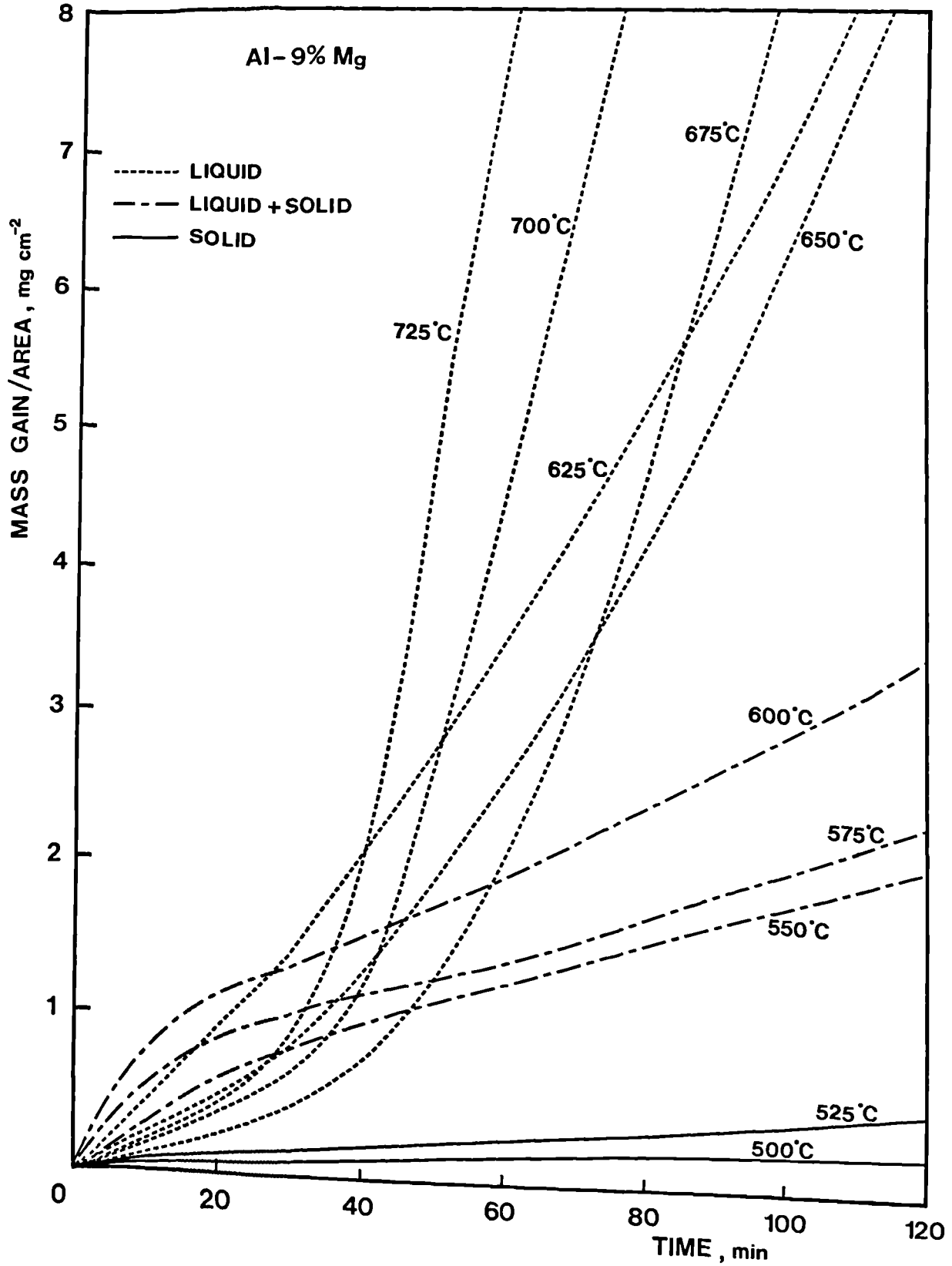

Figure 59. Mass gain as a function of time for Al-9.3% Mg alloy exposed to the dry atmosphere in the temperature range 500-725°C.

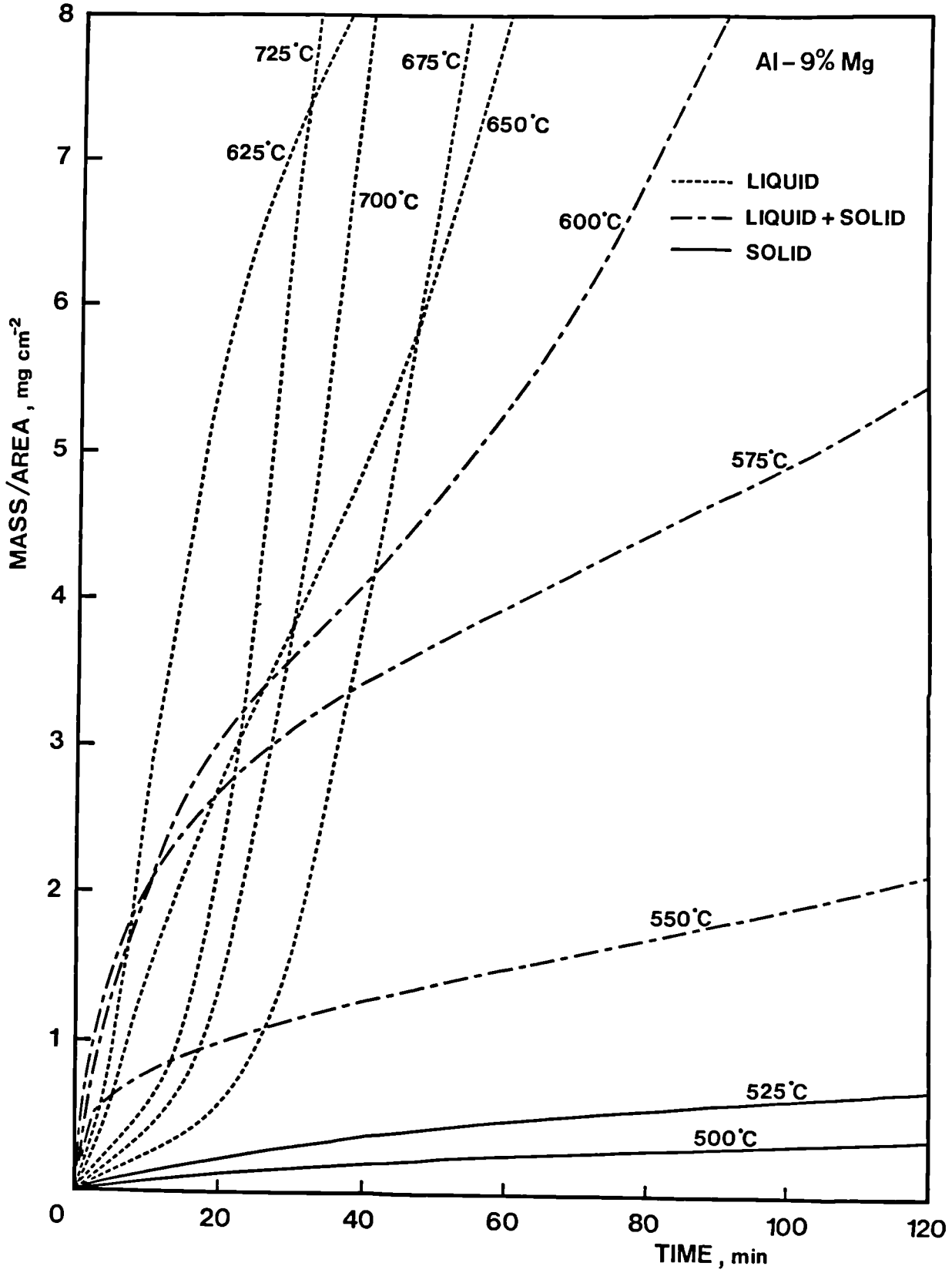

Figure 60. Mass gain as a function of time for Al-9.3% Mg alloy exposed to the moist atmosphere in the temperature range 500-725°C.

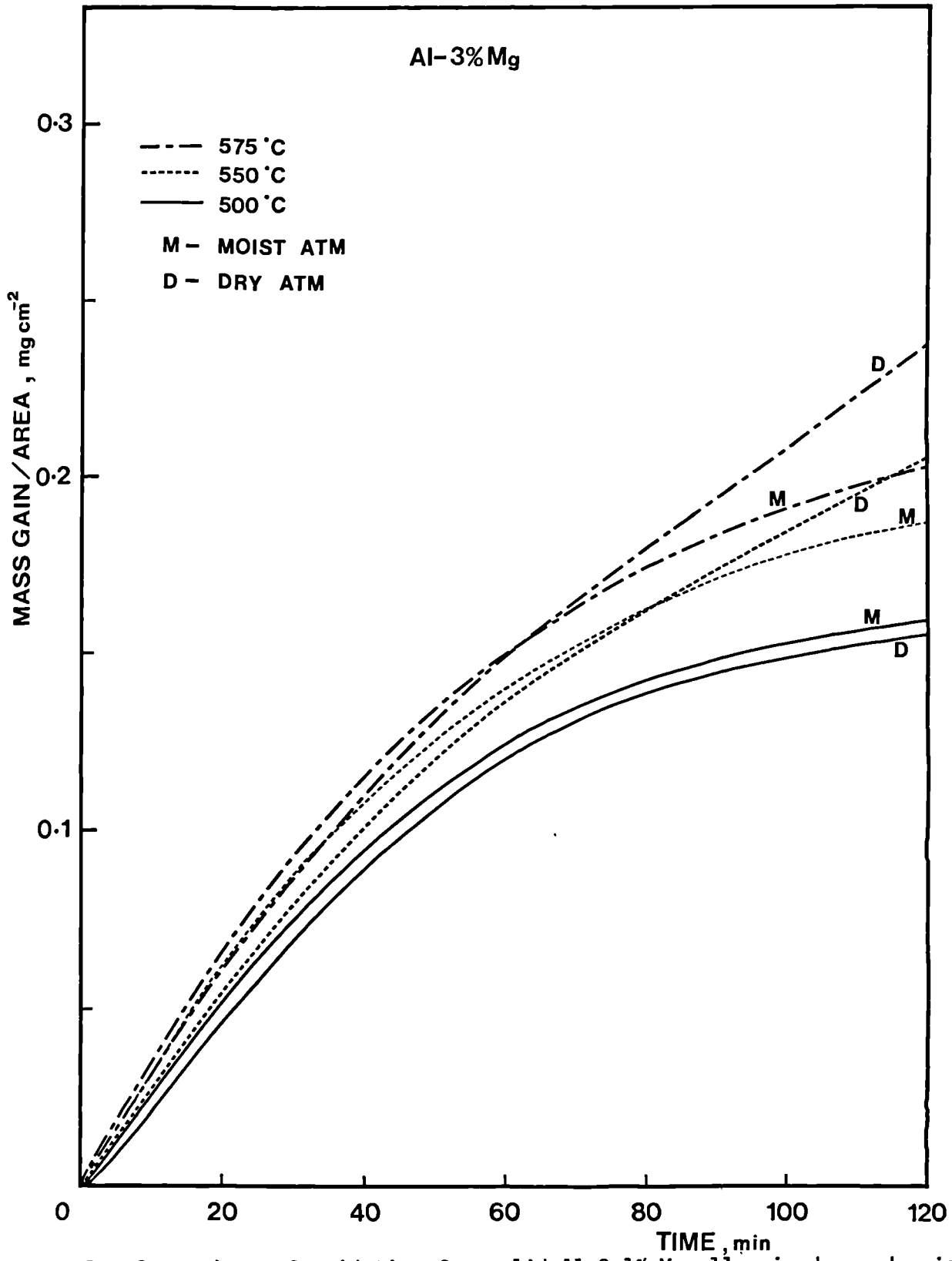

Figure 61. Comparison of oxidation for solid Al-3.1% Mg alloy in dry and moist atmospheres at various temperatures showing:

(a) initial faster oxidation in the moist atmosphere.

(b) crossover of mass gain curves; note that crossover advances to lower critical times (t_c) of oxidation with increasing temperature.

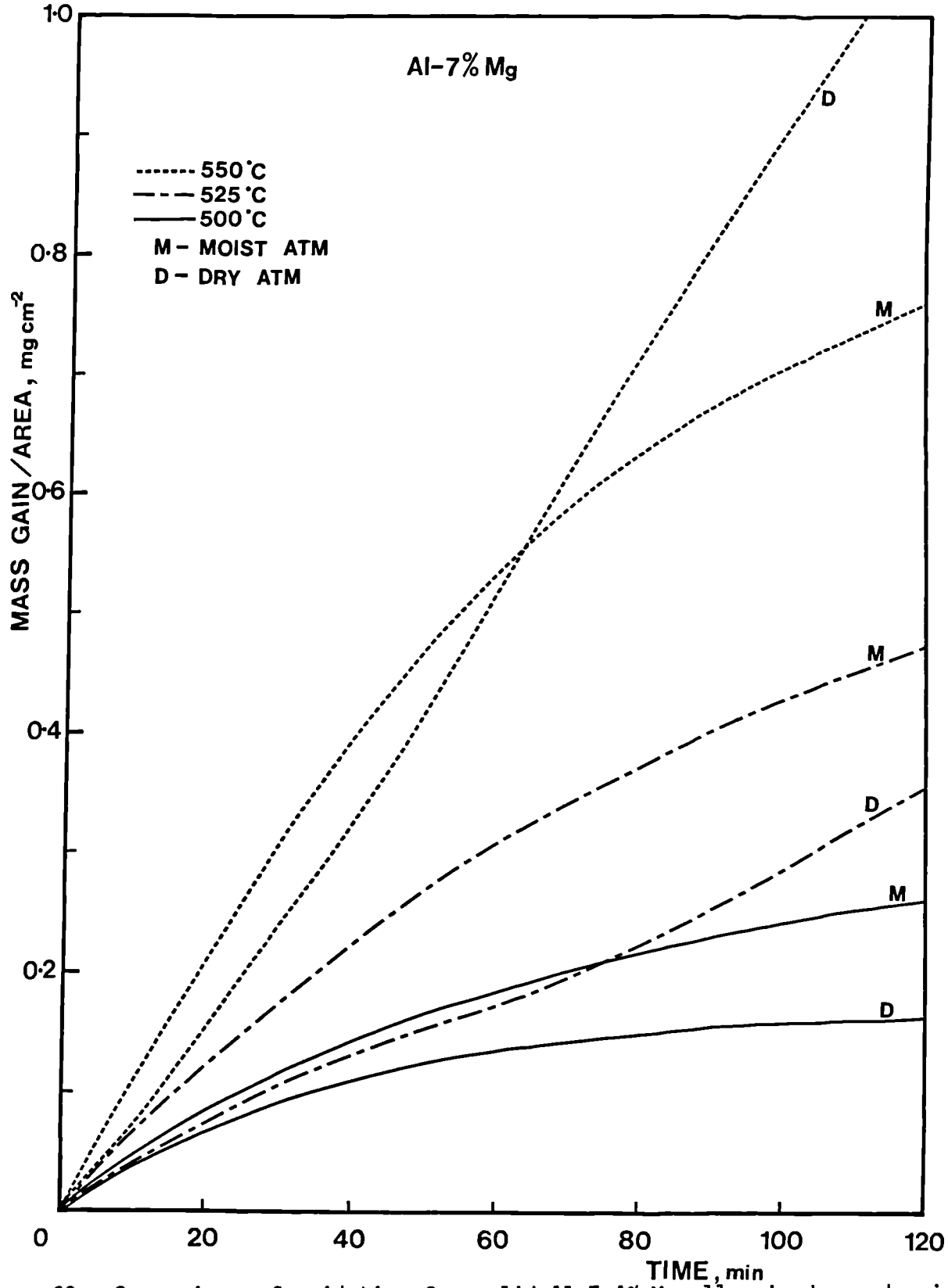

gure 62. Comparison of oxidation for solid Al-7.4% Mg alloy in dry and moist atmospheres at various temperatures showing:

(a) initial faster oxidation in the moist atmosphere.

(b) crossover of mass gain curves; note that crossover advances to lower critical times (t_c) of oxidation with increasing temperature.

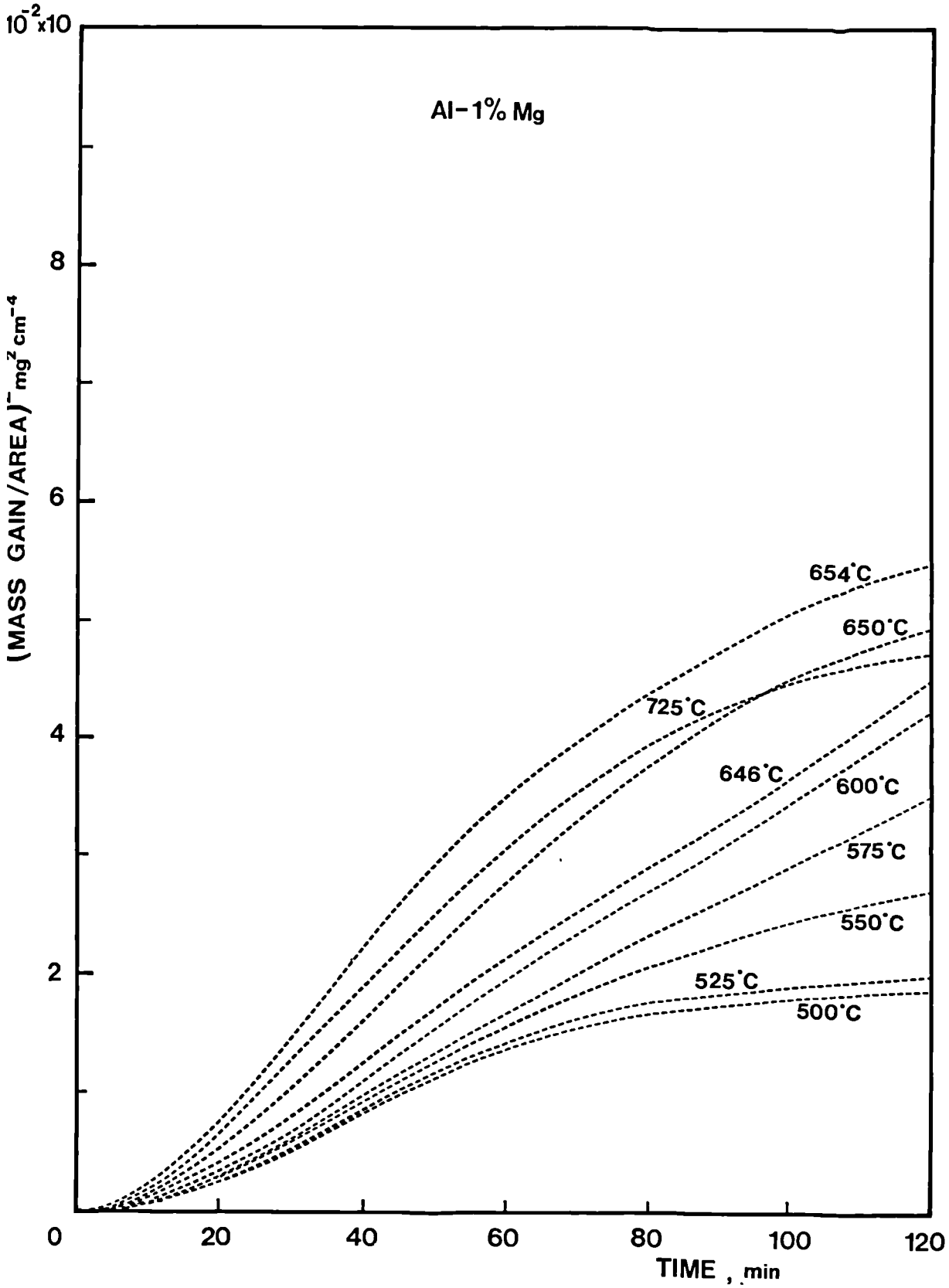

igure 63. Parabolic plots, i.e. Δm^2 v time, for Al-1.3% Mg alloy exposed to the dry atmosphere in the temperature range 500-725^{o}C.

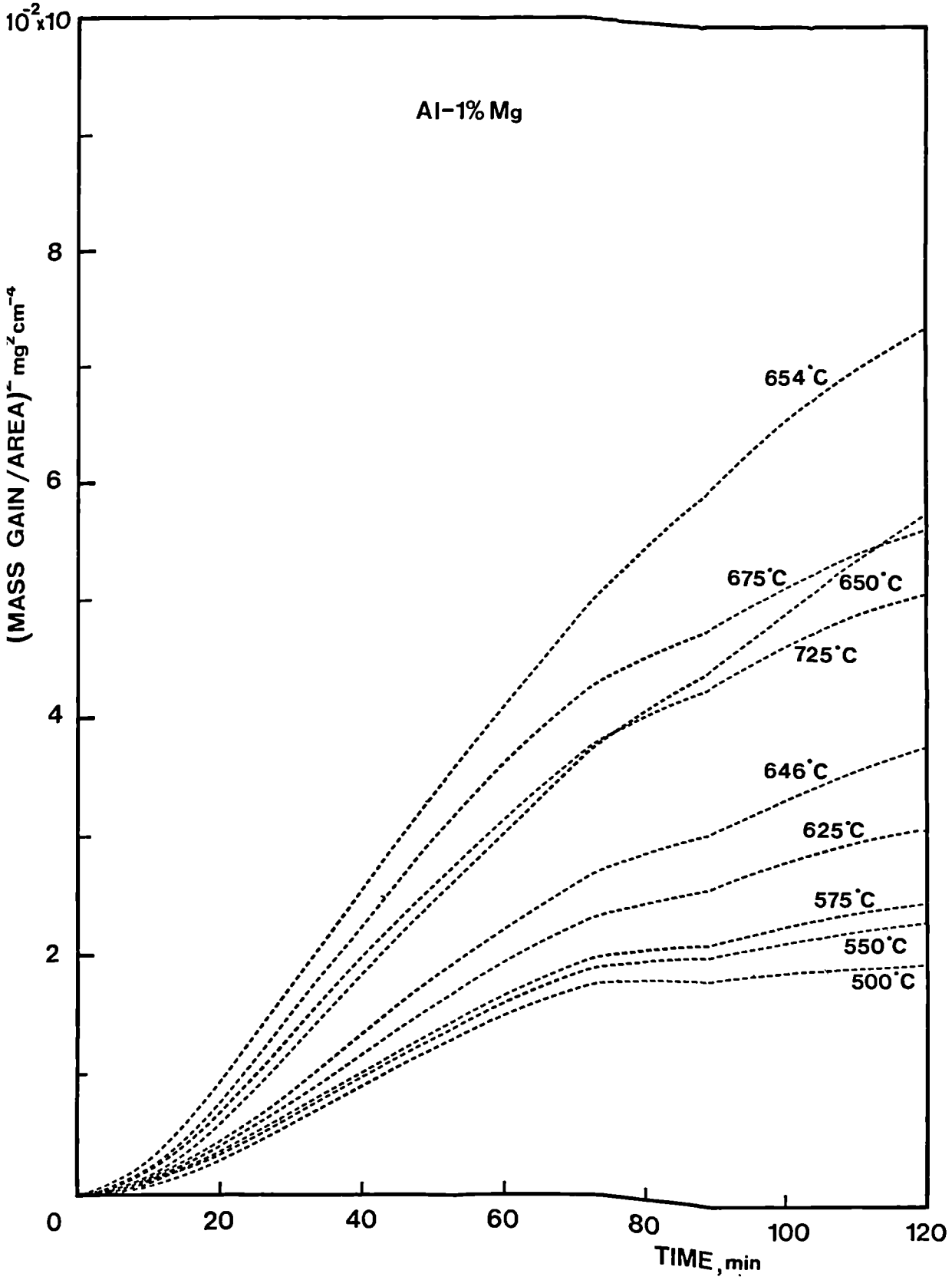

igure 64. Parabolic plots, i.e. Δm^2 v time, for Al-1.3% Mg alloy exposed to the moist atmosphere in the temperature range 500-725^{o}C.

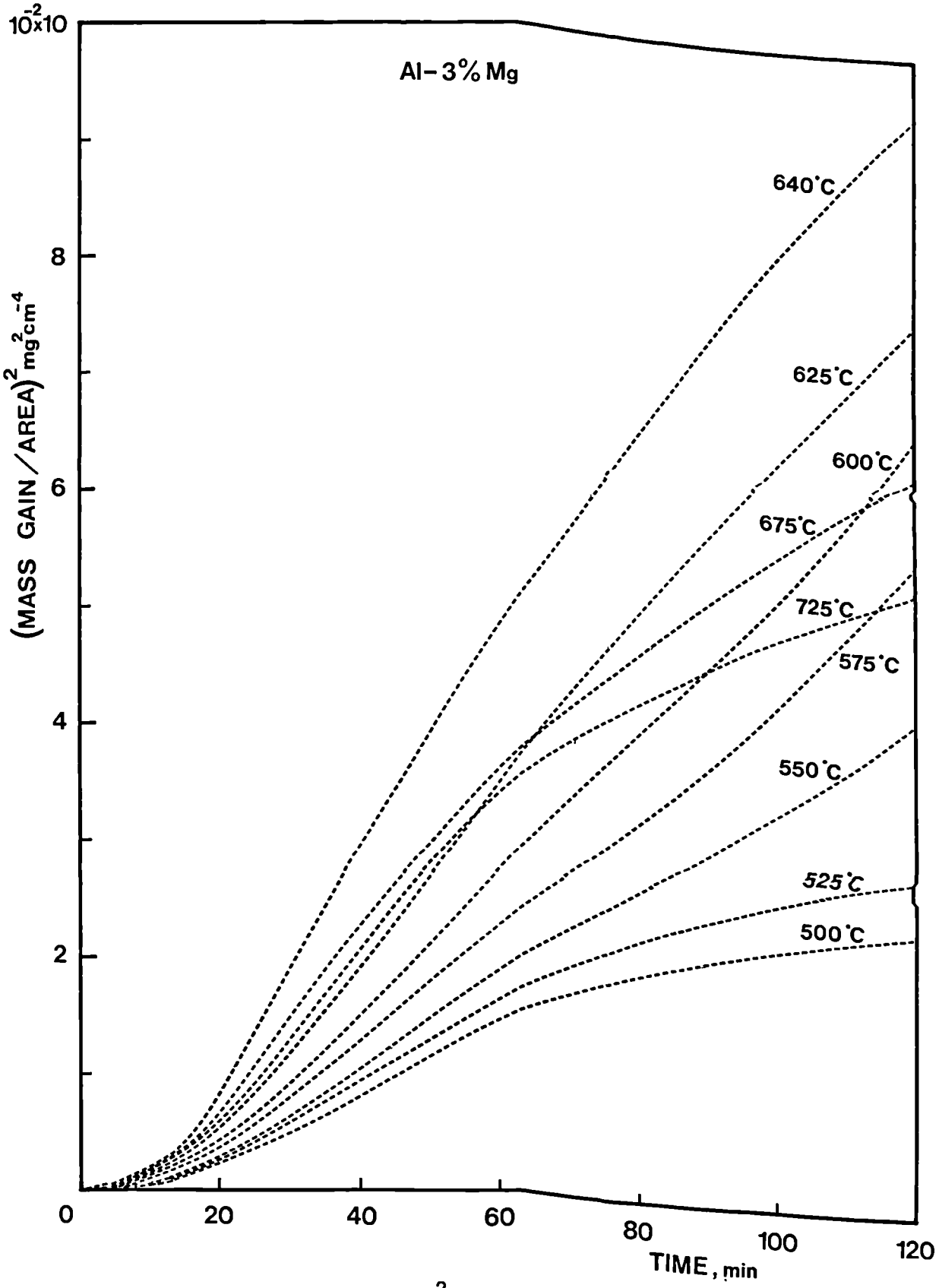

Figure 65. Parabolic plots, i.e. Δm^2 v time, for Al-3.1% Mg alloy exposed to the dry atmosphere in the temperature range 500-725°C.

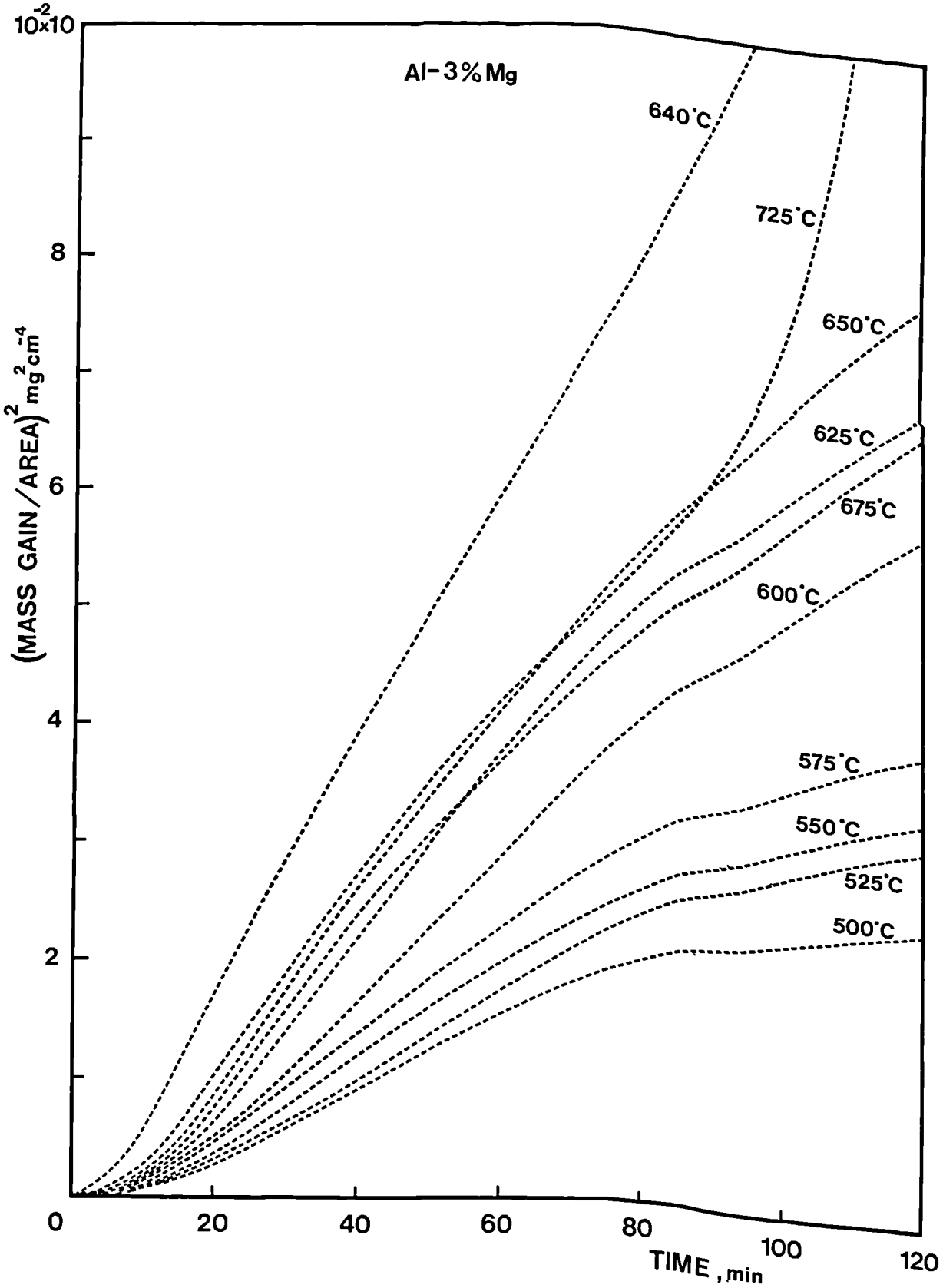

igure 66. Parabolic plots, i.e. Δm^2 v time, for Al-3.1% Mg alloy exposed to the moist atmosphere in the temperature range 500-725°C.

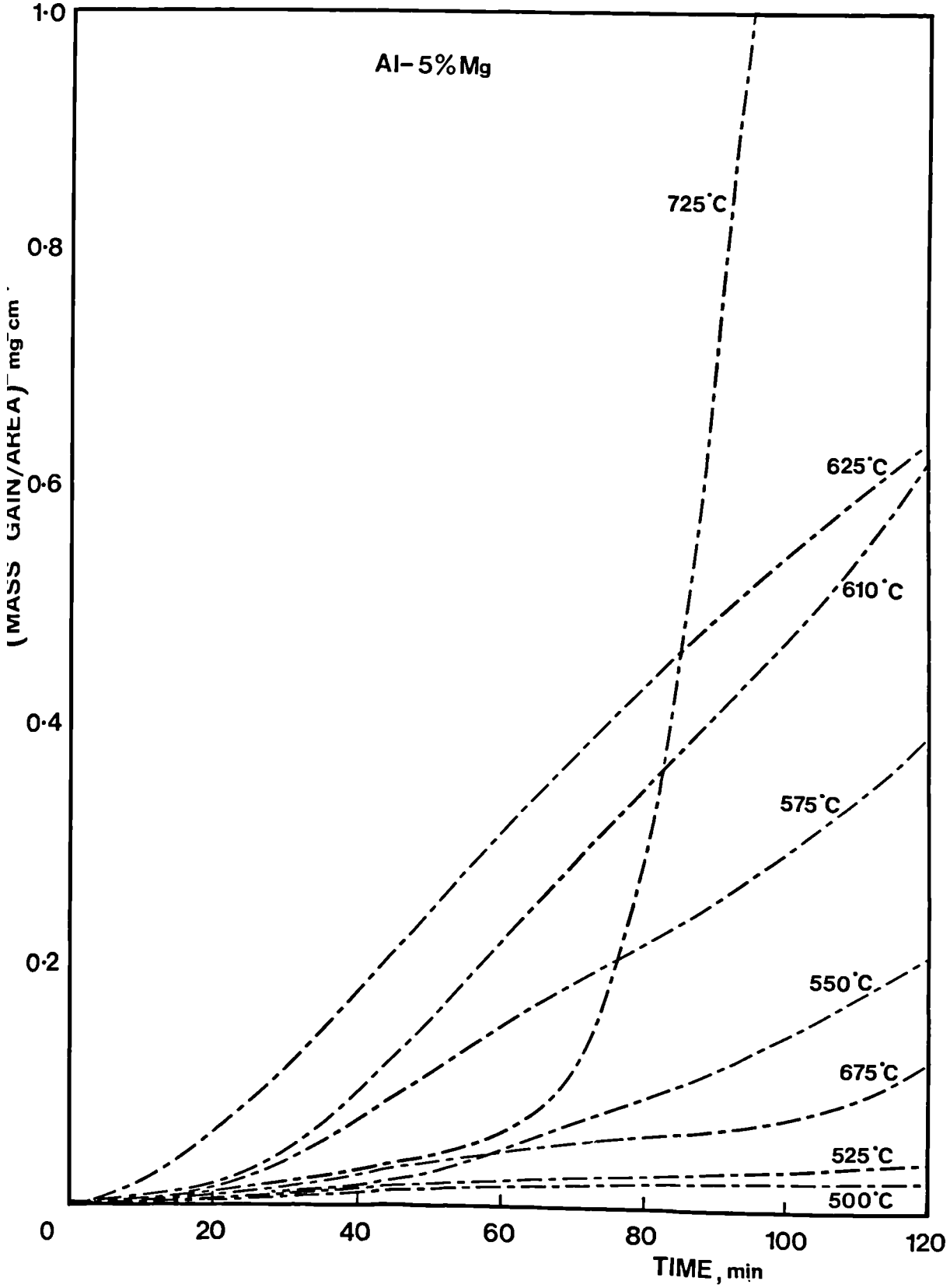

igure 67. Parabolic plots, i.e. Δm^2 v time, for Al-5.1% Mg alloy exposed to the dry atmosphere in the temperature range 500-725°C.

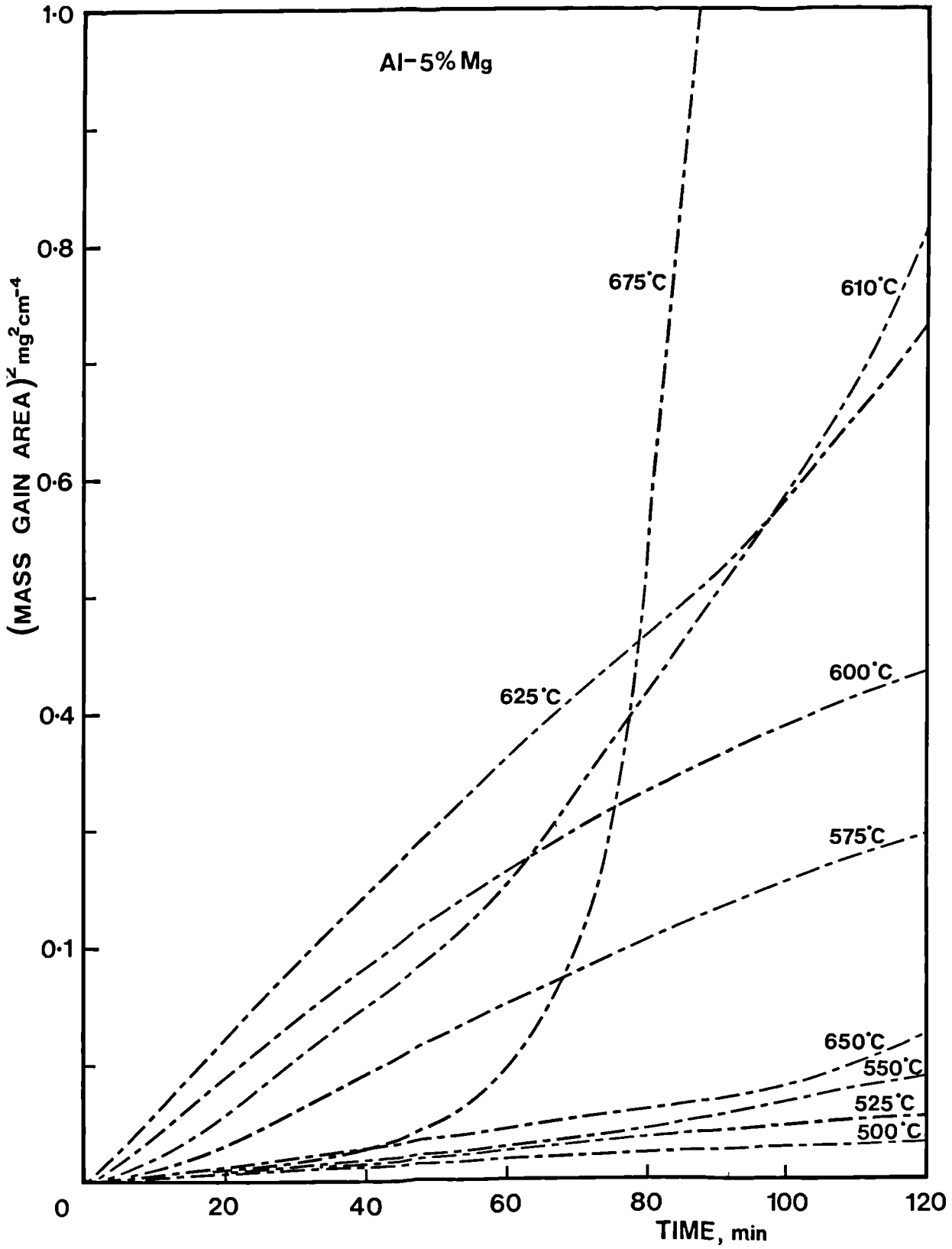

Figure 68. Parabolic plots, i.e. Δm^2 v time, for Al-5.1% Mg alloy exposed to the moist atmosphere in the temperature range 500-725°C.

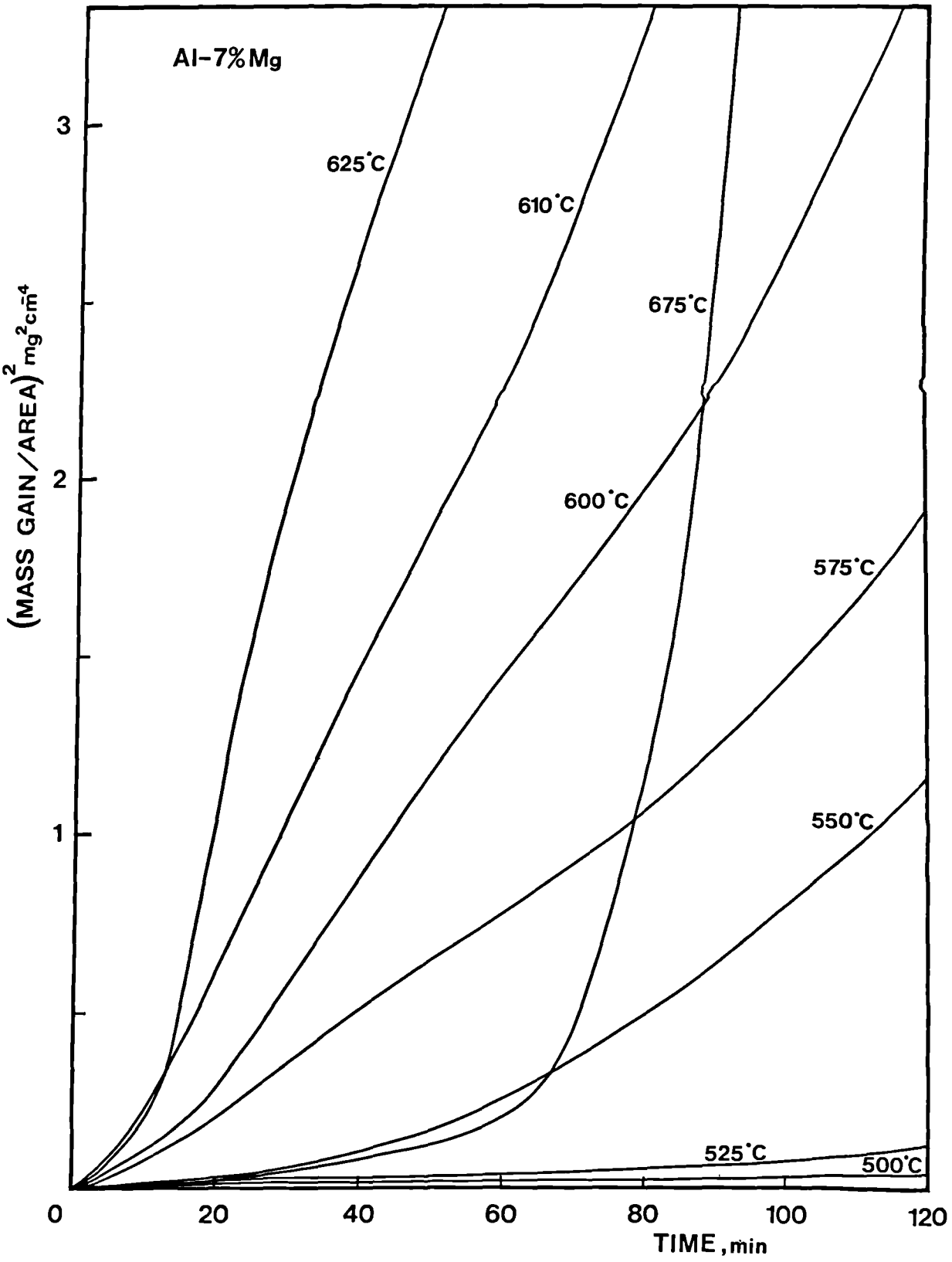

igure 69. Parabolic plots, i.e. Δm^2 v time, for Al-7.4% Mg alloy exposed to the dry atmosphere in the temperature range 500-725^{o}C.

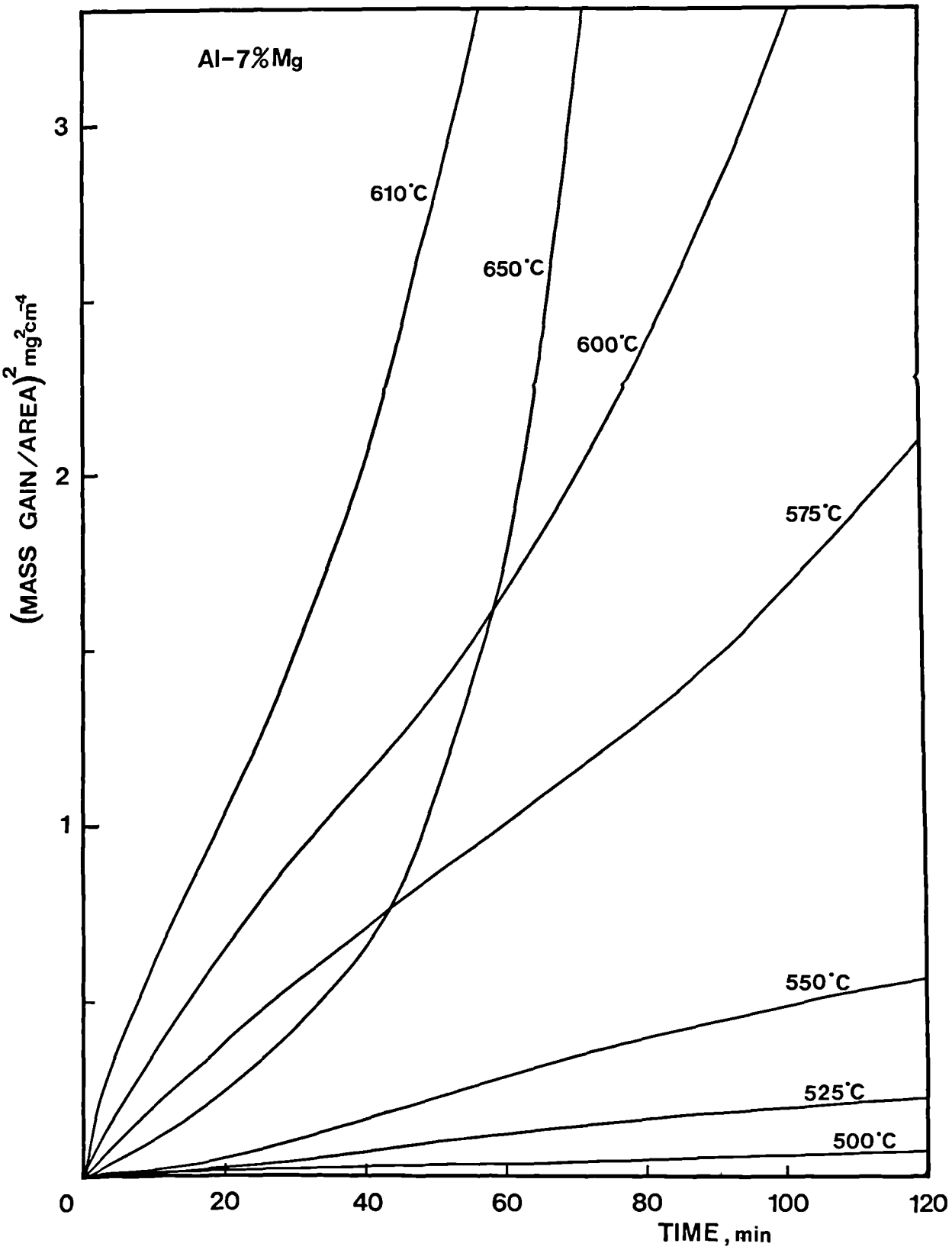

igure 70. Parabolic plots, i.e. Δm^2 v time, for Al-7.4% Mg alloy exposed to the moist atmosphere in the temperature range 500-725^{o}C.

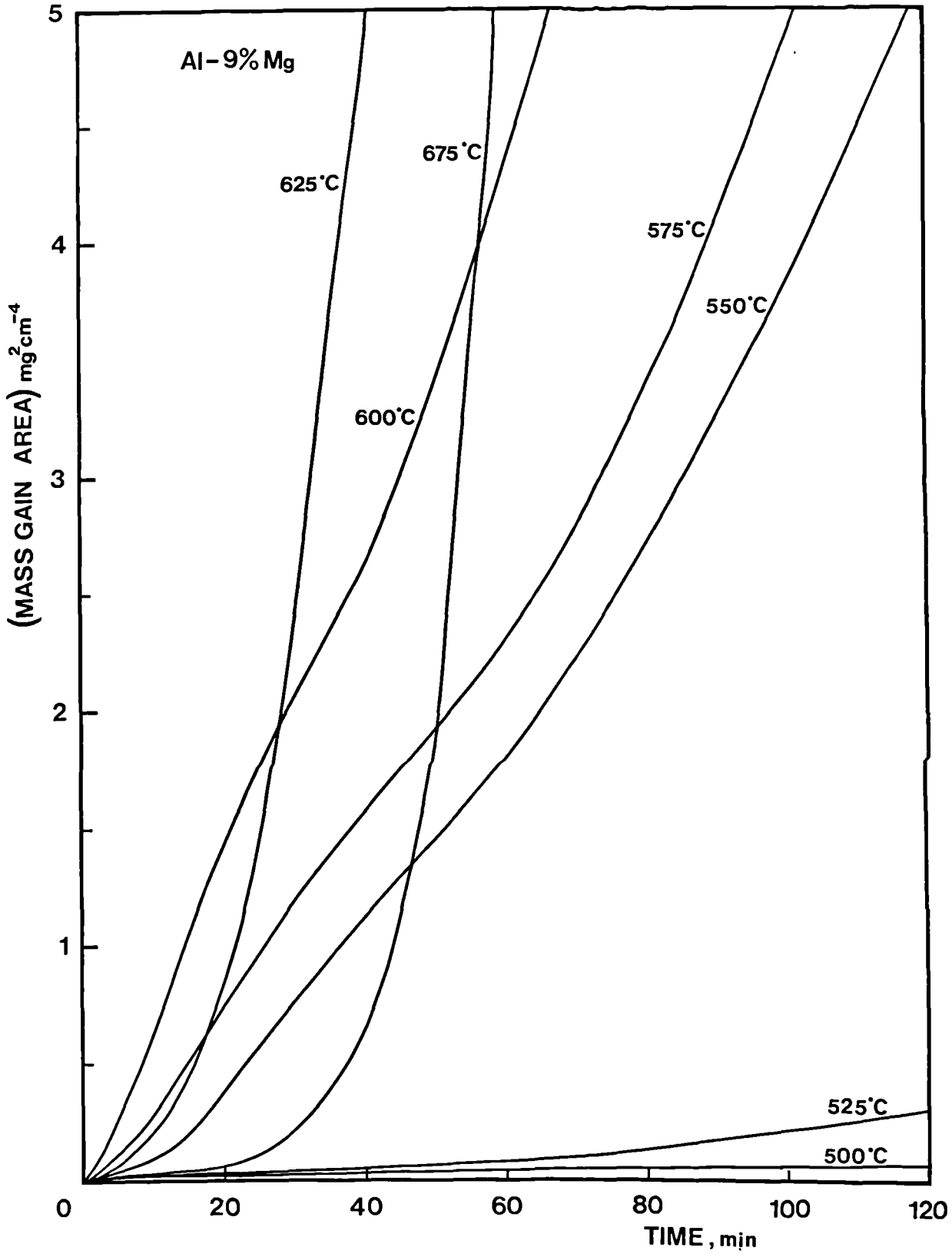

Figure 71. Parabolic plots, i.e. Δm^2 v time, for Al-9.3% Mg alloy exposed to the dry atmosphere in the temperature range 500-725°C.

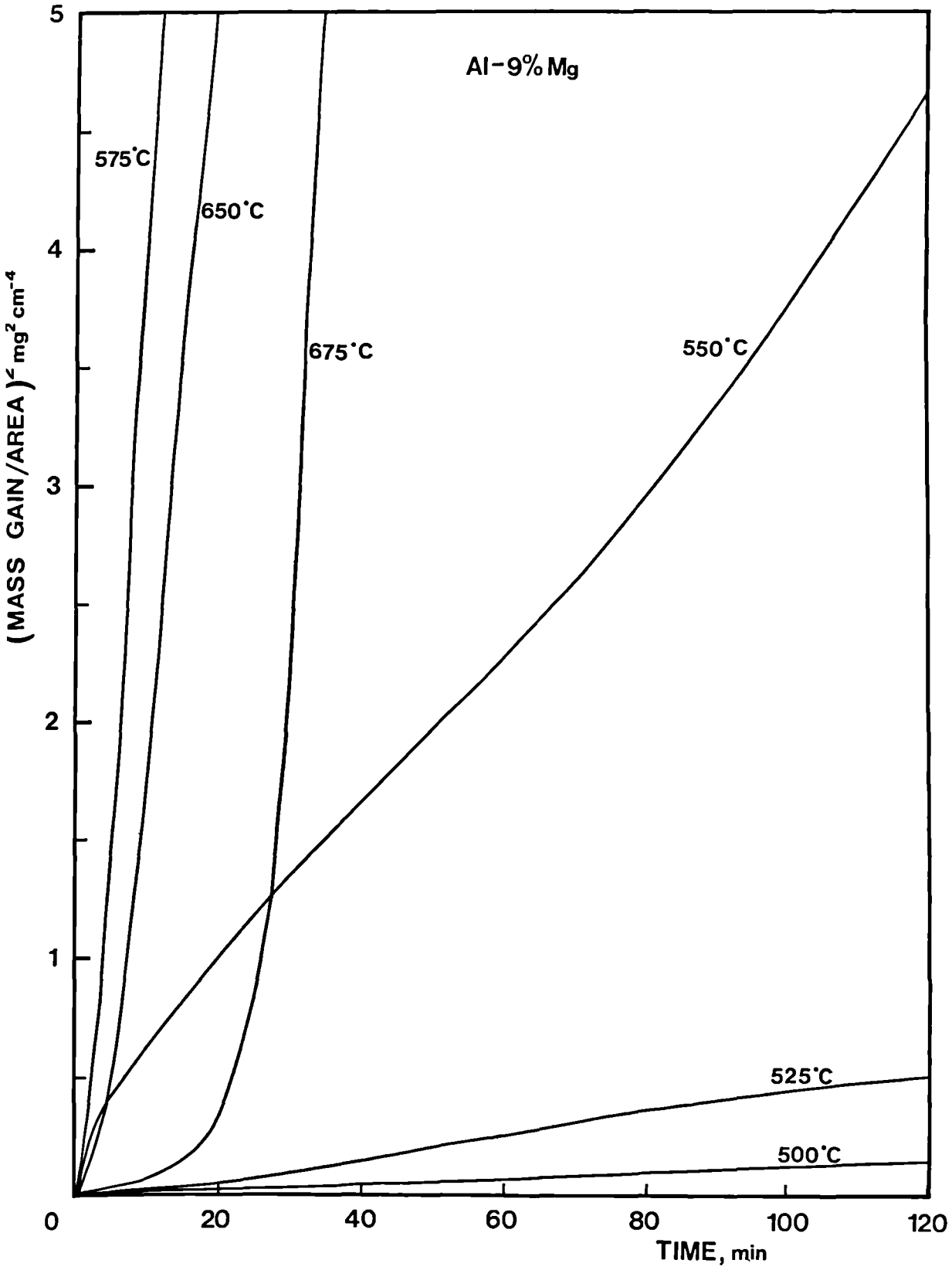

igure 72. Parabolic plots, i.e. Δm^2 v time, for Al-9.3% Mg alloy exposed to the moist atmosphere in the temperature range 500-725^{o}C.

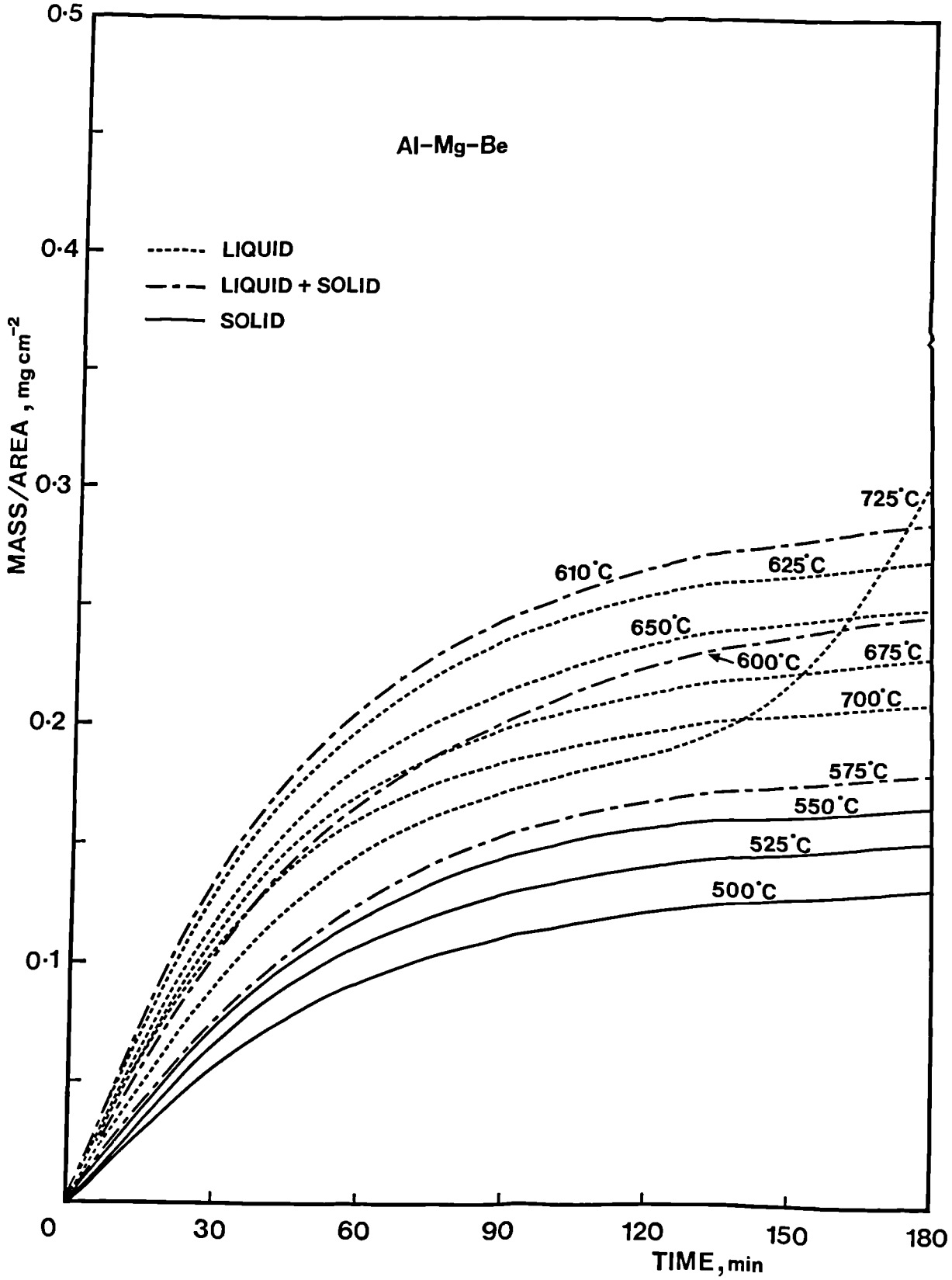

gure 73. Mass gain as a function of time for Al-8.2% Mg-0.003% Be alloy exposed to the dry atmosphere in the temperature range 500-725^{o}C.

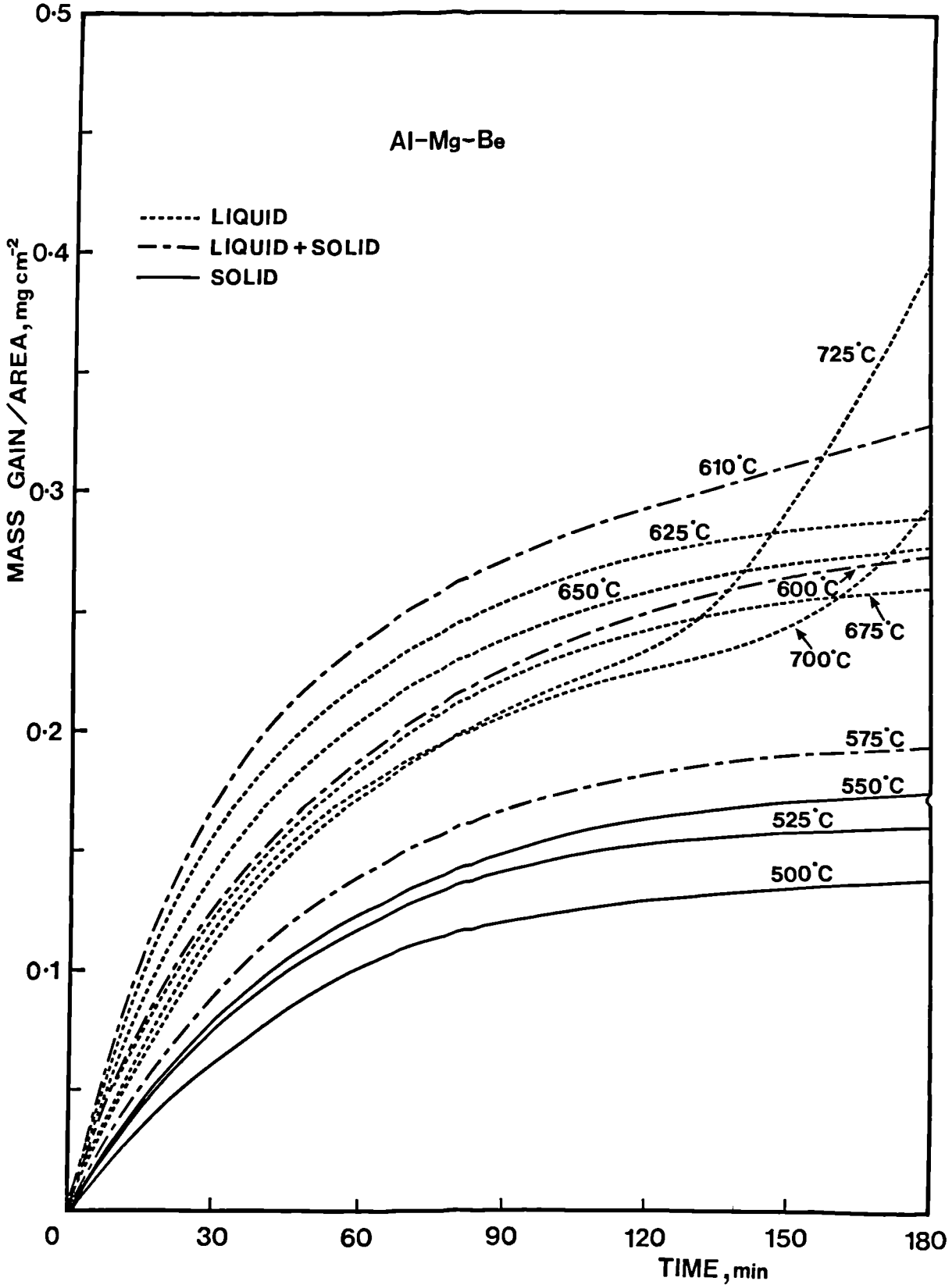

gure 74. Mass gain as a function of time for Al-8.2% Mg-0.003% Be alloy exposed to the moist atmosphere in the temperature range 500-725^{o}C.

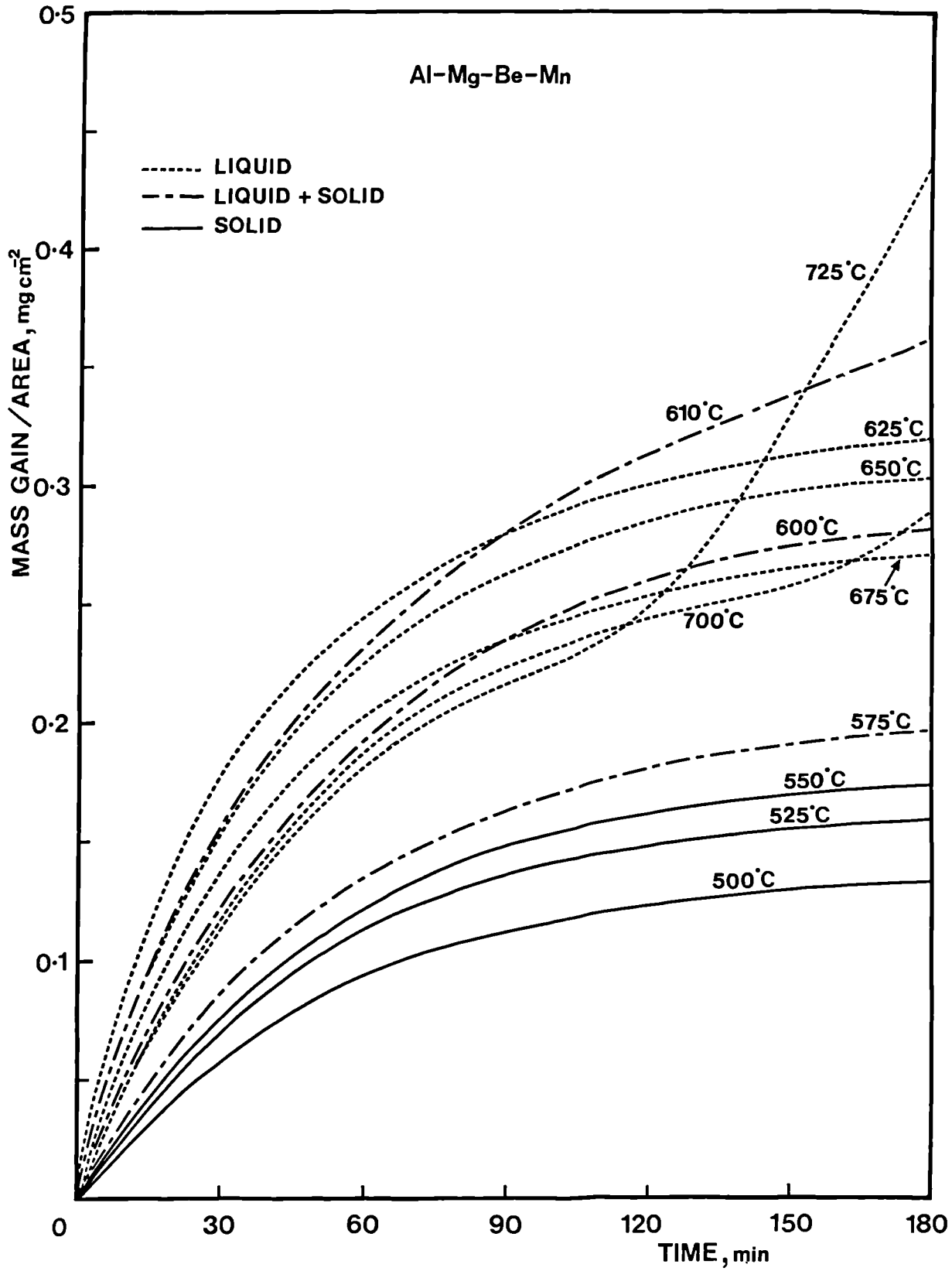

igure 75. Mass gain as a function of time for Al-8.16% Mg-0.003% Be-0.24% Mn alloy exposed to the dry atmosphere in the temperature range 500-725°C.

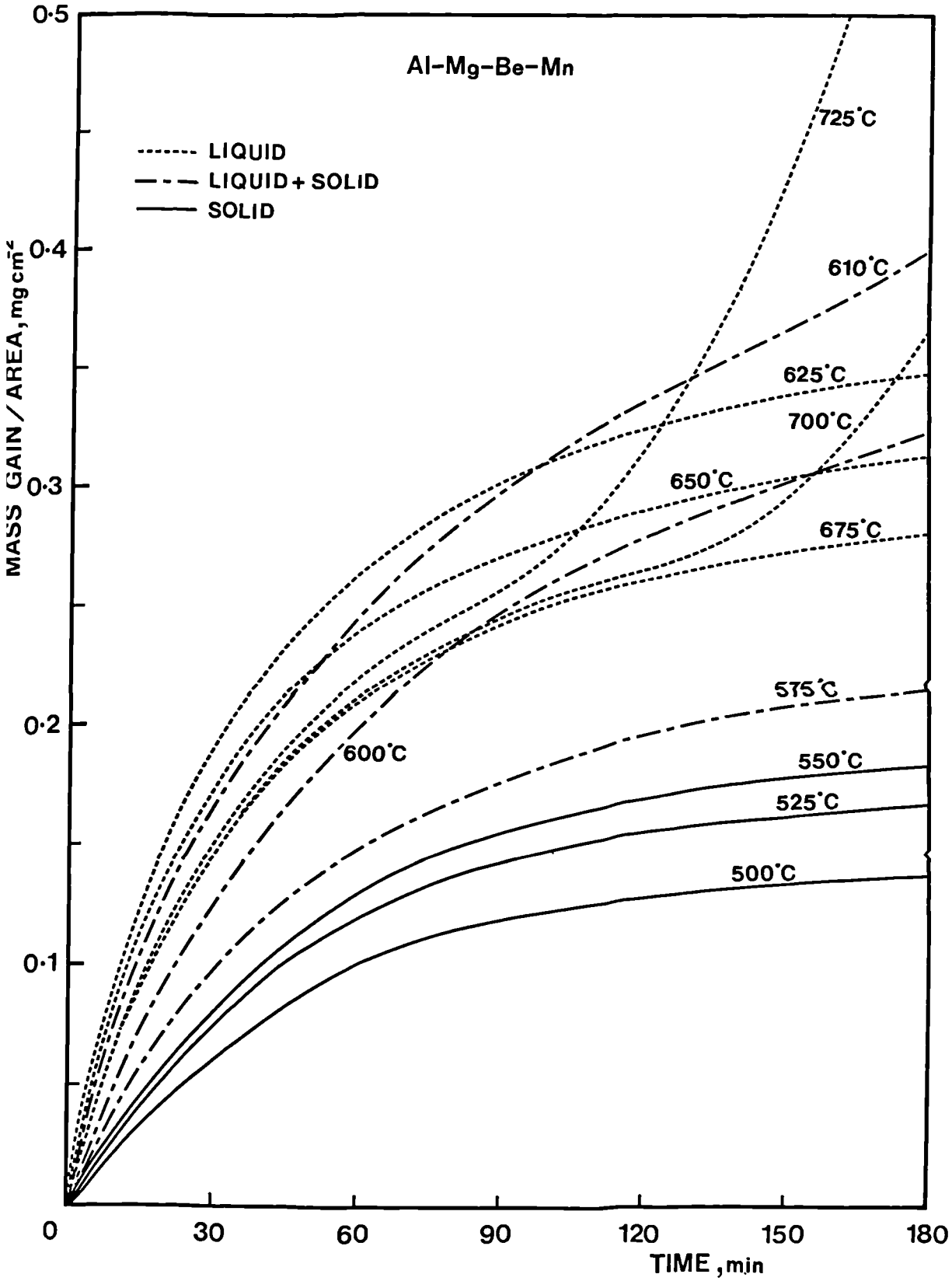

ɟure 76. Mass gain as a function of time for Al-8.16% Mg-0.003% Be-0.24% Mn alloy exposed to the moist atmosphere in the temperature range 500-725^{o}C.

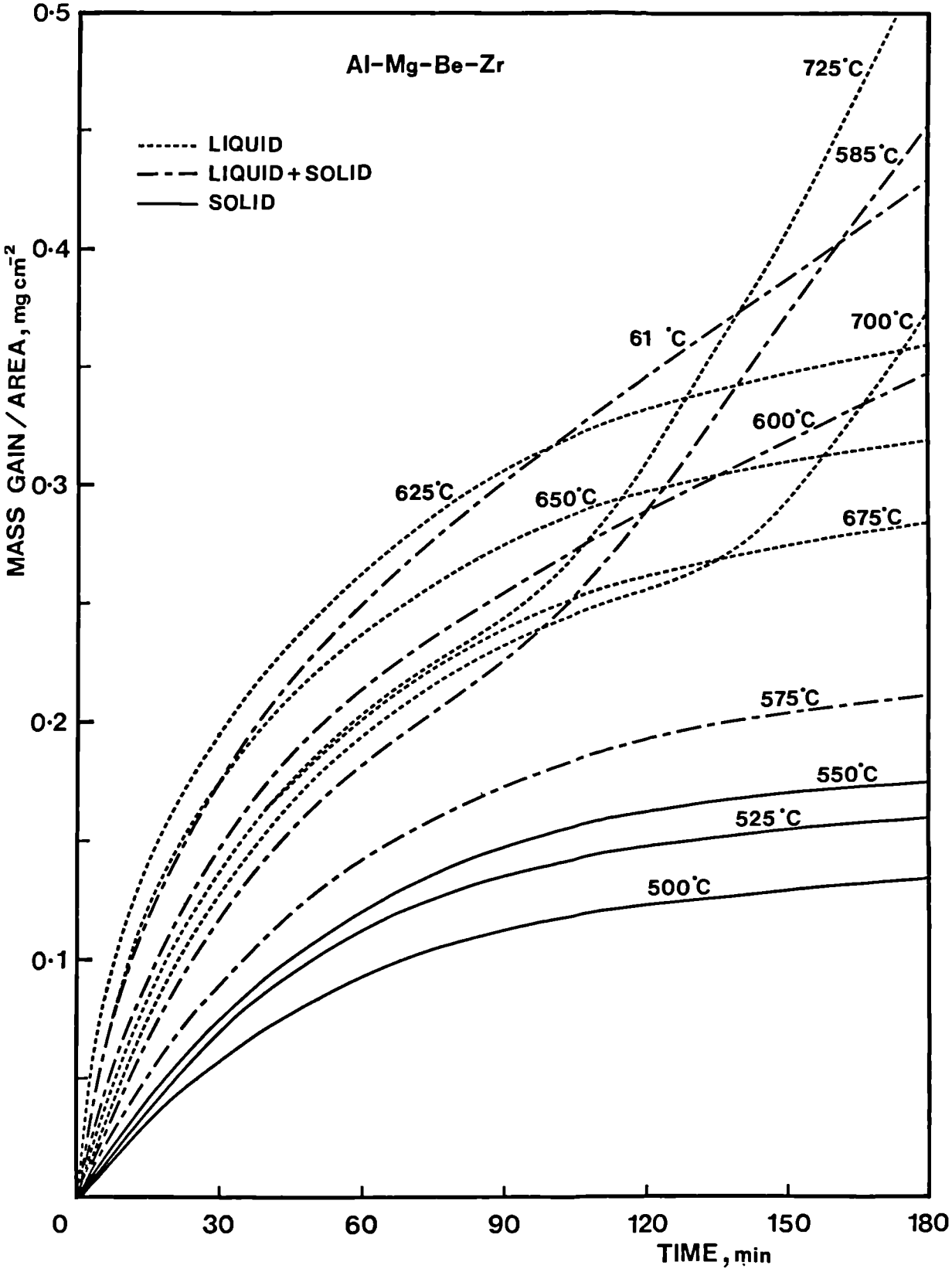

Figure 77. Mass gain as a function of time for Al-8.13% Mg-0.003% Be-0.12% Zr alloy exposed to the dry atmosphere in the temperature range 500-725°C.

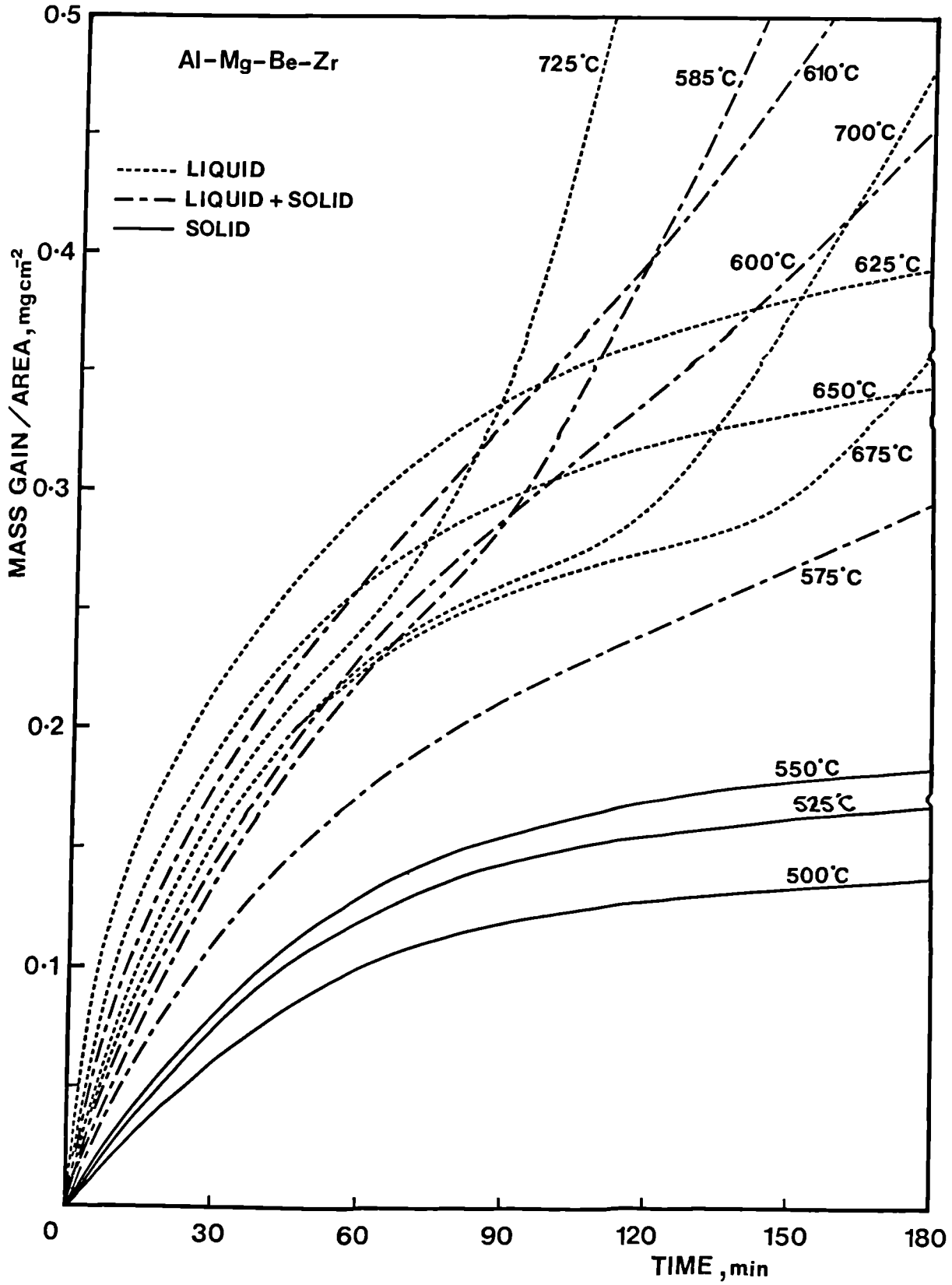

gure 78. Mass gain as a function of time for Al-8.13% Mg-0.003% Be-0.12% Zr alloy exposed to the moist atmosphere in the temperature range 500-725°C.

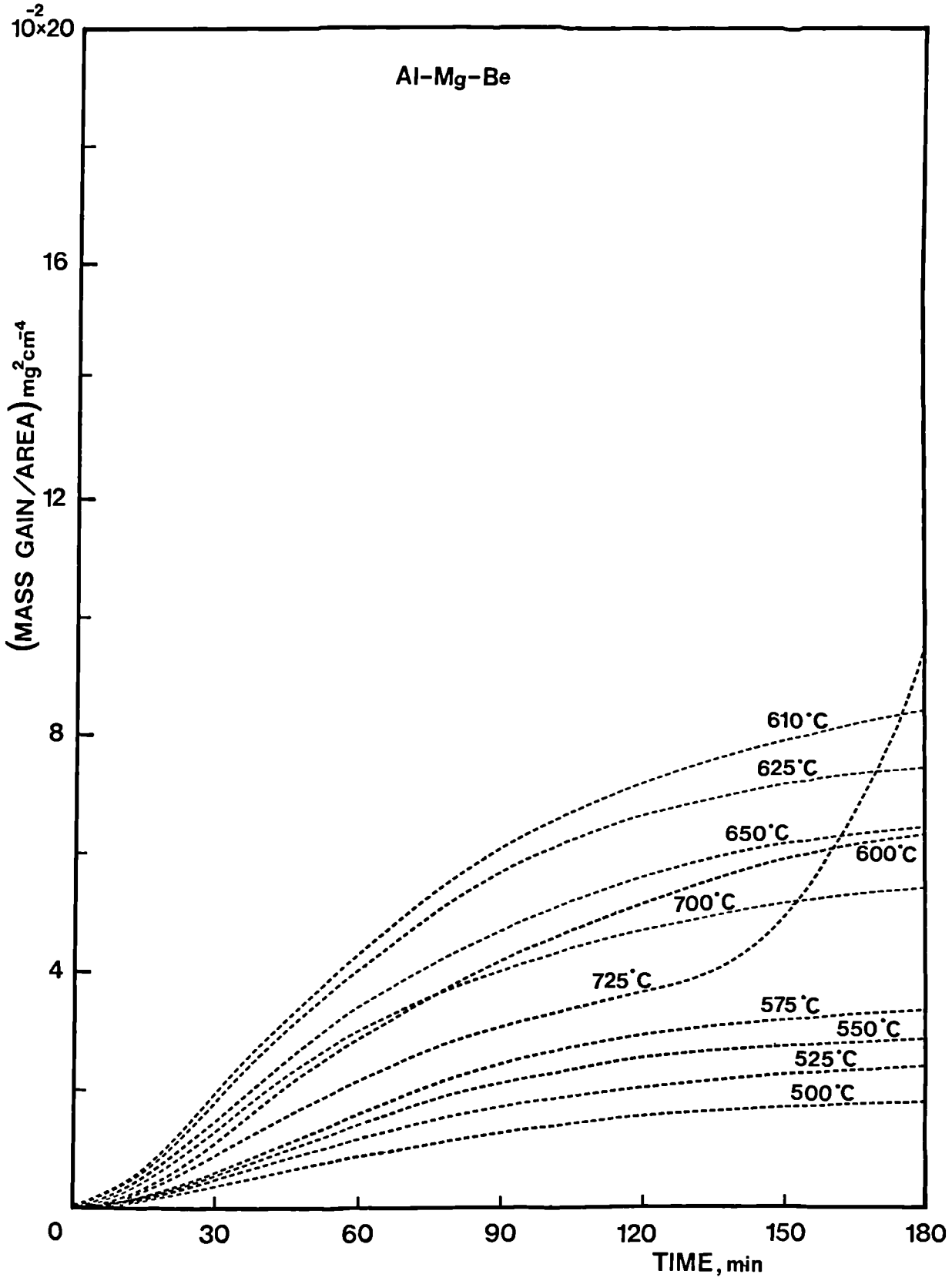

gure 79. Parabolic plots, i.e. Δm^2 v time, for Al-8.2% Mg-0.003% Be alloy exposed to the dry atmosphere in the temperature range 500-725^{o}C.

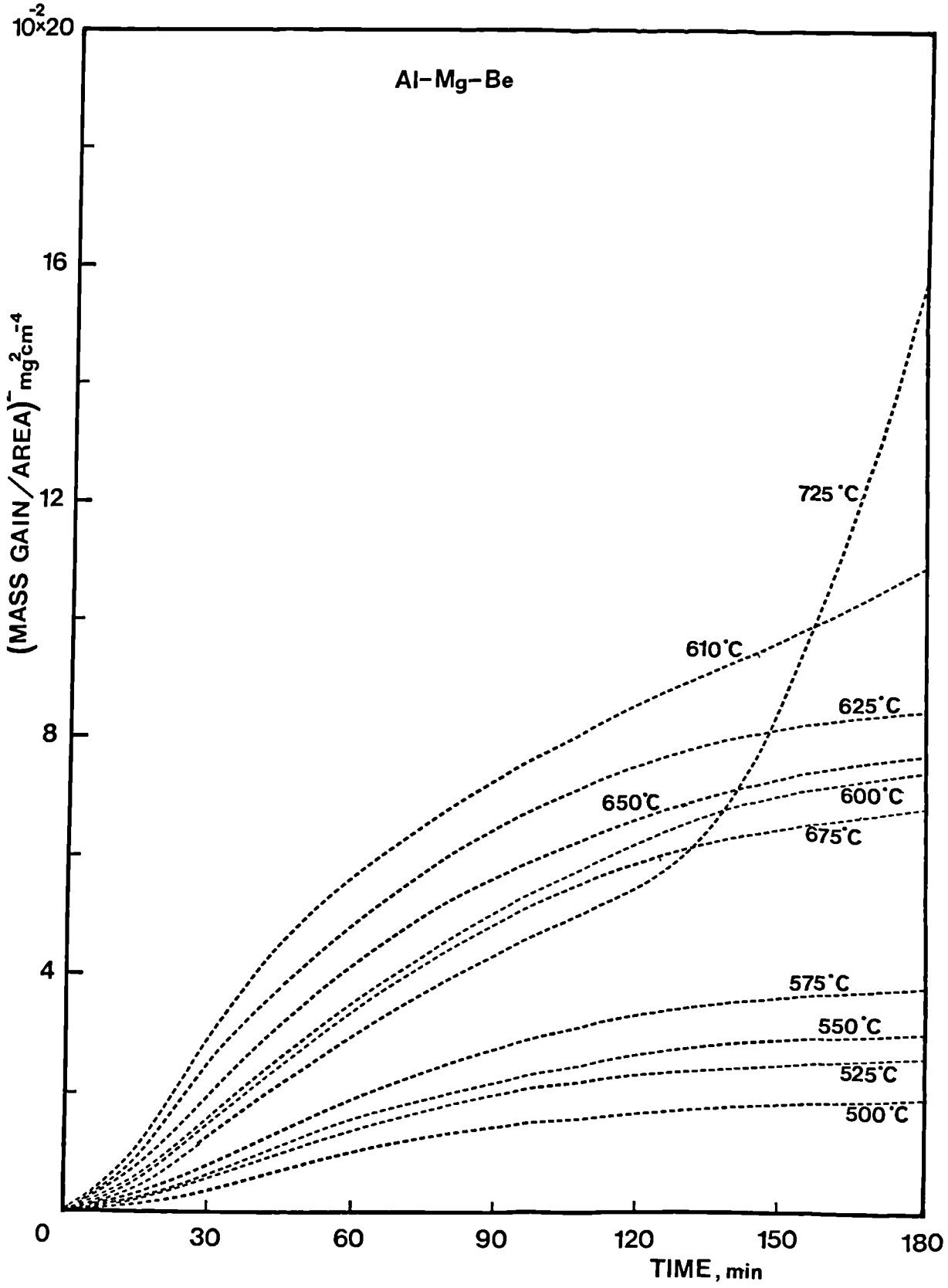

ure 80. Parabolic plots, i.e. Δm^2 v time, for Al-8.2% Mg-0.003% Be alloy exposed to the moist atmosphere in the temperature range 500-725°C.

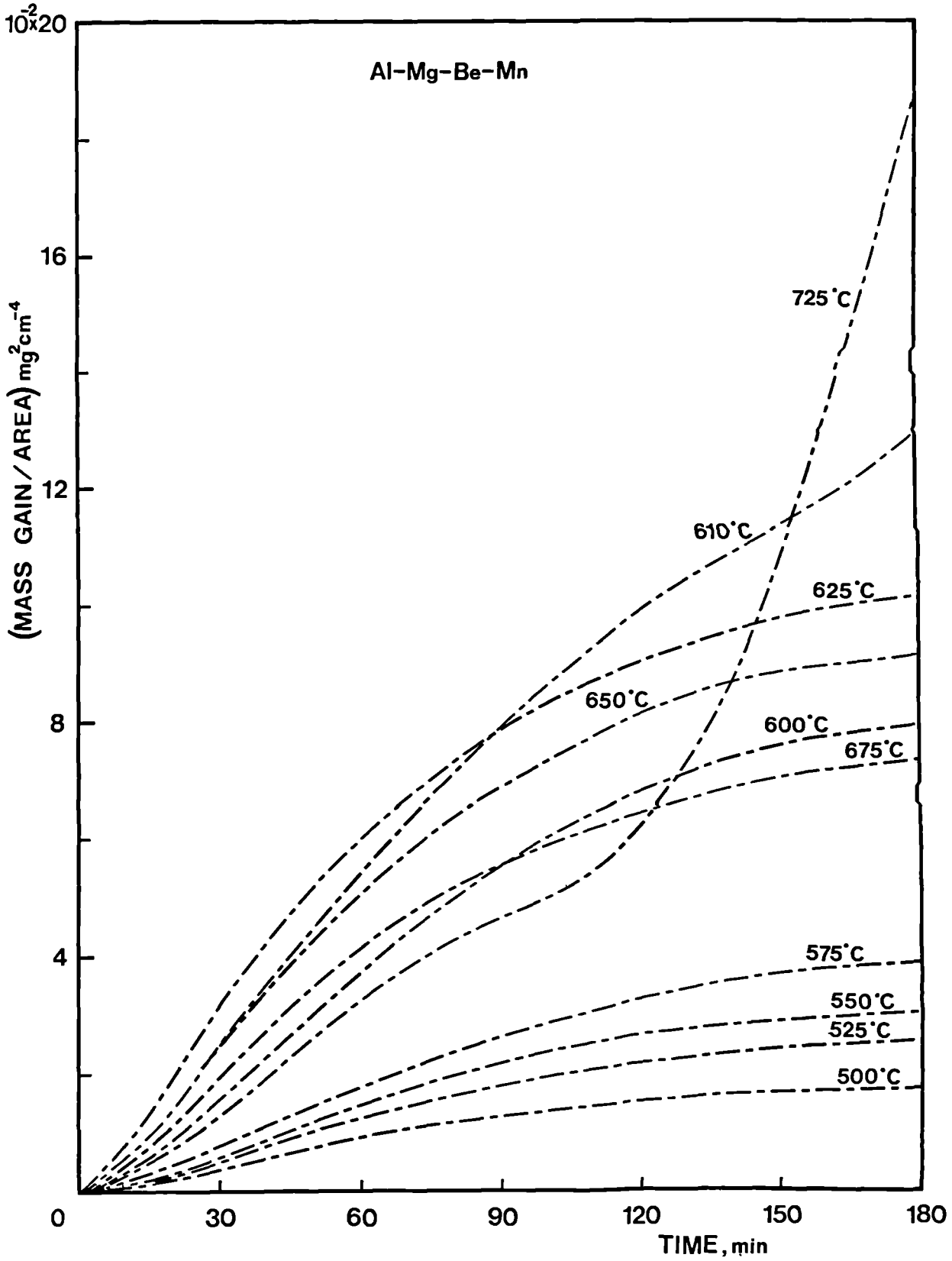

gure 81. Parabolic plots, i.e. Δm^2 v time, for Al-8.16% Mg-0.003% Be-0.24% Mn alloy exposed to the dry atmosphere in the temperature range 500-725°C.

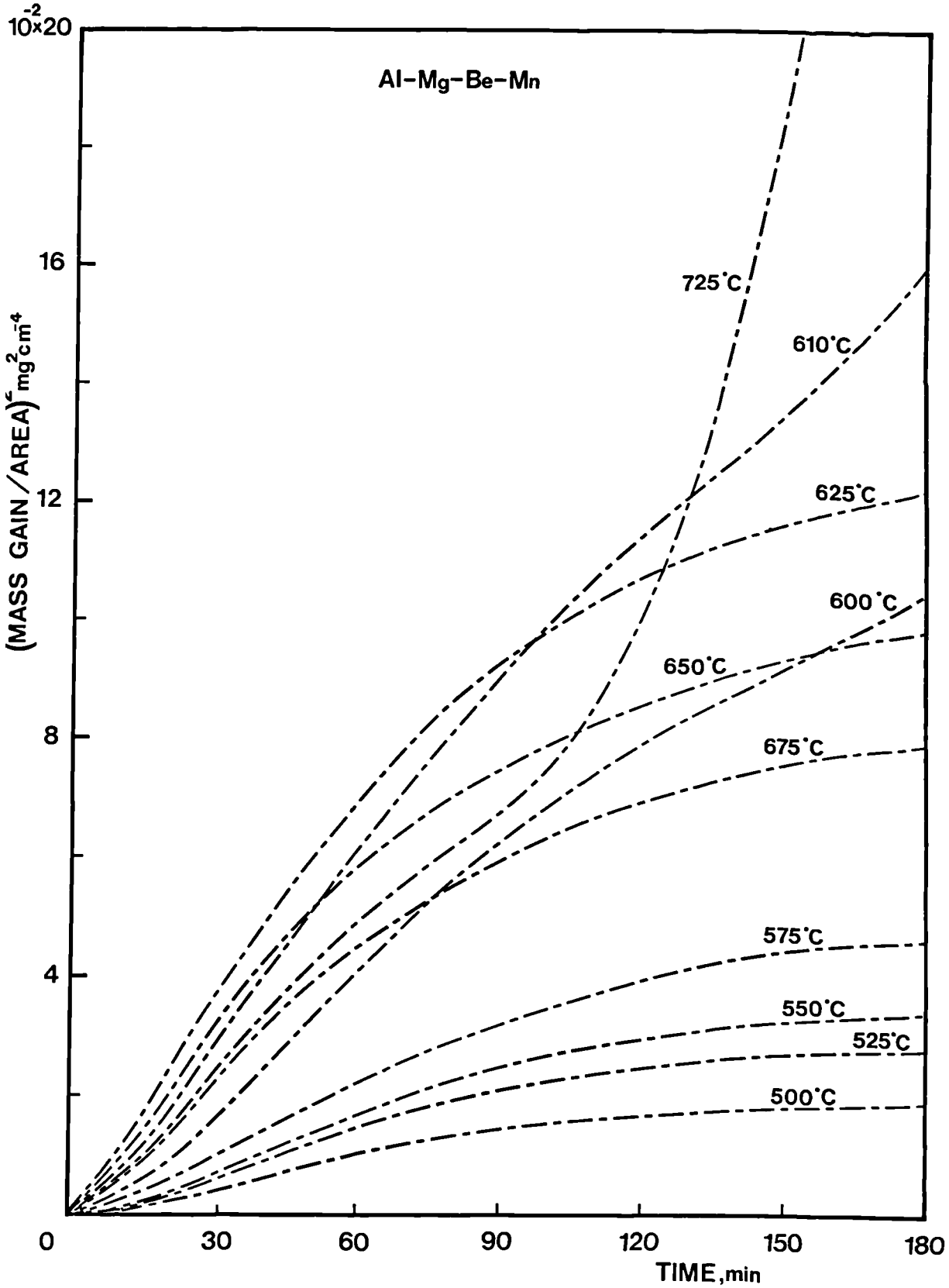

ure 82. Parabolic plots, i.e. Δm^2 v time, for Al-8.16% Mg-0.003% Be-0.24% Mn alloy exposed to the moist atmosphere in the temperature range 500-725^{o}C.

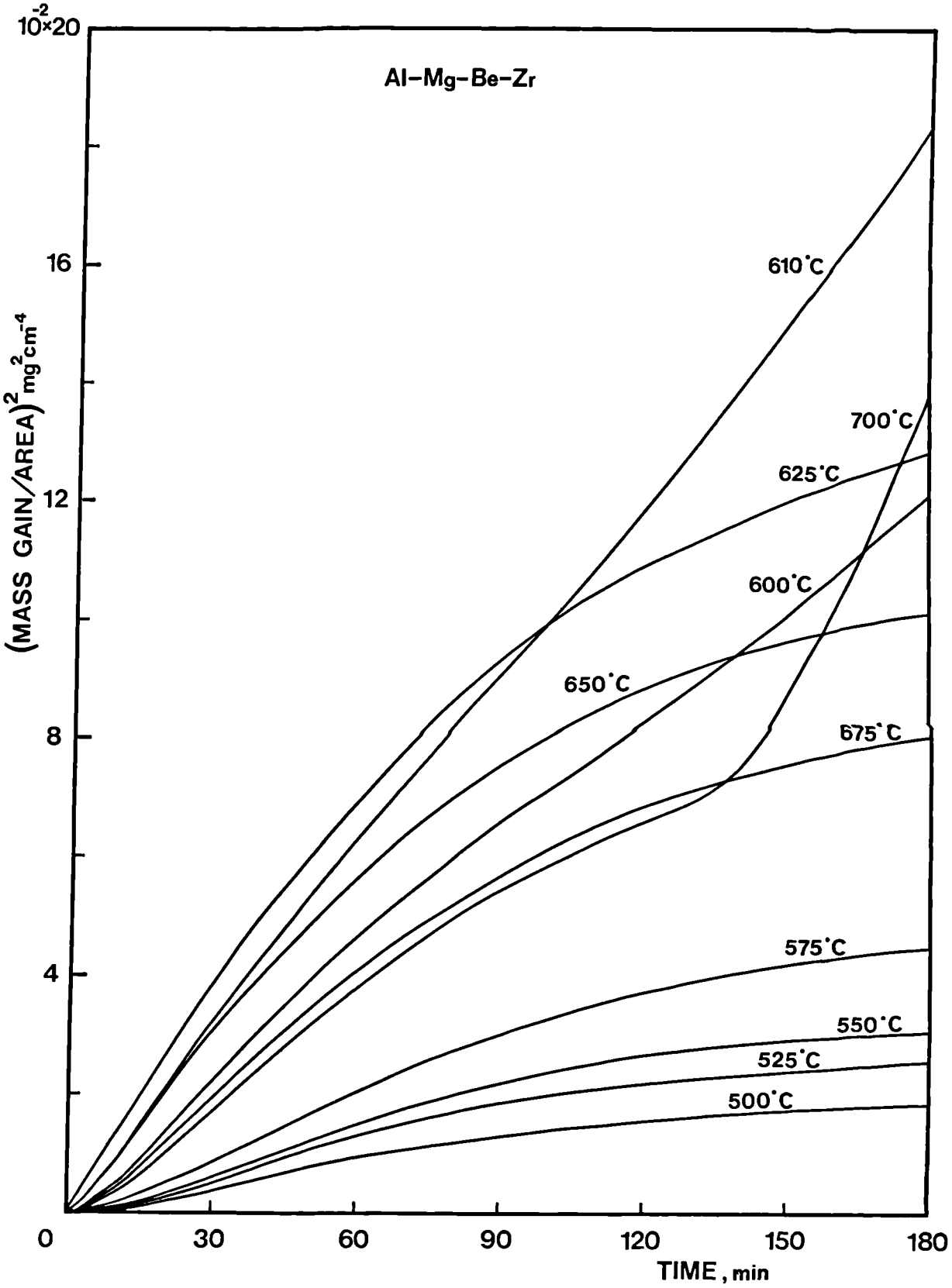

gure 83. Parabolic plots, i.e. Δm^2 v time, for Al-8.13% Mg-0.003% Be-0.12% Zr alloy exposed to the dry atmosphere in the temperature range 500-725^{o}C.

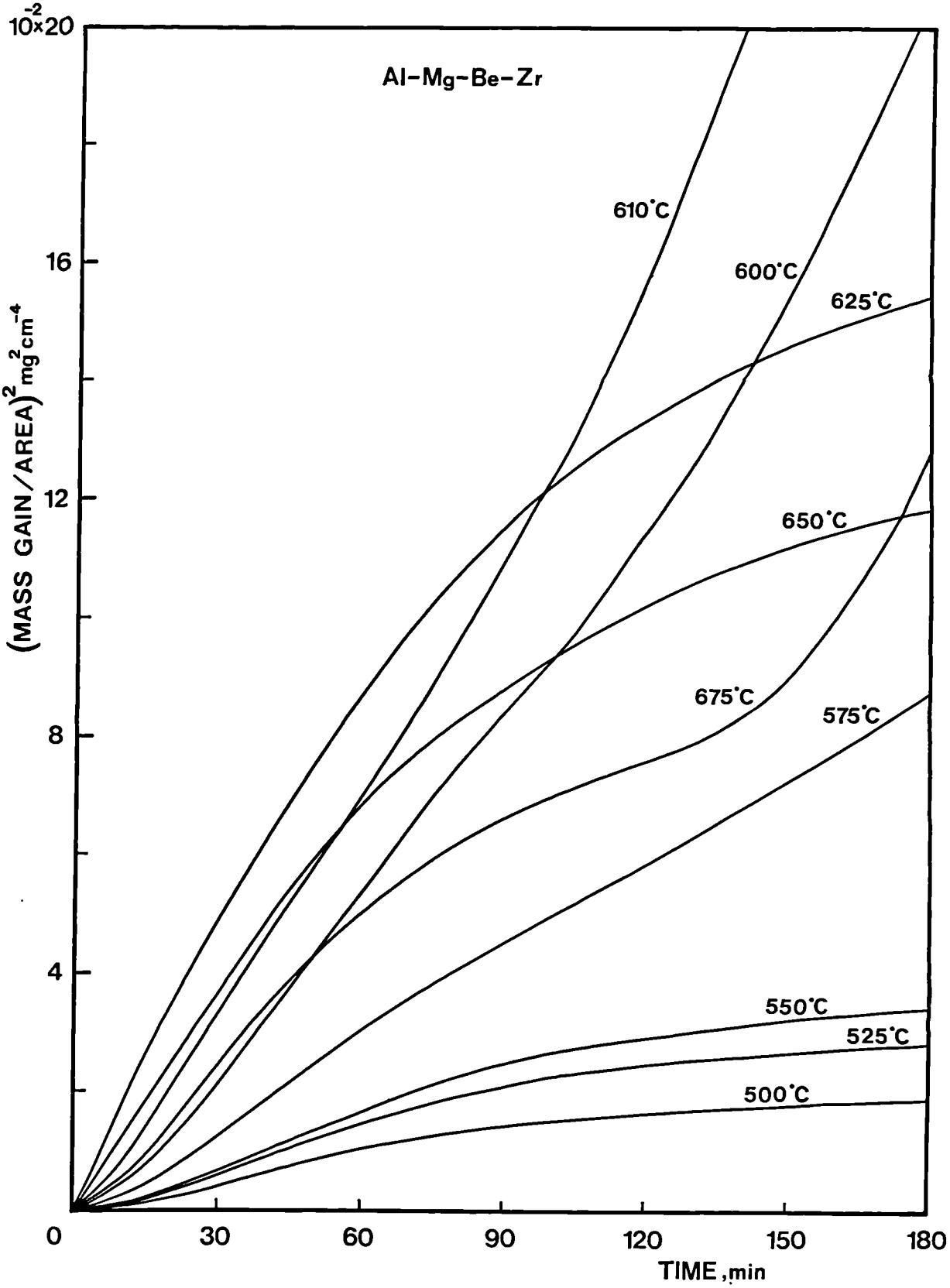

Figure 84. Parabolic plots, i.e. Δm^2 v time, for Al-8.13% Mg-0.003% Be-0.12% Zr alloy exposed to the moist atmosphere in the temperature range 500-725°C.

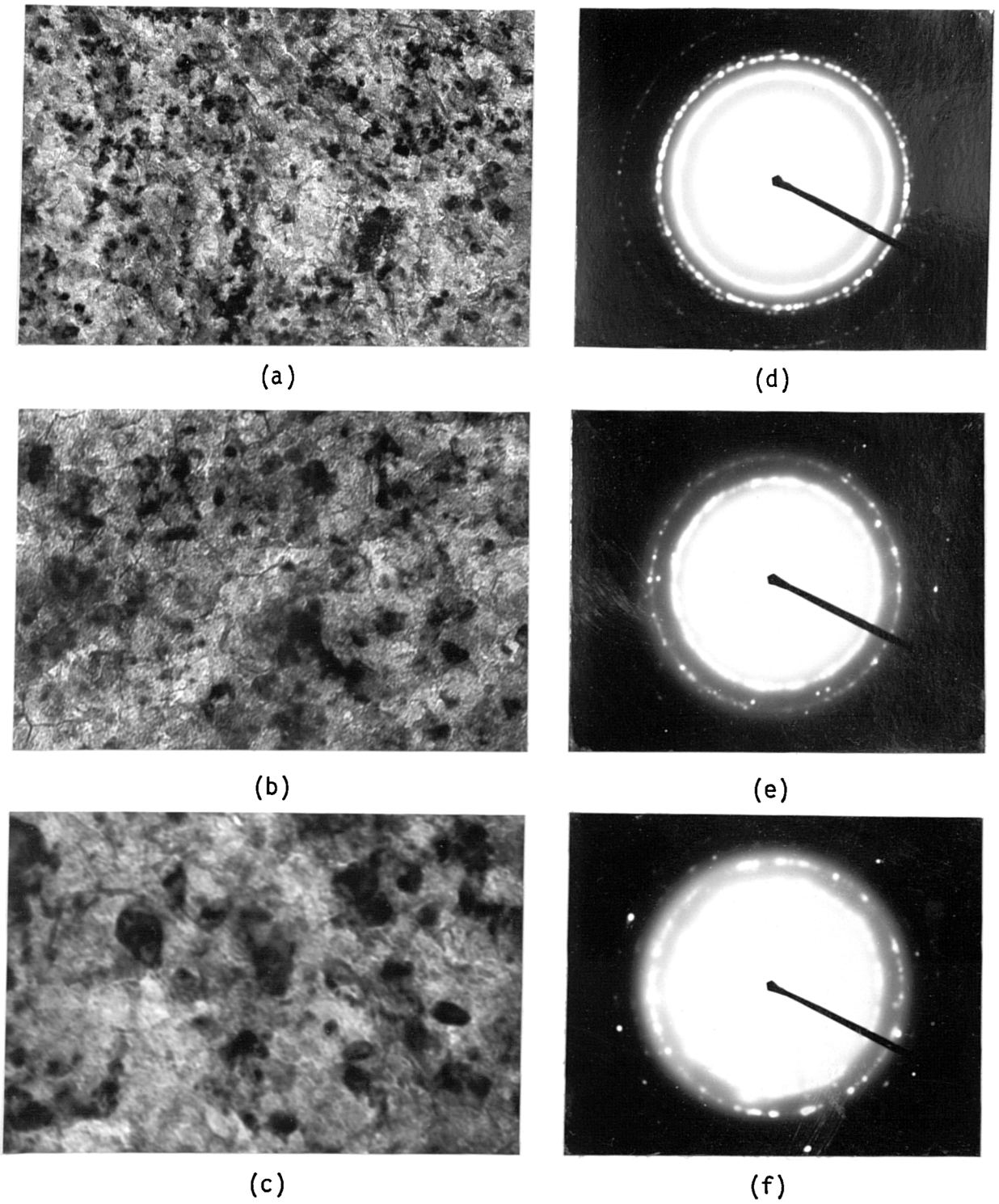

igure 85. TEM micrographs and related electron diffraction patterns from fragments of oxide films formed on solid Al-3.1% Mg alloy after various exposures in the moist atmosphere at 525°C, showing grain growth of MgO film.

(a), (d) : after 30 min (x 120,000)
(b), (e) : after 1h (x 120,000)
(c), (f) : after 2h (x 120,000)

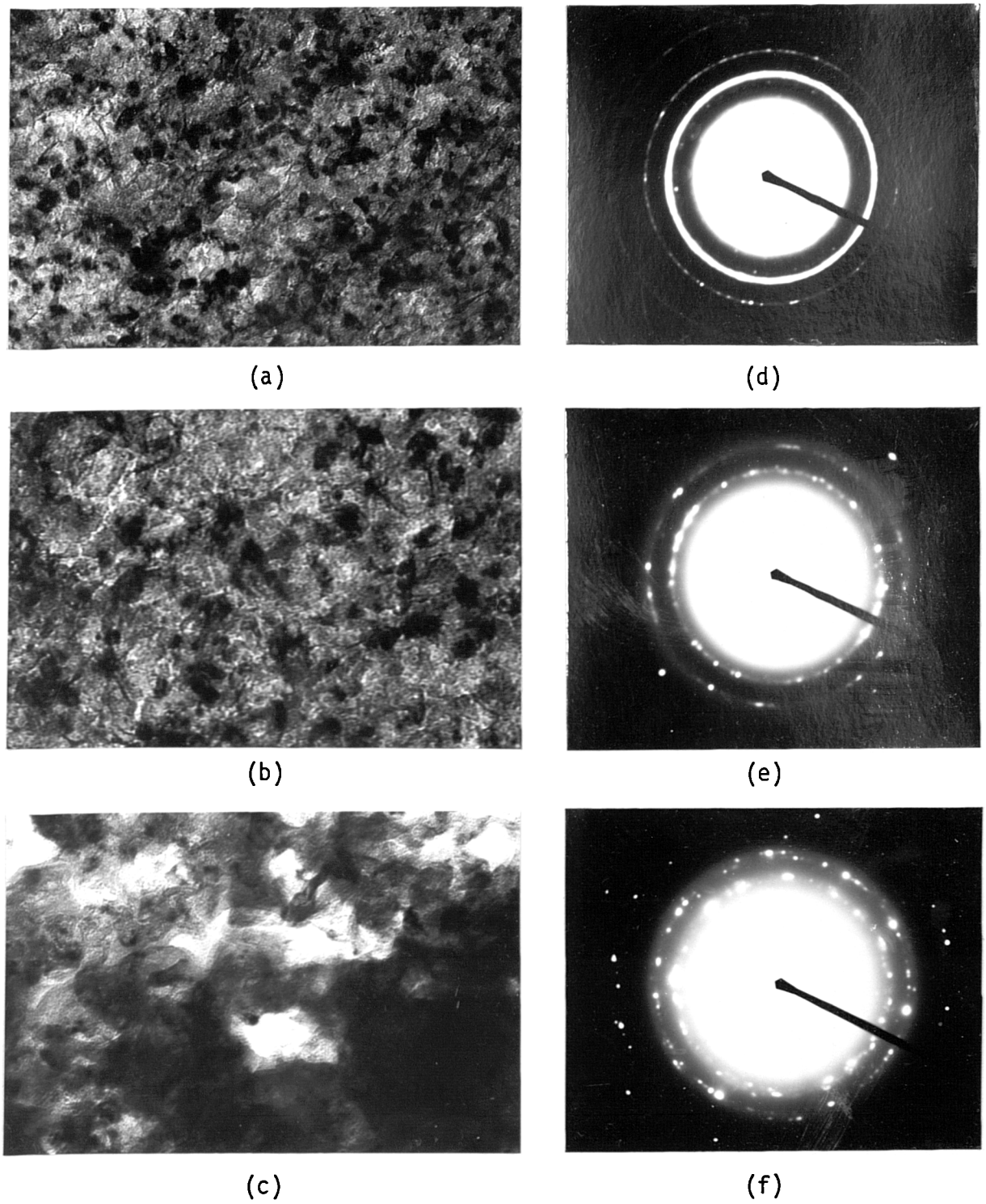

gure 86. TEM micrographs and related electron diffraction patterns from fragments of oxide films formed on solid Al-7.4% Mg alloy after various exposures in the dry atmosphere at 525^{o}C, showing grain growth of MgO film.

(a), (d) : after 30 min (x 120,000)
(b), (e) : after 1h (x 120,000)
(c), (f) : after 2h (x 120,000)

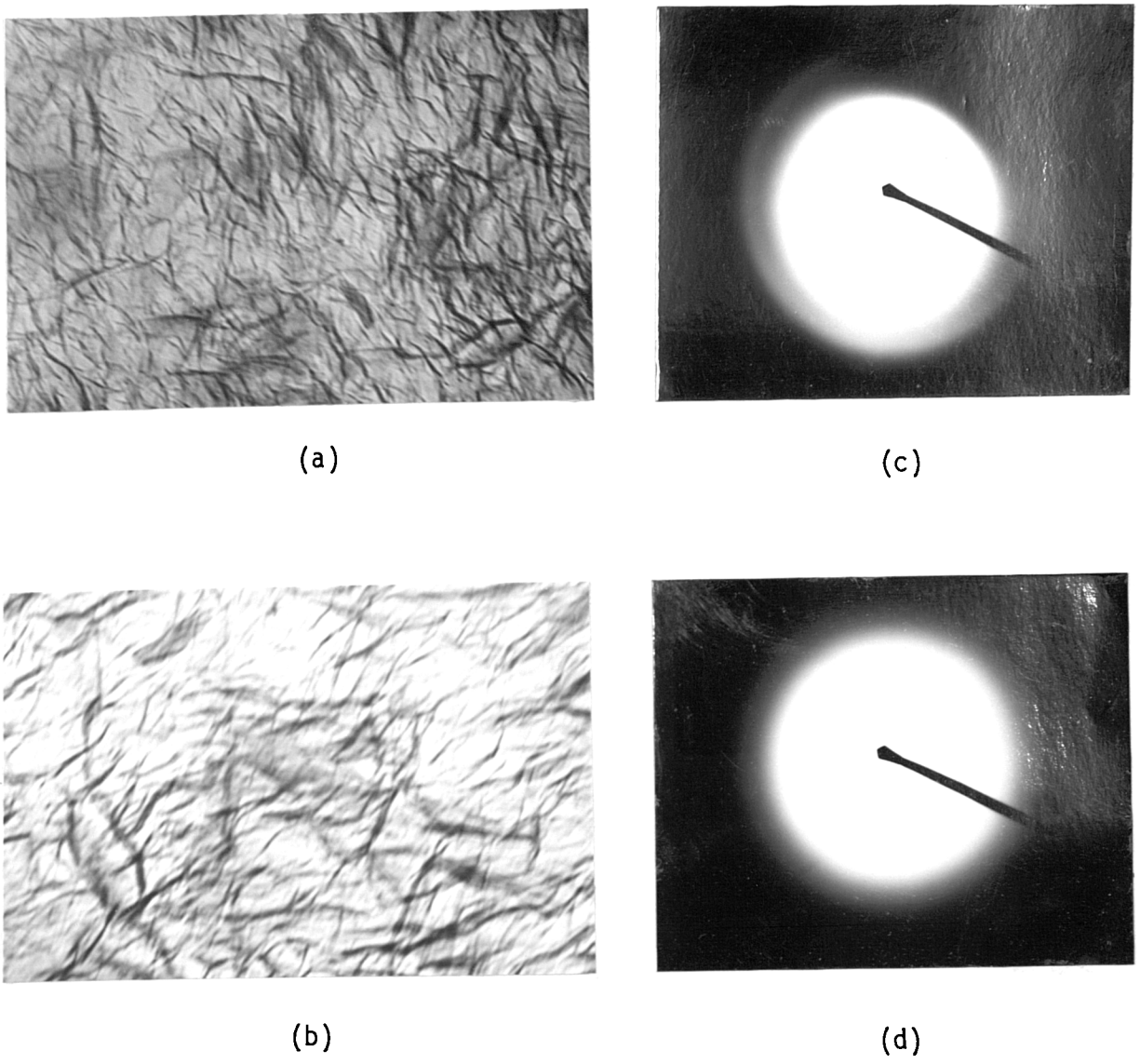

igure 87. TEM micrographs and related electron diffraction patterns from fragments of oxide films formed on liquid Al-3.1% Mg alloy after various exposures in the dry atmosphere at 700°C, showing the formation of only amorphous MgO.

(a), (c) : after 30 min (x 120,000)
(b), (d) : after 2h (x 120,000)

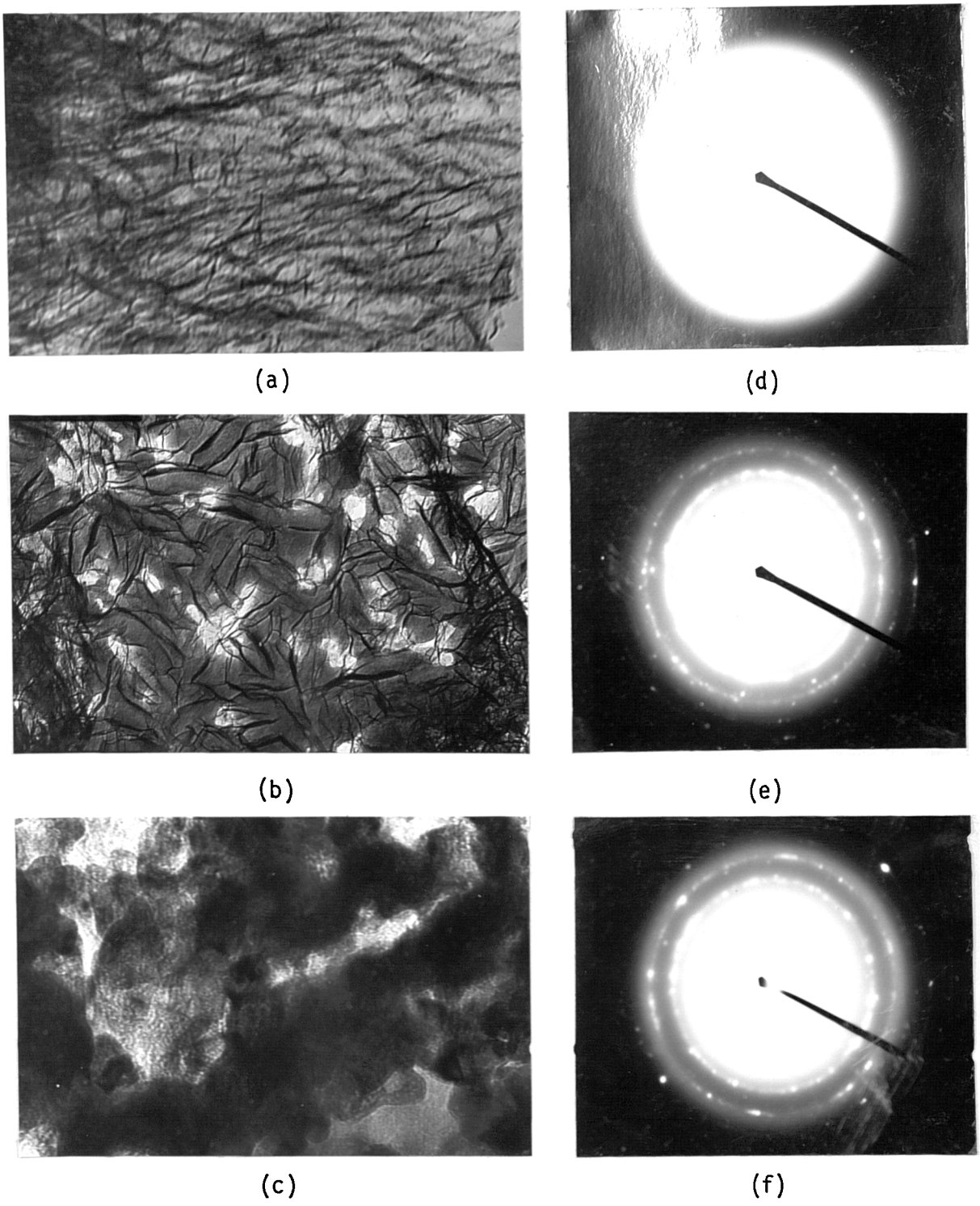

Figure 88. TEM micrographs and related electron diffraction patterns from fragments of oxide films formed on liquid Al-5.1% Mg alloy after various exposures in the moist atmosphere at 650^{o}C, showing crystallisation and grain growth of MgO film.

(a), (d) : after 30 min (x 120,000)
(b), (e) : after 1h (x 120,000)
(c), (f) : after 2h (x 120,000)

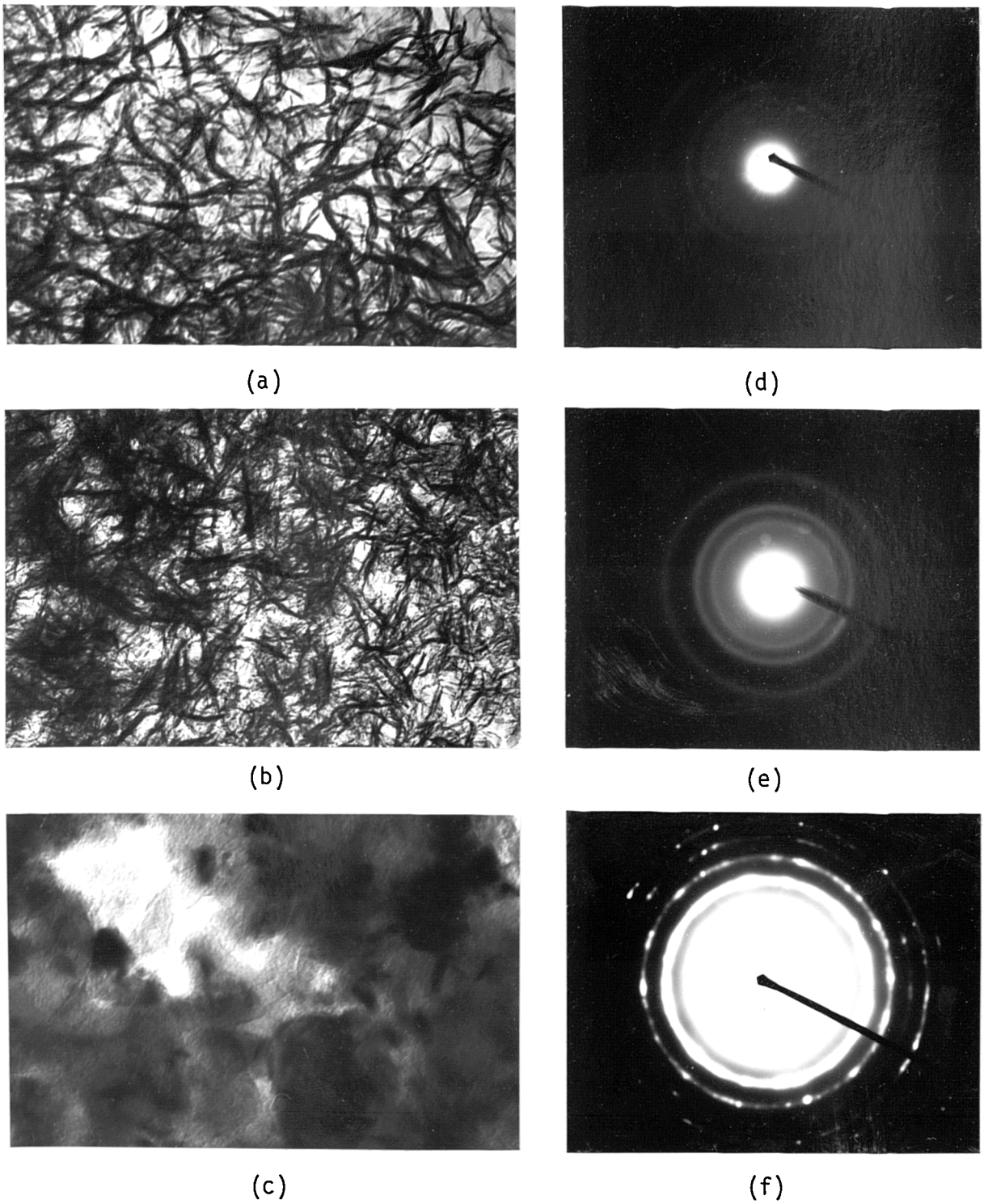

igure 89. TEM micrographs and related electron diffraction patterns from fragments of oxide films formed on liquid Al-9.3% Mg alloy after various exposures in the dry atmosphere at 675^{o}C, showing crystallisation and grain growth of MgO film.

(a), (d) : after 10 min (x 120,000)
(b), (e) : after 20 min (x 120,000)
(c), (f) : after 2h (x 120,000)

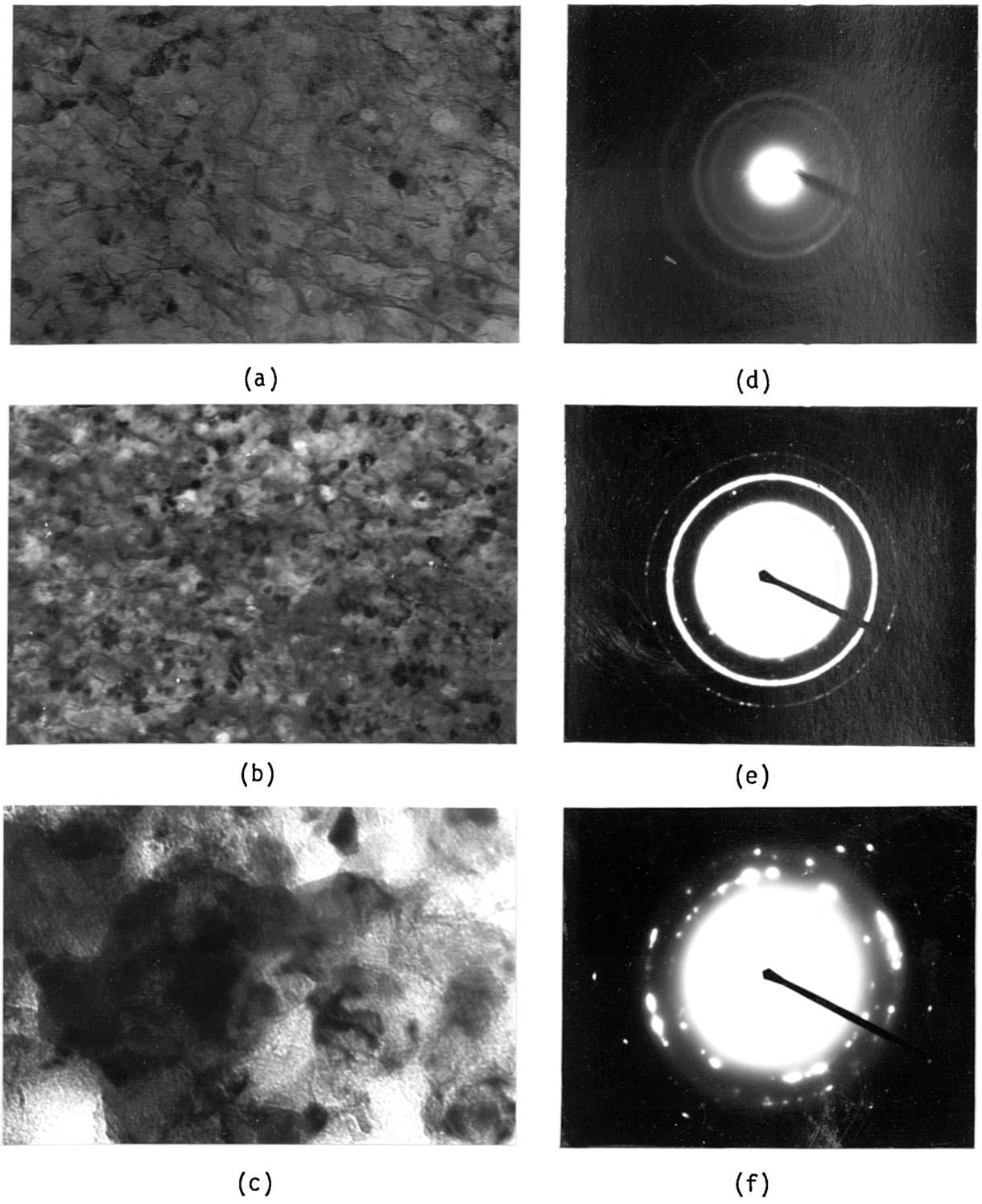

igure 90. TEM micrographs and related electron diffraction patterns from fragments of oxide films formed on semi-liquid Al-3.1% Mg alloy with < 50% liquid after various exposures in the moist atmosphere at 625^{o}C, showing crystallisation and grain growth of MgO film.

(a), (d) : after 5 min (x 120,000)
(b), (e) : after 15 min (x 120,000)
(c), (f) : after 2h (x 120,000)

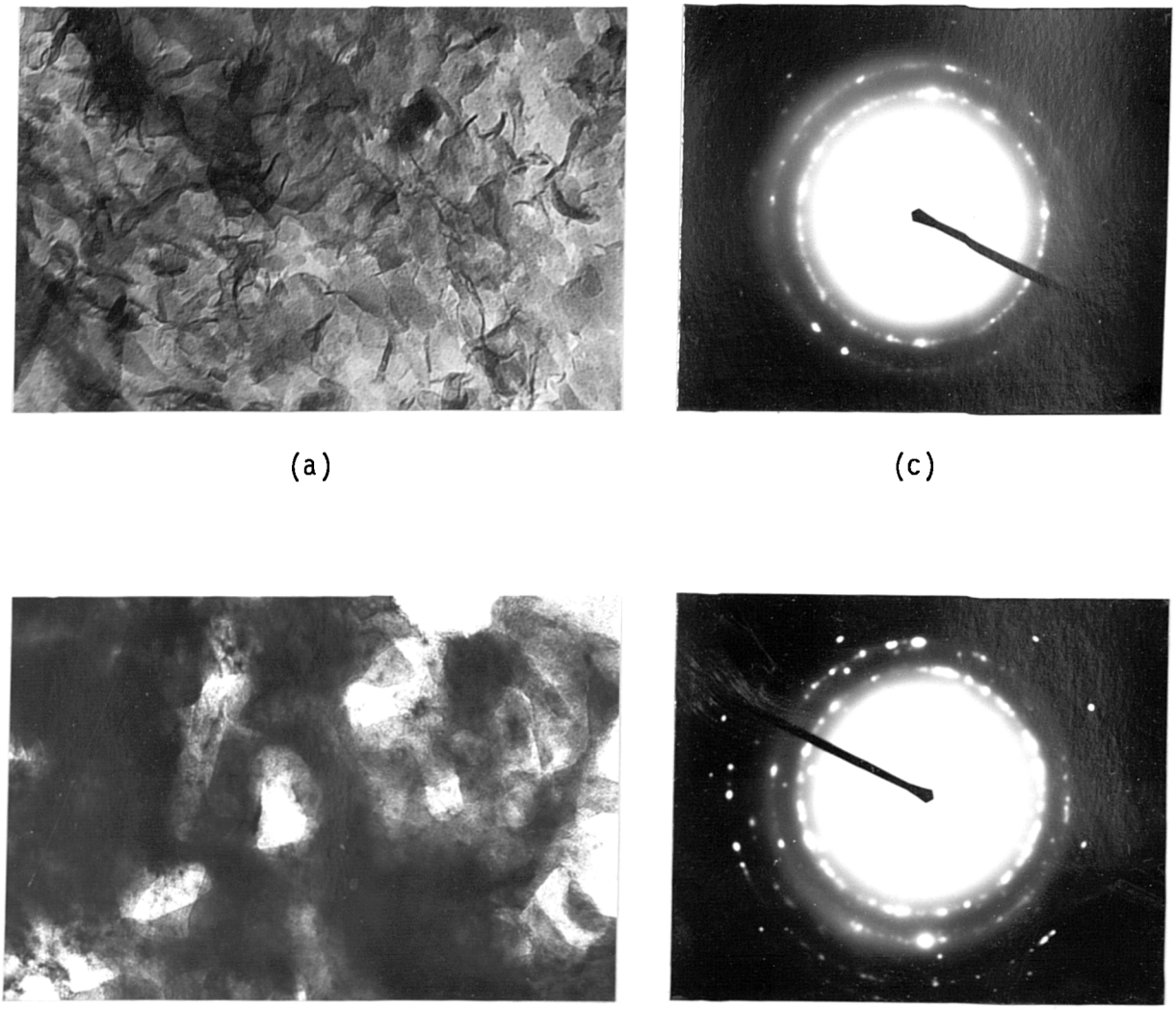

(a) (c)

(b) (d)

igure 91. TEM micrographs and related electron diffraction patterns from fragments of oxide films formed on semi-liquid Al-3.1% Mg alloy with >50% liquid after various exposures in the dry atmosphere at 640^{o}C, showing crystallisation and grain growth of MgO film.

(a), (c) : after 30 min (x 120,000)
(b), (d) : after 2h (x 120,000)

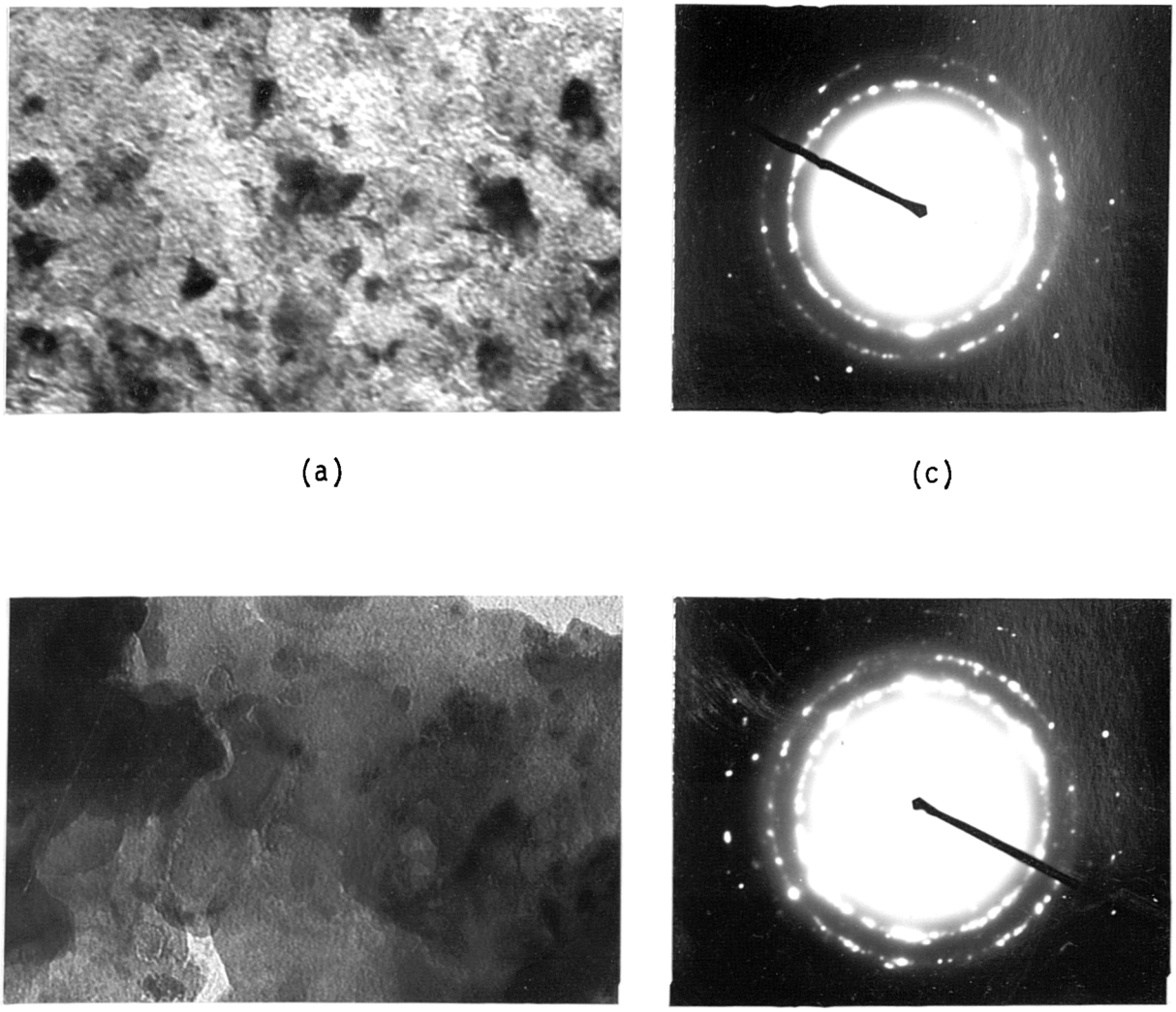

(a) (c)

(b) (d)

igure 92. TEM micrographs and related electron diffraction patterns from fragments of oxide films formed on semi-liquid Al-7.4% Mg alloy with >50% liquid after various exposures in the dry atmosphere at 610^{o}C, showing grain growth of MgO film.

(a), (c) : after 15 min (x 120,000)
(b), (d) : after 2h (x 120,000)

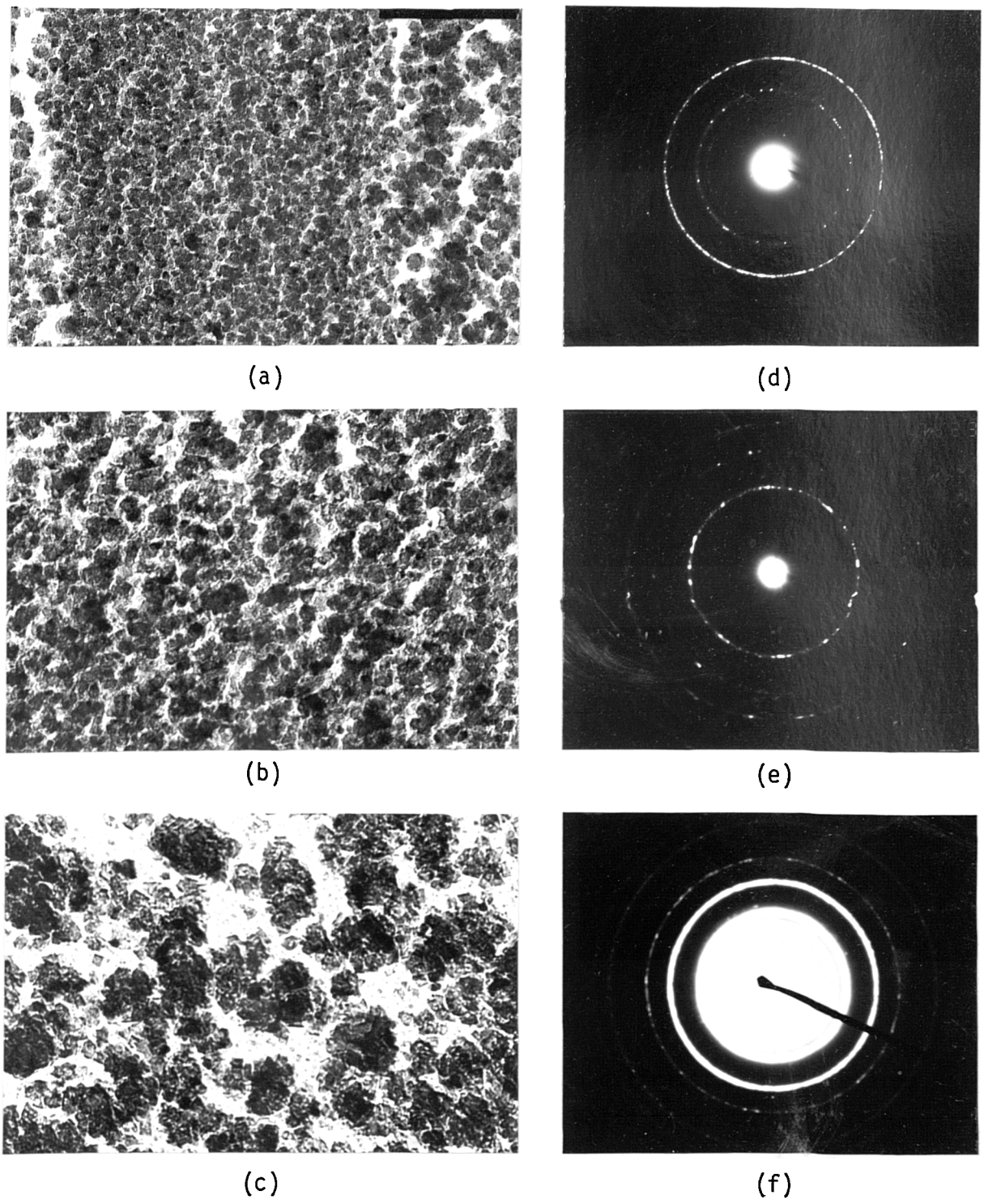

igure 93. TEM micrographs and related electron diffraction patterns from fragments of oxide films formed on solid Al-8.2% Mg-0.003% Be alloy after various exposures in the moist atmosphere at 525°C, showing grain growth of MgO film.

(a), (d) : after 45 min (x 160,000)
(b), (e) : after 1.5h (x 160,000)
(c), (f) : after 3h (x 160,000)

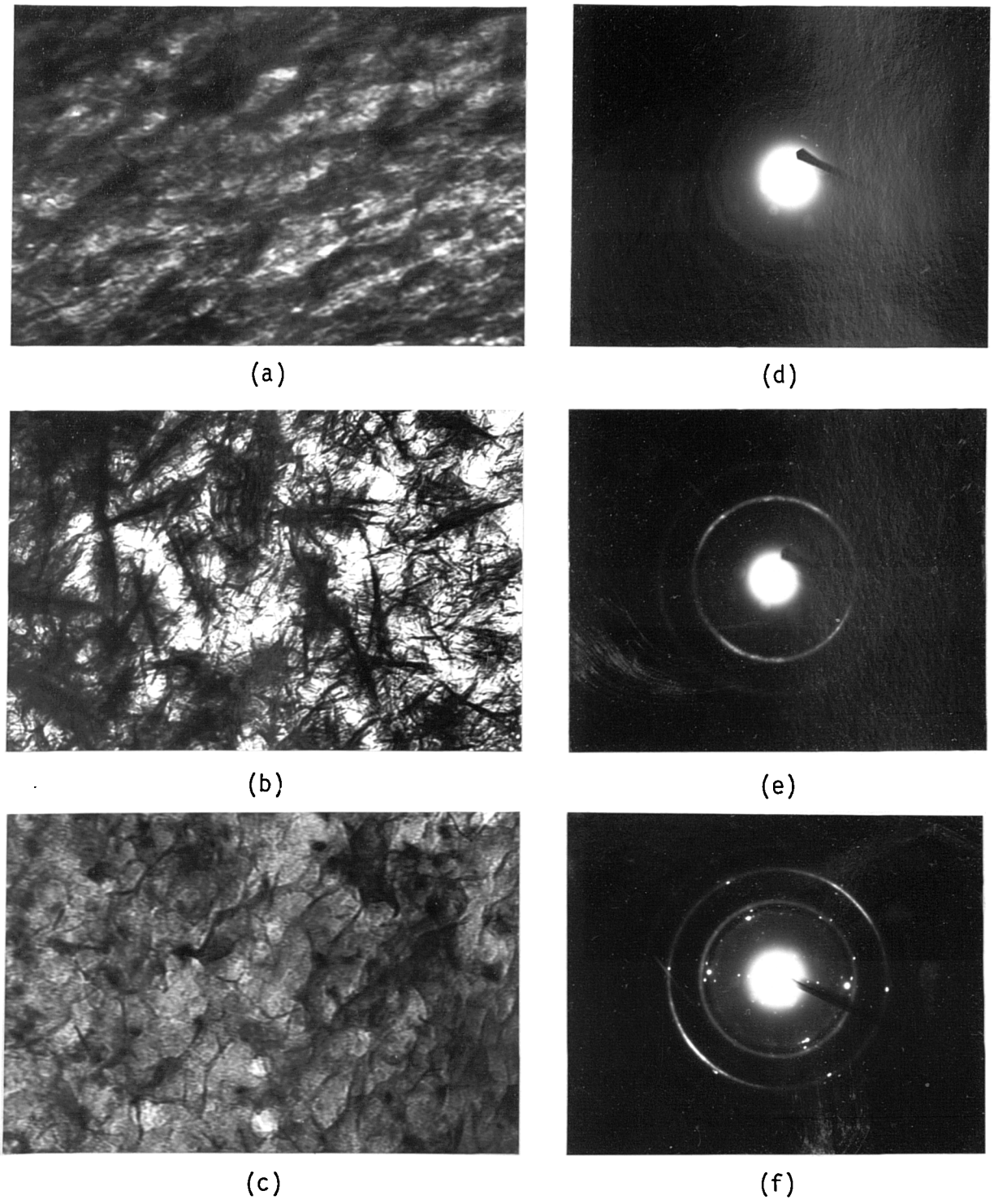

Figure 94. TEM micrographs and related electron diffraction patterns from fragments of oxide films formed on liquid Al-8.16% Mg-0.003% Be-0.24% Mn alloy after various exposures in the dry atmosphere at 700°C, showing crystallisation and grain growth of MgO film.

(a), (d) : after 30 min (x 160,000)
(b), (e) : after 1h (x 160,000)
(c), (f) : after 2h (x 160,000)

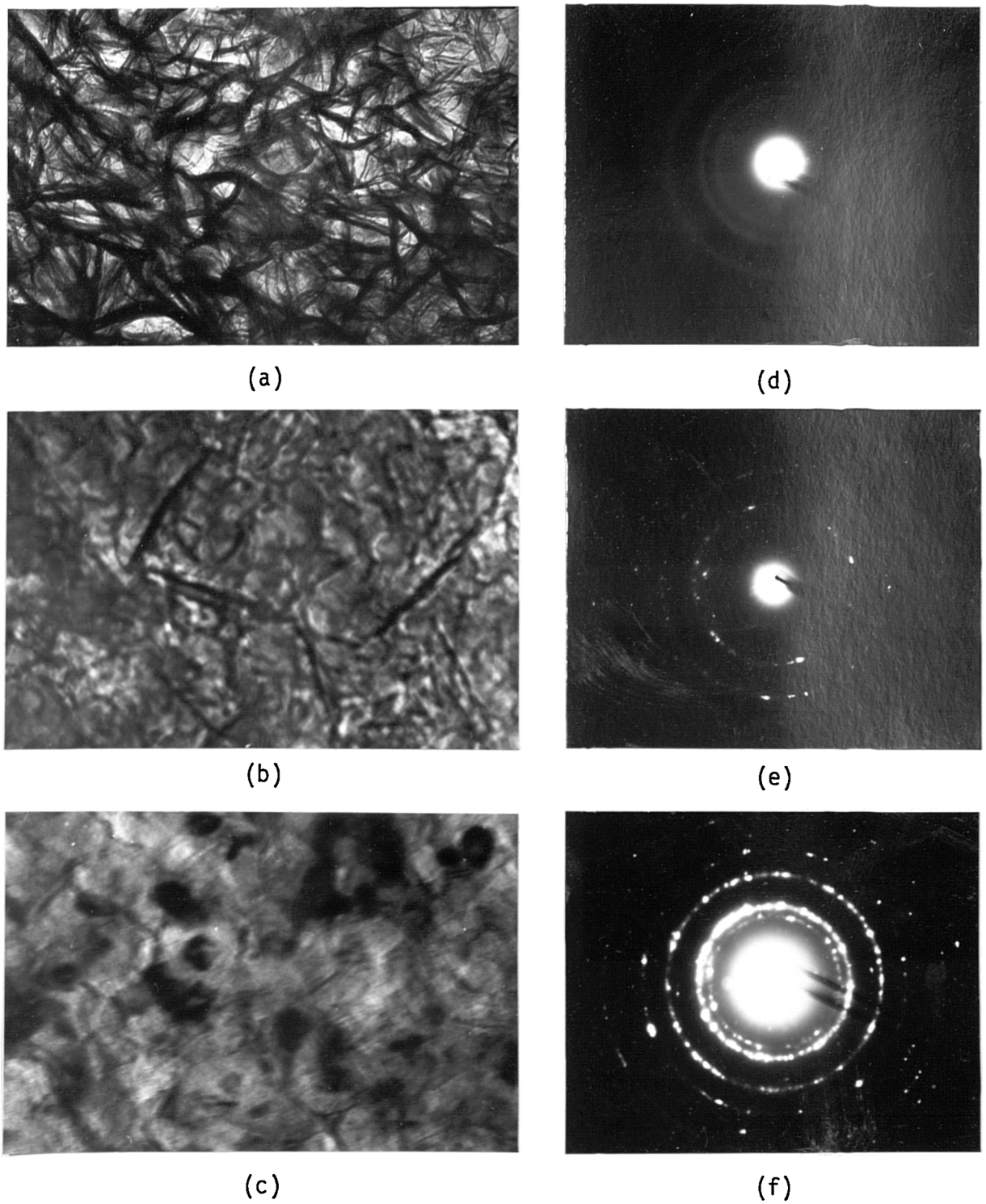

Figure 95. TEM micrographs and related electron diffraction patterns from fragments of oxide films formed on liquid Al-8.13% Mg-0.003% Be-0.12% Zr alloy after various exposures in the moist atmosphere at 700°C, showing crystallisation and grain growth of MgO film.

(a), (d) : after 30 min (x 160,000)
(b), (e) : after 45 min (x 160,000)
(c), (f) : after 3h (x 160,000)

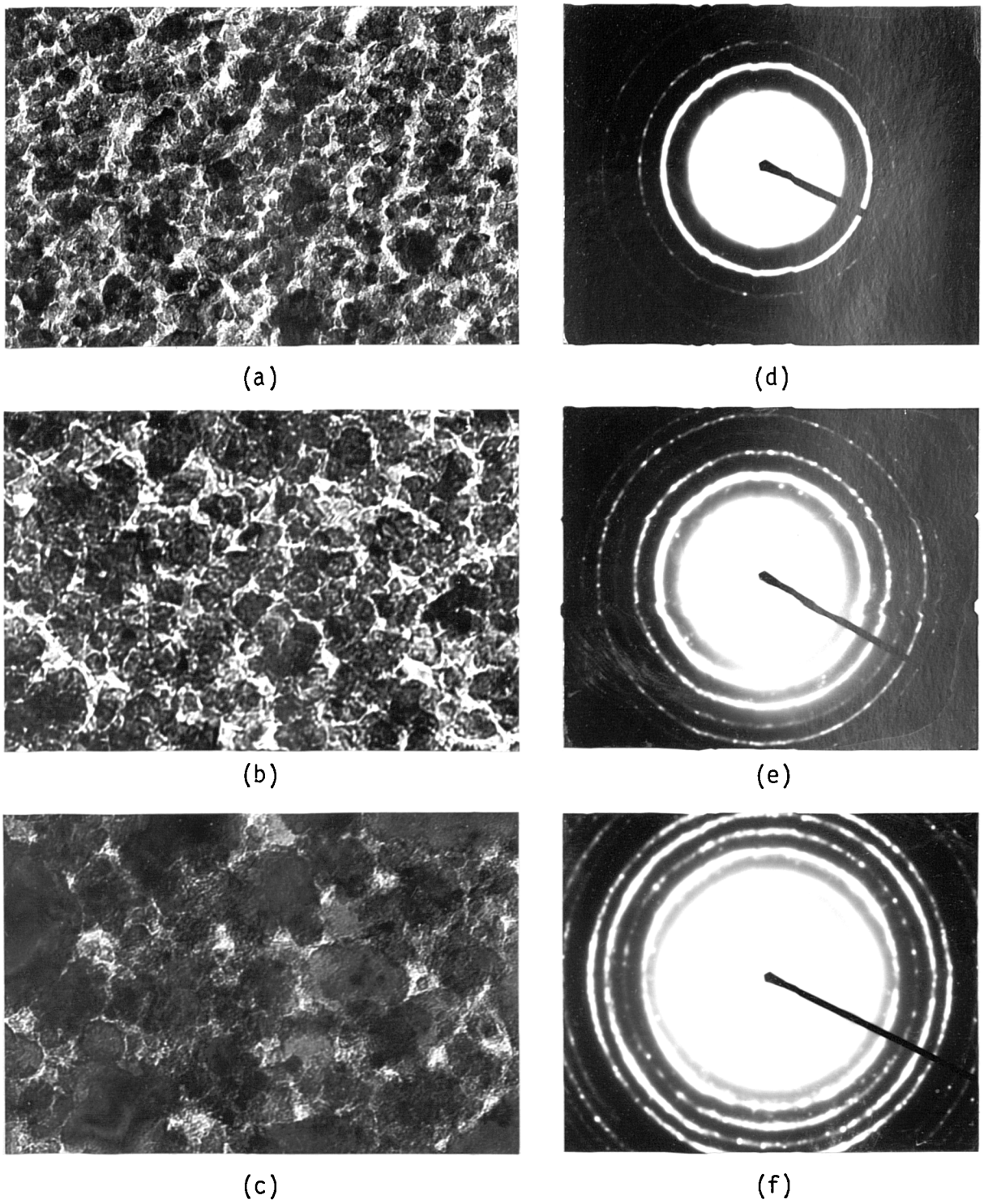

Figure 96. TEM micrographs and related electron diffraction patterns from fragments of oxide films formed on semi-liquid Al-8.2% Mg-0.003% Be alloy with < 50% liquid after various exposures in the dry atmosphere at 575°C, showing grain growth of MgO film.

(a), (d) : after 45 min (x 160,000)
(b), (e) : after 1.5h (x 160,000)
(c), (f) : after 3h (x 160,000)

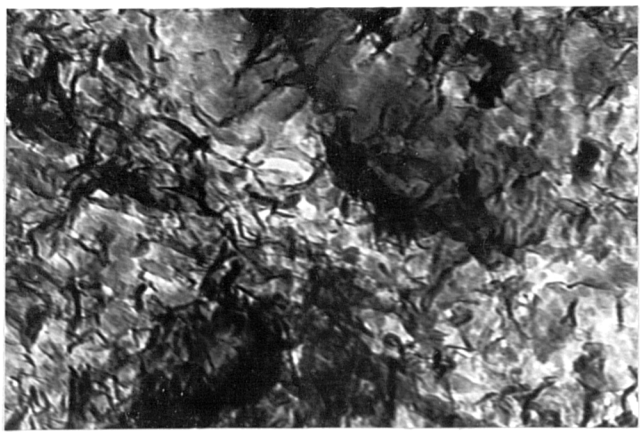

(a)

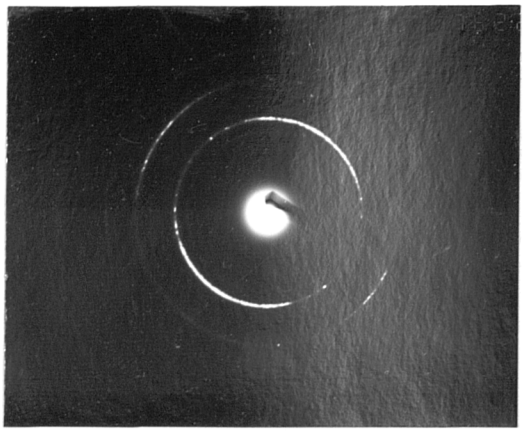

(c)

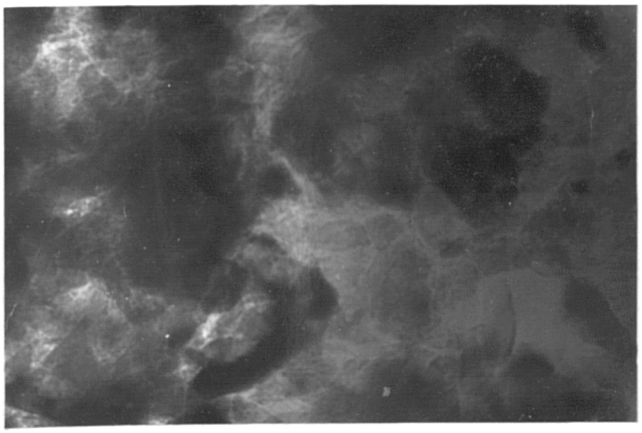

(b)

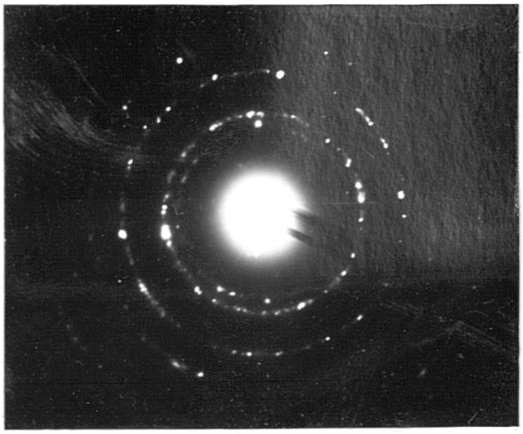

(d)

Figure 97. TEM micrographs and related electron diffraction patterns from fragments of oxide films formed on semi-liquid Al-8.13% Mg-0.003% Be-0.12% Zr alloy with >50% liquid after various exposures in the moist atmosphere at 610°C, showing crystallisation and grain growth of MgO film.

(a), (c) : after 15 min (x 160,000)
(b), (d) : after 3h (x 160,000)

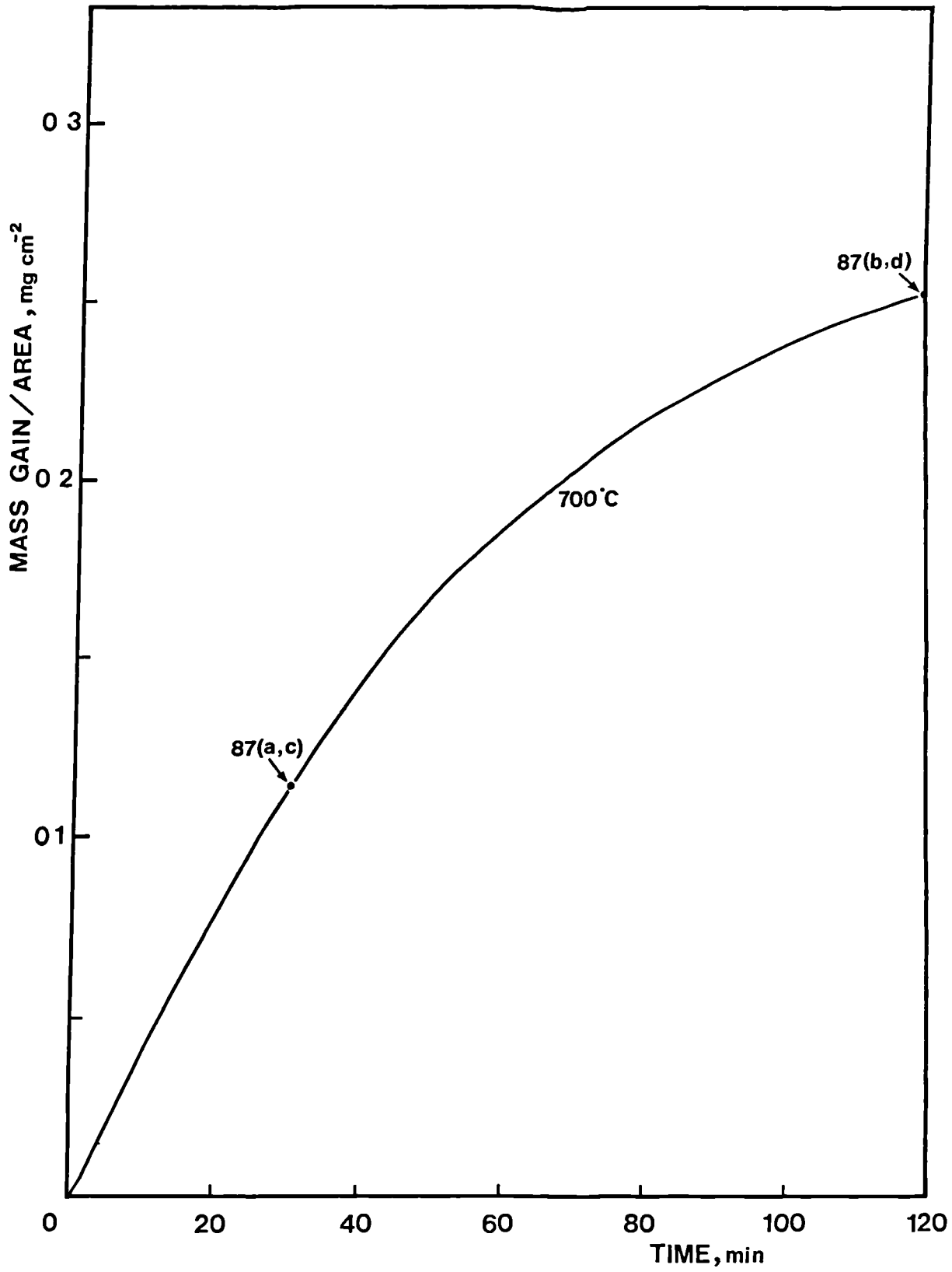

gure 98. Correlation of Figure 87 with the mass gain-time curve extracted from Figure 53.

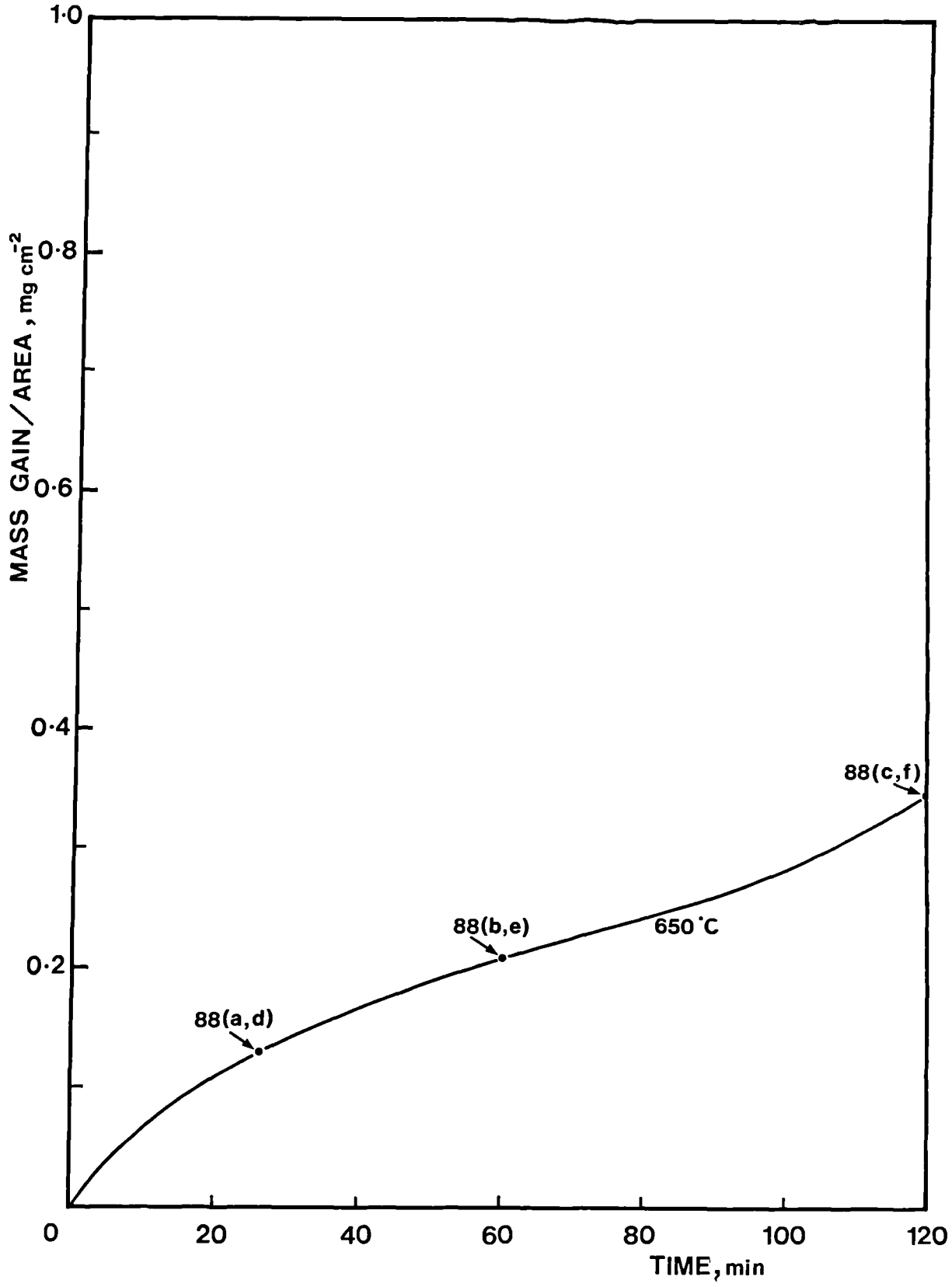

igure 99. Correlation of Figure 88 with the mass gain-time curve extracted from Figure 56.

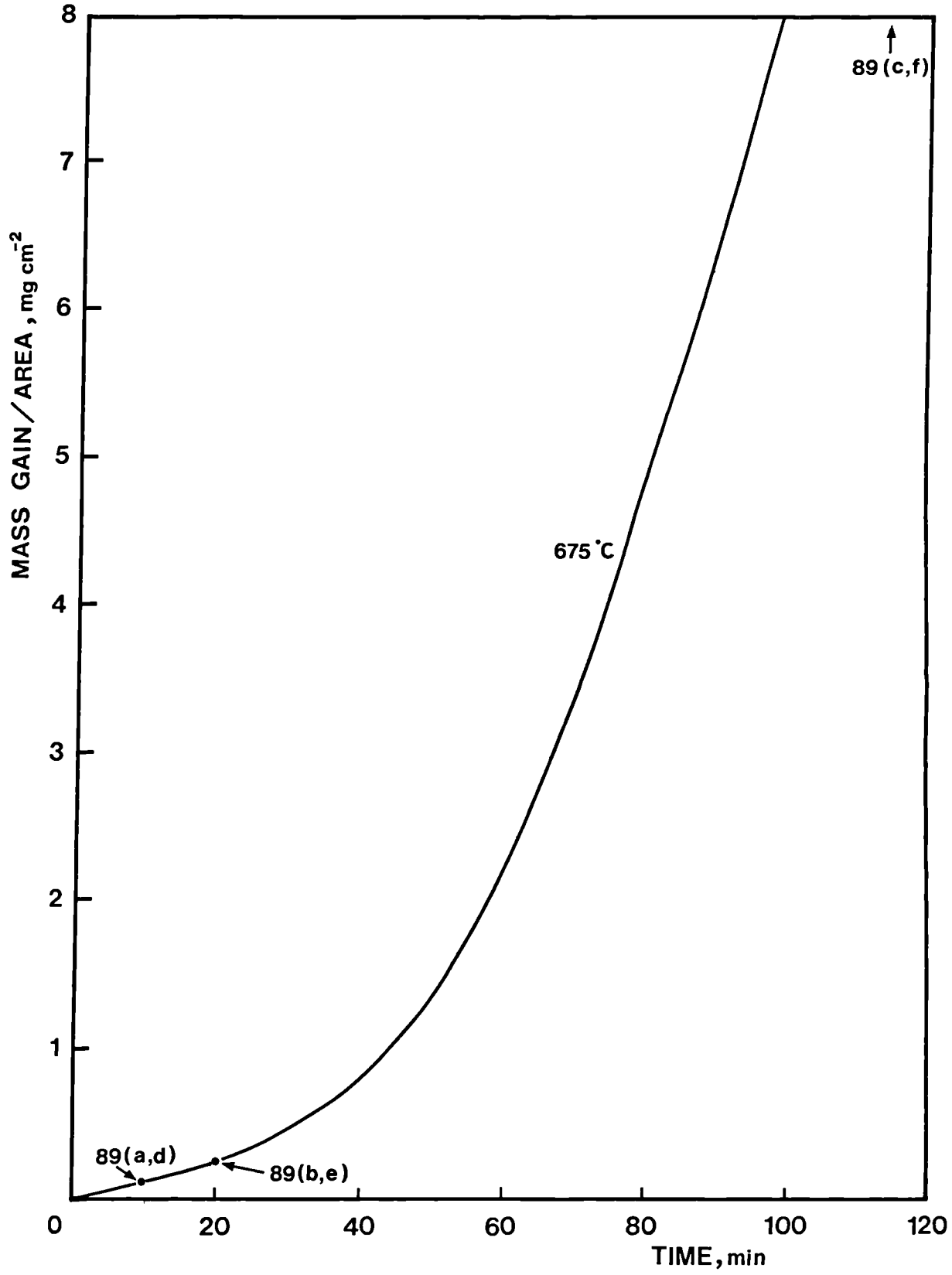

gure 100. Correlation of Figure 89 with the mass gain-time curve extracted from Figure 59.

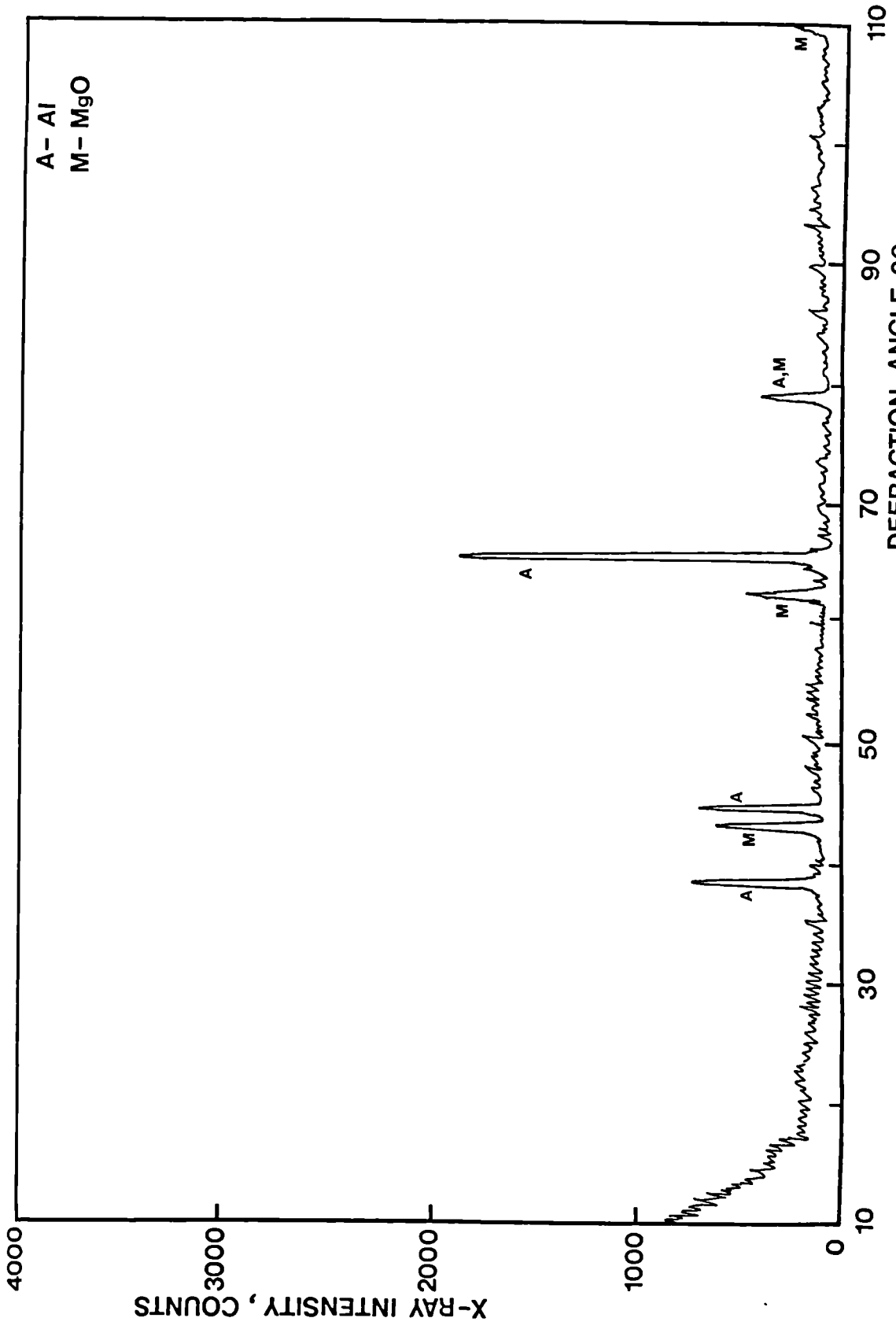

Figure 101. X-ray diffraction spectra from oxidised sample of solid Al-1.3% Mg alloy after 2h exposure in the moist atmosphere at 525°C, confirming the exclusive formation of MgO.

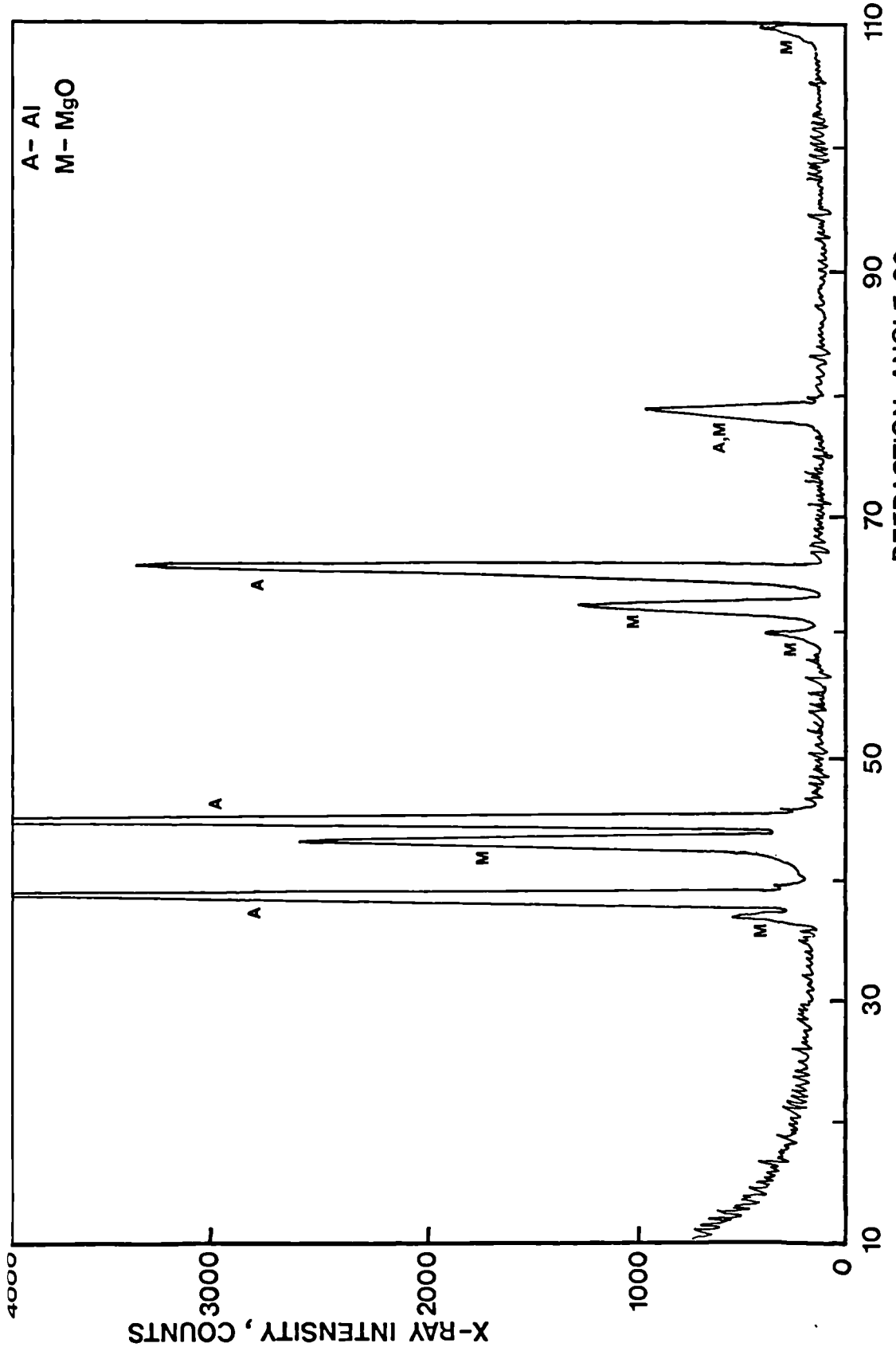

Figure 102. X-ray diffraction spectra from oxidised sample of solid Al-7.4% Mg alloy after 2h exposure in the dry atmosphere at 525^{o}C, confirming the exclusive formation of MgO.

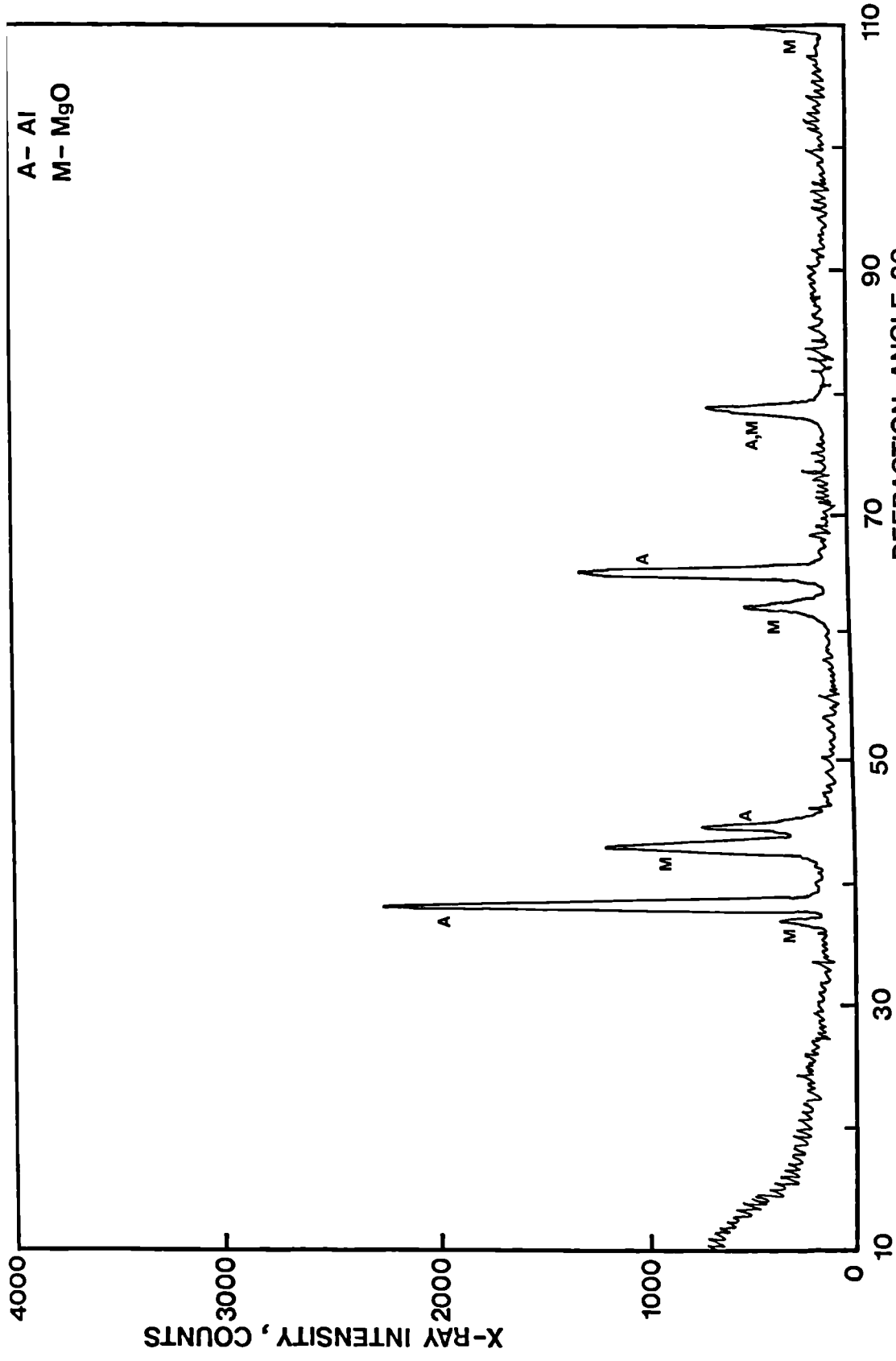

Figure 103. X-ray diffraction spectra from oxidised sample of liquid Al-3.1% Mg alloy after 2h exposure in the moist atmosphere at 700°C, confirming the exclusive formation of MgO.

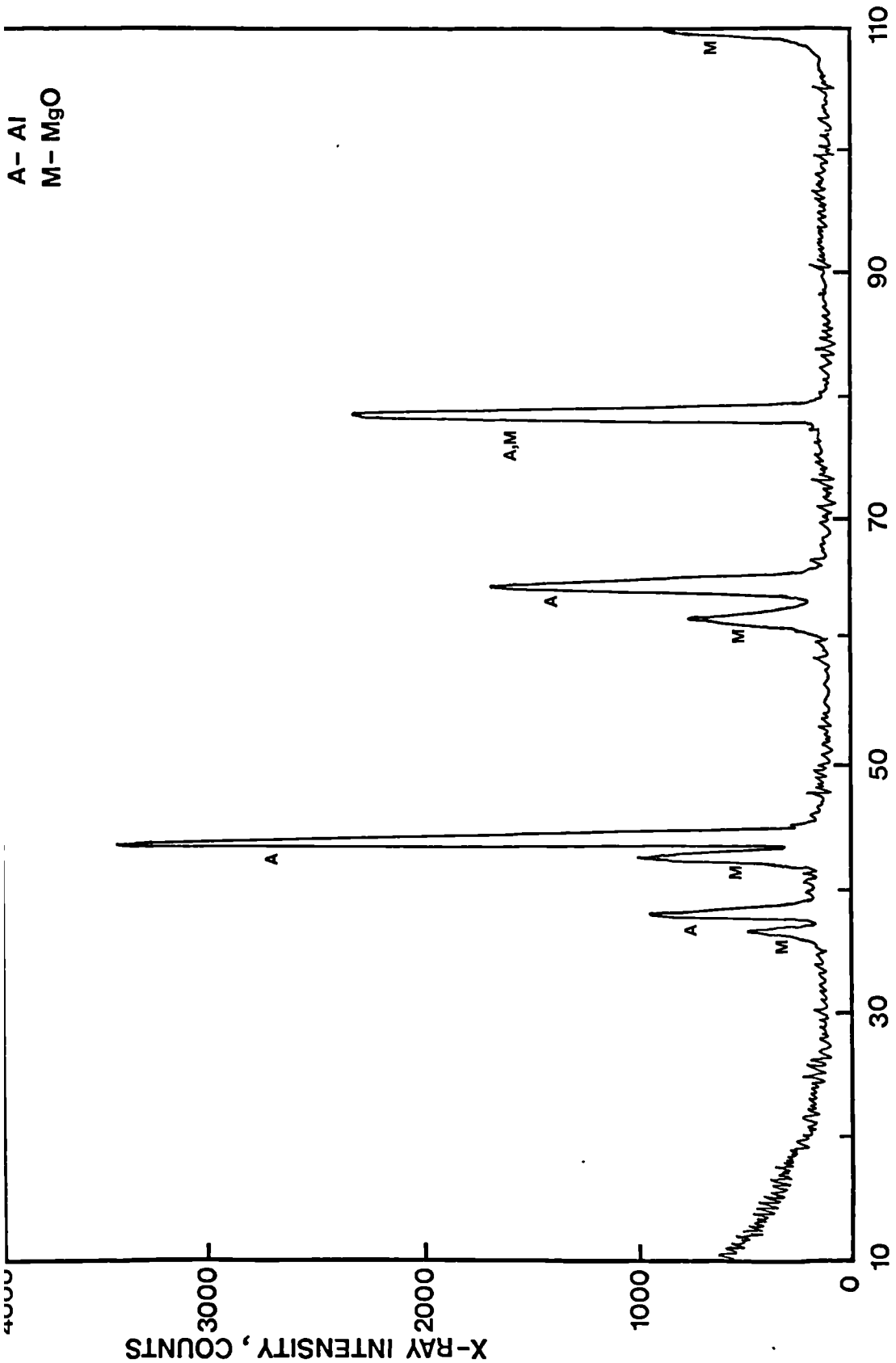

Figure 104. X-ray diffraction spectra from oxidised sample of liquid Al-9.3% Mg alloy after 2h exposure in the dry atmosphere at 700^{0}C, confirming the exclusive formation of MgO.

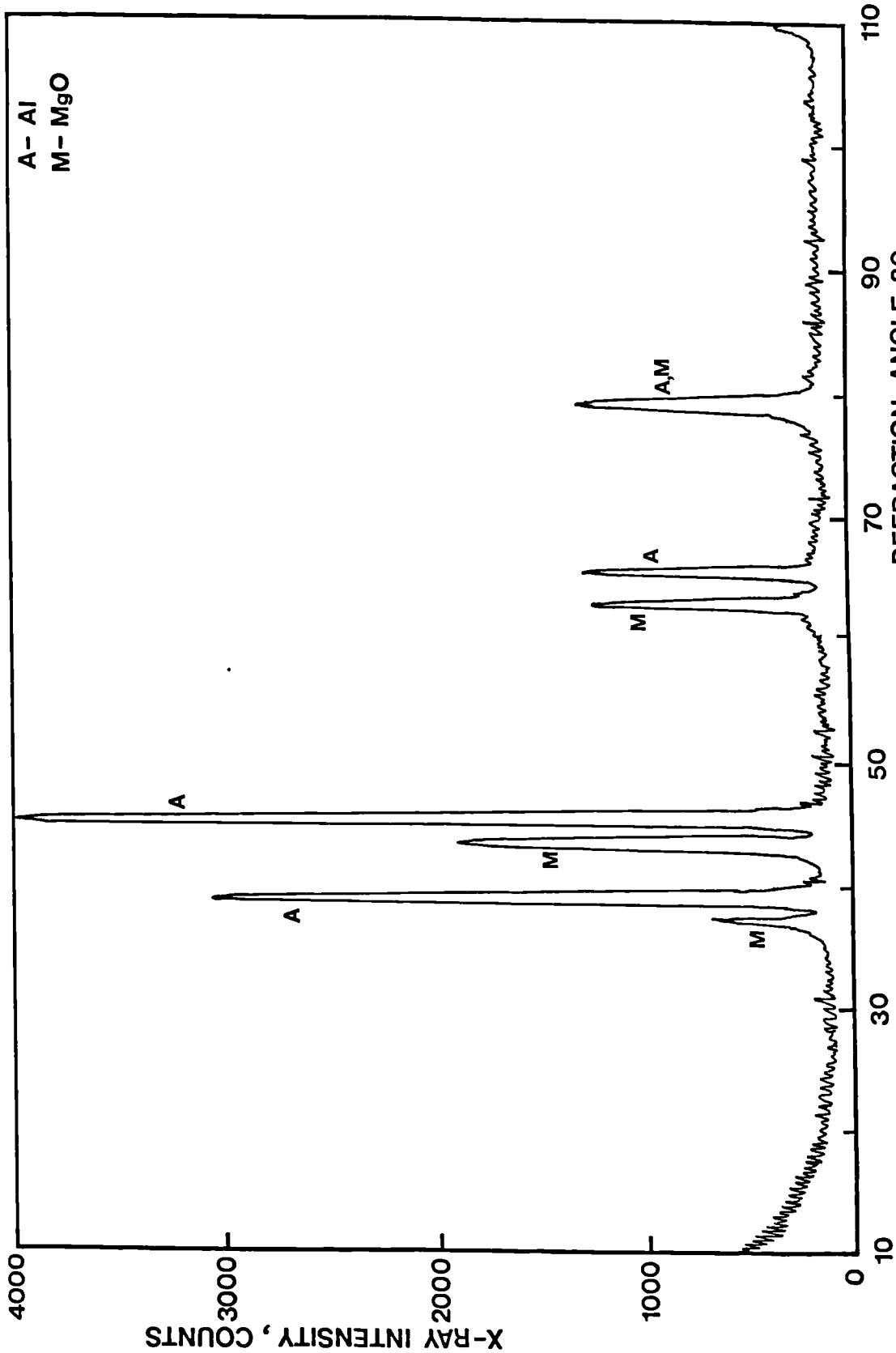

Figure 105. X-ray diffraction spectra from oxidised sample of semi-liquid Al-5.1% Mg alloy with <50% liquid after 2h exposure in the moist atmosphere at 600^{o}C, confirming the exclusive formation of MgO.

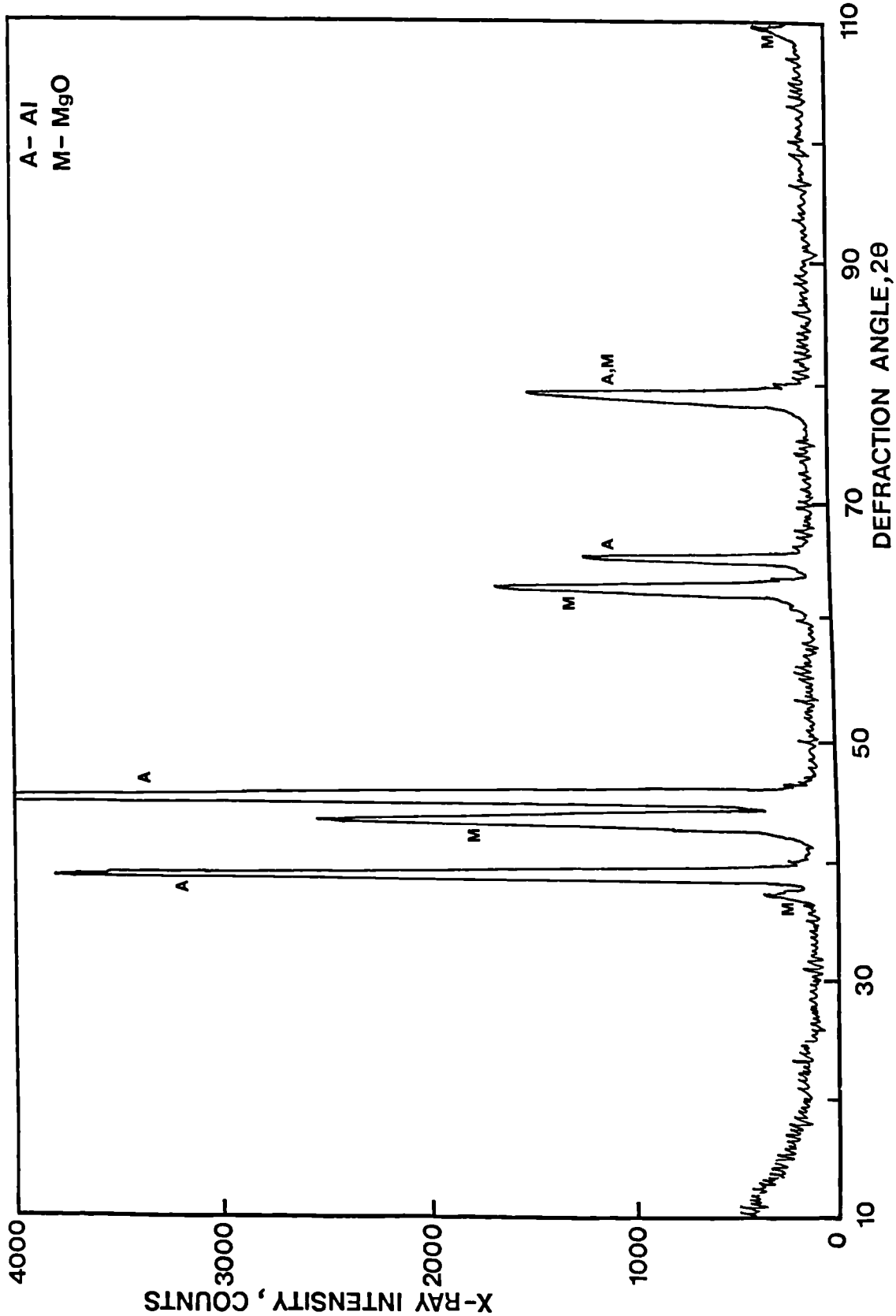

Figure 106. X-ray diffraction spectra from oxidised sample of semi-liquid Al-9.3% Mg alloy with <50% liquid after 2h exposure in the dry atmosphere at 550°C, confirming the exclusive formation of MgO.

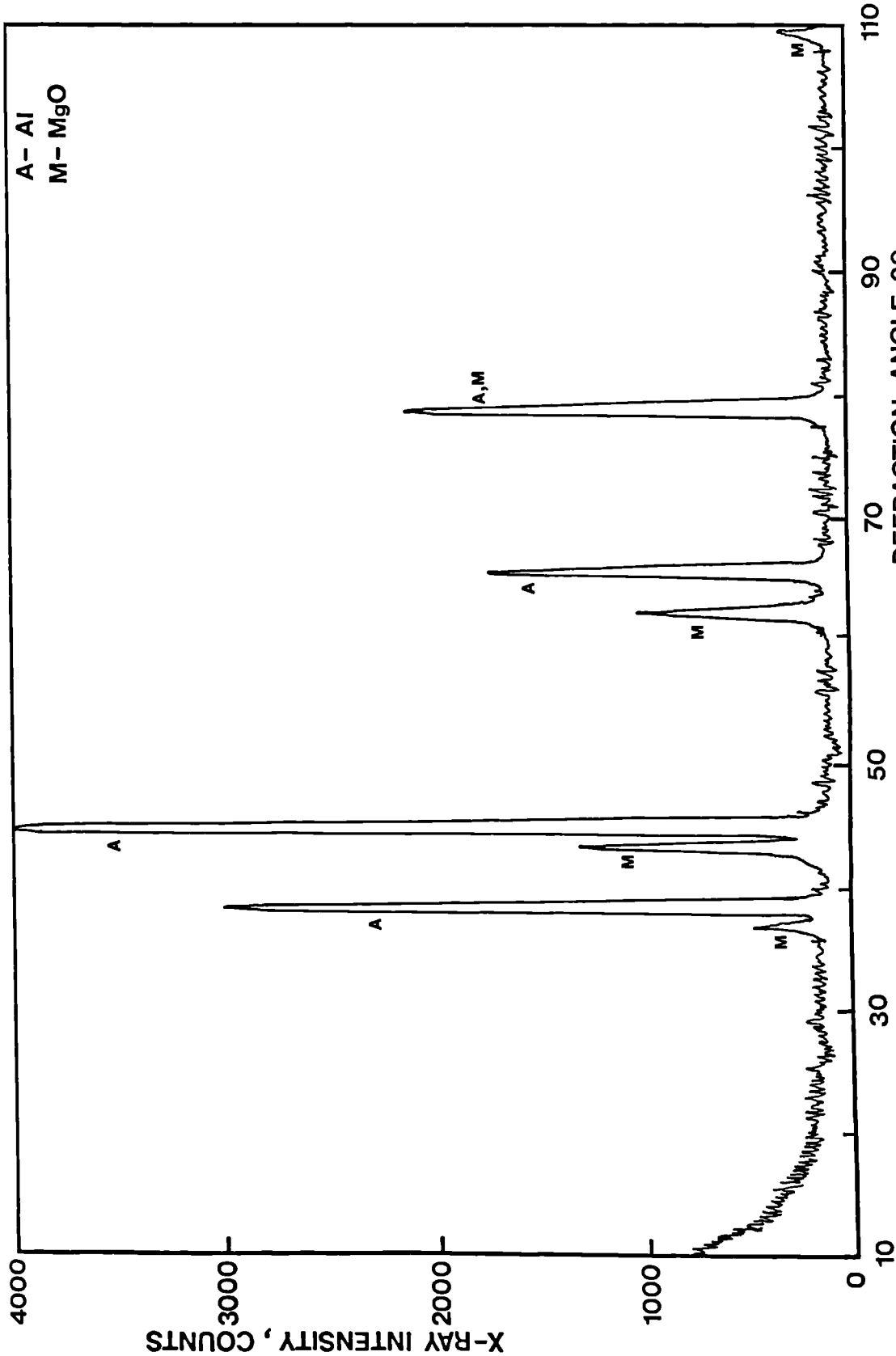

Figure 107. X-ray diffraction spectra from oxidised sample of semi-liquid Al-3.1% Mg alloy with >50% liquid after 2h exposure in the dry atmosphere at 640°C, confirming the exclusive formation of MgO.

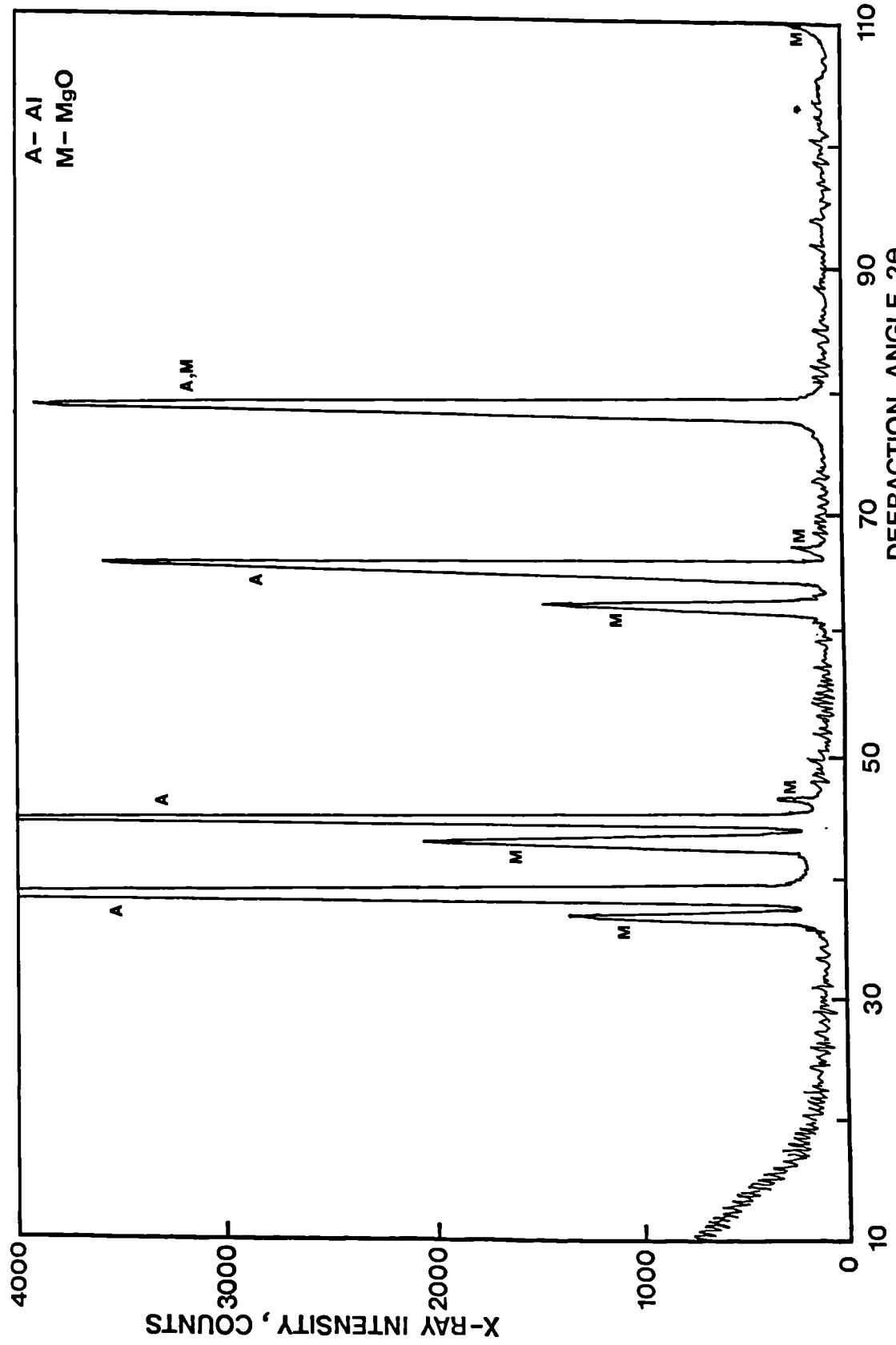

Figure 108. X-ray diffraction spectra from oxidised sample of semi-liquid Al-7.4% Mg alloy with >50% liquid after 2h exposure in the moist atmosphere at 610^{o}C, confirming the exclusive formation of MgO.

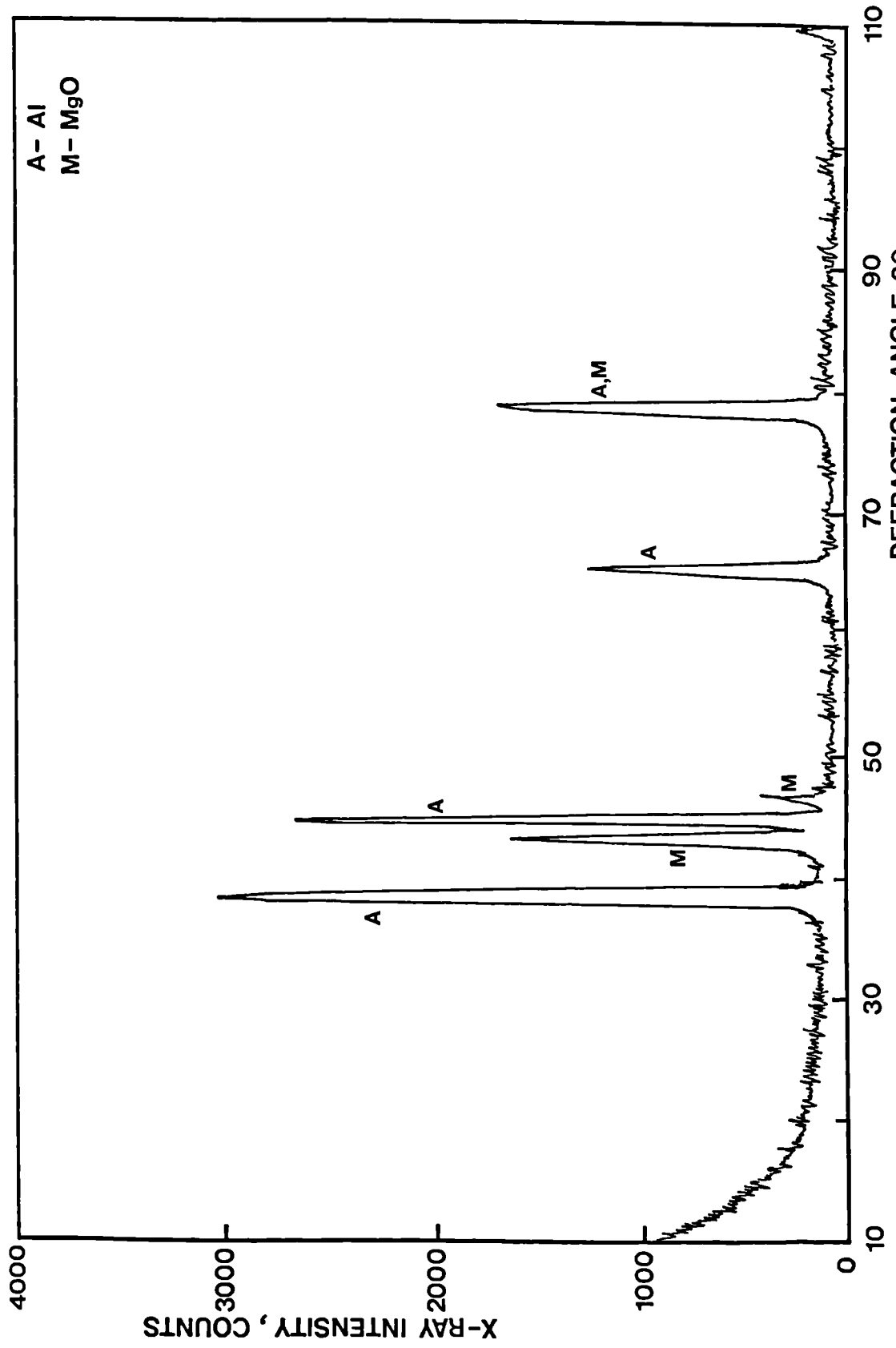

Figure 109. X-ray diffraction spectra from oxidised sample of solid Al-8.2% Mg-0.003% Be alloy after 3h exposure in the dry atmosphere at 525°C, confirming the exclusive formation of MgO.

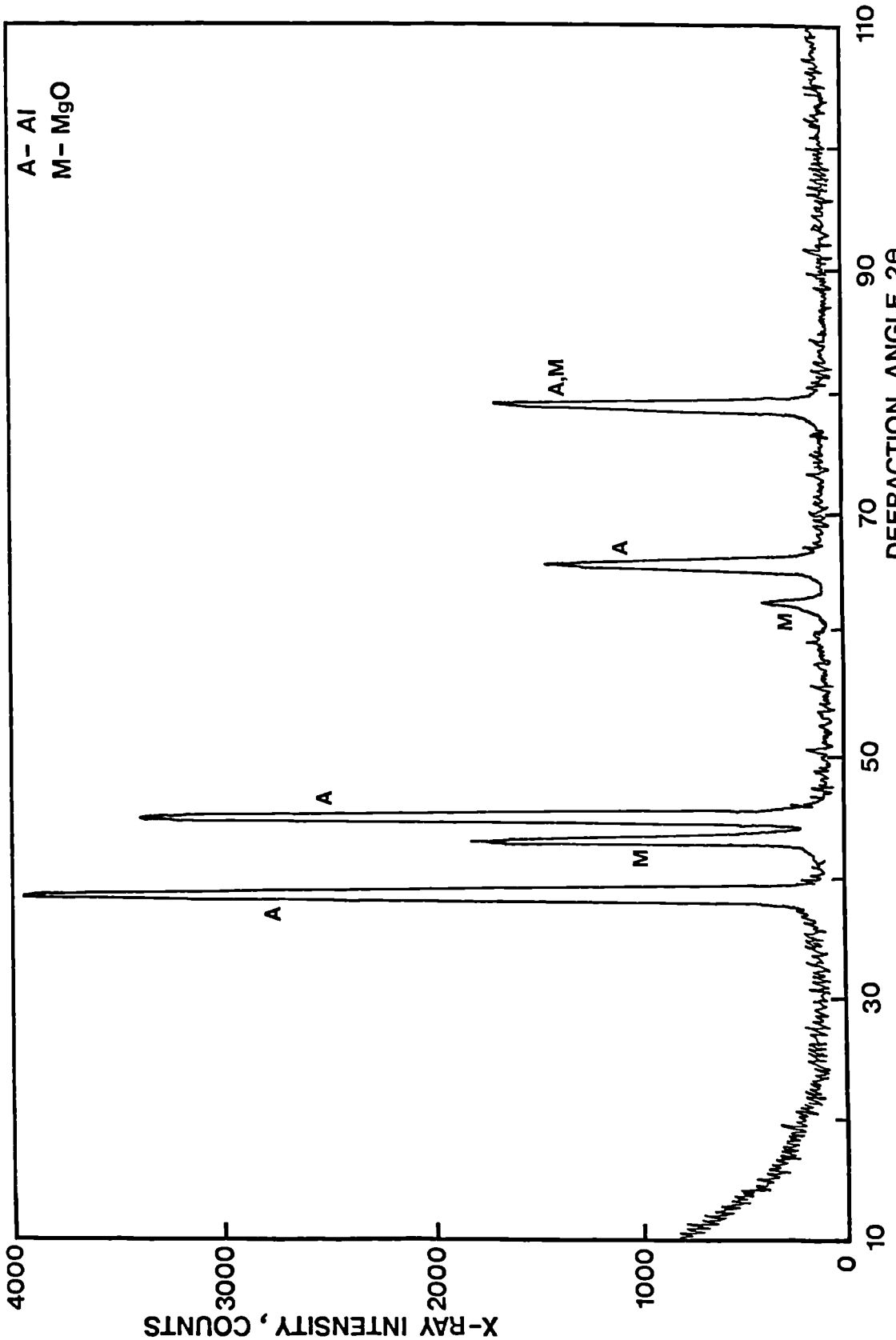

Figure 110. X-ray diffraction spectra from oxidised sample of liquid Al-8.13% Mg-0.003% Be-0.12% Zr alloy after 3h exposure in the moist atmosphere at 700^{o}C, confirming the exclusive formation of MgO.

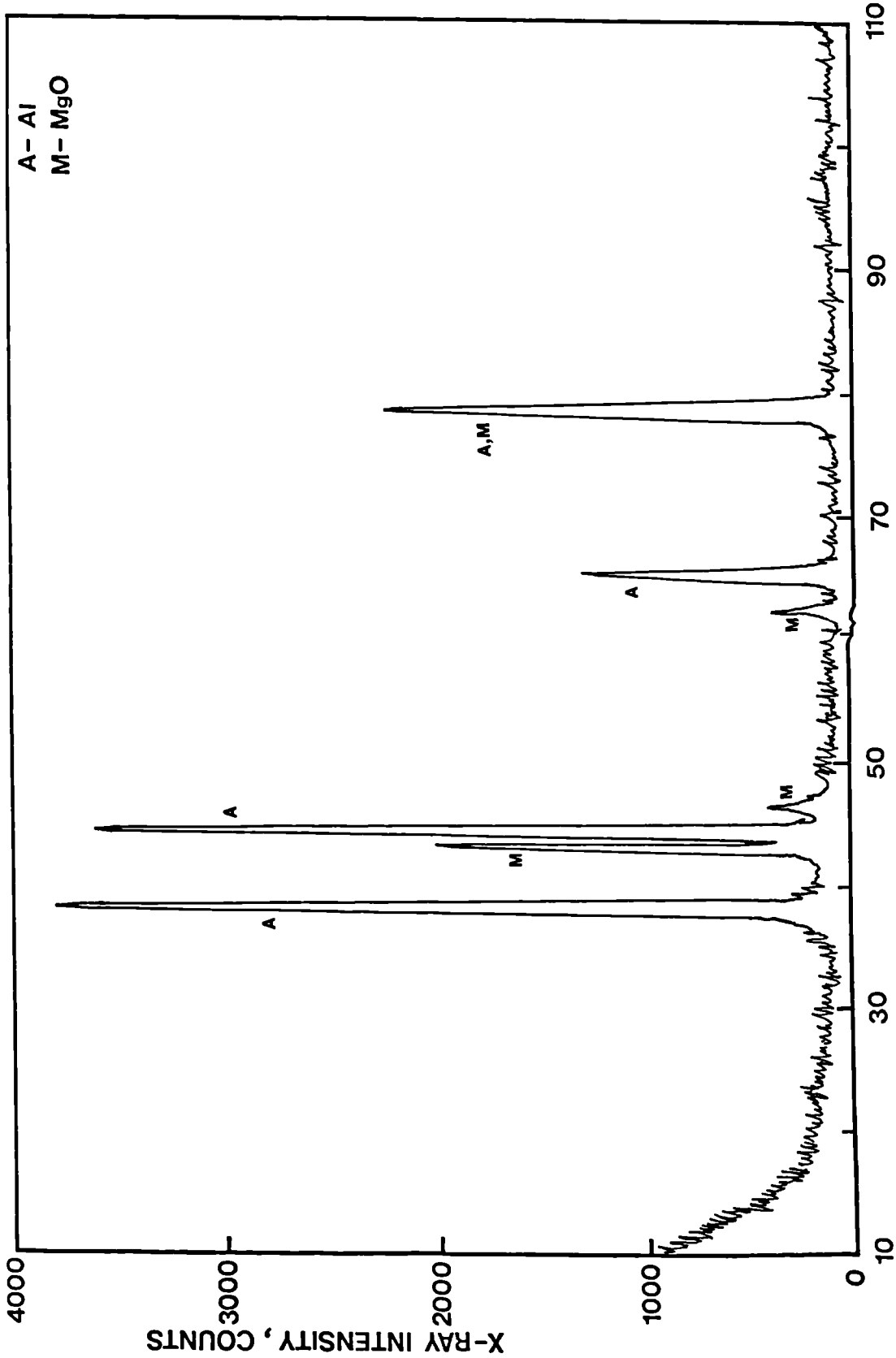

111. X-ray diffraction spectra from oxidised sample of semi-liquid Al-8.13% Mg-0.003% Be-0.12% Zr alloy with <50% liquid after 3h exposure in the dry atmosphere at 575°C, confirming the exclusive formation of MgO.

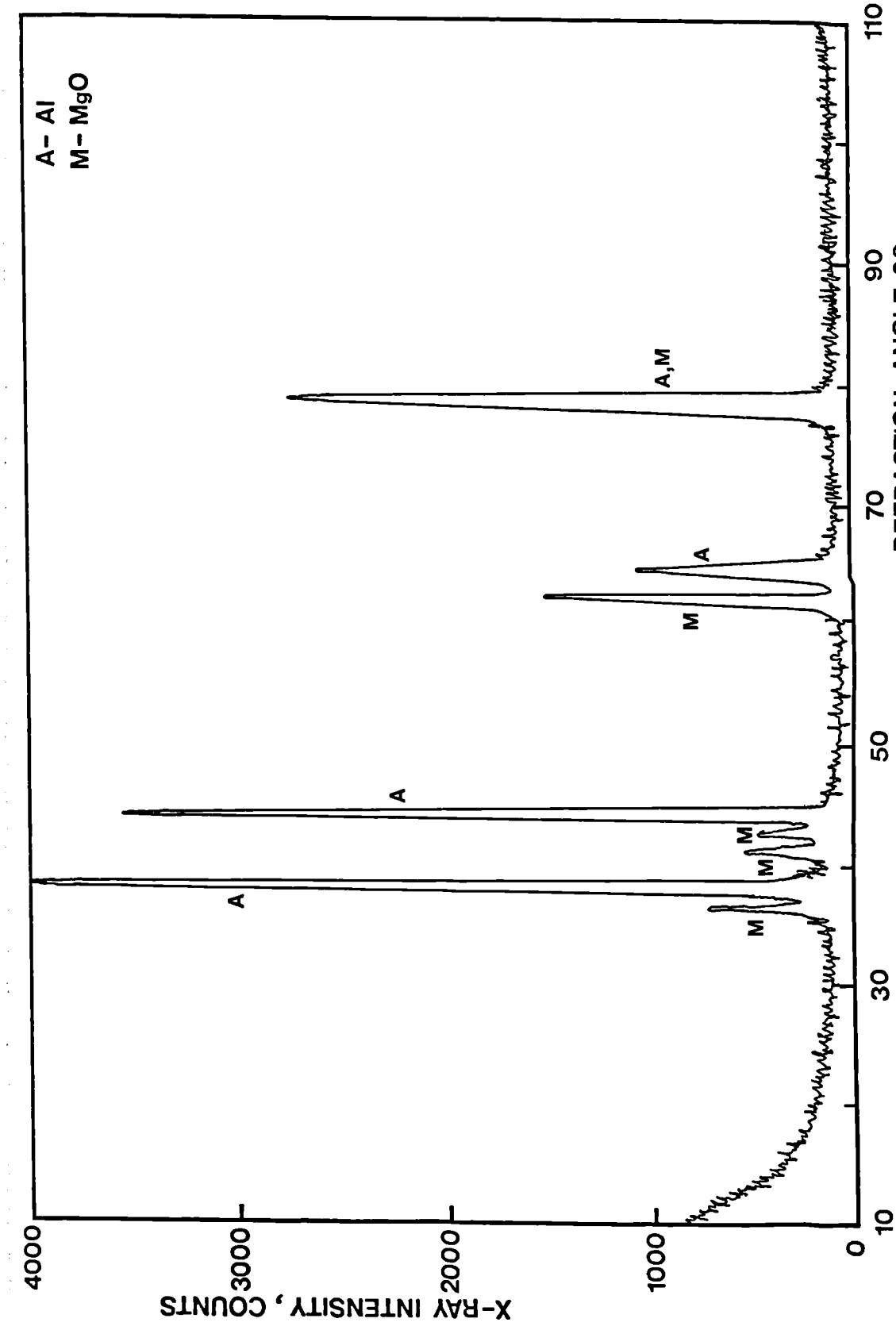

Figure 112. X-ray diffraction spectra from oxidised sample of Al-8.16% Mg-0.003% Be-0.24% Mn alloy with >50% liquid after 3h exposure in the moist atmosphere at 610°C, confirming the exclusive formation of MgO.

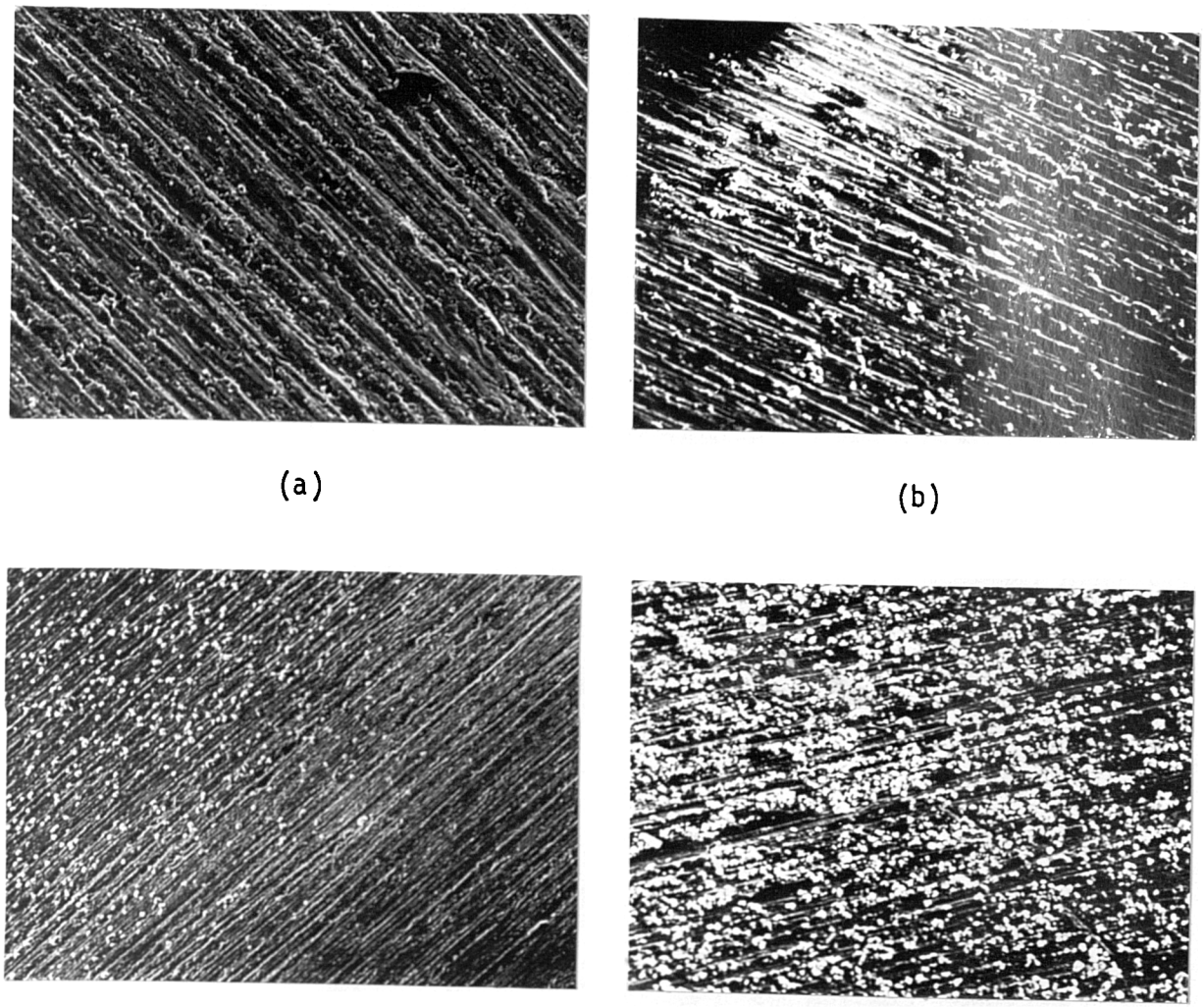

igure 113. SEM micrographs of oxide films formed on solid Al-1.3% Mg alloy after 30 min and 2h exposures in both dry and moist atmosphere at 525°C, showing the development of tertiary MgO.

(a), (b) : dry atmosphere (x 300); note the continuous nucleation of tertiary MgO.

(c), (d) : moist atmosphere (x 300); note the growth of initially formed tertiary MgO.

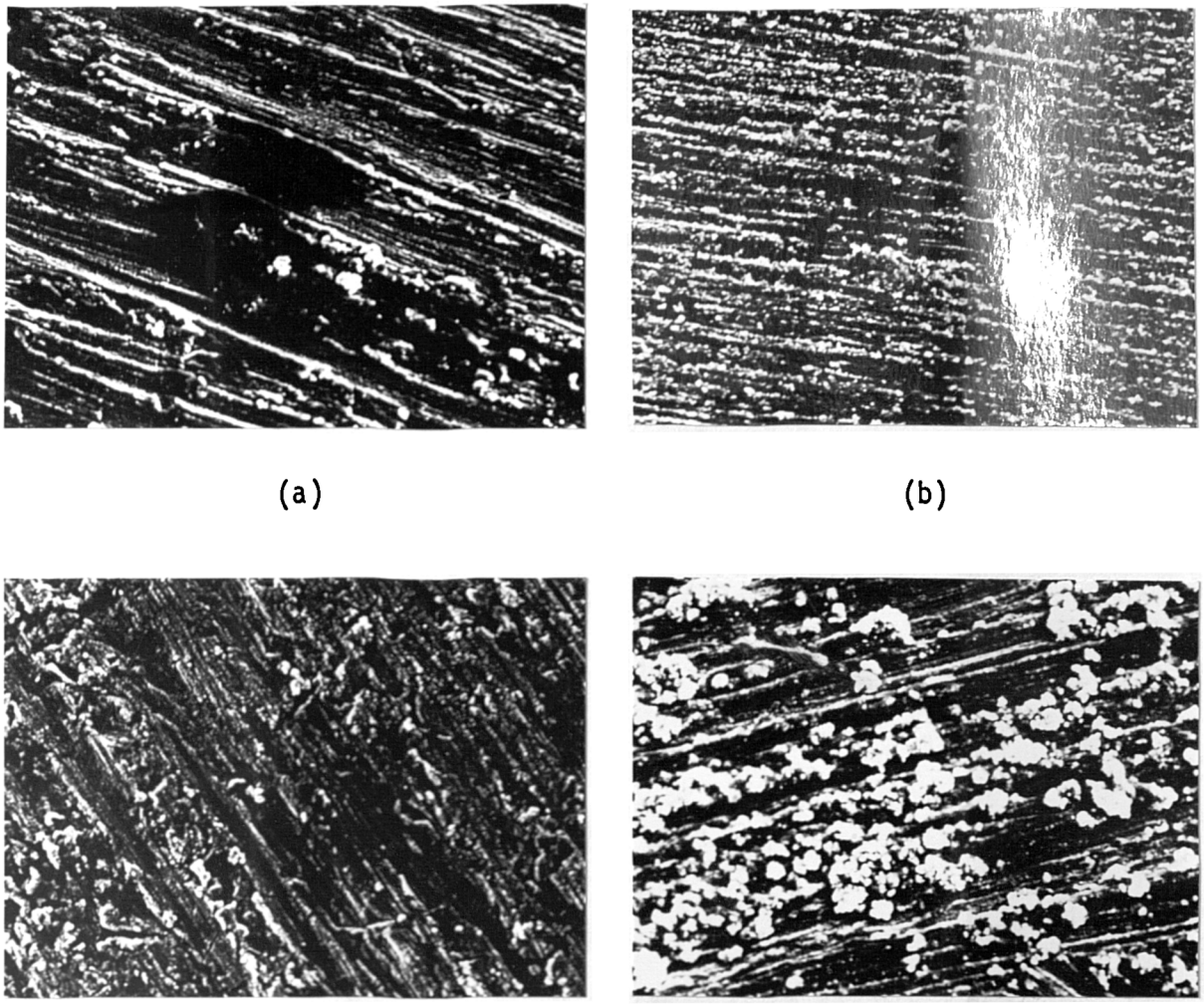

Figure 114. SEM micrographs of oxide films formed on solid Al-3.1% Mg alloy after 30 min and 2h exposures in both dry and moist atmospheres at 525^{o}C, showing the development of tertiary MgO.

(a), (b) : dry atmosphere (x 400); note the continuous nucleation of tertiary MgO.

(c), (d) : moist atmosphere (x 400); note the growth of initially formed tertiary MgO.

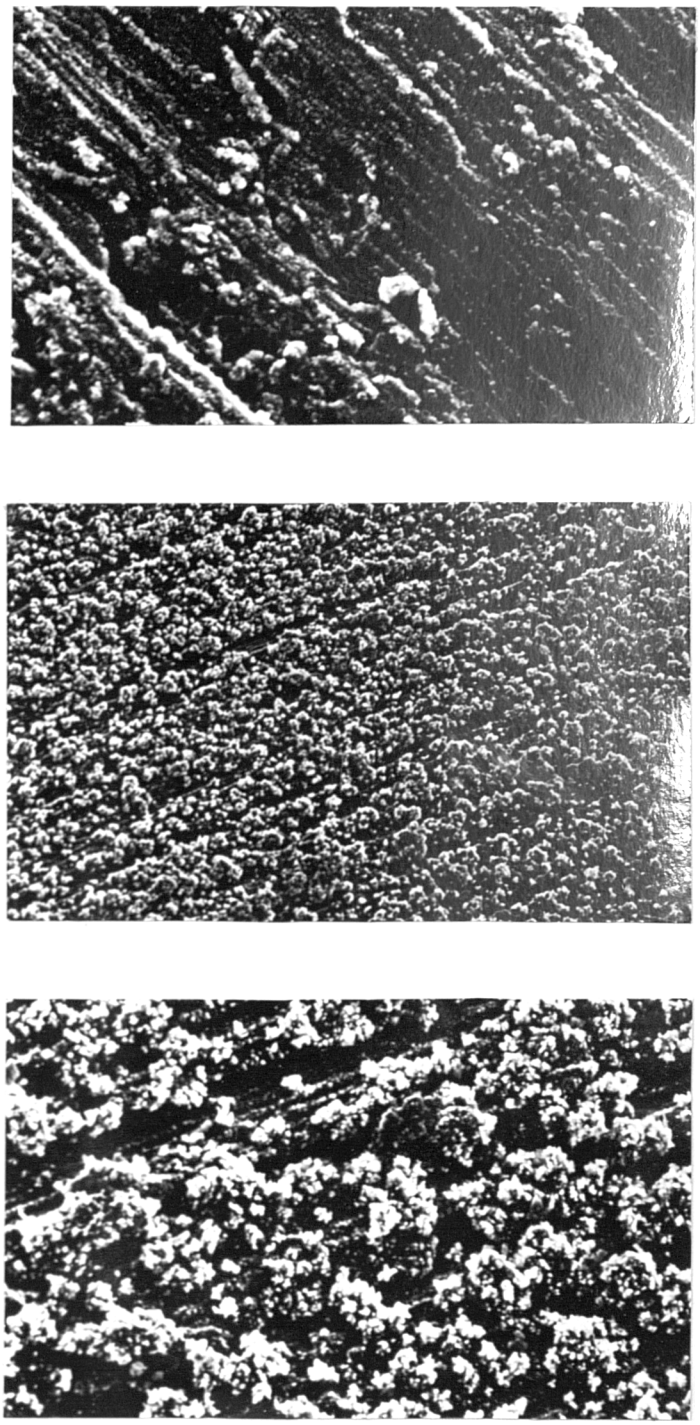

(a)

(b)

(c)

Figure 115. SEM micrographs of oxide films formed on solid Al-5.1% Mg alloy after various exposures in dry and moist atmospheres at 525°C, showing the development of tertiary MgO.

(a), (b) : 30 min and 2h exposures in the dry atmosphere (x 400 and x 300)

(c) : 2h exposure in the moist atmosphere (x 400)

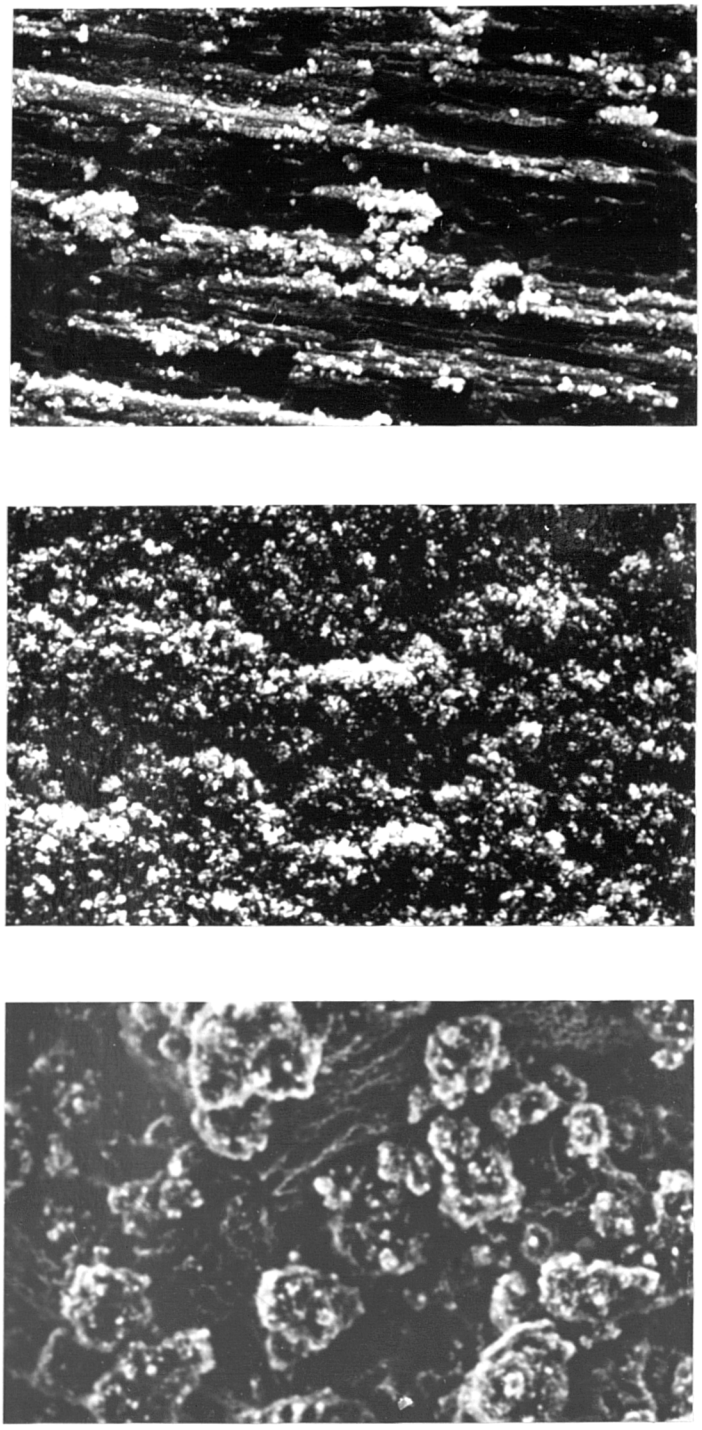

(a)

(b)

(c)

Figure 116. SEM micrographs of oxide films formed on solid Al-7.4% Mg alloy after various exposures in dry and moist atmospheres at 525°C, showing the development of tertiary MgO.

(a), (b) : 30 min and 2h exposures in the dry atmosphere (x 400)

(c) : 2h exposure in the moist atmosphere (x 400)

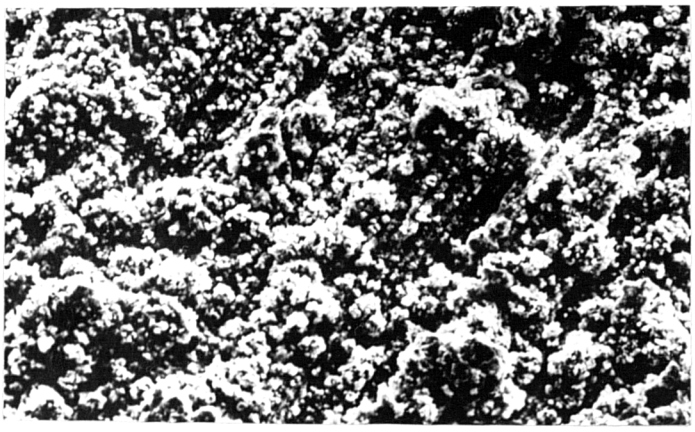

(a)

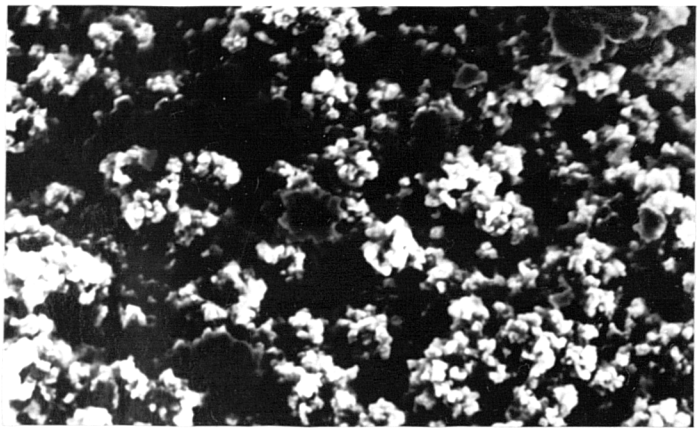

(b)

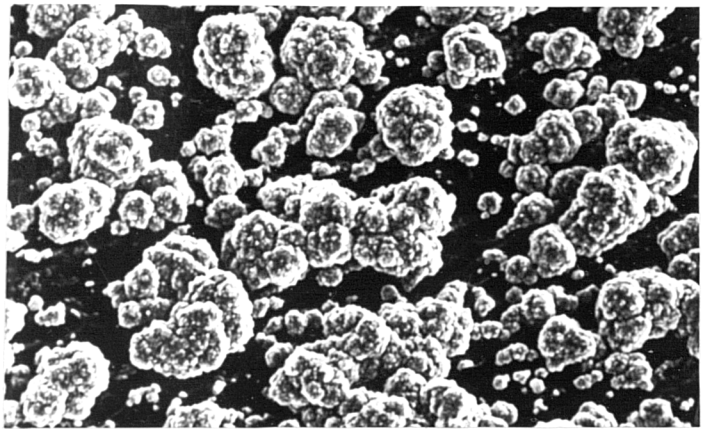

(c)

Figure 117. SEM micrographs of oxide films formed on solid Al-9.3% Mg alloy after various exposures in dry and moist atmospheres at 525°C, showing the development of tertiary MgO.

(a) : 2h exposure in the dry atmosphere (x 400)

(b), (c) : 60 min and 2h exposures in the moist atmosphere (x 400)

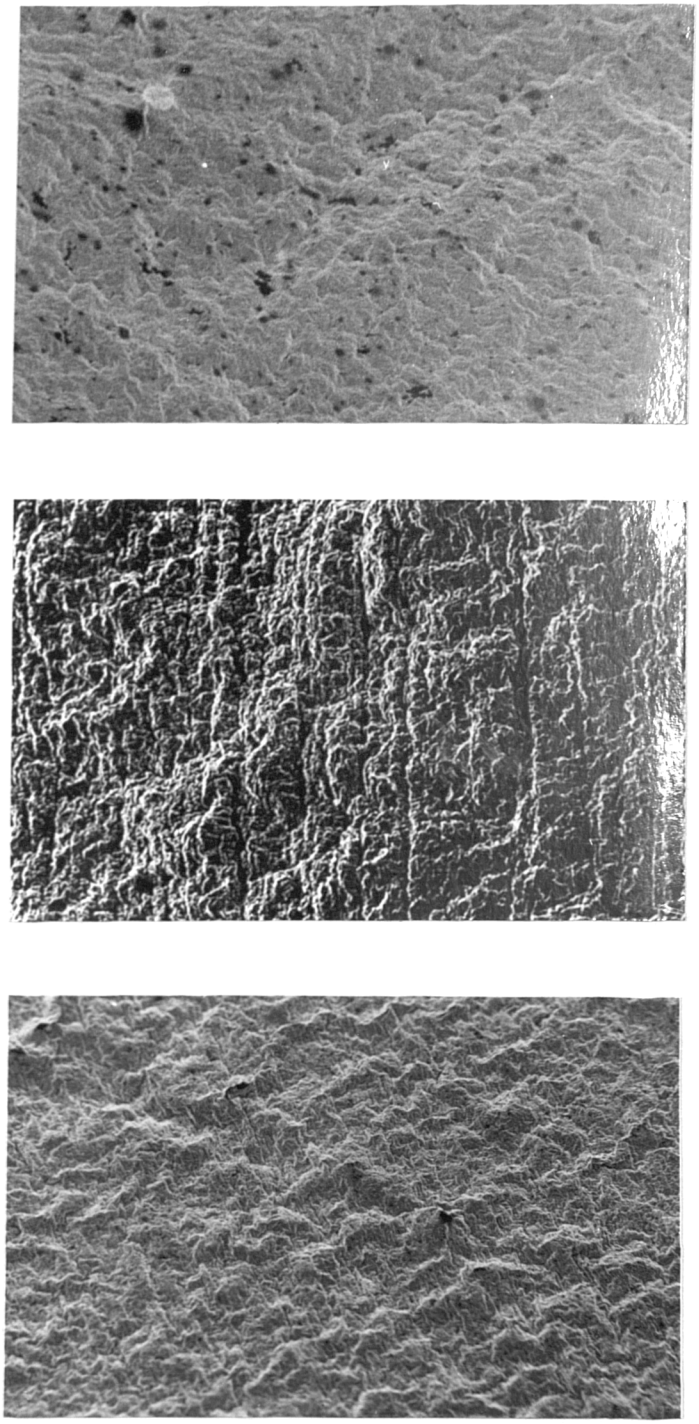

(a)

(b)

(c)

Figure 118. SEM micrographs of oxide films formed on liquid Al-1.3% Mg alloy after 2h exposure in dry and moist atmospheres at various temperatures.

(a) : 725^{o}C in the dry atmosphere (x 400)

(b), (c) : 675^{o}C and 725^{o}C in the moist atmosphere (x 400); note that the oxide becomes smoother with increasing temperature.

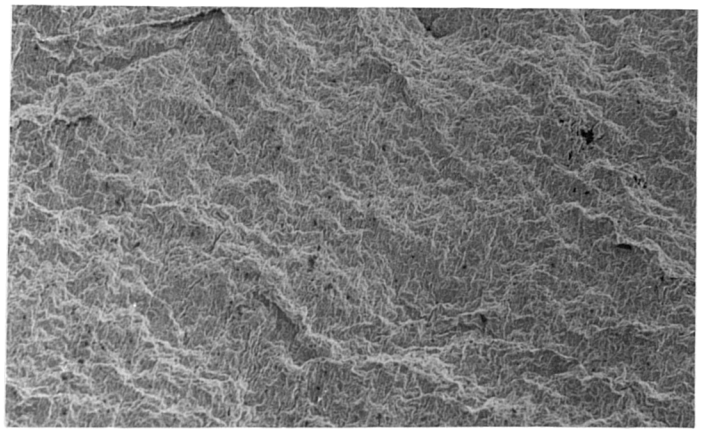

(a)

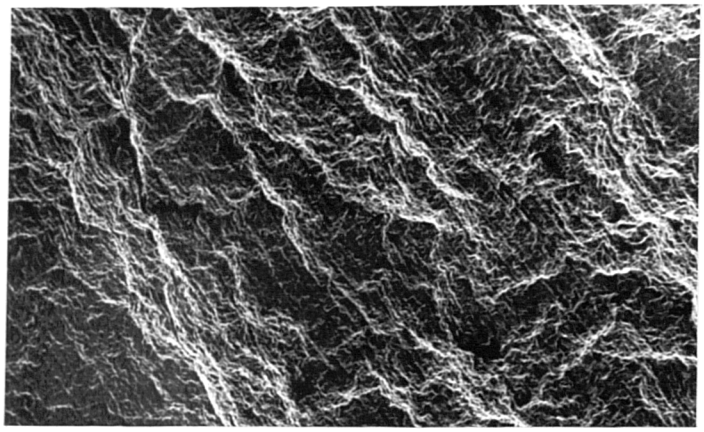

(b)

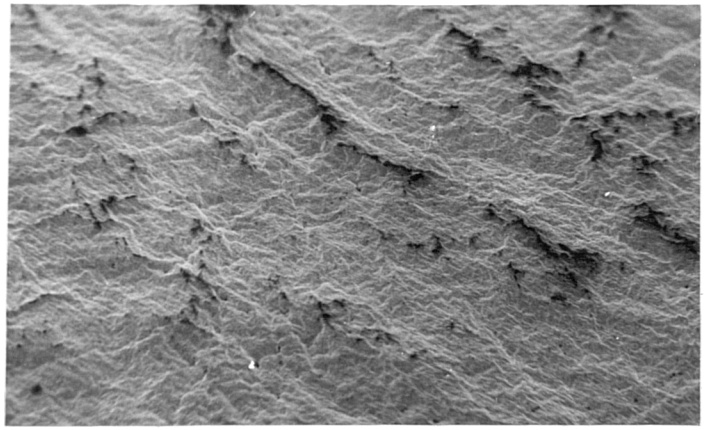

(c)

Figure 119. SEM micrographs of oxide films formed on liquid Al-3.1% Mg alloy after 2h exposure in dry and moist atmospheres at various temperatures.

(a) : 725^{o}C in the dry atmosphere (x 400)

(b), (c) : 675^{o}C and 725^{o}C in the moist atmosphere (x 400); note that the surface becomes smoother with increasing temperature and the development of extended cracks during breakaway oxidation.

(a)

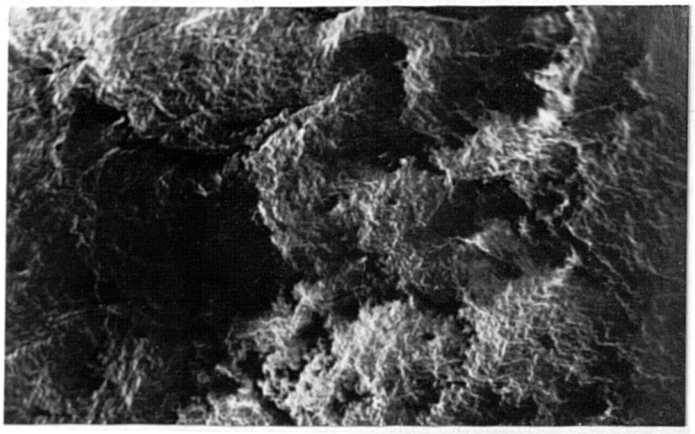

(b)

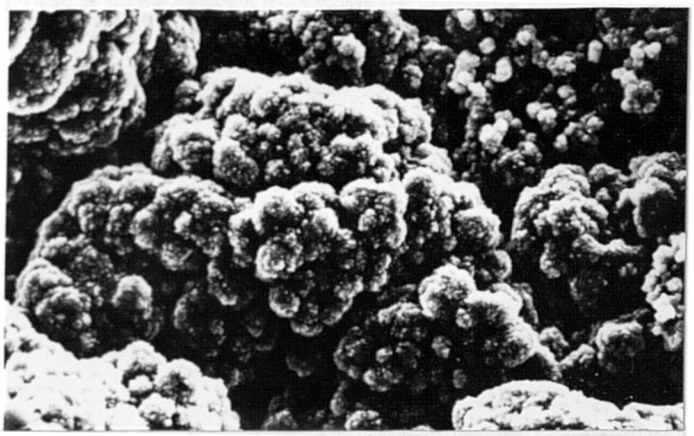

(c)

Figure 120. SEM micrographs of oxide films formed on liquid Al-5.1% Mg alloy after various exposures in dry and moist atmospheres at 700°C, showing the development of cracks and "cauliflower" growths during breakaway oxidation.

(a) : 2h exposure in the dry atmosphere (x 200)

(b), (c) : 1h and 2h exposures in the moist atmosphere. (x 400 and x 600)

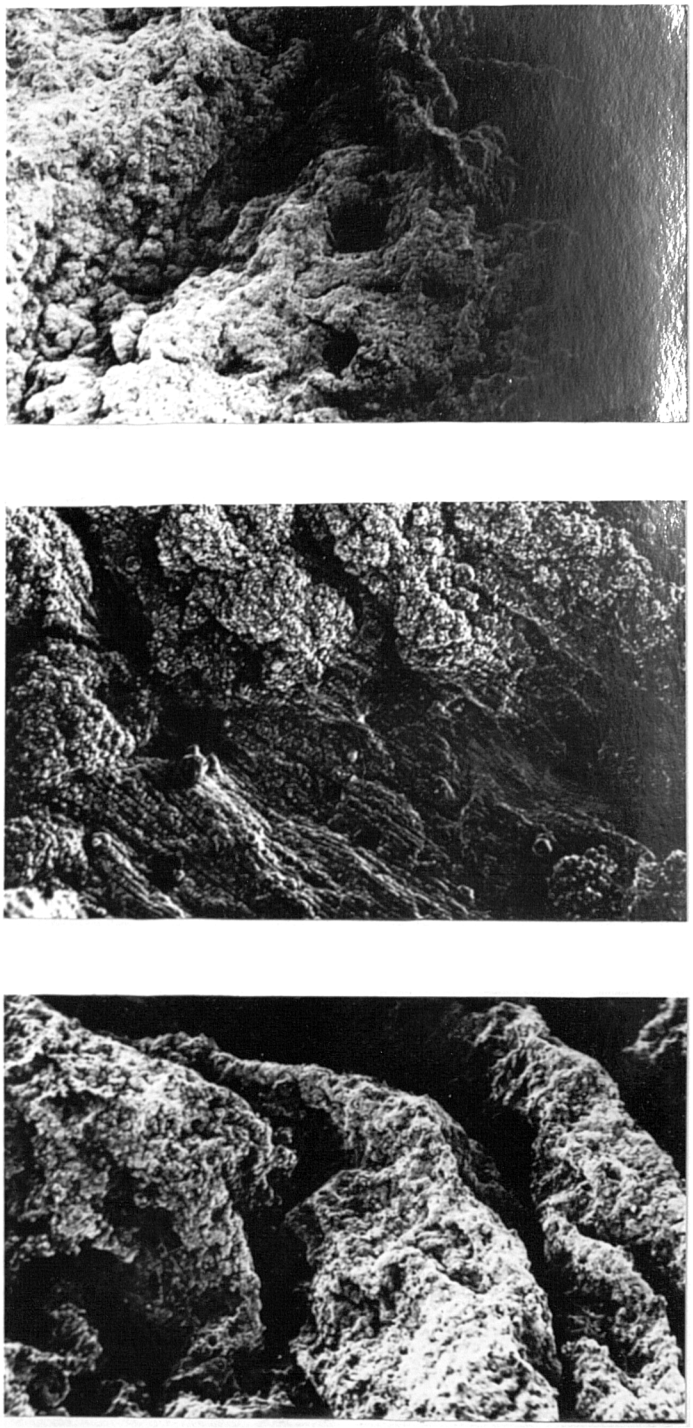

(a)

(b)

(c)

Figure 121. SEM micrographs of oxide films formed on liquid Al-7.4% Mg alloy after various exposures in dry and moist atmospheres at 625°C, i.e. near the liquidus temperature, showing the development of corrugated surfaces.

(a) : 2h exposure to the dry atmosphere (x 400)

(b), (c) : 1h and 2h exposures in the moist atmosphere (x 400); note that wrinkling of the oxide increases with progressive oxidation.

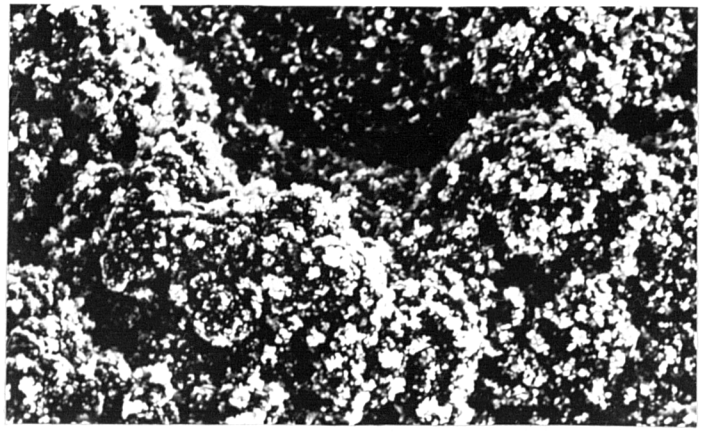

(a)

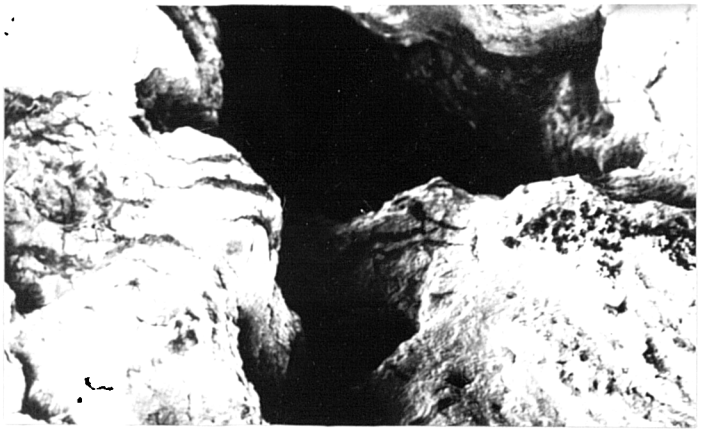

(b)

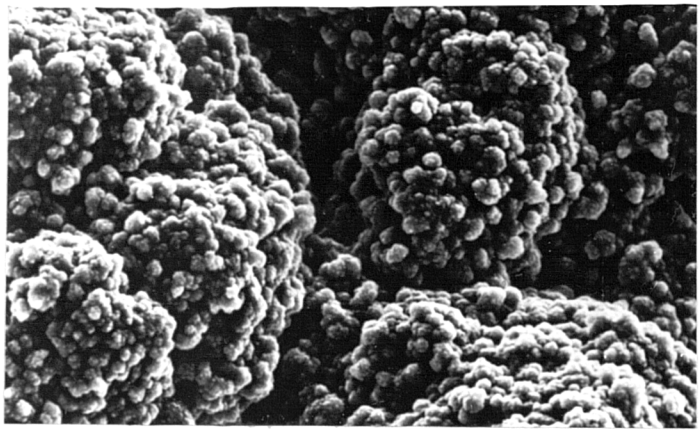

(c)

Figure 122. SEM micrographs of oxide films formed on liquid Al-7.4% Mg alloy after various exposures in dry and moist atmospheres at 700°C, i.e. well above the liquidus temperature, showing the development of "cauliflower" growths.

(a) : 2h exposure in the dry atmosphere (x 400)

(b), (c) : 30 min and 2h exposures in the moist atmosphere. (x 200 and x 500)

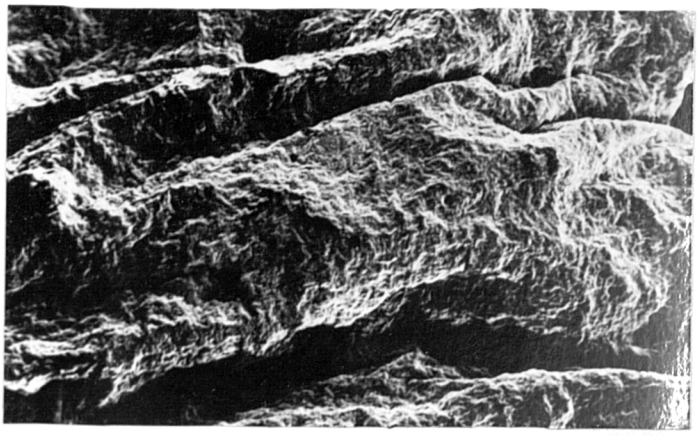

(a)

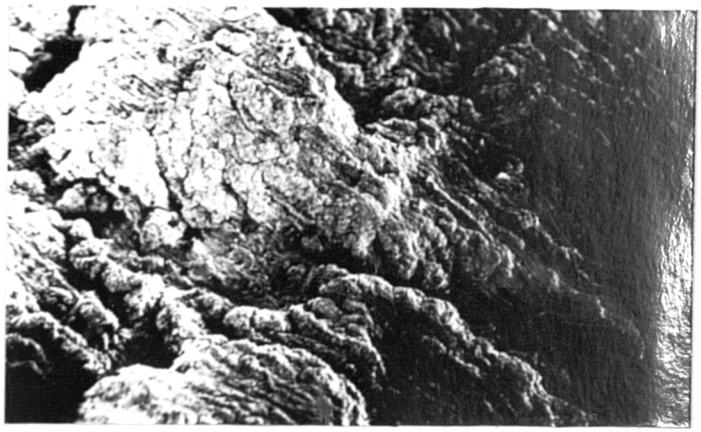

(b)

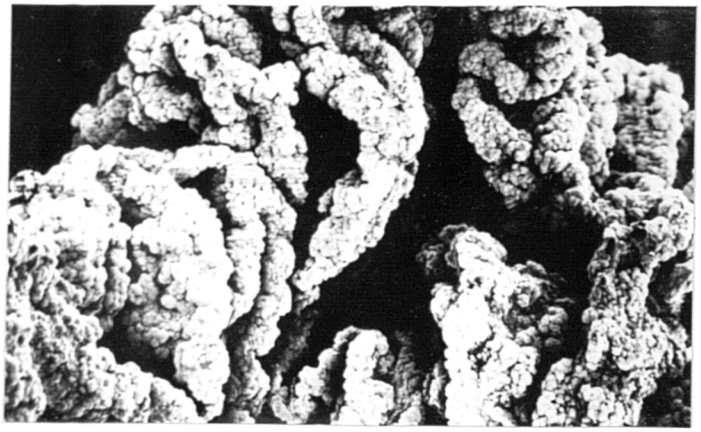

(c)

igure 123. SEM micrographs of oxide films formed on liquid Al-9.3% Mg alloy after various exposures in dry and moist atmospheres at 625°C, i.e. near the liquidus temperature, showing the development of corrugated surfaces.

(a) : 2h exposure in the dry atmosphere (x 400)

(b), (c) : 1h and 2h exposures in the moist atmosphere (x 400)

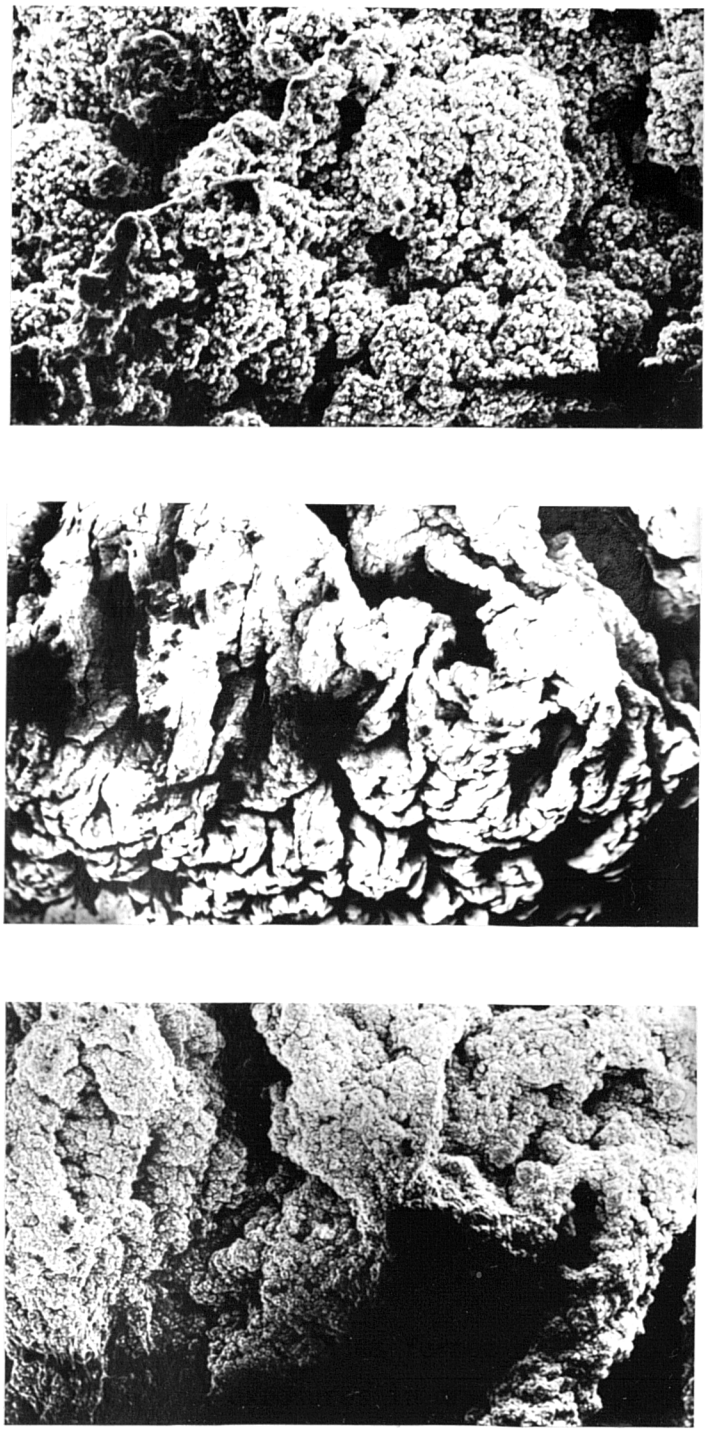

(a)

(b)

(c)

Figure 124. SEM micrographs of oxide films formed on liquid Al-9.3% Mg alloy after various exposures in dry and moist atmospheres at 700°C, i.e. well above the liquidus temperature, showing the development of "cauliflower" growths.

(a) : 2h exposure in the dry atmosphere (x 400)

(b), (c) : 1h and 2h exposures in the moist atmosphere (x 200 and x 400)

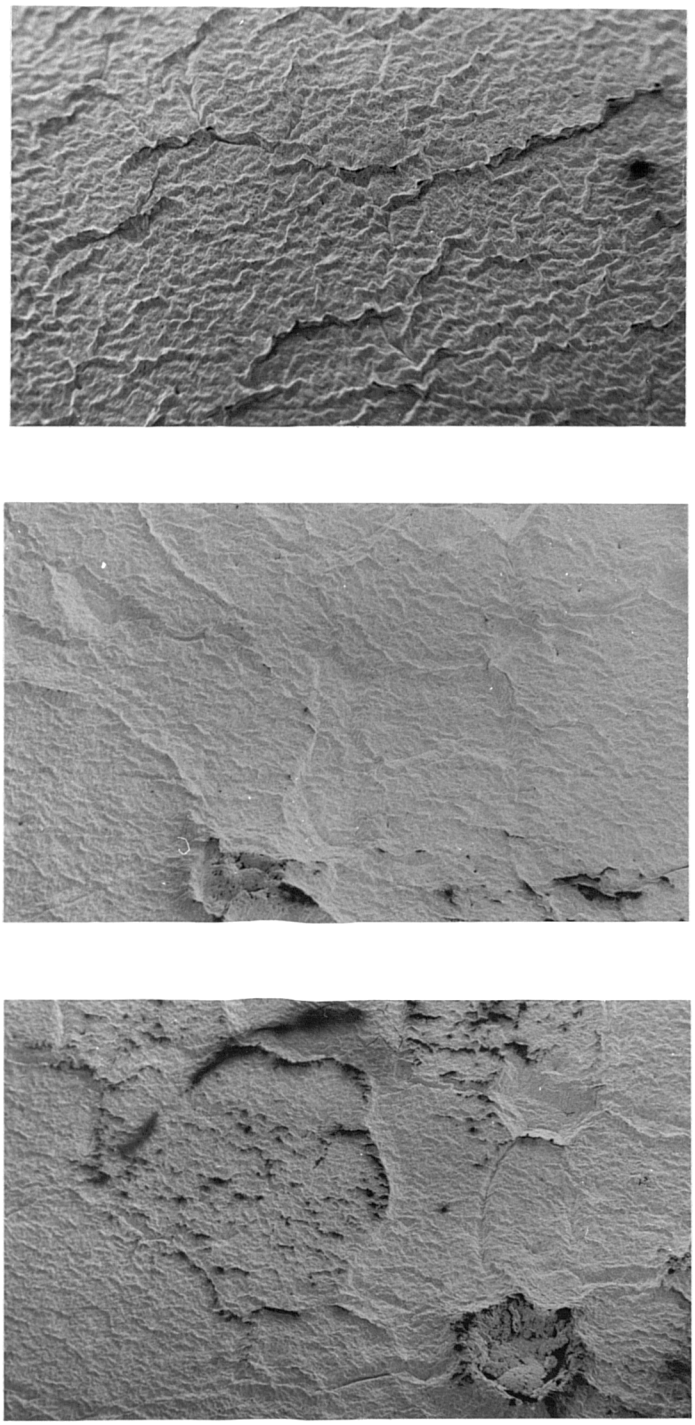

(a)

(b)

(c)

Figure 125. SEM micrographs of oxide films formed on semi-liquid Al-1.3% Mg alloy with <50% liquid after various exposures in dry and moist atmospheres at 646^{o}C.

(a) : 2h exposure in the dry atmosphere (x 250); note the development of tertiary MgO both in grains and along grain boundaries.

(b), (c) : 30 min and 2h exposures in the moist atmosphere (x 250); note the development of tertiary MgO preferentially along magnesium enriched grain boundaries.

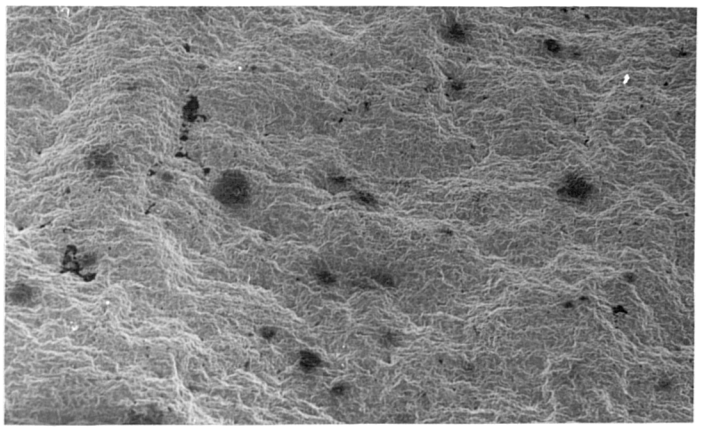

(a)

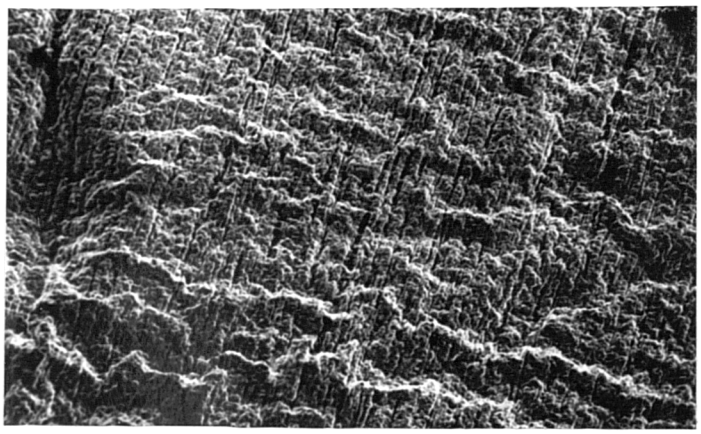

(b)

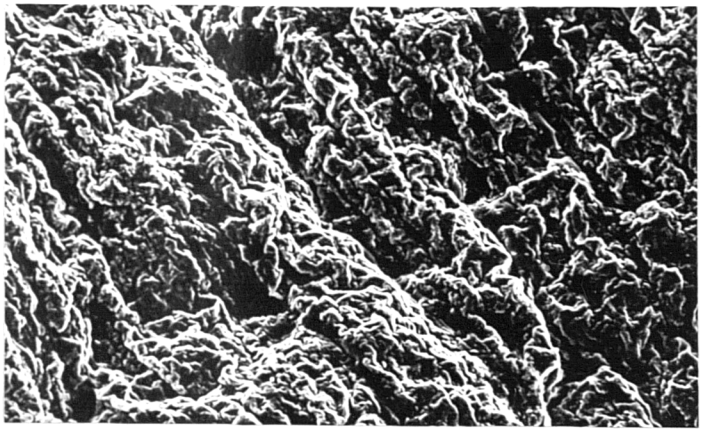

(c)

Figure 126. SEM micrographs of oxide films formed on semi-liquid Al-1.3% Mg alloy with >50% liquid after various exposures in dry and moist atmospheres at 654°C, showing stress-relief by wrinkling of the oxide film.

(a) : 2h exposure in the dry atmosphere. (x 250)

(b), (c) : 1h and 2h exposures in the moist atmosphere (x 250); note that the oxide becomes progressively wrinkled with elapse of time as for the liquid alloys in Figure 121.

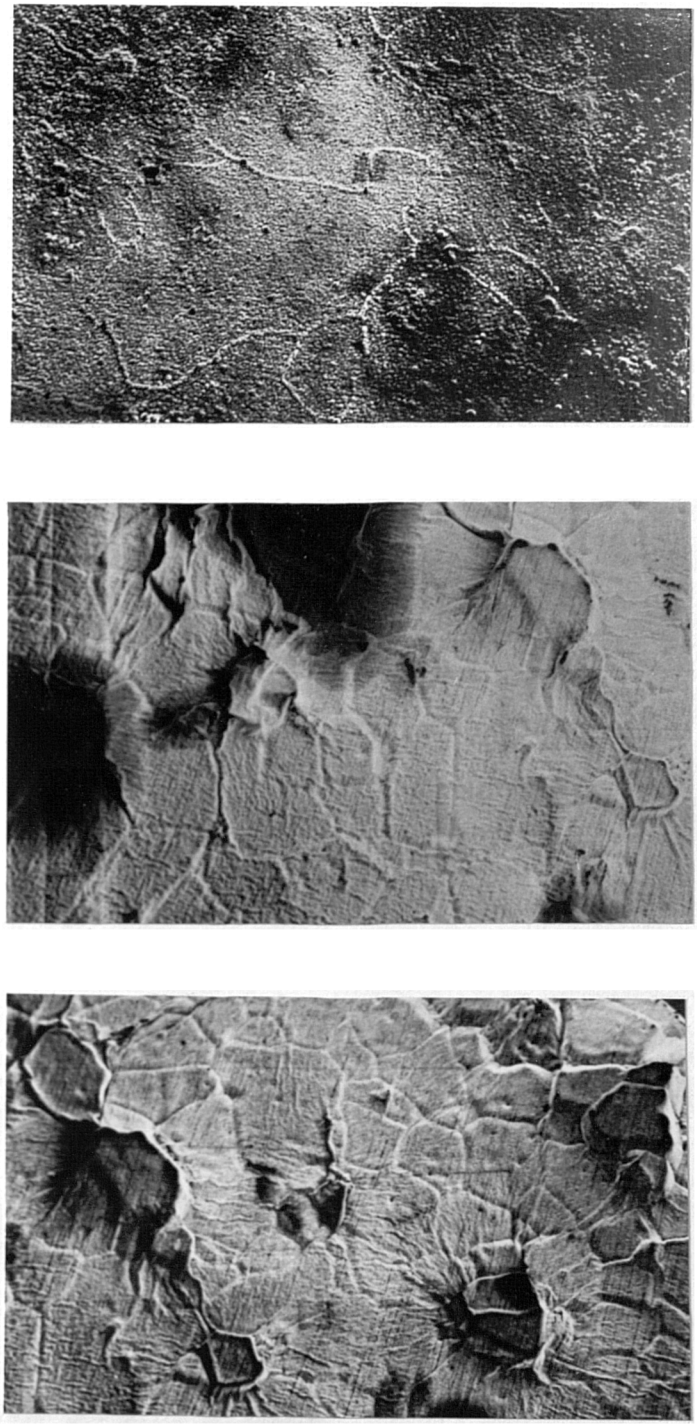

(a)

(b)

(c)

Figure 127. SEM micrographs of oxide films formed on semi-liquid Al-3.1% Mg alloy with < 50% liquid after various exposures in dry and moist atmospheres at 625°C.

(a) : 2h exposure in the dry atmosphere (x 250); note the development of tertiary MgO both in grains and along grain boundaries.

(b), (c) : 1h and 2h exposures in the moist atmosphere (x 250); note severe grain boundary oxidation by the development of tertiary MgO preferentially along grain boundaries.

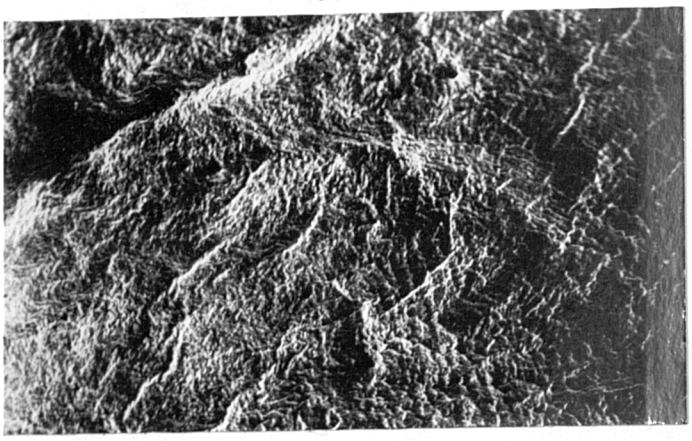

(a)

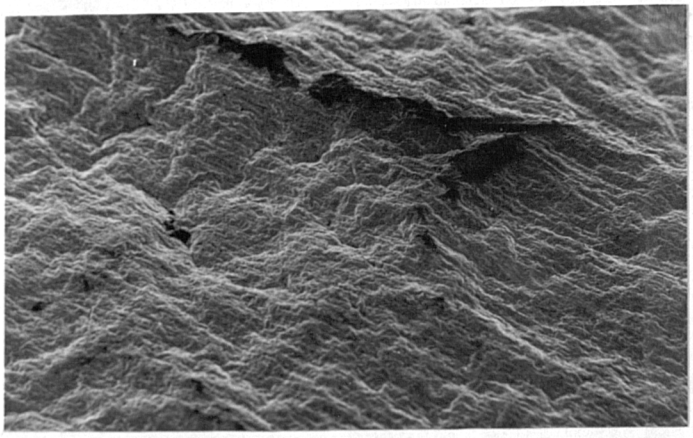

(b)

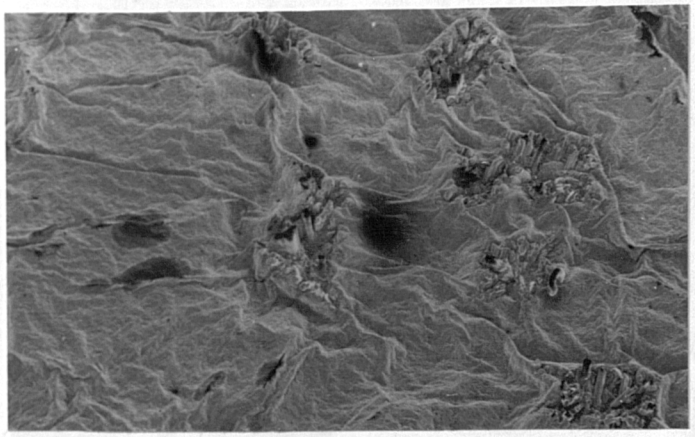

(c)

Figure 128. SEM micrographs of oxide films formed on semi-liquid Al-3.1% Mg alloy with >50% liquid after various exposures in dry and moist atmospheres at 640°C.

(a) : 2h exposure in the dry atmosphere (x 250); note stress-relief by wrinkling of the oxide film.

(b), (c) : 1h and 2h exposures in the moist atmosphere (x 250); note wrinkling and cracking of the oxide film reducing the protection afforded thereby stimulating oxidation.

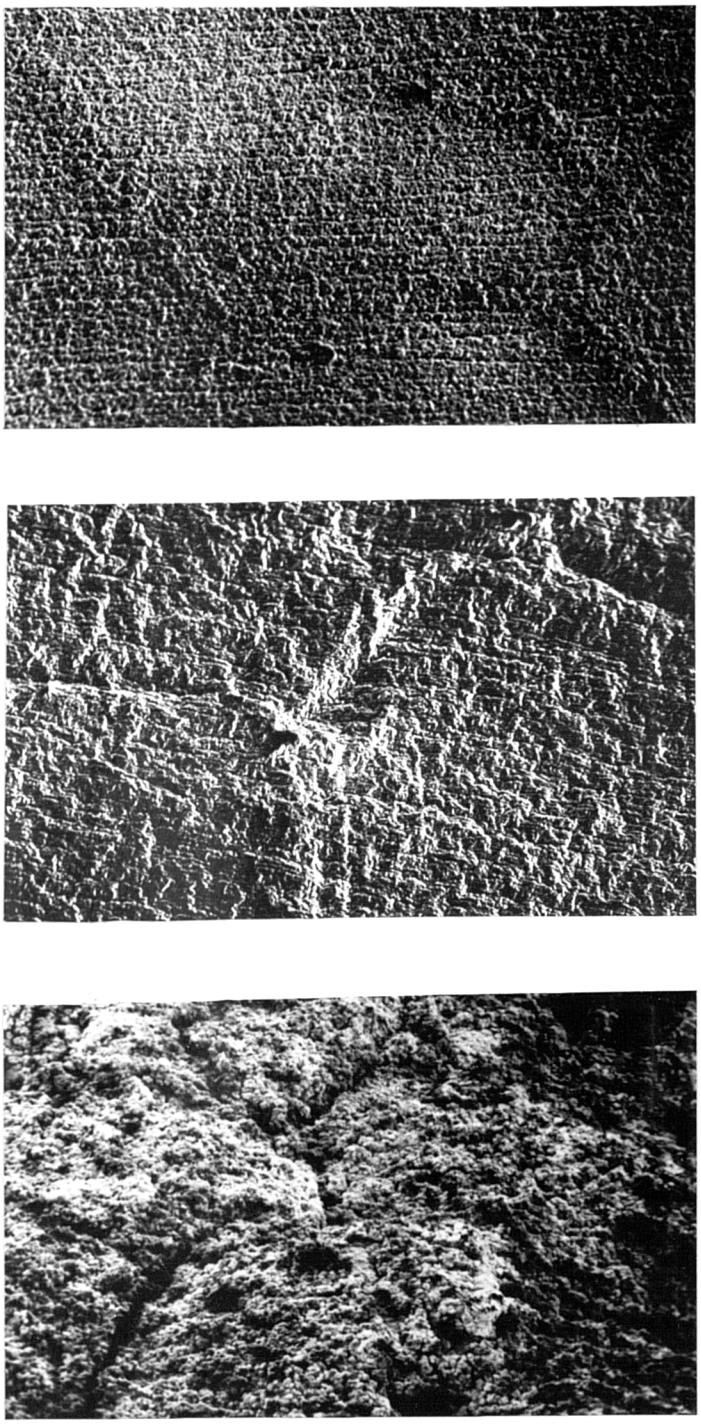

(a)

(b)

(c)

Figure 129. SEM micrographs of oxide films formed on semi-liquid Al-5.1% Mg alloy after 2h exposure in dry and moist atmospheres at various temperatures.

(a), (b) : alloy with < 50% liquid in dry and moist atmospheres at 600°C (x 250 and x 500)

(c) : alloy with ∿50% liquid in the moist atmosphere at 610°C (x 250); note destruction of the alloy due to intergranular oxidation and disintegration.

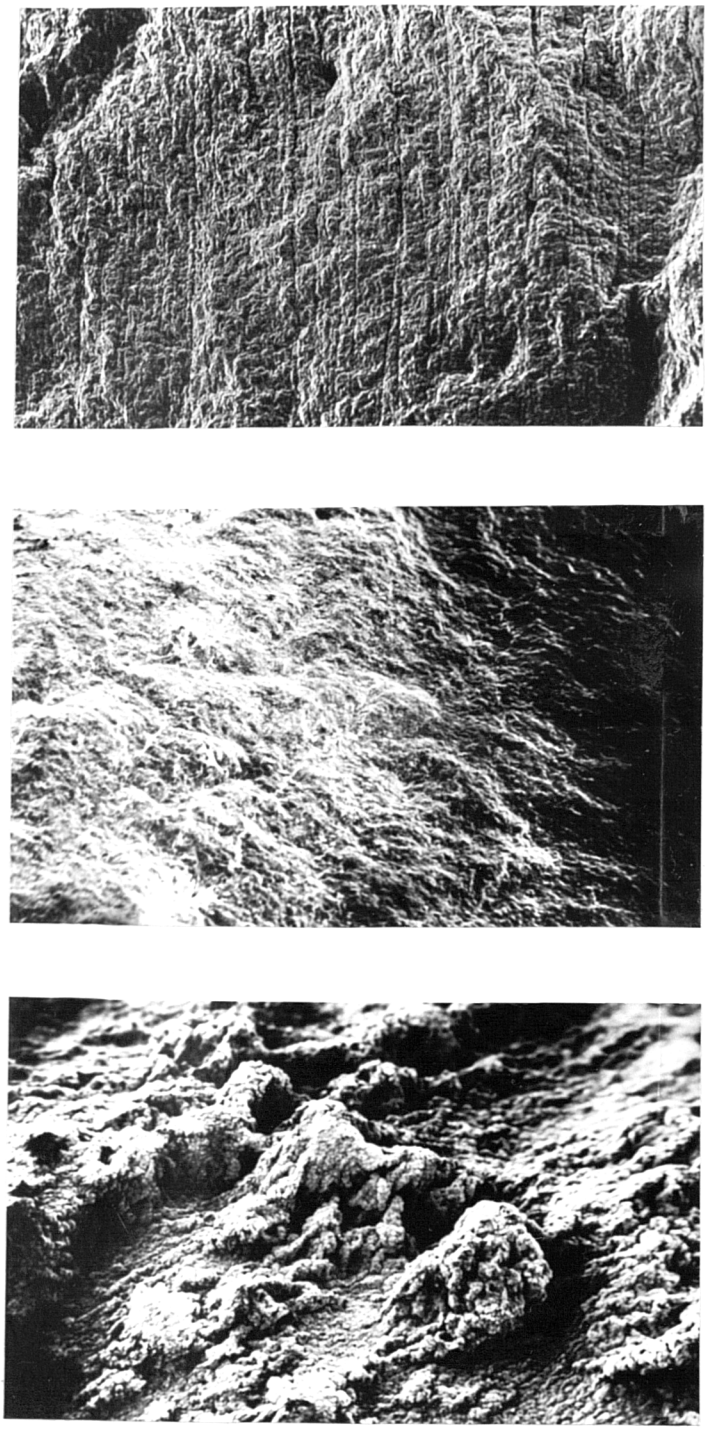

(a)

(b)

(c)

Figure 130. SEM micrographs of oxide films formed on semi-liquid Al-5.1% Mg alloy with >50% liquid after various exposures in dry and moist atmospheres at 625^{o}C.

(a) : 2h exposure in the dry atmosphere (x 250); note stress-relief by corrugation of the oxide film.

(c), (d) : 1h and 2h exposures in the moist atmosphere (x 250); note the development of disruptive growth of tertiary MgO.

(a)

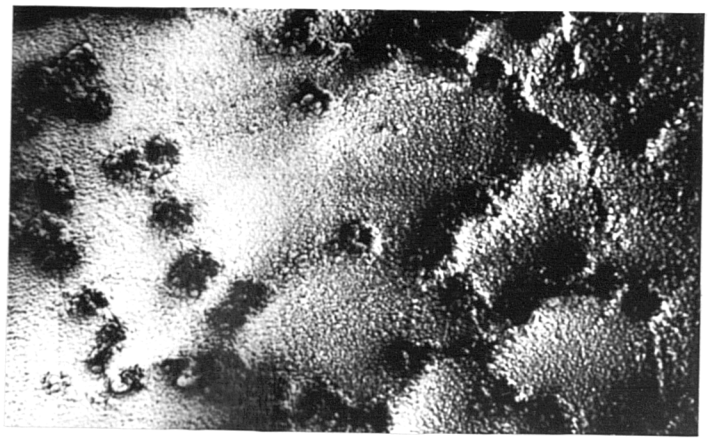

(b)

Figure 131. SEM micrographs of oxide films formed on semi-liquid Al-7.4% Mg alloy with <50% liquid after 2h exposure in dry and moist atmospheres at 575°C, showing the dense development of tertiary MgO over the entire surface.

(a) : dry atmosphere (x 250)
(b) : moist atmosphere (x 250)

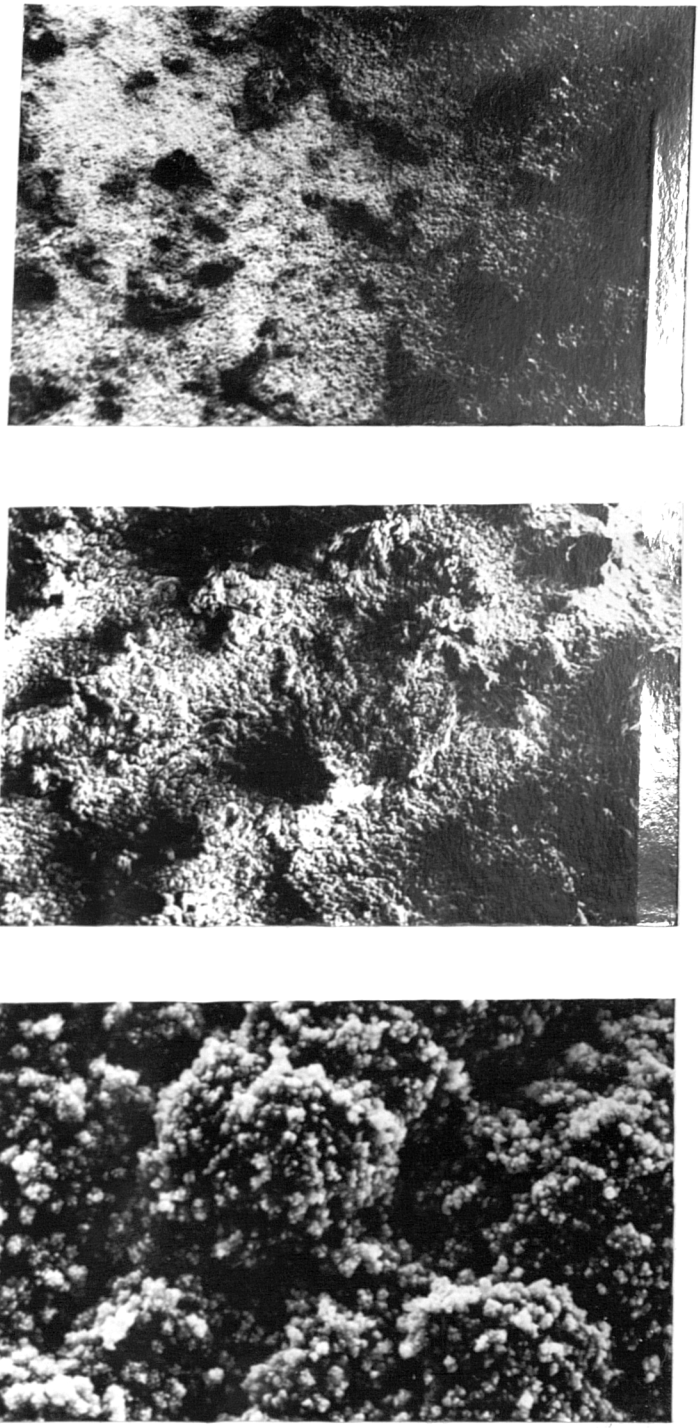

Figure 132. SEM micrographs of oxide films formed on semi-liquid Al-7.4% Mg alloy with >50% liquid after various exposures in dry and moist atmospheres at 610°C, showing disruptive oxidation presumably due to the influence of suspended solid particles in the alloy leading to "cauliflower" growths.

(a) : 2h exposure in the dry atmosphere (x 250)
(b), (c) : 1h and 2h exposures in the moist atmosphere (x 250)

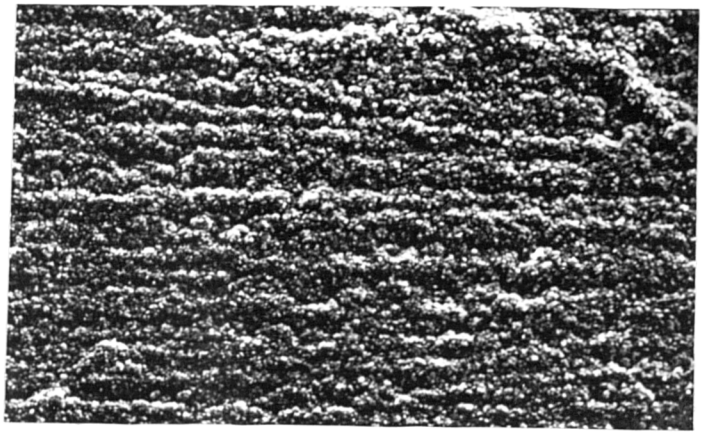

(a)

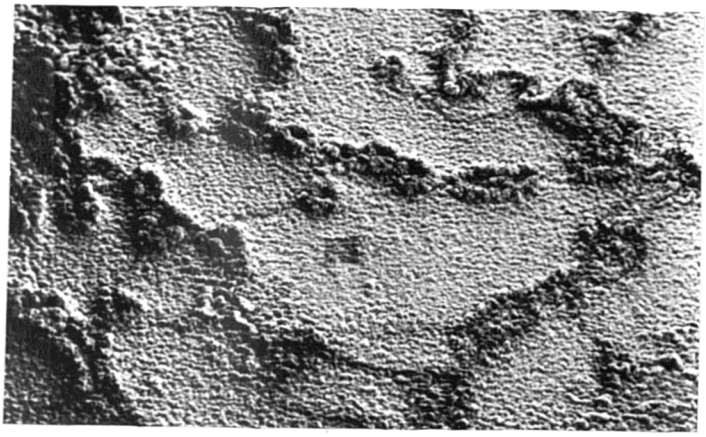

(b)

Figure 133. SEM micrographs of oxide films formed on semi-liquid Al-9.3% Mg alloy with <50% liquid after 2h exposure in dry and moist atmospheres at 550°C, showing the dense development of tertiary MgO over the entire surface.

(a) : dry atmosphere (x 250)
(b) : moist atmosphere (x 250)

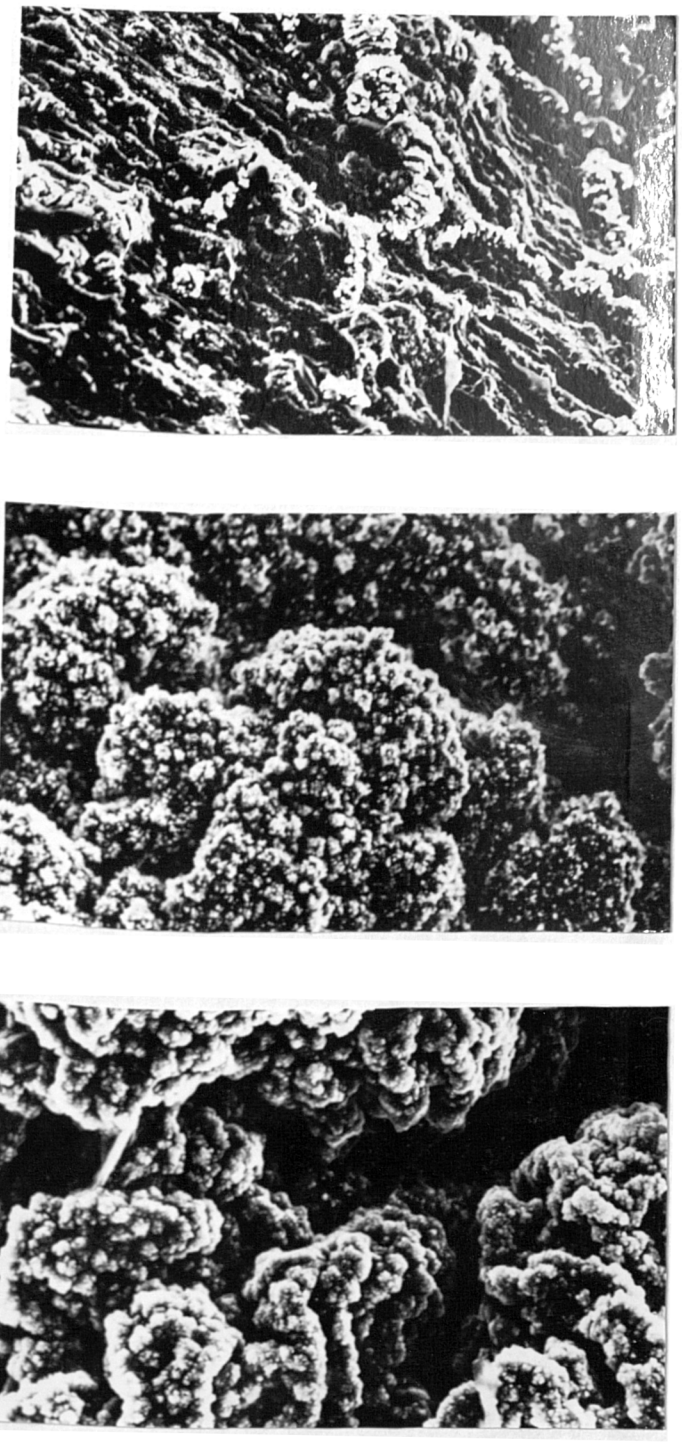

(a)

(b)

(c)

Figure 134. SEM micrographs of oxide films formed on semi-liquid Al-9.3% Mg alloy with >50% liquid after various exposures in dry and moist atmospheres at 600°C, showing disruptive oxidation presumably due to the influence of suspended solid particles in the alloy leading to "cauliflower" growths.

(a) : 2h exposure in the dry atmosphere (x 250)

(b), (c) : 1h and 2h exposures in the moist atmosphere (x 250)

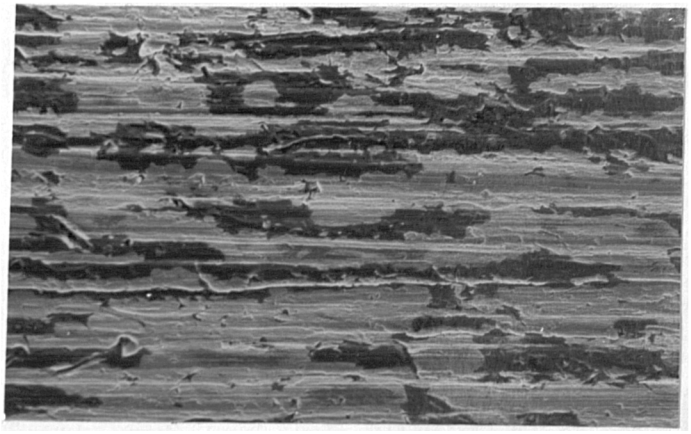

(a)

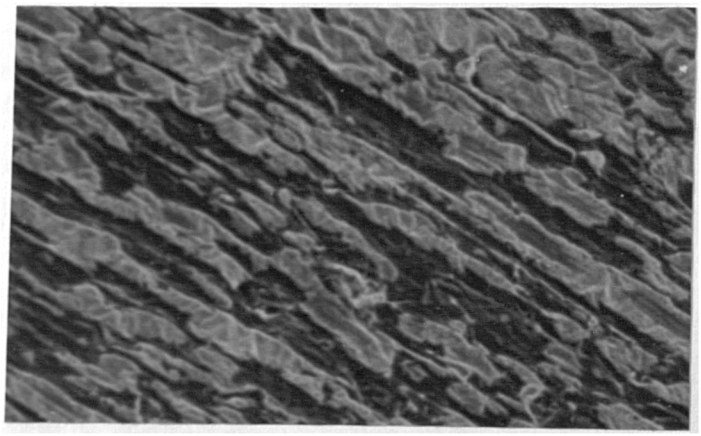

(b)

Figure 135. SEM micrographs of oxide films formed on solid Al-8.2% Mg -0.003% Be alloy after 3h exposure in dry and moist atmospheres at 525°C, showing no nucleation of tertiary MgO.

(a) : dry atmosphere (x 5,000)
(b) : moist atmosphere (x 5,000)

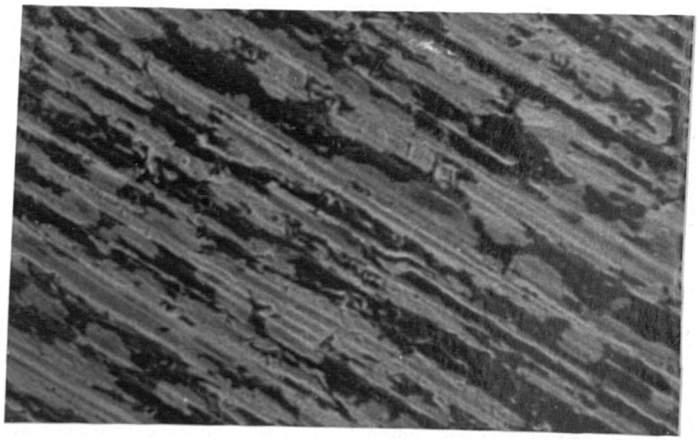

(a)

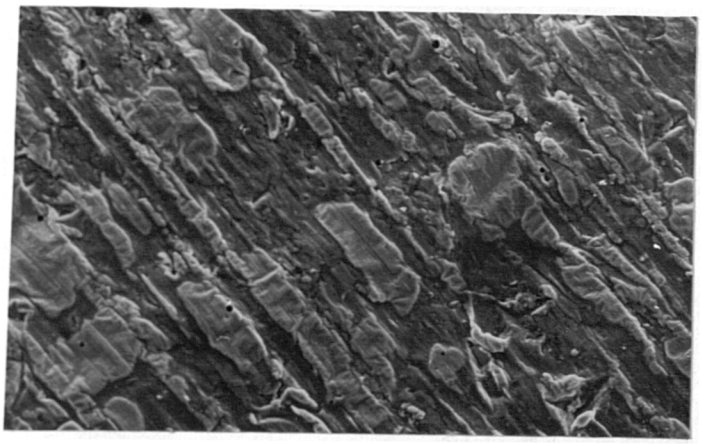

(b)

Figure 136. SEM micrographs of oxide films formed on solid Al-8.16% Mg -0.003% Be-0.24% Mn alloy after 3h exposure in dry and moist atmospheres at 525^{o}C showing no nucleation of tertiary MgO.

(a) : dry atmosphere (x 5,000)
(b) : moist atmosphere (x 5,000)

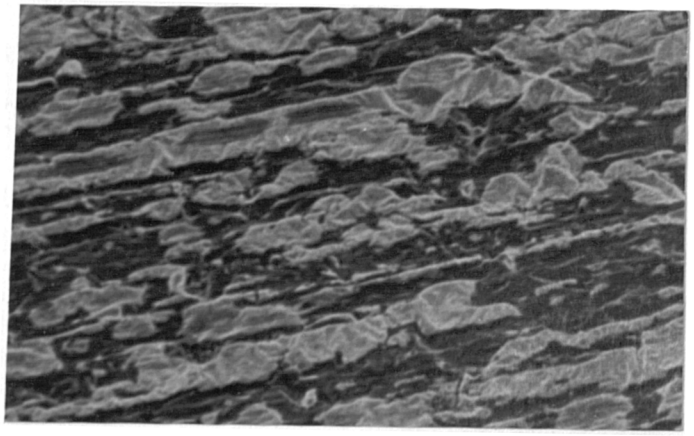

(a)

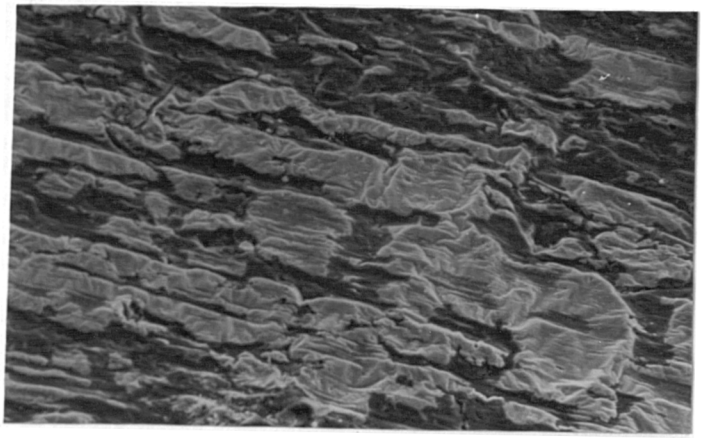

(b)

Figure 137. SEM micrographs of oxide films formed on solid Al-8.13% Mg -0.003% Be-0.12% Zr alloy after 3h exposure in dry and moist atmospheres at 525^{o}C showing no nucleation of tertiary MgO.

(a) : dry atmosphere (x 5,000)
(b) : moist atmosphere (x 5,000)

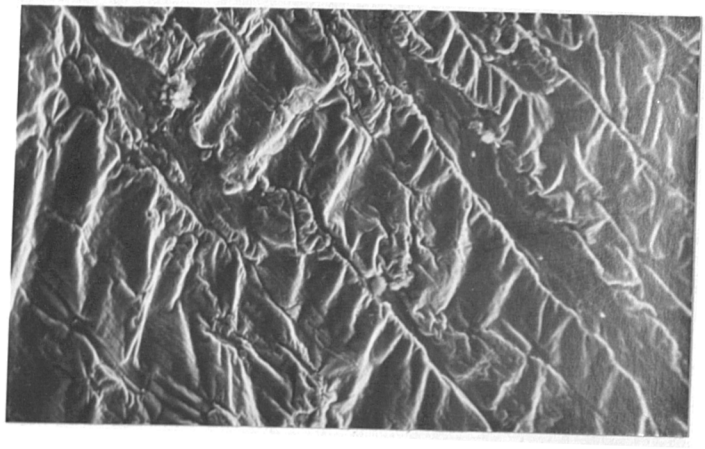

(a)

(b)

Figure 138. SEM micrographs of oxide films formed on liquid Al-8.2% Mg -0.003% Be alloy after 3h exposure in dry and moist atmospheres at 675°C, showing stress-relief by wrinkling of the oxide film.

(a) : dry atmosphere (x 5,000)
(b) : moist atmosphere (x 5,000)

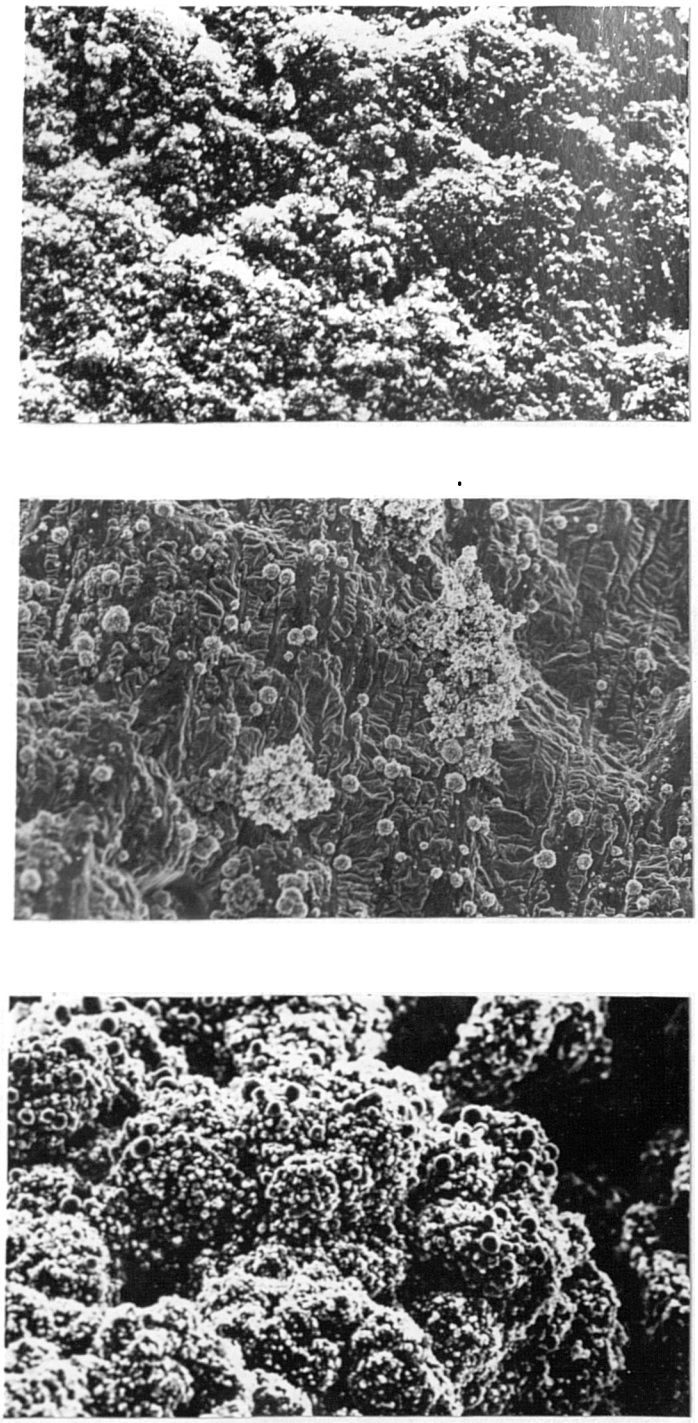

(a)

(b)

(c)

Figure 139. SEM micrographs of oxide films formed on liquid Al-8.16% Mg -0.003% Be-0.24% Mn alloy after various exposures in dry and moist atmospheres at 700°C, showing continuous nucleation and growth of tertiary MgO particles via cracks leading to "cauliflower" growths.

(a) : 3h in the dry atmosphere (x 5,000)

(b), (c) : 1.5h and 3h in the moist atmosphere (x 5,000)

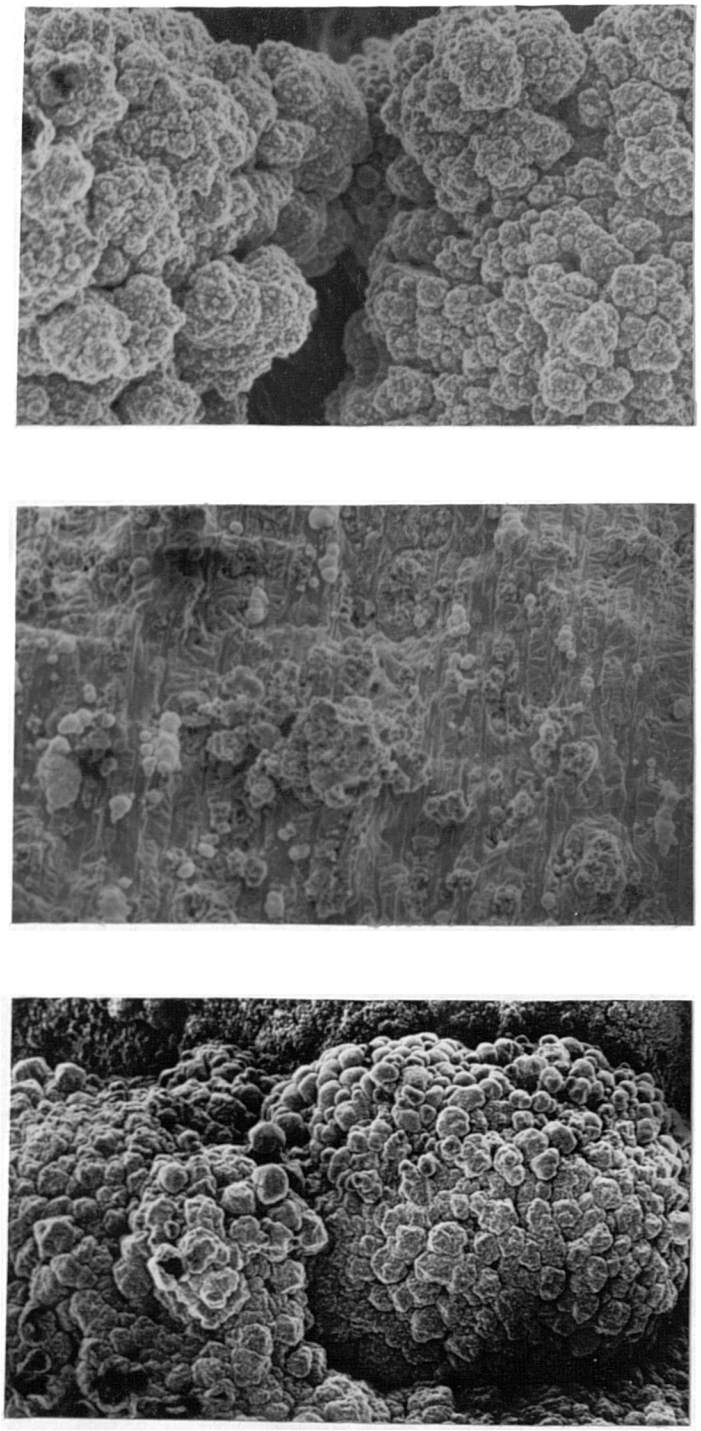

(a)

(b)

(c)

Figure 140. SEM micrographs of oxide films formed on liquid Al-8.13% Mg -0.003% Be-0.12% Zr alloy after various exposures in dry and moist atmospheres at 700°C, showing continuous nucleation and growth of tertiary MgO particles via cracks leading to "cauliflower" growths.

(a) : 3h in the dry atmosphere (x 5,000)

(b), (c) : 1h and 3h in the moist atmosphere (x 5,000)

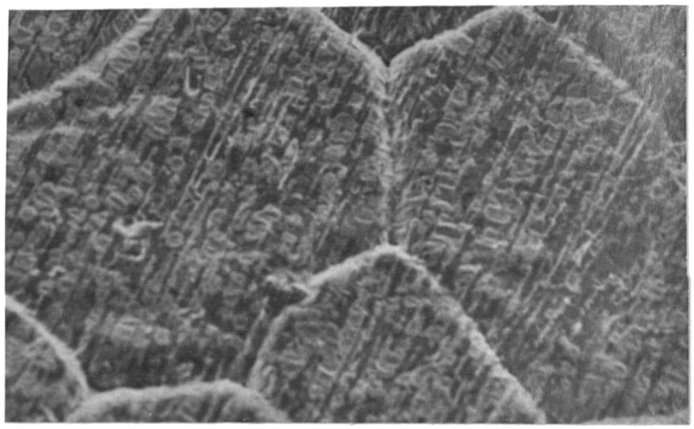

(a)

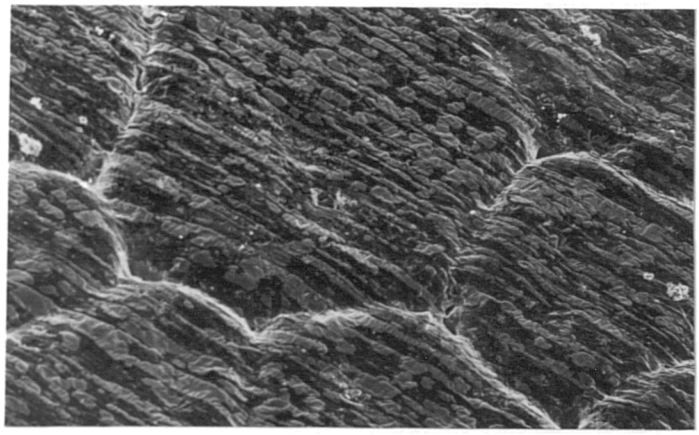

(b)

Figure 141. SEM micrographs of oxide films formed on semi-liquid Al-8.2% Mg-0.003% Be alloy with <50% liquid after 3h exposure in dry and moist atmospheres at 575°C, showing that no tertiary MgO particles develop along grain boundaries as for binary Al-Mg alloys.

(a) : dry atmosphere (x 5,000)
(b) : moist atmosphere (x 5,000)

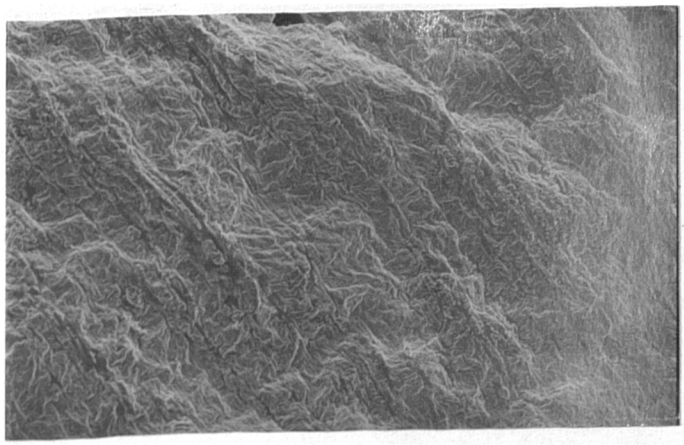

(a)

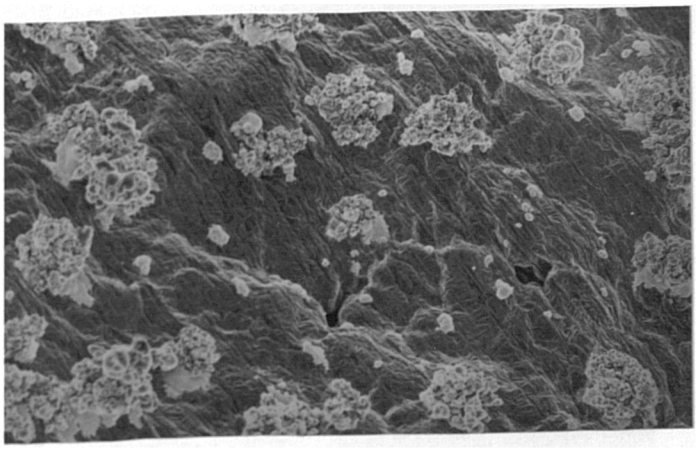

(b)

Figure 142. SEM micrographs of oxide films formed on semi-liquid Al-8.2% Mg-0.003% Be alloy with >50% liquid after 3h exposure in dry and moist atmospheres at 610°C.

(a) : dry atmosphere (x 5,000); note stress-relief by wrinkling of the oxide film.

(b) : moist atmosphere (x 5,000); note the nucleation and growth of tertiary MgO particles scattering along grain boundaries.

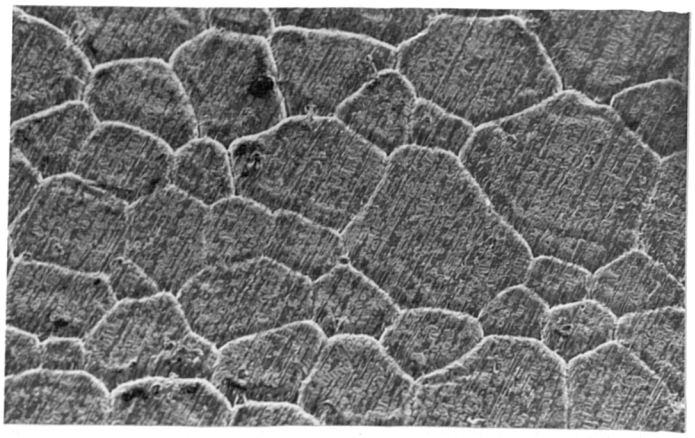

(a)

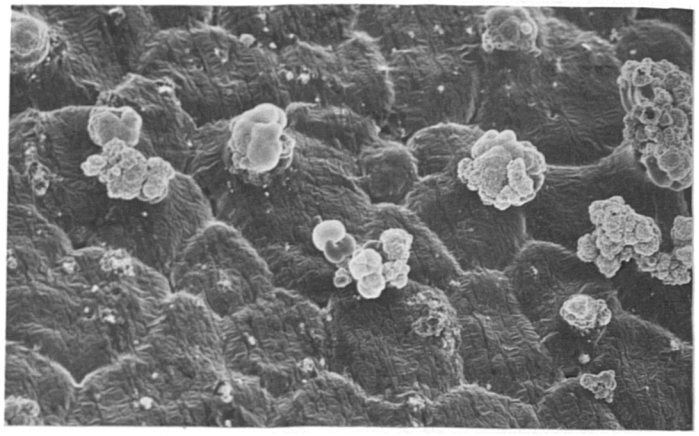

(b)

Figure 143. SEM micrographs of oxide films formed on semi-liquid Al-8.16% Mg-0.003% Be-0.24% Mn alloy with < 50% liquid after 3h exposure in dry and moist atmospheres at 575°C.

(a) : dry atmosphere (x 5,000); note that no tertiary MgO particles develop along grain boundaries.

(b) : moist atmosphere (x 5,000); note the nucleation and growth of tertiary MgO particles scattering along grain boundaries.

(a)

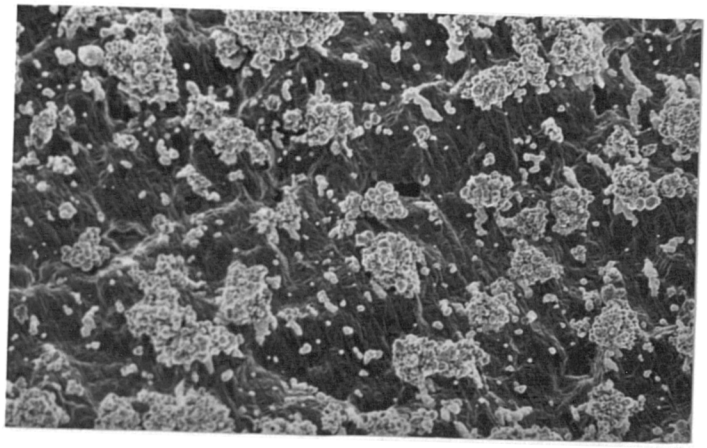

(b)

Figure 144. SEM micrograpahs of oxide films formed on semi-liquid Al-8.16% Mg-0.003% Be-0.24% Mn alloy with > 50% liquid after 3h exposure in dry and moist atmospheres at 610°C, showing the development of tertiary MgO particles both in grains and along grain boundaries.

(a) : dry atmosphere (x 5,000)
(b) : moist atmosphere (x 5,000)

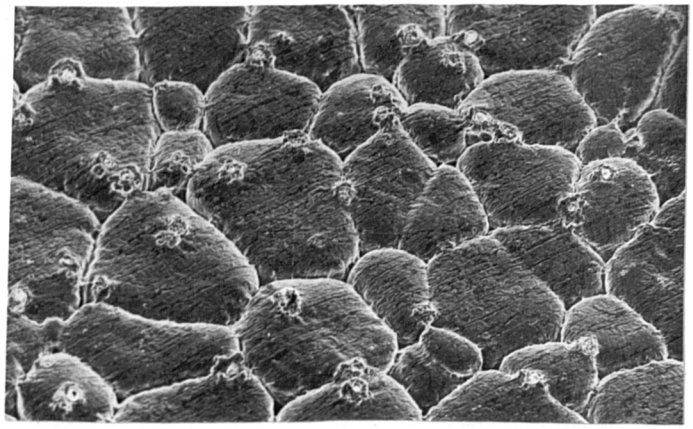

(a)

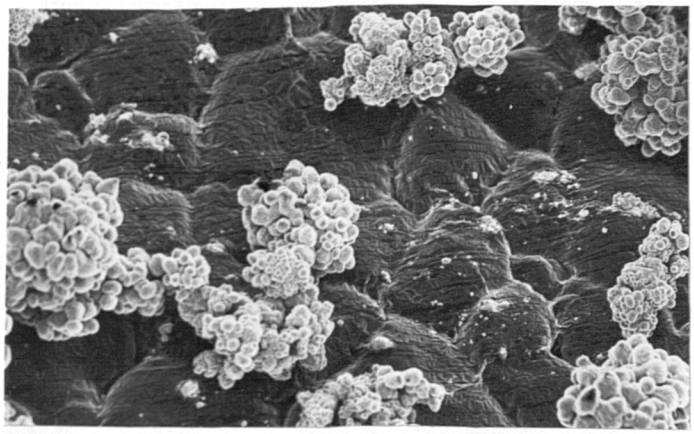

(b)

Figure 145. SEM micrographs of oxide films formed on semi-liquid Al-8.13% Mg-0.003% Be-0.12% Zr alloy with < 50% liquid after 3h exposure in dry and moist atmosphere at 575°C.

(a) : dry atmosphere (x 5,000); note the nucleation of tertiary MgO particles mainly along grain boundaries.

(b) : moist atmosphere (x 5,000); note the nucleation and growth of tertiary MgO particles both in grains and along grain boundaries.

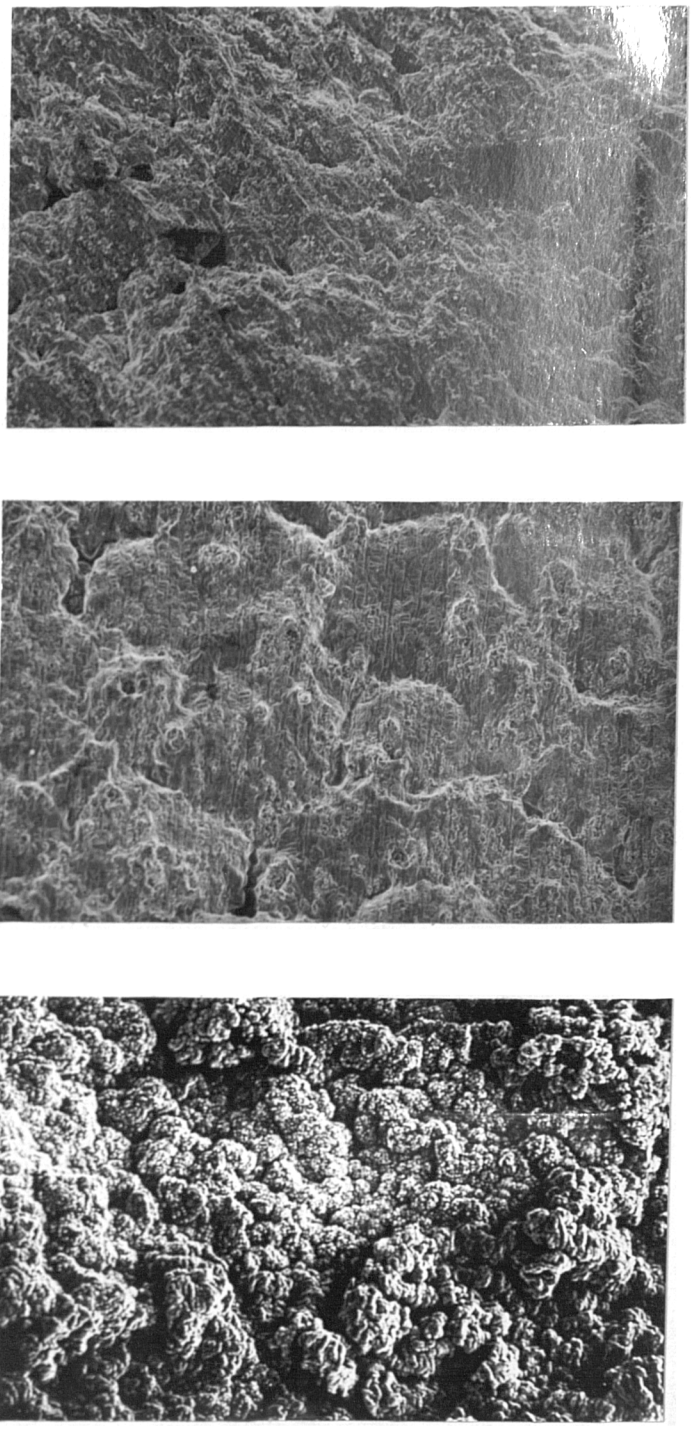

(a)

(b)

(c)

Figure 146. SEM micrographs of oxide films formed on semi-liquid Al-8.13% Mg-0.003% Be-0.12% Zr alloy with ∿50% liquid after various exposures in dry and moist atmospheres at 585°C, showing a dense distribution of weak friable MgO with total destruction of the alloy integrity.

(a) : 3h in the dry atmosphere (x 5,000)
(b),(c): 1h and 3h in the moist atmosphere (x 5,000)

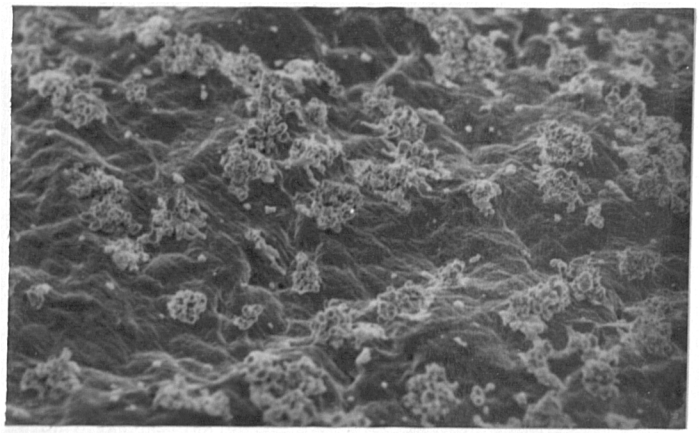

(a)

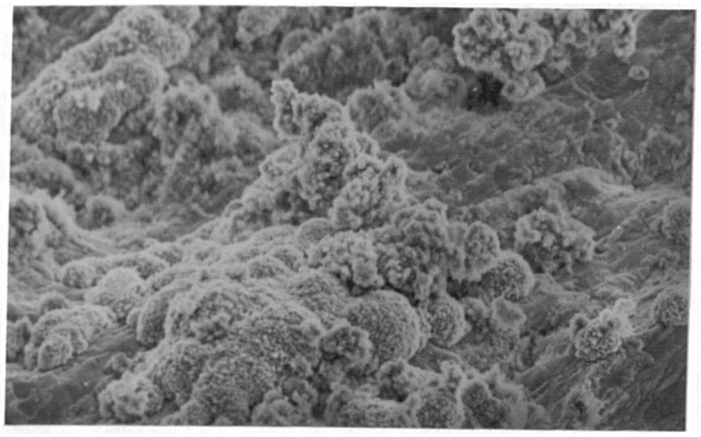

(b)

Figure 147. SEM micrographs of oxide films formed on semi-liquid Al-8.13% Mg-0.003% Be-0.12% Zr alloy with >50% liquid after 3h exposure in dry and moist atmospheres at 610°C.

(a) : dry atmosphere (x 5,000)

(b) : moist atmosphere (x 5,000); note the dense development of tertiary MgO over the entire surface.

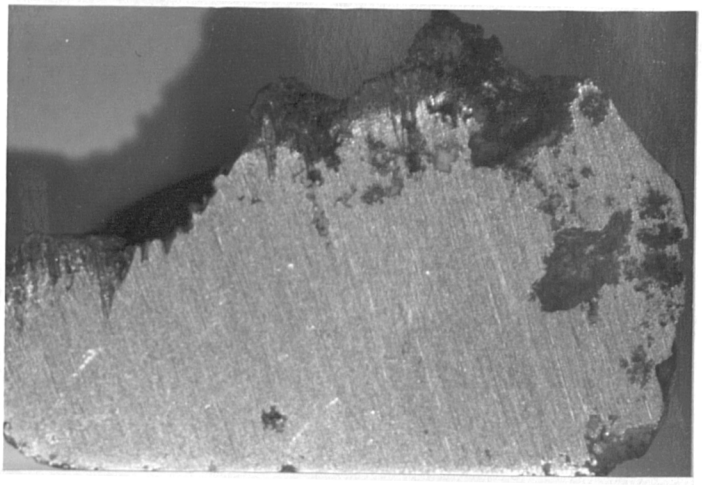

(a)

(b)

Figure 148. Optical micrographs of the Al-5.1% Mg alloy after various exposures in dry and moist atmospheres at 725°C.

(a) : 1.5h in the dry atmosphere (x 6)

(b) : 1h in the moist atmosphere (x 6)

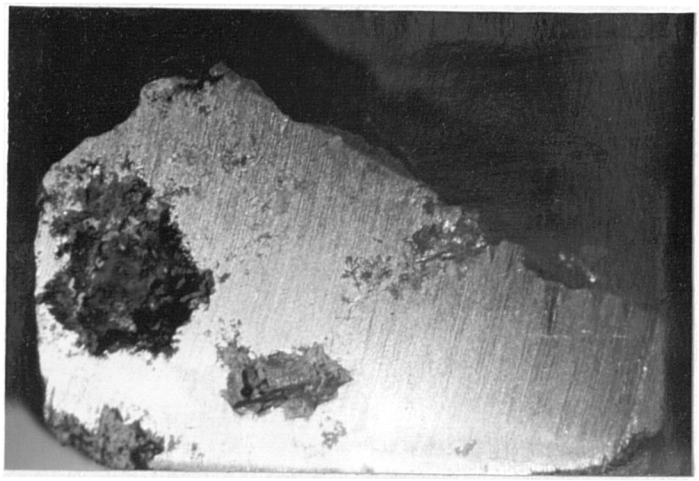

(a)

(b)

Figure 149. Optical micrographs of the Al-7.4% Mg alloy after various exposures in dry and moist atmospheres at 700°C.

(a) : 2h in the dry atmosphere (x 6)
(b) : 1h in the moist atmosphere (x 6)

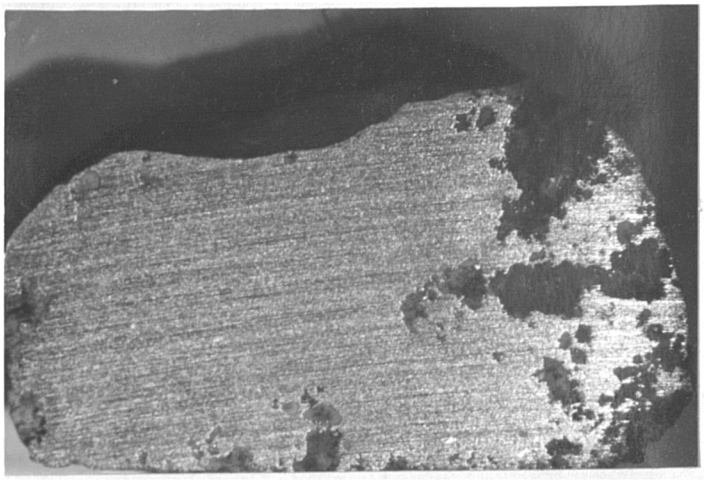

(a)

(b)

Figure 150. Optical micrographs of the Al-8.13% Mg-0.003% Be-0.12% Zr alloy after 2h exposure in dry and moist atmospheres at 725°C.

(a) : in the dry atmosphere (x 6)

(b) : in the moist atmosphere (x 6)

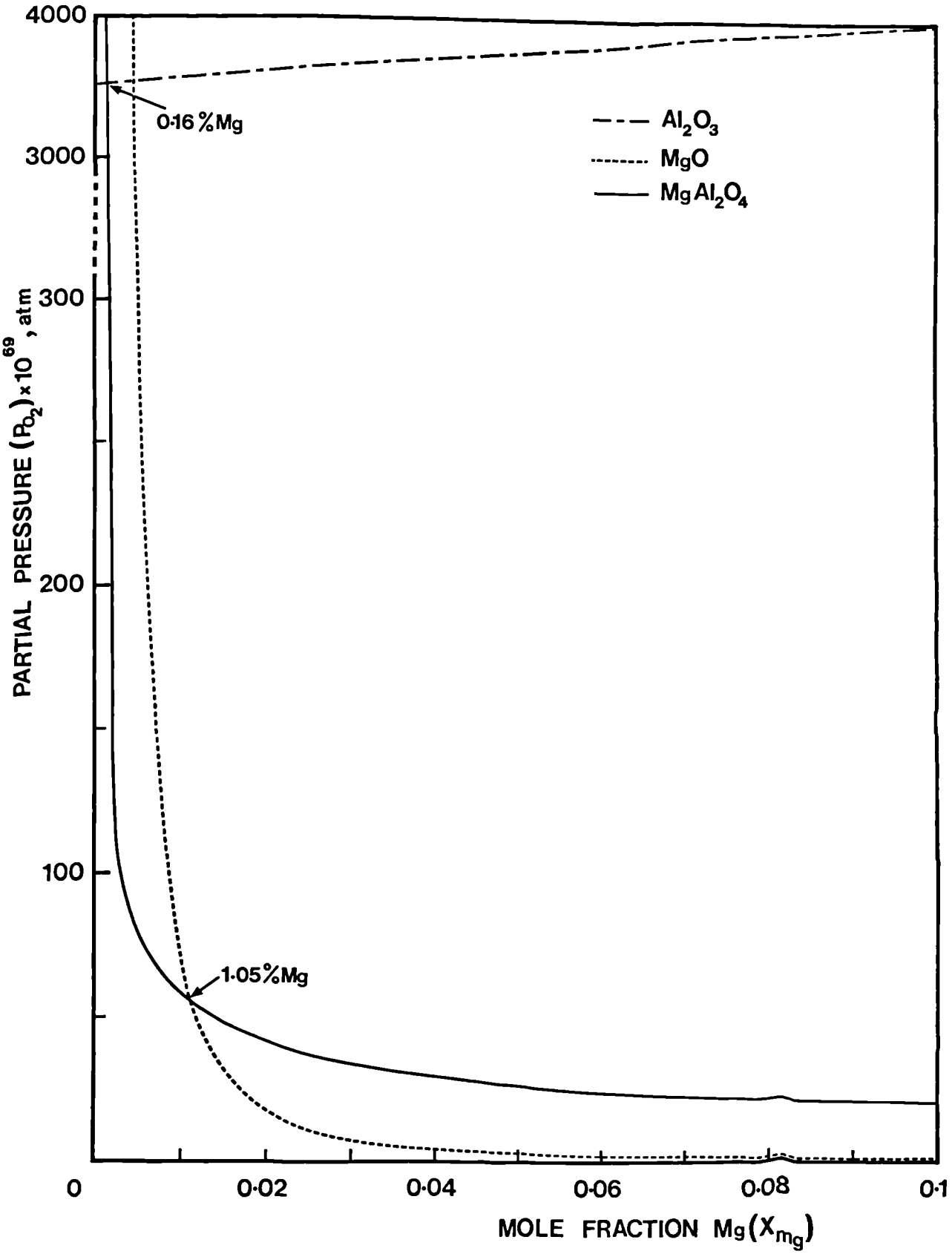

Figure 151. Thermogravimetric stabilities of oxides on binary solid Al-Mg alloys containing 1-10% magnesium at 500°C.
Note the change of scale for P_{O_2} (Al_2O_3).

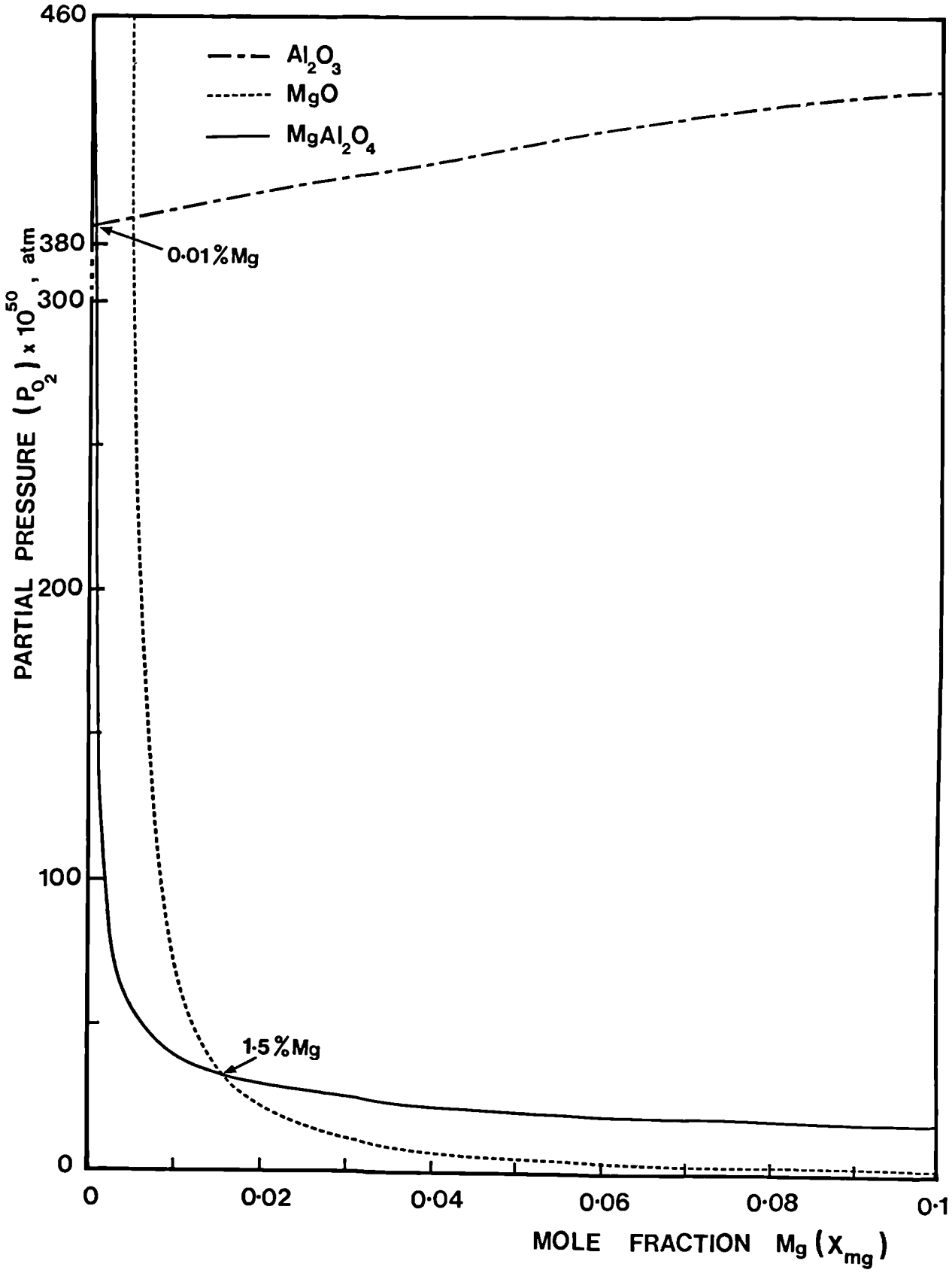

Figure 152. Thermogravimetric stabilities of oxides on binary liquid Al-Mg alloys containing 1-10% magnesium at 725°C.
Note the change of scale for P_{O_2} (Al_2O_3).

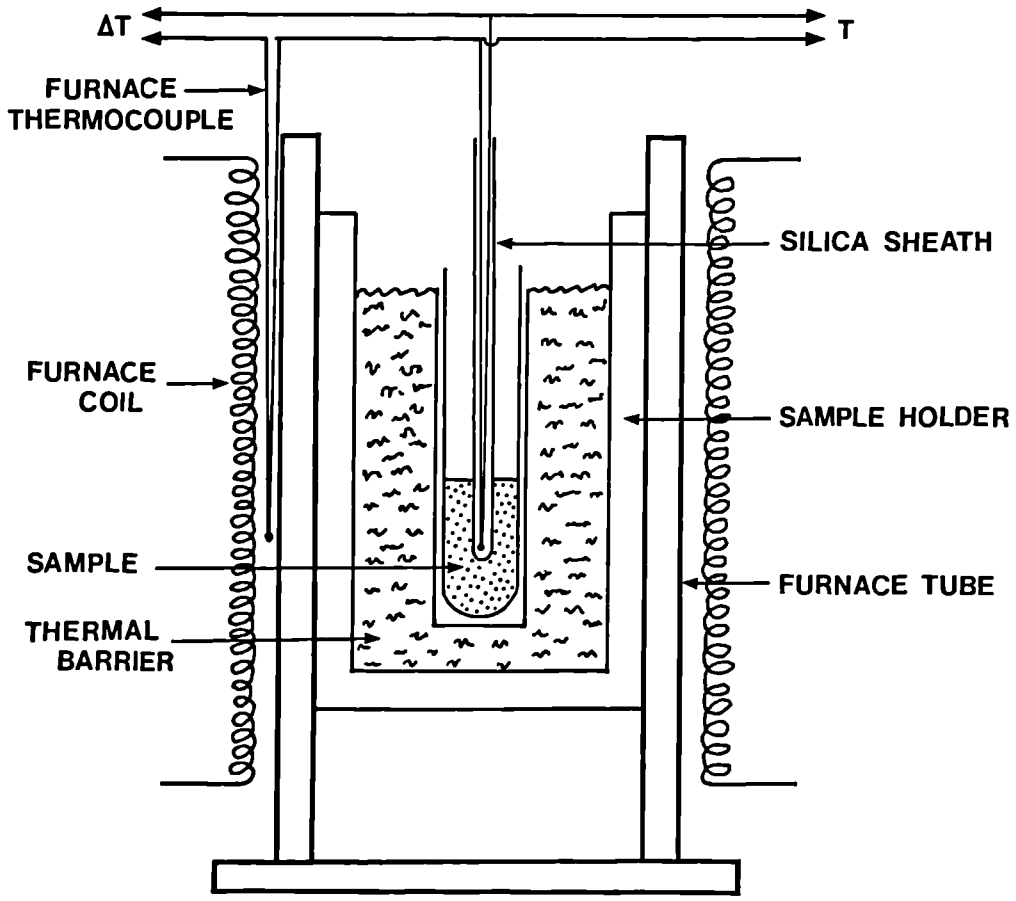

Figure 153. Smith thermal analysis (STA)[216].

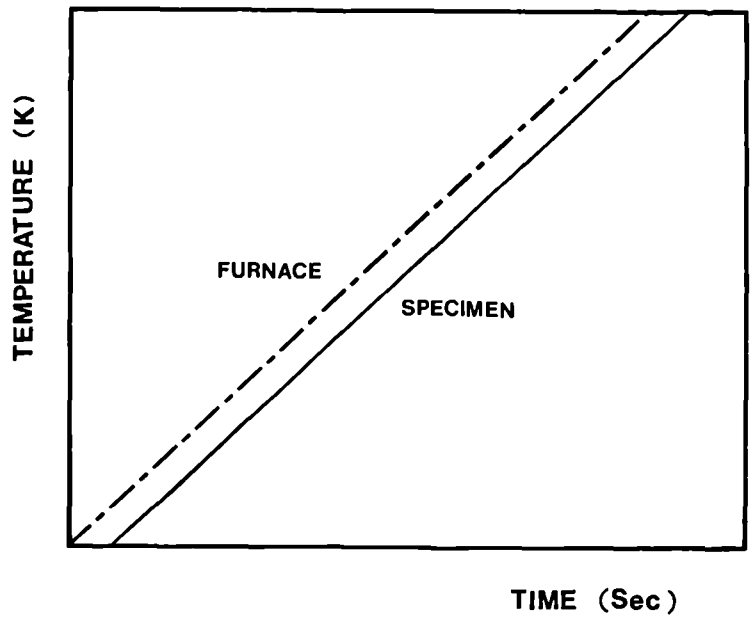

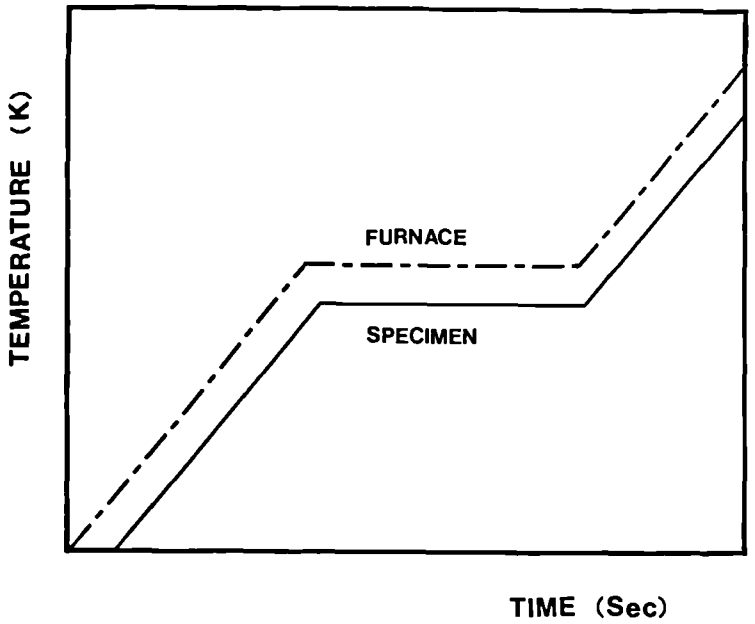

Figure 154. Smith thermal analysis time/temperature curves.
(a) for a thermally inert sample,
(b) for a sample undergoing an isothermal phase transformation.

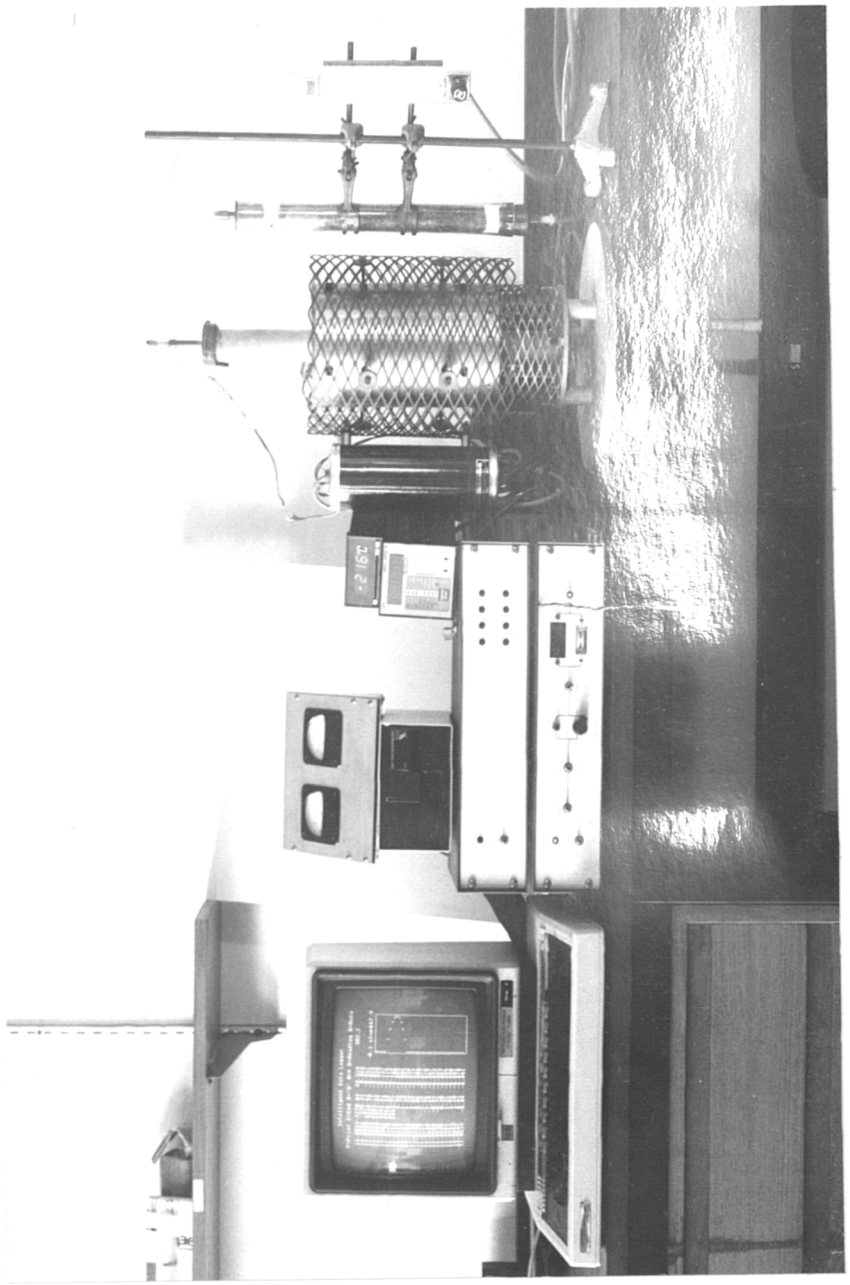

Figure 155. Complete Smith Thermal Analysis apparatus.

Table 1. Notation of Point defects

Symbol	Defect
$(O^{2-}\square)/_O$	Anion vacancy at oxygen interface
$(O^{2-}\square)/_X$	Anion vacancy at oxide interface
$(O^{n-}\bullet)/_O$	Anion interstitial at oxygen interface
$(M^{n+}\square)/_X$	Cation vacancy at oxide interface
$(M^{n+}\bullet)/_O$	Cation interstitial at oxygen interface
$(e\ \square\ )/_X$	Quasi-free hole in the valence band at oxide interface
$(e\ \bullet\ )/_O$	Quasi-free electron in the conduction band at oxygen interface

Table 2. Activation energies for charge carriers in magnesium oxide

Species	Activation energy	
	eV	J
Intrinsic Mg^{2+}	3.50	5.6×10^{-19}
Extrinsic Mg^{2+}	0.92	1.47×10^{-19}
Intrinsic O^{2-}	5.20	8.32×10^{-19}
Extrinsic O^{2-}	2.70	4.32×10^{-19}

Table 3. Summary chart of the predictions by the Wagner-Hauffe theory[164]

Product		Defect	Effect of higher valent cation		Effect of lower valent cation	
			On Oxidation	On electrical conductivity	On Oxidation	On electrical conductivity
Semi-conductor	p-type	Metal Vacancies	Increase	Decrease	Decrease	Increase
		Oxygen Interstitials	Increase	Decrease	Decrease	Increase
	n-type	Oxygen Vacancies	Decrease	Increase	Increase	Decrease
		Metal Interstitials	Decrease	Increase	Increase	Decrease
Ionic conductor	Cationic	Cation Vacancies	Decrease	Decrease	Increase	Increase
		Cation Interstitials	Increase	Increase	Decrease	Decrease
	Anionic	Anion Vacancies	Increase	Increase	Decrease	Decrease
		Anion Interstitials	Decrease	Decrease	Increase	Increase

Table 4. Solubility of hydrogen in pure aluminium and some aluminium-magnesium alloys at one atmospheric pressure as a function of temperature (cm^3 per 100 g)[201]

Material	Temperature °C										
	670	680	700	710	715	730	740	750	760	770	820
Pure Al		0.70		0.95	0.98			1.20	1.22	1.35	
Al-0.5% Mg		0.80			1.05		1.28		1.22	1.48	1.70
Al-2.5% Mg			0.99	1.10		1.28			1.39		
Al-5% Mg	0.80		1.00					1.4			

Table 5. Heat-treatment temperatures and chemical analyses of binary aluminium-magnesium alloys

Nominal Wt% Mg	Analyses as a percentage of weight									Heat-treatment temperature ^{o}C
	Mg	Fe	Si	Cu	Zn	Ti	Cr	Mn	Na	
1	1.3	0.004	0.002	0.004	<0.001	<0.001	<0.001	<0.001	<0.001	575
3	3.1	0.005	0.003	0.003	<0.001	<0.001	<0.001	<0.001	<0.001	550
5	5.1	0.006	0.003	0.005	<0.001	<0.001	<0.001	<0.001	<0.001	500
7	7.4	0.003	0.002	0.006	<0.001	<0.001	<0.001	<0.001	<0.001	450
9	9.3	0.004	0.004	0.004	<0.001	<0.001	<0.001	<0.001	<0.001	400

Table 6. Heat-treatment temperatures and chemical analyses of aluminium-magnesium-beryllium alloys

Nominal Wt% Mg	Analyses as a percentage of weight									Heat-treatment temperature °C
	Mg	Be	Mn	Zr	Fe	Si	Zn	Cu	Every other element	
8.0	8.20	0.003	-	-	0.002	0.001	0.001	0.001	< 0.001	450
8.0	8.16	0.003	0.24	-	0.002	0.001	0.002	0.001	< 0.001	450
8.0	8.13	0.003	-	0.12	0.002	0.001	0.001	0.002	< 0.001	450

Table 7. Results for Solidus and Liquidus temperatures determined by the Smith thermal analysis technique

Wt% Mg	Wt% Be	Wt% Mn	Wt% Zr	Solidus Temperatures °C			Literature Values[215] °C	Liquidus Temperatures °C			Literature Values[215] °C
				Heating	Cooling	Average		Heating	Cooling	Average	
1.3	-	-	-	643	640	641.5	639.5	656	655	655.5	654
3.1	-	-	-	615	615	615	615	647	644	645.5	646
5.1	-	-	-	586	584	585	586.5	632	633	632.5	637.5
7.4	-	-	-	559	558	558.5	553.5	623	620	621.5	627
9.3	-	-	-	538	536	537	530	614.5	612	613.3	617.5
8.20	0.003	-	-	550	550	550	546	621	619	620	624
8.16	0.003	0.240	-	551	550	550.5	546	619.5	619.5	619.5	624
8.13	0.003	-	0.120	549	549	549	546	619	617	618	624

Table 8. Assessment of effective surface area for oxidation of the bottom face of oxidised samples

Wt% Mg	Wt% Be	Wt% Mn	Wt% Zr	Atmosphere	Effective equivalent fraction of surface area	Average
1.3	-	-	-	dry	0.21	0.215
1.3	-	-	-	moist	0.22	
3.1	-	-	-	dry	0.22	0.220
3.1	-	-	-	moist	0.22	
5.1	-	-	-	dry	0.25	0.245
5.1	-	-	-	moist	0.24	
7.4	-	-	-	dry	0.28	0.270
7.4	-	-	-	moist	0.26	
9.3	-	-	-	dry	0.29	0.285
9.3	-	-	-	moist	0.28	
8.2	0.003	-	-	dry	0.22	0.22
8.2	0.003	-	-	moist	0.22	
8.16	0.003	0.24	-	dry	0.21	0.22
8.16	0.003	0.24	-	moist	0.23	
8.13	0.003	-	0.12	dry	0.255	0.24
8.13	0.003	-	0.12	moist	0.225	

Table 9. Magnesium Content after Oxidation in Solid, Semi-Liquid and Liquid States

	Dry Atmosphere			Moist Atmosphere		
(a) Al-Mg Binary Alloys						
Temperature (°C)	625	654	675	625	654	675
Initial Mg%	1.3	1.3	1.3	1.3	1.3	1.3
Final Mg%	1.274	1.277	1.277	1.277	1.273	1.276
Temperature (°C)	600	640	650	600	640	725
Initial Mg%	3.1	3.1	3.1	3.1	3.1	3.1
Final Mg%	3.036	3.064	3.070	3.061	3.057	3.058
Temperature (°C)	575	625	725	575	610	725
Initial Mg%	5.1	5.1	5.1	5.1	5.1	5.1
Final Mg%	5.03	5.02	4.94	5.05	5.01	4.89
Temperature (°C)	550	610	725	550	610	725
Initial Mg%	7.4	7.4	7.4	7.4	7.4	7.4
Final Mg%	7.27	7.14	6.26	7.31	6.98	6.13
Temperature (°C)	525	600	725	525	600	725
Initial Mg%	9.3	9.3	9.3	9.3	9.3	9.3
Final Mg%	9.23	8.93	7.89	9.24	8.28	7.68
(b) Al-Mg Alloys with Be						
Al-Mg-Be Alloy:						
Temperature (°C)	550	610	725	550	610	725
Initial Mg%	8.2	8.2	8.2	8.2	8.2	8.2
Final Mg%	8.178	8.173	8.169	8.178	8.167	8.161
Al-Mg-Be-Mn Alloy:						
Temperature (°C)	550	610	725	550	610	725
Initial Mg%	8.16	8.16	8.16	8.16	8.16	8.16
Final Mg%	8.138	8.125	8.118	8.137	8.121	8.101
Al-Mg-Be-Zr Alloy:						
Temperature (°C)	550	610	725	550	610	725
Initial Mg%	8.13	8.13	8.13	8.13	8.13	8.13
Final Mg%	8.09	8.086	8.078	8.107	8.064	8.022

Table 10. Magnesium loss for alloys heated to and held at the test temperature for 20 min.

Wt% Mg	Evaporation (mg)	
	700°C	725°C
7.4	-	0.02 ± 1
8.1	0.01 ± 1	0.03 ± 1
9.3	0.03 ± 1	0.05 ± 2

Table 11. Thermodynamic data for MgO formation on solid Al-Mg alloys at 500°C $K(MgO, 773K) = 2.897 \times 10^{70}$

x_{mg}	a_{mg}	a_{mg}^2	Po_2 at 500°C (atm.)
0.0025	0.0055	3.025×10^{-5}	1141.0×10^{-69}
0.005	0.011	1.21×10^{-4}	285.3×10^{-69}
0.01	0.022	4.84×10^{-4}	71.3×10^{-69}
0.02	0.044	1.94×10^{-3}	17.8×10^{-69}
0.03	0.066	4.36×10^{-3}	7.92×10^{-69}
0.04	0.088	7.74×10^{-3}	4.45×10^{-69}
0.05	0.110	1.21×10^{-2}	2.85×10^{-69}
0.06	0.131	1.72×10^{-2}	2.00×10^{-69}
0.07	0.152	2.31×10^{-2}	1.49×10^{-69}
0.08	0.172	2.96×10^{-2}	1.16×10^{-69}
0.09	0.191	3.65×10^{-2}	0.94×10^{-69}
0.10	0.210	4.41×10^{-2}	0.78×10^{-69}

Table 12. Thermodynamic data for Al_2O_3 formation on solid Al-Mg alloys at 500°C $K(Al_2O_3, 773K) = 2.841 \times 10^{65}$

x_{mg}	a_{Al}	$a_{Al}^{4/3}$	Po_2 at 500°C (atm.)
0.0025	0.9975	0.9967	3531×10^{-69}
0.005	0.9950	0.9933	3543×10^{-69}
0.01	0.990	0.9867	3567×10^{-69}
0.02	0.980	0.9734	3616×10^{-69}
0.03	0.970	0.9602	3666×10^{-69}
0.04	0.960	0.9470	3717×10^{-69}
0.05	0.950	0.9339	3769×10^{-69}
0.06	0.940	0.9208	3822×10^{-69}
0.07	0.931	0.9091	3872×10^{-69}
0.08	0.923	0.8987	3916×10^{-69}
0.09	0.916	0.8896	3957×10^{-69}
0.10	0.910	0.8818	3992×10^{-69}

Table 13. Thermodynamic data for $MgAl_2O_4$ formation on solid Al-Mg alloys at 500°C $K(MgAl_2O_4, 773K) = 1.21 \times 10^{68}$

x_{mg}	a_{mg}	a_{Al}	$a_{mg}^{1/2}$	P_{O_2} at 500°C (atm.)
0.0025	0.0055	0.9975	0.074	111.9×10^{-69}
0.005	0.011	0.9950	0.105	79.1×10^{-69}
0.01	0.022	0.990	0.148	56.4×10^{-69}
0.02	0.044	0.980	0.210	40.2×10^{-69}
0.03	0.066	0.970	0.257	33.15×10^{-69}
0.04	0.088	0.960	0.297	29.98×10^{-69}
0.05	0.110	0.950	0.332	26.20×10^{-69}
0.06	0.131	0.940	0.362	24.29×10^{-69}
0.07	0.152	0.931	0.390	22.76×10^{-69}
0.08	0.172	0.923	0.415	21.58×10^{-69}
0.09	0.191	0.916	0.437	20.64×10^{-69}
0.10	0.210	0.910	0.458	19.83×10^{-69}

Table 14. Thermodynamic data for MgO formation on liquid Al-Mg alloys at 725°C $K\ (MgO, 998K) = 1.43 \times 10^{52}$

a_{mg}	x_{mg}	a_{mg}^2	P_{O_2} at 725°C (atm.)
0.0025	0.0025	6.25×10^{-6}	1118.8×10^{-50}
0.005	0.005	2.50×10^{-5}	279.7×10^{-50}
0.01	0.010	1×10^{-4}	69.9×10^{-50}
0.02	0.018	3.24×10^{-4}	21.6×10^{-50}
0.03	0.025	6.25×10^{-4}	11.18×10^{-50}
0.04	0.035	1.22×10^{-3}	5.71×10^{-50}
0.05	0.040	1.60×10^{-3}	4.37×10^{-50}
0.06	0.045	2.02×10^{-3}	3.45×10^{-50}
0.07	0.050	2.50×10^{-3}	2.79×10^{-50}
0.08	0.055	3.02×10^{-3}	2.31×10^{-50}
0.09	0.058	3.36×10^{-3}	2.08×10^{-50}
0.10	0.060	3.60×10^{-3}	1.94×10^{-50}

Table 15. Thermodynamic data for Al_2O_3 formation on liquid Al-Mg alloys at 725°C $K(Al_2O_3, 998K) = 2.58 \times 10^{47}$

x_{mg}	a_{Al}	$a_{Al}^{4/3}$	P_{O_2} at 725°C (atm.)
0.0025	0.9975	0.9967	388.9×10^{-50}
0.005	0.995	0.9933	390.2×10^{-50}
0.01	0.990	0.9867	392.8×10^{-50}
0.02	0.980	0.9734	398.2×10^{-50}
0.03	0.970	0.9602	403.7×10^{-50}
0.04	0.960	0.9470	409.3×10^{-50}
0.05	0.950	0.9339	415.0×10^{-50}
0.06	0.941	0.9221	420.3×10^{-50}
0.07	0.933	0.9116	425.2×10^{-50}
0.08	0.927	0.9039	428.9×10^{-50}
0.09	0.922	0.8974	431.9×10^{-50}
0.10	0.919	0.8935	433.8×10^{-50}

Table 16. Thermodynamic data for $MgAl_2O_4$ formation on liquid Al-Mg alloys at 725°C $K(MgAl_2O_4, 998K) = 2.59 \times 10^{49}$

x_{mg}	a_{mg}	a_{Al}	$a_{mg}^{1/2}$	P_{O_2} at 725°C (atm.)
0.0025	0.0025	0.9975	0.050	77.4×10^{-50}
0.005	0.005	0.995	0.071	54.9×10^{-50}
0.01	0.010	0.990	0.100	39.0×10^{-50}
0.02	0.018	0.980	0.134	29.36×10^{-50}
0.03	0.025	0.970	0.158	25.17×10^{-50}
0.04	0.035	0.960	0.187	21.51×10^{-50}
0.05	0.040	0.950	0.200	20.32×10^{-50}
0.06	0.045	0.941	0.212	19.35×10^{-50}
0.07	0.050	0.933	0.224	18.47×10^{-50}
0.08	0.055	0.927	0.235	17.72×10^{-50}
0.09	0.058	0.922	0.241	17.39×10^{-50}
0.10	0.060	0.919	0.245	17.15×10^{-50}

Table 17. Alloy composition ranges for oxide stabilities

Wt% Mg	Temp.^{o}C	Stable Oxide
0.00 - 0.16	500	Al_2O_3
0.16 - 1.05	500	$MgAl_2O_4$
1.05 -10.00	500	MgO
0.00 - 0.01	725	Al_2O_3
0.01 - 1.50	725	$MgAl_2O_4$
1.50 - 10.00	725	MgO

APPENDIX 1

Derivation of Parabolic Growth Rates Using an Electrochemical Model[124].

The reacting system is considered to be an electrochemical cell in which the oxide scale serves as an electrolyte for the ionic transport and as a circuit for transport of electrons.

The cathodic reaction at the oxide/atmosphere interface is represented by:

$$O_2 + 2e \longrightarrow O^{2-}$$

and the anodic reaction at the oxide/metal interface is represented by:

$$Me \longrightarrow Me^{2+} + 2e$$

The total resistance, R, (ionic plus electronic) of a film with area A cm^2 and thickness y cm

$$R = R_{ionic} + R_{electronic}$$

If K is specific conductivity, then

$$R = \left[\frac{\tau_a + \tau_c + \tau_e}{(\tau_a + \tau_c)\ K} + \frac{\tau_a + \tau_c + \tau_e}{\tau_e\ K} \right] \frac{y}{A}$$

where τ_a, τ_c and τ_e are transport numbers of anions, cations and electrons respectively.

Since $\tau_a + \tau_c + \tau_e = 1$

$$R = \frac{y}{(\tau_a + \tau_c)\ \tau_e\ A\ K}$$

Providing Ohms law is obeyed then the current, i, flowing through the cell is:

$$i = \frac{E\ (\tau_a + \tau_c)\ \tau_e\ K\ A}{y}$$

where E is the EMF of the cell.

A current flowing for dt seconds produces i.dt coulombs. These will produce i.dt.J/Z.ρ.F. volume of oxide, where J, ρ, Z are molar mass of oxide, density of oxide, number of electrons interchanged during the formation of a mole of oxide and F is the Faraday constant.

In dt seconds the volume of oxide produced = d y. A

hence,

$$dy = \frac{i.dt.J}{Z \rho F A}$$

substituting for i

$$\frac{dy}{dt} = \frac{E (\tau_a + \tau_c) \tau_e K J}{Z \rho F y}$$

From this

$$\frac{dy}{dt} = \frac{k}{y}$$

where k is a constant

and

$$y^2 = kt$$

APPENDIX 2

Determination of Solidus and Liquidus Temperatures Using Smith Thermal Analysis (STA).

(a) Principles of Operation

The thermal analysis apparatus is based on a design by Smith[216] and Humpston[236] which originally intended to measure heats of transformation quantitatively. It embodies the principle of using the specimen temperature to influence the temperature of the furnace in which it resides. This is achieved by separating the specimen from the furnace windings with

barrier of moderate thermal conductivity and using a differential thermocouple to maintain a constant temperature gradient across the barrier as in Figure 153.

For a thermally inert specimen, both the specimen and furnace temperatures increase linearly with time, as shown in Figure 154(a). In practice, both curves are asymptotic to some higher temperature because the thermal properties of the barrier vary with time.

If it is assumed that the energies associated with phase transformations are predominantly due to enthalpies of transformation, then when a specimen undergoes a phase transformation heat is required. If the arrest is isothermal the enthalpy of transformation will dominate the heat capacity of the specimen and hence the temperature of the specimen will remain constant for the duration of the phase transformation, as illustrated in Figure 154(b). The controller responds to maintain the temperature of the furnace at either just above or just below the specimen temperature, depending on whether the specimen was being heated or cooled when the arrest was encountered and further temperature change does not occur until the phase transformation is complete. This results in a far more homogeneous specimen after the phase transformation and a sharp decrease of the heating rate of the specimen. Thus a satistically reliable number of measurements can be obtained for the transformation temperature.

(b) Furnace and Specimen Holder

The furnace was constructed around an Aluminous porcelain tube with 33 mm internal diameter and 2 mm wall thickness. The heated section of the furnace was 19 cm long with 12 cm protruding cooling zones above and below the main body to facilitate the attachment of gas seals. The furnace tube was surrounded by a concentric cylinder of 0.5 mm thick stainless steel sheet 16 cm diameter to protect the winding. A cement/asbestos disc of

6 mm thick x 16 cm diameter was attached at either end of the furnace tube. To facilitate cooling, a ring of 6 mm diameter holes were drilled circumferentially on the asbestos disc to allow the passage of air through the otherwise sealed chamber.

The specimen holder was suspended from the top gas seal and its water-cooled jacket by three stainless steel wires, so that the holder would be within the region of constant temperature and the alloy under examination would be in the centre of the zone. The holder, 14 cm long with a wall thickness of 2 mm and an external diameter of 33 mm, was concentric with the furnace tube. A 1 mm diameter hole was pierced midway along the holder wall to allow a thermocouple to rest against the furnace wall. The specimen thermocouple was arranged at the same height inside the crucible. The intervening space was tightly packed with asbestos wool to act as the thermal barrier with a temperature difference of 20°C. Figure 153 schematically illustrates the general arrangement.

(c) Temperature measurement

The temperature measuring thermocouples (chromel/alumel) were regularly calibrated against the melting points of tin and zinc. The temperature measurements are considered to be accurate to within ±1°C, though the short-term reproducibility was typically an order of magnitude better. The thermocouple cold-junction was maintained at 30.0±0.05°C by a fully proportional temperature controller. When performing the thermal analysis, care was taken to ensure that the thermocouple bead was located in the centre of the mass of every specimen to minimise the errors associated with end effects. The temperature and heating rate of the specimen could be independently controlled.

(d) Data acquisition system

The outputs of the thermocouples were acquired by a data logging system

capable of measuring small voltages with high resolution and accuracy. It consisted of (a) an analogue-to-digital converter with an accuracy and resolution of 0.3 μV in 20 mV and providing sufficient data to measure temperatures to $\pm 0.7^{o}C$, and (b) a single chip micro-computer, machine-coded to utilize the working capacity of A.D.C.

The measured EMF of the thermocouples in analogue form were fed to the host computer, a B.B.C. Model B which manipulated and displayed the results in a convenient format.

(e) System computer algorithm

The host computer instructed the data acquisition unit to make periodic measurements of the specimen temperature and after manipulating the data, store and print results as required.

The programme was written in B.B.C. basic running in a continuous loop from which six subroutines were called in turn.

(f) Experimental procedure

Cylindrical specimens, 7 mm diameter and 20 mm long were machined from each alloy with a 2 mm diameter hole drilled half-way through the centre of the specimen to accommodate the silica sheath in which the thermocouple resides as illustrated in Figure 153. The specimens were rapidly heated in silica crucibles to about $100^{o}C$ below the solidus temperature, i.e.$\sim 5^{o}C\ min^{-1}$, and then the heating rate was controlled to traverse the solidus and liquidus temperatures at a nominal rate of $1^{o}C\ min^{-1}$. When the specimens reached about $50^{o}C$ above the liquidus temperature, after a short homogenisation period of 15 mins, they were re-examined on cooling through the range at a nominal rate of $1^{o}C\ min^{-1}$.

Both heating and cooling curves were displayed and printed by the computer. These curves were used to identify deflection points indicating the solidus

and liquidus temperatures. A photograph of the equipment is given in Figure 155.

All thermal analyses were performed under a dry reducing atmosphere of helium to minimise oxidation.

APPENDIX 3

Calibration Procedure for the Sartorius Model 4410 Microbalance

The microbalance is designed as a double beam weighing system. Weight gains or losses are registered directly in mg on the DVM illustrated in Figure 42. Three ranges are provided, i.e. 0 - 2800 mg (Range 1), 0 - 280 mg (Range 2), 0 - 28 mg (Range 3). Calibration is required to ensure that the readings on the DVM are accurate.

The DVM is calibrated using a microprocessor incorporated in it for the purpose. It is switched on by depressing a special button at the back. Before it is switched on, weights are added to pans on both sides of the balance beam until the coarse weight indicator beneath the digital display of the DVM registers approximately zero. At this stage the digital display also registers approximately zero. The three ranges are calibrated separately in the following sequence:

Range 3

Range 3 is selected by depressing the appropriate button. The microbalance is balanced by adding weights to its right hand pan until the digital display registers -68,000±2,500. If the balance is not tared within these limits it is not possible to calibrate it. When the display registers -68,000±2,500 the balance is allowed sufficient time to stabilise as indicated by a display of "g" notation. The tare button is then depressed and the display registers approximately zero. A standard 10 mg weight is added to the right hand pan producing a reading of

25,000 - 28,000 with stable "g" notation. The balance is again tared and the display then registers approximately 10,000 mg. This completes the calibration for range 3.

Range 2

The 10 mg weight used in calibrating range 3 is removed and the DVM registers zero. Range 2 is selected by depressing the appropriate button and the digital display registers approximately 68,000 with "g" notation when conditions have stabilised. The tare button is then depressed and the display registers approximately zero. A standard 100 mg weight is added to the right hand pan producing a reading of 25,000 - 28,000 with stable "g" notation. The balance is again tared and the display then registers approximately 10,000 mg. This completes the calibration for range 2.

Range 1

The 100 mg weight used in calibrating range 2 is removed and DVM registers zero. Range 1 is selected by depressing the appropriate button and the digital display registers approximately 68,000 with "g" notation when the conditions are stabilised. The tare button is then depressed and the display registers approximately zero. A standard 1000 mg weight is added to the right hand pan producing a reading of 25,000 - 28,000 with stable "g" notation. The balance is again tared and the display then registers approximately 10,000 mg. This completes the calibration for range 1.

If, during the calibration, any step of the procedure is performed incorrectly the error is indicated by the appearance of H or of 88888 on the display instead of the readings given above.

Finally, the 1000 mg weight is removed and the micro-processor is switched off by depressing the red button. The latter action converts the system

to the normal or working mode and the equipment is now ready for use.

APPENDIX 4

Operating Principles of the X-ray Diffractometer

The diffracted X-rays are received by the X-ray counter which records the diffraction X-ray intensity in photon counts as a function of diffraction angle[219]. Since the sample tilts at half the speed of the X-ray counter and in the same direction, the diffraction angle is half the actual angle of rotation of the X-ray counter. The information was preserved on a recorder chart.

APPENDIX 5

Operating Principles of the Scanning Electron Microscope

The electron optical column focuses electrons generated by a tungsten electron gun into a fine electron probe which interacts with the specimen producing a variety of signals. These interaction products are collected and analysed to assess the properties of the material[237,238].

(a) Surface topography

The electron beam produced by shaping the electrons by condenser lenses and apertures, is scanned or rastered over the surface of the specimen. Both low energy secondary electrons emitted from the specimen due to inelastic scattering and high energy primary electrons reflected from the specimen surface with no loss of energy are detected at the collector by a positively biased grid. The detected electrons are converted into light photons and then to electrical signals which are imaged on a CRT screen, the raster of which is synchronised with the raster of the electron beam. The image has a marked three-dimensional appearance because the contrast is produced by variation in number of electrons emitted or reflected from

different parts of the sample as a result of the high depth of focus.

APPENDIX 6

Operating Principles and Application of the Transmission Electron Miscroscope

(a) Operating principles

The TEM uses a finely-focused static beam of electrons to image thin samples[239,240]. An electron beam, generated by applying a high voltage to a heated tungsten filament, is focused into a fine electron probe by condenser lenses and condenser apertures. The sample is placed in the path of the electron beam in the region of the objective lens and only the primary electrons transmitted without deflection[239] are admitted by the objective apertures to a fluorescent screen for viewing or to a photographic plate for recording. The samples must be <150nm thick for the electron beam to penetrate them.

In selected area diffraction the transmitted electrons which are diffracted interfere with each other destructively and non-destructively and the diffraction pattern is thereby formed in the back focal plane of the objective lens. This pattern is projected to the fluorescent screen in enlarged form by the projector lenses. Structural information is obtained by comparing interplanar spacings calculated as described in Section (b) below with the ASTM data files and with the patterns obtained from known materials.

Using the ancillary STEM and EDX systems provided, selected areas of the imaged samples can also be analysed for elemental identification as follows. The TEM in STEM mode uses a fine probe of electrons scanned across the sample in the form of a raster. The transmitted primary electrons with no deflection are collected by a detector situated beneath the fluorescent screen and the amplified image is displayed on a CRT screen. During

scanning to obtain undeflected transmitted electrons for image formation under STEM, characteristic X-rays are also emitted due to inelastic scattering of the electron beam in the sample and are detected for energy measurement using EDX for elemental analysis. The measured X-ray energy spectrum which can be related to the elements in the samples is displayed on a CRT monitor or plotted on a chart recorder.

(b) Calculation of interplanar spacings

The calculation of interplanar spacings from the photographic records of the diffraction pattern usually comprises two steps, i.e. (i) determination of the camera constant, k (ii) application of the camera constant, k.

(i) Determination of the camera constant

Since the camera constant changes with conditions used in TEM, it is essential to determine the valid camera constant for every set of unknown diffraction patterns obtained under identical conditions. This was accomplished by taking a diffraction pattern of a known material, i.e. Al, Mg, under the same conditions and subsequently measuring the ring radii of the pattern to calculate the camera constant, k, using the relation:

$$k = rd$$

where r is the measured ring radii of the diffraction pattern of known material and d is the standard interplanar spacing obtained from ASTM data files. The average of nearly equal k values obtained for different rings of the known diffraction pattern is used as the standard value for the particular set of unknown diffraction patterns.

(ii) Application of the camera constant,k

Interplanar spacings are calculated by substituting the standard camera constant, k and measured ring radii of the known diffraction patterns

of the oxides in the relation:

$$d = k/r$$

The interplanar spacings, d, can then be compared with standard values for anticipated materials given in the ASTM data files.

(d) Standard interplanar spacings for anticipated oxides

(i) α-Alumina

Crystallographic plane, hkl	Intensity I/I_0	Interplanar spacings,d (A^o)
012	75	3.479
104	90	2.552
110	40	2.379
006	<1	2.165
113	100	2.085
202	2	1.964
024	45	1.740
116	80	1.601
211	4	1.546
122	6	1.514

(ii) η-Alumina

Crystallographic plane, hkl	Intensity I/I_0	Interplanar spacings,d (A^o)
110	40	4.60
220	20	2.80
311	60	2.40
222	30	2.27
400	80	1.97
333	20	1.52
440	100	1.40
533	10	1.21
444	20	1.14
553	10	1.03

(iii) γ-Alumina

Crystallographic plane, hkl	Intensity I/I_o	Interplanar spacings,d (A^o)
111	40	4.560
220	20	2.800
311	80	2.390
222	50	2.280
400	100	1.977
511	30	1.520
440	100	1.395
444	20	1.140
731	10	1.027
800	10	0.989

(iv) Magnesium Oxide, MgO

Crystallographic plane, hkl	Intensity I/I_o	Interplanar spacings,d (A^o)
111	10	2.431
200	100	2.106
220	52	1.489
311	4	1.270
222	12	1.216
400	5	1.053
331	2	0.966
420	17	0.942
422	15	0.860
511	3	0.811

(v) Magnesium Aluminate, $MgAl_2O_4$

Crystallographic plane, hkl	Intensity I/I_o	Interplanar spacings,d (A^o)
111	35	4.660
220	40	2.858
311	100	2.437
222	4	2.335
400	65	2.020
422	10	1.650
511	45	1.555
440	55	1.429
531	4	1.366

(vi) Beryllium Oxide, BeO

Crystallographic plane, hkl	Intensity I/I_o	Interplanar spacings,d (A^o)
100	91	2.337
002	61	2.189
101	100	2.061
102	22	1.598
110	29	1.349
103	24	1.238
200	4	1.168
112	16	1.148
201	5	1.128
004	1	1.096